MAGNETOSPHERE-IONOSPHERE COUPLING USING INTEGRATED MEASUREMENTS

A THESIS

SUBMITTED TO THE UNIVERSITY OF MUMBAI

FOR THE

Ph.D. (SCIENCE) DEGREE IN PHYSICS

Submitted by

SHIPRA SINHA

Under the guidance of

Dr. GEETA VICHARE

INDIAN INSTITUTE OF GEOMAGNETISM

PLOT NO. 5, SECTOR 18, NEAR KALAMBOLI HIGHWAY

NEW PANVEL (W), NAVI MUMBAI – 410218

MAHARASHTRA, INDIA

NOVEMBER 2022

Dedicated to

Mummy, Papa and Nanu.

STATEMENT BY THE CANDIDATE

As required by the University Ordinances 770, I wish to state that the work embodied in this thesis titled “Magnetosphere-Ionosphere Coupling Using Integrated Measurements”, forms my own contribution to the research work carried out under the guidance of Dr. Geeta Vichare at the Indian Institute of Geomagnetism, New Panvel, Navi Mumbai. This work has not been submitted for any other degree of this or any other University. Wherever references have been made to previous works of others, it has been clearly indicated as such and included in the Bibliography.

Signature of Candidate

Full Name: Shipra Sinha

Certified by:

Signature of Guide

Name: Dr. Geeta Vichare

Statement required under 0.770 **Statement No. 1**

I hereby declare that the work described in the thesis has not been submitted previously to this or any other University for Ph.D. or any other degree.

Statement required under 0.771 **Statement No. 2**

"Whether the work is based on the discovery of new facts by the candidate or of new relations of facts observed by others, and how the work tends to the general advancement of knowledge".

The present thesis is an attempt to address the unresolved problems and less understood theories of the magnetosphere-ionosphere coupled system, which is responsible for the exchange of energy between the Sun and Earth. High-latitude regions are significantly exposed to the energy deposition processes, like, geomagnetic substorms, solar flares and solar proton events, as compared to mid and low latitudes that are perfectly shielded by the Earth's magnetic field. Hence, this thesis focuses on understanding the dynamics at high latitude regions during magnetosphere-ionosphere coupling process using multi-instrument analysis. The ground and satellite-based instruments, that are set up to target different regions of magnetosphere and ionosphere, are used to study the interactions at those locations. The present thesis combines the results of these instruments to study geomagnetic events and utilize the datasets to widen the dimension of the analysis in terms of space and time. Chapter 1 of the present thesis provides a general overview of the solar wind-magnetosphere-ionosphere coupled system. Chapter 2 discusses the instrumentation and data analysis part of the thesis. Chapter 3, 4 and 5 elaborates the original work carried out by the candidate. The major findings are summarized in Chapter 6 with suggestions for future research.

A brief summary of the major findings of this thesis are as follow:

- All magnetic substorms may not necessarily follow the same onset mechanism of particle injection via magnetic reconnection. If a strong pressure impulse coincides with

the time of the substorms onset, injection of particles in these cases are likely to happen due to Kelvin-Helmholtz instability.

- Due to the Kelvin-Helmholtz instability, particle injection takes place from the flanks of the magnetosphere during impulse-induced substorms. This reveals new entry points of the energetic particles inside the Earth's magnetosphere during substorms.
- The injection of particles from the flanks of the magnetosphere can lead to their precipitation near dawn and dusk. This shifts the onset location of a substorm from typical midnight sector to dawn and dusk.
- The categorization of a substorm based on its triggering agent and onset mechanism, as IMF Bz induced or IMF By induced or impulse-induced, can be done using the SuperMAG SML-LT index. If a substorm is IMF Bz-induced, the SML-LT index shows maximum dip in the midnight sector. If it is IMF By-induced, then SML-LT index has maximum dip in the near-midnight sector. And, if a substorm is impulse-induced, maximum dip in the SML-LT index is centered near dawn/morning sector. The idea of identifying the substorm type using SML-LT index is new and is the contribution of the present thesis. Using SML-LT index for the classification of substorms becomes important in cases when multiple triggering agents are present and it is difficult to categorize them by simply looking at the interplanetary conditions.
- Substorms are not usually isolated, and more than one triggering agent is frequently present at or before the time of the commencement. In cases where multiple triggering agents are present, the next step is to identify which driving mechanism will dominate over the other and how a substorm will evolve. Our analysis reveals that in such cases, the intensities of the two elements, i.e., interplanetary magnetic field (IMF) (Bz and By) and pressure pulse, will determine the likelihood of the dominance. If pressure pulse is sufficiently strong to overcome the impact of magnetic reconnection, the substorm will have its onset and expansion from a local time sector away from midnight.
- For cases where a substorm has its onset and expansion from a local time sector away from midnight, either a pressure pulse or a large IMF By component could be responsible. However, the two cases are different in terms of the mechanisms that leads to the onset. IMF By induced substorms follows the magnetic reconnection process and the impulse-induced substorms follows the viscous interaction process for the injection of particles. During IMF By induced substorms, the deviation in the onset location is mostly limited to pre- and post-midnight sectors and does not reach dawn and dusk.

- A direct dependency of solar zenith angle and flare intensity on the magnitude of solar flare induced sudden cosmic noise absorption (SCNA) for two high latitudes near conjugate stations are shown. In addition, latitudinal position is a very important factor for determining the effects of SCNA at high latitudes. If a station falls in the auroral or polar region, the effects of previously occurred substorm and polar cap absorption (PCA) can alter the background condition. This leads to variations in the actual effects of solar flares.
- The variations in the effects of solar flare get further amplified if there is an ongoing PCA event coinciding with the time of SCNA. The perturbation in the solar flare effects will then depend upon phase (inclining or declining) of PCA.

Statement required under 0.771 **Statement No. 3**

"The source from which this information has been derived and to the extent to which he has based his work on the work of others, and shall indicate which portion or portions of his thesis he claims as original".

The information mentioned is derived by the candidate during the course of research work which is reported in the thesis. Some of the results presented in the thesis are published in the following research articles:

- Papers Published and communicated in Journals

1. **Shipra Sinha**, Geeta Vichare and A. K. Sinha. 'A comparative analysis of the role of Interplanetary Magnetic Field (IMF) and Sudden Impulse (SI) in triggering a Substorm'. *Advances in Space Research* (2022), doi: https://doi.org/10.1016/j.asr.2022.08.037

2. Mitsunori Ozaki, Kazuo Shiokawa , Richard B. Horne , Mark J. Engebretson4, Marc Lessard5, Yasunobu Ogawa , Keisuke Hosokawa , Masahito Nose , Yusuke Ebihara , Akira Kadokura, Satoshi Yagitani , Yoshizumi Miyoshi , Shion Hashimoto , **Shipra Sinha**, Ashwini K. Sinha, Gopi K. Seemala , and Chae-Woo Jun "Magnetic Conjugacy of Pc1 Waves and Isolated Proton Precipitation at Subauroral Latitudes: Importance of Ionosphere as Intensity Modulation Region." *Geophysical Research Letter* (2021), doi: 10.1029/2020GL091384

3. **Shipra Sinha**, Geeta Vichare and A.K. Sinha**. '**Solar Flare associated Cosmic Noise Absorption (SCNA) at near conjugate stations: Maitri (70.75°S, 11.75°E) and Abisko (68.4°N, 18.9°E)'. Under Revision in *Advances of Space Research*.

4. **Shipra Sinha**, Geeta Vichare, A. K. Sinha, Harald U. Frey, Rahul Rawat, Gopi K. Seemala and Antti Kero. 'Differences in the characteristics and triggering mechanisms of two successive substorm onsets on 21st January 2005'. Under Review in *Journal of Atmospheric and Solar Terrestrial Physics*.

- Papers presented in National and International conferences

1. **Shipra Sinha**, Sneha Gokani, Rahul Rawat, Ashwini K Sinha and Geeta Vichare. 'Sub-auroral characteristics of super-substorms as observed from Indain Antarctic station Maitri'. URSI AP-RASC, March 9-15, 2019, New Delhi, India. *IEEE Xplore* DOI: 10.23919/URSIAP-RASC.2019.8738204

2. **Shipra Sinha**, Geeta Vichare, A. K. Sinha and Rahul Rawat. Cosmic Noise Absorption Characteristics of Supersubstorms. NCPS, 20-22 August, 2019, Vasco-da-Gama, Goa.

3. **Shipra Sinha,** Geeta Vichare, A. K. Sinha, Rahul Rawat and Gopi Seemala. Characteristics During Impulse-Induced Substorm: A New type of Substorm. IAGA-IASPEI, participated online from 20-27 August, 2021

4. **Shipra Sinha**, Geeta Vichare, Sneha Gokani, A. K. Sinha, Harald U. Frey, Rahul Rawat, Gopi Seemala and Antti Kero. 'Cosmic Noise Absorption Characteristics during

the Impulse-Induced Supersubstorm of 21st January 2005'. URSI-GASS, Participated online from August 28 to September 4, 2021. *IEEE Xplore* DOI: 10.23919/URSIGASS51995.2021.9560256

5. **Shipra Sinha**, Geeta Vichare and A. K. Sinha. Role of IMF Bz and Sudden Impulse in triggering a Substorm. American Geophysical Union (AGU) Fall Meeting, participated online from 13-17 December, 2021.

6. **Shipra Sinha,** Nilam Bhosale, Geeta Vichare, S. Tulasiram and A. K. Sinha. Low-latitude Geomagnetic H-component Variations during Impulse-Induced Storm time Substorms. 15th Quadrennial Solar-Terrestrial Physics (STP-15) symposium, 21-25 February 2022 (virtual platform).

7. **Shipra Sinha,** Geeta Vichare, A. K. Sinha and Rahul Rawat. Hemispheric Asymmetry in the Cosmic Noise Absorption Response during Intense Solar Flare Events. 10th SCAR Open Science Conference, 1-10 August, 2022 (virtual platform).

8. **Shipra Sinha**, Geeta Vichare and A.K. Sinha. Categorization of Substorm Triggering Mechanism based on the Ground Observations. 44th COSPAR Scientific Assembly, participated online from 16-24 July, 2022.

- Awards, Training and Workshop

1. Young Scientist Award, 34th General Assembly and Scientific Symposium, URSI, Rome, Italy, 29 August-4th September, 2021.

2. SCOSTEP Visiting Scholar fellowship Awardee, 2021, for visiting GSFC, NASA.

3. Summer Member of 39th Indian Scientific Expedition to Antarctica, November 2019-February 2020.

4. International School of Space Science, 1-5 February, 2021 (Virtual Participation).

Statement required under 0.771 **Statement No. 4**

"Where a candidate presents joint work, he shall clearly state the portion which is his own contribution as distinguished from the portion contributed by his collaborators."

The complete analytical and observational work are carried out by the candidate in the papers mentioned in Statement No. 3. Dr. Geeta Vichare is the guiding teacher and has helped in formulating the problems, interpreting the observations, as well as provided guidance and encouragement throughout the course of the work. Dr. A. K. Sinha have also contributed towards formulating the problems and interpretating the results obtained during the course of research work presented in this thesis.

(Dr. Geeta Vichare) (Shipra Sinha)

Guiding Teacher Candidate

Acknowledgements

It is difficult to summarize in few pages a life time of memories, challenges and support that I have received during the last 5 years of my Ph.D. journey, but I will give it a try. Undoubtedly, this has been a great learning experience for me, not just in terms of science but also in terms of life. I have grown and evolved to be a better version of myself, and the credit goes to so many people around me.

With a heart full of gratitude, I express my sincere thanks to my supervisor Dr. Geeta Vichare, who has been a great mentor, and I look up to her every day. She has guided me, supported me, encouraged me and brought the best out of me in the most efficient way. Without her perseverance and motivation, I might not have made it to this point. It will be my aim to emulate her strong work ethics and her relentless pursuit of excellence in whatever she does. I consider myself extremely fortunate to have been associated with her in my Ph. D. journey.

I am blessed to have not just one, but two mentors, who have been and will be there to guide me in my journey. My deepest gratitude is extended to Dr. Ashwini K. Sinha, who was solely responsible for beginning my research career. His immense knowledge and understanding of the subject have always amazed me and inspired me. His constant guidance, encouragement and support have helped me grow in life.

I extend my sincere thanks to Mr. Rahul Rawat, who has never hesitated to spare his valuable time for helping me out in my analysis, especially during my initial years of research. I would also like to thank Dr. Gopi Seemala for his guidance and encouragement.

I wish to thank Dr. A. P Dimri, Director, Indian Institute of Geomagnetism, for his cooperation and encouragement during the course of my thesis. I am highly obliged to Dr. D. S. Ramesh, ex-director of IIG, for the opportunities he gave me to grow as a researcher. With his ultimate support, encouragement and faith in me, I was able to become the first female research scholar from IIG to participate in the Indian Scientific Expedition to Antarctica. His appreciation in every small and big achievement of mine has always strived me to work harder and do better in life.

I take this opportunity to convey my deepest gratitude to whole APC committee for their support, suggestions and valuable discussions during annual talks. I would like to thank Dr. Smita Chandra and entire library staff for making rare references and books available whenever

needed. I also thank Mr. Mahendra Doiphode, Mrs. Nanda Shah and entire computer section for their assistance during my tenure. I am very thankful to the administrative section for their cooperation, help and support.

In no words I could ever express my love and gratitude to my friends in IIG who have been like a family away from home. From day one till today and beyond, if there is one person who has been and will be my strongest ally, it is Adhitya Pavithran. She showed me a kind of friendship, I never knew existed after school days. From my happiness, to pain, to secrets, to important documents, she owns it all, including a piece of my heart.

The bond that I share with Dr. Aditi Upadhay is one that I will cherish forever. Being with her feels like what a sister of same age would have been. From having fun to having fights, from laughter to sorrows, we have seen it all together like siblings. We reflect each other's character so much, that most of the times I haven't felt the need to express myself in words.

I have made great friends in IIG. Atul Prajapati, Nilesh Chauhan, Nilam Bhosale, Pankaj Soni and Sreelakshmi are among them, and I share a very special bond with all of them. They are the people I have always counted on and I know will be there for me whenever I need them.

I have been extremely lucky to have found lifelong friends in Yashodhara and Jahnavi. I know them from decades and they have been there for me always. The way they encourage and appreciate me, gives me so much strength. Sumit has been my constant support since a very long time and someone I have always counted on. He has walked me through most of my hard days and he is the first person I could think of when in trouble. Towards the end of my Ph.D. journey, I discovered a great friend in Ranjan. He helped me overcome my difficult times, especially during the past few months, and I cannot thank him enough for that. With them, I can share anything and everything I want. These people are truly my treasure for life.

I cannot put words to the feelings that I have today for my mother, father and brother. My entire family is my biggest support system. Their care is beyond measure, their love is endless. I am what I am is because of them, and I do what I do is for them.

I have always been a confident person and have believed in myself. But today, I am also very proud of myself. And I thank each and every person who has brought me to a point where I can say this.

Shipra Sinha

Contents

List of Figures

List of Tables

Chapter 1

Introduction

1.1 The Sun-Earth Interaction: An Overview

The Sun-Earth interaction refers to the physical mechanisms occurring in the solar-terrestrial environment that leads to energy transfers. The Sun continuously emits energy in the form of electromagnetic radiations and highly charged particles, emerging radially outward from its surface. The radiations travelling at a speed of light (~$3x10^8$ m/sec) reaches the Earth in about ~8 minutes and ionizes the sun-lit part of the Earth's atmosphere. The charged particles, on the other hand, are frozen-in with the Sun's magnetic field and they travel together in the interplanetary space in the form of solar wind. The solar wind is in the state of plasma and flows at supersonic speed (~500 m/sec). When the solar wind hits the Earth's magnetosphere, it leads to the interaction of energetic charged particles with the electric and magnetic fields in the Earth's environment. The energy-exchange between the Sun and the Earth are mainly governed by these interactions, which are quite complex and non-linear in nature. Over the past few decades, enormous efforts have been made to understand the solar-terrestrial interactions and their effect on Earth. Scientists have performed various remote sensing and in-situ experiments, using several ground and satellite-based instruments, to study the interaction mechanisms right from the Earth's vicinity to the surface of the Sun. From years of observations, measurements and analysis, we are now much advanced in our understanding of the solar-terrestrial environment. This understanding has helped us in monitoring and forecasting the directly affecting space weather and space climate events. However, with the increasing day-to-day developments in the navigation, communication, satellite and spacecraft technologies, it is crucial to advance our present understanding of the Sun-Earth interaction and associated effects.

From our present knowledge of this system, we know that the solar energetic particles do not have a direct entry into the Earth's surface due to its protective shield of dipole magnetic field. The structure of the Earth's magnetic field, however, changes continuously because of the pressure of the incoming solar wind. The geomagnetic field lines get compressed from the dayside and elongates in the night-side, due to this pressure, forming a bow shock. The space around the Earth consisting of the geomagnetic field and trapped charged particles that forms the Earth's magnetosphere. The elongated night-side magnetosphere is also referred as the 'magnetotail region'. Our present understanding of the solar wind particle entry into the magnetosphere is explains via the injection from the night-side magnetotail region through magnetic reconnection. There are several ongoing research till date to understand completely the process of magnetic reconnection. According to early researchers (McPherron, 1970; Mcpherron, 1979; Rostoker et al., 1980; Tsurutani & Meng, 1972), this reconnection happens at the subsolar point when southward directed interplanetary magnetic field (IMF) merges with the northward directed geomagnetic field. This leads to the formation of new field lines which has one end attached to the Earth's surface and the other end free to move in the space. This newly formed magnetic field lines, along with the magnetic flux, is then eroded from the dayside magnetopause to the night-side magnetotail region due to the incoming solar wind. This period of enhanced convection is often referred to as the 'loading' mechanism. When the loading becomes unstable, the particles get unloaded and reach the Earth's surface following the field lines. The process of loading and unloading of charged particles from the night-side magnetotail region into the Earth's atmosphere at high latitudes following the field lines is called 'magnetospheric substorm' (Burch, 1972; Tsurutani & Meng, 1972; X. Zhou & Tsurutani, 2001). This whole process forms an essential part of the solar wind-magnetosphere-ionosphere coupling system and the sections ahead will discuss all the stages of this coupled system in detail.

1.2 The Sun and its Activity

The Sun is a massive ball of hot, ionized gas (or *plasma*), that consists mainly of hydrogen (~90%) and helium (~10%). It is situated at a distance of ~1.49×10^8 km from Earth and has a radius of ~7×10^5 km. Though the distance between the two might sound huge, the Sun is the nearest star from Earth and its proximity makes it of the 9most immediate interest. The mass of the Sun is 1.99×10^{33} g, which is about 330 thousand times that of the Earth. It is estimated that the temperature of the center of the Sun is as high as 1.5×10^7 K. The energy is produced in the core of the Sun through nuclear fusion of hydrogen into helium.

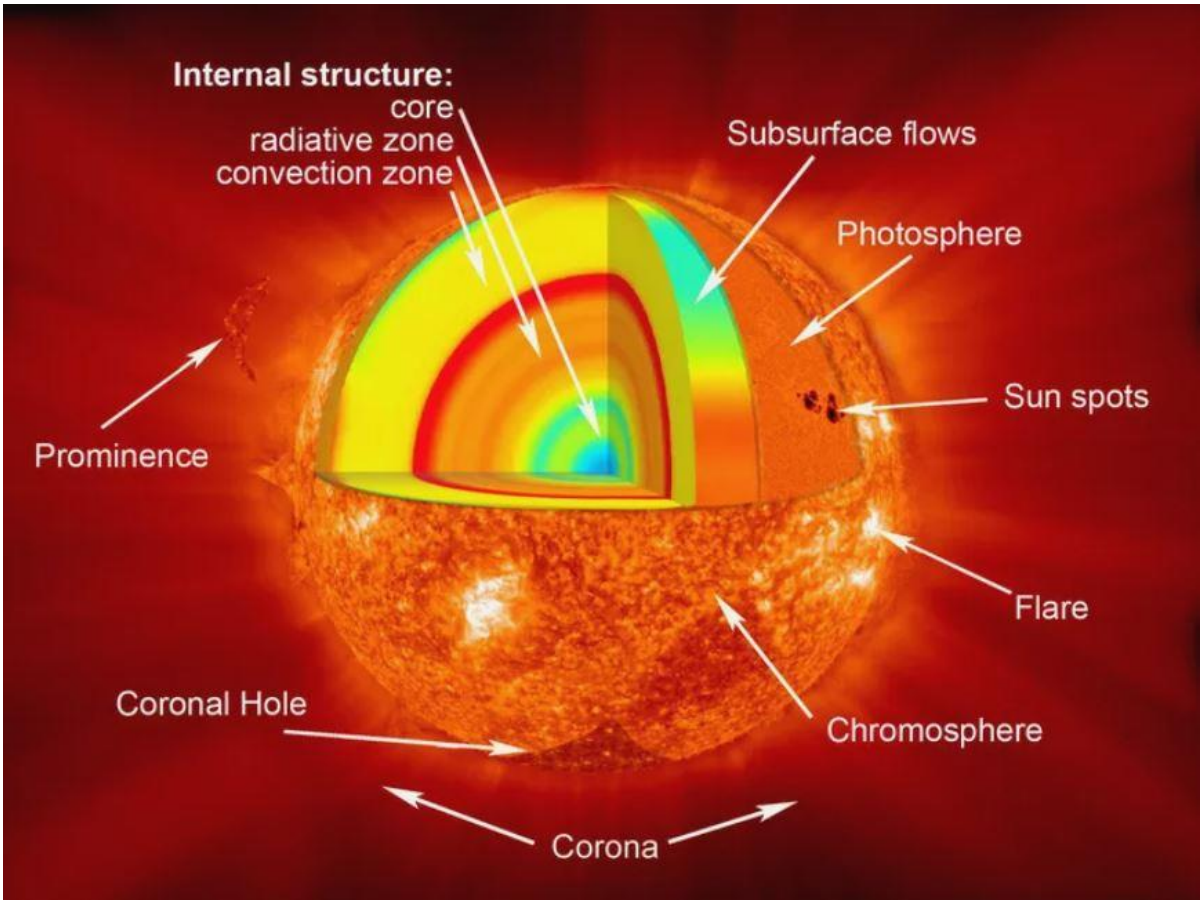

Figure 1. 1 The Sun, its layered structure, exterior surface and atmosphere. [Credit: NASA, https://www.thoughtco.com/basic-information-about-the-sun-3073700]

Figure 1 shows the layers of the Sun's structure from its core to the surface and beyond. The *radiative zone* and the *convection zone* surround the core. Near the Sun's equator, the convection zone rotates with a period of 26 days, while at poles, it rotates with a period of 37 days. The differential rotation of this nonlinear dynamo and convection in the interior of the Sun produces magnetic field that regulates the solar activity. The so-called *solar cycle* is a result of variations in this activity.

Photosphere is the boundary separating the interior of the Sun from its atmosphere. It is what humans perceive to be the Sun's "surface", since it accounts for the majority of the total solar luminosity emitted by the Sun. The regions of the atmosphere of the Sun are defined according to their temperature and density. The lower region is called *chromosphere*, having a thickness of about 2000-3000 km and temperature of ~4300 K to 10^4 K, from bottom to top. The uppermost layer is called *corona* which is surprisingly much hotter than the photosphere. The

temperature of the corona is ~$2x10^6$ K and that of the photosphere is nearly 5800 K. As the photosphere is the brightest region of the Sun, the corona can be seen only on full solar eclipse days when the photosphere is completely blocked out. The solar corona extends into the outer space where it gradually becomes the part of interplanetary medium forming the *solar wind*.

1.2.1 Solar Wind

The *solar wind* is a stream of charged particles, which are in the plasma state, released by the solar corona into the space. Since these particles are constantly heated, the gravity of the Sun is unable to hold down this plasma. It then moves following the lines of the radially outward extending magnetic field of the Sun. These magnetic field lines are wound up into a massive spinning spiral as the Sun rotates (once every 27 days), producing a steady stream of solar wind in the process. Such emissions, or streamers, are assumed to originate from large bright areas of the Sun's corona known as *coronal holes*. The magnetic field lines originating from these coronal holes are dragged by the solar wind into the space forming the interplanetary magnetic field (IMF) which envelops every planet in our solar system. Due to high conductivity, the solar wind magnetic field lines remain frozen into the plasma as it transports into the interplanetary medium.

The speed, density, and direction of the magnetic field imbedded in the solar wind are all important factors that affects the space weather. Solar wind has speed ranging from 400 to 800 km/s depending upon the region of origin on the Sun’s surface. Large, enduring coronal holes at the sun's north and south poles cause the solar wind to travel quickly through high latitudes. The slow speed wind, with speeds of around 400 km/s, is the most prevalent kind of solar wind on the equatorial plane, around which the Earth and the other planets revolve.

1.2.2 Sunspots and Solar Cycle

Sunspots are areas on the photosphere having the strongest magnetic field, about 2,500 times stronger than Earth's, and much higher than anywhere else on the Sun. These strong magnetic field causes the magnetic pressure to rise and the atmospheric pressure in the surrounding region decreases. The hot and fresh gases from the Sun's interior are, thus, prevented from flowing to the surface. Hence, they form regions of comparatively lower surface temperature and appear darker than the surrounding regions on the visible solar disc. A typical sunspot has an *umbra*, which is a dark region, and a *penumbra*, which is a lighter region, around it. The temperature of the photosphere is about 10,000 °F, while the umbra is only 6,300 °F. Sunspots are quite large, the average size being the same as the size of the Earth. The magnetically

active areas linked to sunspots are where most of the solar activities originate, like the solar flares and CMEs (Coronal Mass Ejection). Secondary solar phenomena such prominences, reconnection events, and coronal loops are present in conjunction with sunspots.

Sunspots typically come in opposite magnetic polarity pairs. The solar cycle, or periodic increase and reduction in the number of sunspots, lasts for around 11 years. A single sunspot may last for a few days to several months. Since the year 1749, there have been 24 complete solar cycles, during which the number of sunspots has varied from a minimum to a maximum and then back to the next minimum during roughly 11-year intervals. High sunspot activity during the solar cycle maxima, results in a sharp increase in ultraviolet radiation, which can have significant effects on the Earth's atmosphere. The solar cycle 24 was completed in the year 2020 and the maxima of this cycle was seen in the year 2014 when about more than 100 sunspots were observed in a month. The number of sunspots observed every month in the solar cycle 23, 24 and ongoing 25 is shown in figure 1.2.

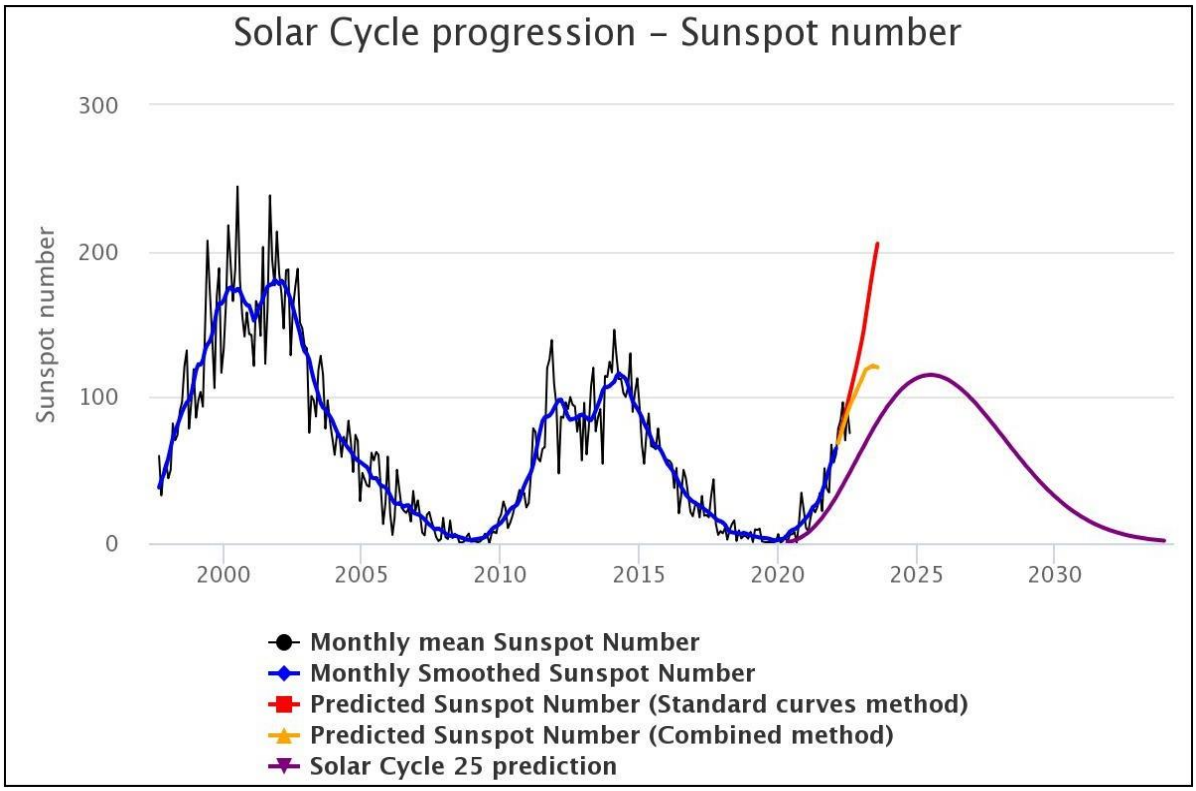

Figure 1. 2 The monthly average number of sunspots observed in the solar cycle 23, 24 and ongoing solar cycle 25. [Credit: WDC-SILSO, Royal Observatory of Belgium, Brussels. https://www.spaceweatherlive.com/en/solar-activity/solar-cycle.html]

1.2.3 Solar Activity

A *solar flare* is a massive explosion that occurs when huge magnetic loops, called *prominences*, built up in the solar atmosphere, is suddenly released. They release a burst of radiation that includes radio waves, X-rays, and gamma rays and covers the entire electromagnetic spectrum. Particles in the solar atmosphere, such as electrons, protons, and heavy nuclei, are heated and accelerated as the magnetic energy is released during a solar flare eruption. Typically, a flare releases energy at a rate of 10^{27} ergs per second. Large flares have an energy output of up to 10^{32} ergs. This energy is 10 million times more powerful than that of a volcanic eruption on Earth. On the other hand, it represents less than a tenth of the Sun's entire daily energy output. A solar flare normally goes through three stages. The release of magnetic energy is triggered during the *precursor stage*, which comes first. In this stage, soft x-ray emission is discovered. Protons and electrons are accelerated to energies more than 1 MeV in the second stage, often known as the *impulsive stage*. Radio waves, hard X-rays, and gamma rays are released during the impulsive stage. In the third stage, known as the *decay stage*, soft x-rays gradually accumulate and decay. The time between these stages can range from a few seconds to an hour. According to their brightness in X-ray wavelengths, scientists categorize solar flares in three categories. X-class flares are large, significant events that have the power to cause global radio blackouts and persistent radiation storms in the upper atmosphere. M-class flares are medium intensity flares that may also result into brief radio blackouts. M-class flares can occasionally be followed by weak radiation storms. C-class flares are minor and have negligible effects on Earth when compared to X- and M-class occurrences.

Large-scale magnetized plasma formations known as *coronal mass ejections (CMEs)* are released from the Sun and carried into the heliosphere. CME eruption removes most of the built-up magnetic energy and plasma from the solar corona and releases it into the interplanetary space. Hence, they are responsible for most of the severe space weather effects on Earth as well as at other planets and spacecraft throughout the heliosphere. CMEs have cool prominence material (8000 K) in the core and coronal material at a temperature of a few MK in the outer structure. The compressed sheath behind the shock when the CME is driving it may have a higher temperature and density than the surrounding corona. The frontal structure of CMEs near the Sun is anticipated to contain the inner corona, whose density is typically 10^8 cm^{-3} (Gopalswamy, 2006). In a specific eruptive event, the CME and flare are believed to be two separate forms of the same energy release (Harrison, 1995). Solar flares always accompany CMEs, particularly if

we use soft X-ray enhancement to spot flares. The reverse is, however, not true as all flares are not associated with a CME.

High Speed Solar Wind (HSSW) streams (>750–800 km/s) from coronal holes collide with slow streams (300–400 km/s) near the ecliptic plane to create areas of high magnetic field and is known as *Corotating Interaction Regions (CIR).* In times of low to moderate solar activity, corotating interaction areas may be important in determining how the sun modulates galactic and anomalous cosmic rays. Both CME and CIR results into disturbances on Earth known as geomagnetic storms. Storms that are CME-driven are more common during solar maximum, whereas storms that are CIR-driven are more common during a solar cycle's decreasing phase. As a result of the Sun's rotation, CIR-driven storms repeat with a period of around 27 days, primarily during a solar cycle's decreasing phase, but CME-driven storms have an erratic occurrence pattern with the highest frequency during solar maximum. Additionally, CME-driven storms have a recovery period that lasts for only a few days, but CIR-driven storms might have a recovery phase that lasts for several days. Storms with sudden onsets (SSC) are connected to interplanetary shocks caused by CMEs, whereas storms with slow onsets are caused by HSSW streams.

1.2.4 Solar Energetic Particle

Solar Energetic Particle (SEP) are high-energy plasma that originate from the Sun during solar activities. They consist of protons, electrons and other heavy ions emerging from the solar corona, having energies from tens of keV to even GeV. In extreme cases, SEPs can be accelerated within 5-10 solar radii (5% of the Sun–Earth distance) that can reach Earth in a matter of minutes. Accelerated solar energetic particles that originate either from a solar flare site or by shock waves associated with CMEs, gives rise to *solar particle events or SPE*. Solar energetic particles are capable of escaping into interplanetary space by following the interplanetary magnetic field. During SPE, also known as Solar Proton Events, the Earth's magnetic field directs solar energetic particles towards the north and south poles, where they can enter the upper atmosphere of polar regions.

When energetic protons are guided into the polar regions, they collide with the elements of the atmosphere and release energy through ionization. Frequently the energies of these particles are lost at around 50-80 km in altitude from the Earth’s surface resulting into enhanced ionization of the atmosphere. As a result, most of the energy from radio signals is absorbed here,

making this region crucial for radio communications. Incoming energetic protons has the potential to even entirely block all radio communications throughout the polar regions. Increase in radiation have also been observed during SEPs in high altitude commercial transpolar aircraft flights, although a warning mechanism prevents these impacts by informing pilots to reduce their cruising altitudes. The likelihood of an influence from SPEs on aircraft flights away from the polar areas is significantly lower. Even the spacecrafts can be electrically charged by energetic protons from SPEs to amounts that may harm the electronic components. Astronauts who are outside of the magnetosphere's shield may be exposed to significant proton radiation. The impacts can be reduced, though, if the astronauts are in a low-Earth orbit area. With orbital inclination, proton radiation levels in low earth orbit rises consequently, as spacecraft gets nearer to the polar regions.

1.3 The Earth's Magnetosphere

It was in the 1600, when research into the magnetosphere was initiated after William Gilbert discovered that the magnetic field on Earth's surface mirrored that of a terrella, a small, magnetized sphere. The dynamo theory hypothesis, first proposed by Walter M. Elsasser in the 1940s, connects the movement of the molten iron in outer core of the Earth to the magnetic field of the planet. Earth's magnetic field is, thus, believed to be generated by electric currents produced during the convective motion of these molten iron. Scientists have been able to investigate the fluctuations in the Earth's magnetic field as functions of time, latitude, and longitude using magnetometers. After several centuries of further investigations, the Earth's magnetic field is now understood to be highly complex, although it can still mostly be considered as a dipole with north and south poles similar to a basic bar magnet. Magnetosphere is the space around Earth within which this geomagnetic field is confined. Although the Earth's magnetic field is dipole in nature, the structure of the magnetosphere is not symmetric in the day and night sides. The pressure exerted by the incoming solar wind directly contributes to this distortion. In the sunward side, the magnetosphere is compressed to be confined to 6-10 Earth radii (Re) creating a *Bow Shock* as shown in fig 1.3. The length of the night-side magnetosphere, which is dragged out by the solar wind, can be up to 1000 times that of the Earth radii. The *Magnetotail* is the name given to this extension of the magnetosphere. *Magnetopause* is the outer limit of the restricted geomagnetic field of Earth. Most of the solar wind particles that hits the bow shock get heated up, slow down, and diverts around the Earth forming the *magnetosheath* region. The magnetosphere of the Earth is a very dynamic structure that reacts strongly to the solar activities. The structure of the Earth's magnetosphere is shown in figure 1.3.

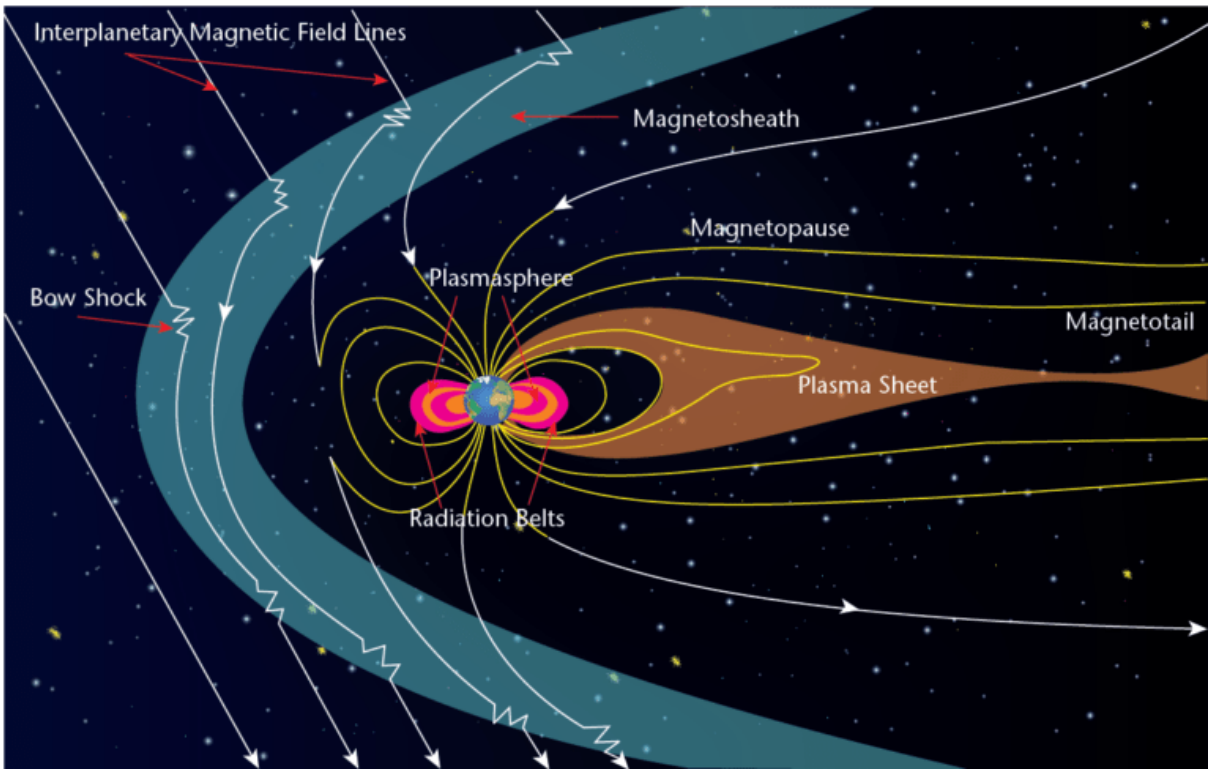

Figure 1. 3 Schematic diagram of the Earth's magnetosphere. [Credit: https://physicsteacher.in/2022/01/18/]

1.3.1 Geomagnetic Field and its Components

Since Earth's magnetic field is a vector quantity, its strength and direction can be determined at every location in space. We require three quantities in order to completely describe it. These include:

- three orthogonal strength components (X, Y, and Z);
- the total field strength and two angles (F, D, and I); or
- two strength components and an angle (H, Z, and D)

Earth's magnetic field has the following elements: (i) total intensity (F), (ii) vertical component (Z), (iii) horizontal component (H), and the (iv) north (X) and (v) east (Y) components of the horizontal intensity. Declination (D) and inclination (I), which are both expressed in degrees, are the components that describe the direction of the field. The angle between true north and magnetic north is called "D," and it is positive when the angle is measured east of true north

and negative when it is measured west. I is the angle between the total field vector (F) and the horizontal plane. These components are shown in figure 1.4.

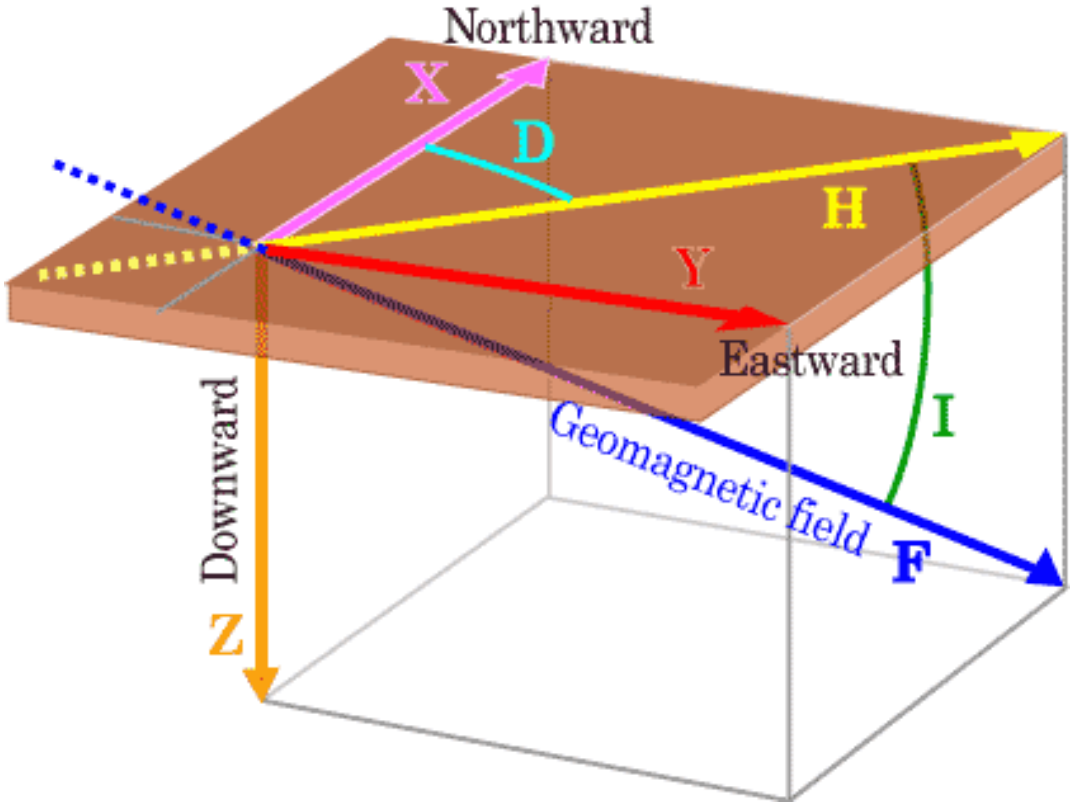

Figure 1. 4 Earth's Magnetic Field and its Components. [Credit: https://wdc.kugi.kyoto-u.ac.jp/element/eleexp.html]

Equations (1.1) to (1.5) relates the values of the elements of Earth's magnetic field as follows:

$$F^2 = (X^2 + Y^2 + Z^2)^{1/2} = (H^2 + Z^2)^{1/2} \quad (1.1)$$

$$H = F * \cos(I) \quad (1.2)$$

$$Z = F * \sin(I) \quad (1.3)$$

$$X = H * \cos(D) \quad (1.4)$$

$$Y = H * \sin(D) \quad (1.5)$$

At the surface, the main magnetic field of the Earth is constantly changing over time. Secular variations are long-term changes in the components of Earth's magnetic field across time. Some of these variations are established, while research is still being done on their periodicities.

Variations with spans of 60-80, 500, 2000, or 5000 years and more, for instance, have been documented. Secular variations are mostly due to the changes in the Earth's interior, while more rapid changes occur due to currents in the ionosphere and magnetosphere.

1.3.2 Inner and Outer Magnetosphere

The inner magnetosphere starts at an altitude of about 1000 km from the Earth's surface and extends up to 6-8 Earth radii (Re) at both day and night sides, excluding the regions above the poles. It mostly consists of cold and dense plasma and is comparatively stable than the huge outer magnetosphere, whose plasma is significantly more energetic. The inner and outer radiation belts (Van Allen & Frank, 1959) consisting of energetic particles (>~100 keV), the encircling ring current (~1-100 keV) and the plasmasphere (~eV), are all confined within the inner magnetosphere. Due to the inhomogeneous magnetic field lines that thread the inner magnetosphere and the highly dynamic behavior of the regions that border and supply plasma to it, the plasma-velocity distributions in this region are extremely anisotropic and non-Maxwellian.

The *plasmasphere,* shown in fig. 1.3, is the region in the inner magnetosphere consisting of cold and dense plasma, having the number density of plasma higher than the ambient number density. These plasmas have a number density greater than ~10^3 cm^{-3} at L=2 (distance equal to twice the Earth radii from the center) and steadily decreases with increasing L (Carpenter & Anderson, 1992). At plasmapause, the density abruptly decreases by an order of magnitude. The magnetic local time (MLT) and magnetic activity affect the L-value of the plasmapause. The plasmapause is at L=7 during magnetic quiet times and reaches L=2 during disturbed times (Carpenter, 1966; Chappell et al., 1970). The plasmasphere has a bulged shape on the dusk side when mapped to the equatorial plane which is due to the combination of the convection and corotation electric fields. The formation of the plasmasphere is suggested by three principal processes: (1) the loss of thermal plasma from the ionosphere along the magnetic field line (N. Singh & Horwitz, 1992), (2) pitch angle scattering of the supplied plasma (Schulz & Koons, 1972), and (3) drift motion of thermal plasma due to large-scale electric fields (Nishida, 1966).

The inner magnetosphere also consists the radiation belts, which are regions of enhanced populations of energetic electrons and protons of solar origin surrounding the Earth. These belts are highly dynamic regions, and their radius increases and decreases on time scales of minutes to years. These regions can be harsh for the satellites due to the high levels of radiation caused by the energetic electrons and protons present here. It is still not well understood how the

energization, transport and loss of these radiation belt particles happen, even though number of satellites have made observations ever since its discovery in 1958 by James A. Van Allen.

The outer magnetosphere consists of a thick plasma sheet, which is centered in magnetotail, having density 0.3-0.5 ions/cc. At local midnight, the plasma sheet is normally about 6 Re thick. Due to reductions in temperature and density, the plasma sheet thickness at 60 Re is nearly half that at 18 Re, and the energy density is reduced by a factor of around 5. Occasional injection of fresh solar origin plasma from the night side makes the outer magnetosphere very dynamic. Two tail lobes exist north and south of the plasma sheet that has relatively smooth magnetic field. In comparison to plasma sheet, the plasma in the high-latitude tail region (attached to the polar cap) is very thin and cold. Two enormous bundles of almost parallel magnetic field lines make up the majority of the tail's volume. While the southern bundle points away from Earth and is connected to the southern polar region, the bundle north of the equator points toward Earth and connects to a roughly circular region that includes the northern magnetic pole. These two bundles, referred to as the "tail lobes," are located far from Earth. Satellites have discovered them to be clearly defined even at a distance of 200–220 Re. The lobes are almost completely empty at those distances with densities being around 0.01 ion/cc or even less.

1.3.3 Motion of Charged Particles inside the Magnetosphere

When a plasma interacts with the Earth's magnetic field, the ions and electrons in the plasma move according to the magnetic field lines due to the Lorentz Force exerted on them. In addition, Birkeland currents and heat movement also influence the motion in a way that it eases the motion along them and blocks the motion in the other direction. Three types of common particle motions are traversed by a charged particles in the Earth's dipole field: gyration, bounce, and drift. The trajectory of an electron performing the three motions are shown in fig. 1.5. In order to understand these motions, single particle approach is used, where the assumptions are made that the charged particles do not interact with each other and does not affect the magnetic field significantly.

The Lorentz equation 1.6 describes the gyro motion of a particle in a uniform magnetic field $\vec{B}$.

$$m\frac{d\vec{v}}{dt} = q(\vec{v}X\vec{B}) \qquad 1.6$$

Where, m is the mass, q is the charge and $\vec{v}$ is the velocity of the particle in motion.

The particle will perform a helical motion parallel to the magnetic field as shown in fig 1.5. The circular part of this motion is called the '*gyromotion*' or '*cyclotron motion*'. The angular frequency ' ω_g ' and the gyro-radius 'r' will be given by equation 1.7 and 1.8.

$$\omega_g = \frac{qB}{m} \tag{1.7}$$

$$r = \frac{mv}{qB} \tag{1.8}$$

The magnetic force does not perform any work and neither consumes nor produces energy because it is perpendicular to the velocity. As a result, magnetic fields (like the one found on Earth) have the power to significantly alter particle motion without requiring an external source of energy. The motion is essentially helical, however, due to the nonuniformity of the geomagnetic field, two extra modes of motion are introduced on both broad spatial and temporal scales. These are the bounce motion and the drift motion (figure 1.5).

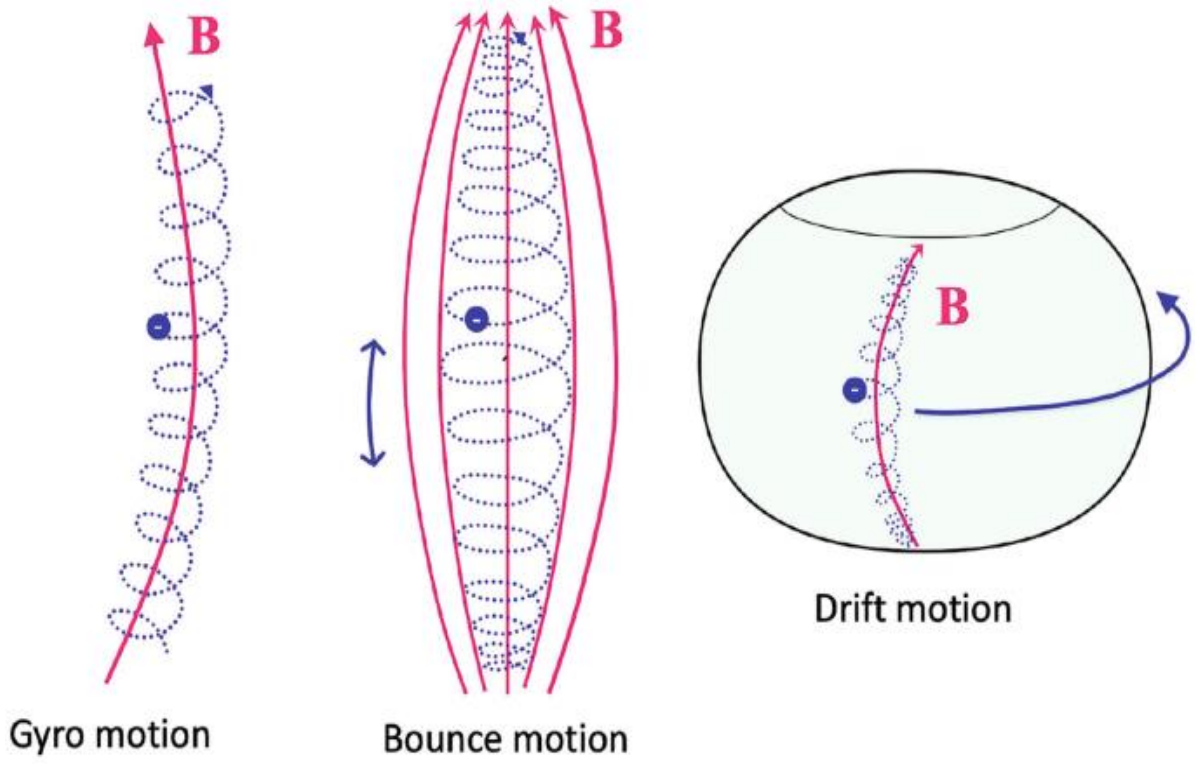

Figure 1. 5 Representation of the types of motions performed by an electron in the geomagnetic field. [credit: https://link.springer.com/chapter/10.1007/978-3-030-82167-8_2]

The *bounce motion* is the periodic north-south oscillation along the "guiding line" or field line, that passes through the helix. As the particle goes closer to areas with a greater magnetic field, it moves more slowly and reflects back at "mirror points." The bounce motion has a longer duration than the cyclotron motion and is significantly slower.

The particles are propelled across field lines and in the equatorial (azimuthal) direction by the drift motion, which is perpendicular to the bounce motion. Drift motion generally accelerates with increasing distance. If no collision among particles or interactions with EM waves occur, the particles in dipole-like fields are stuck on closed "drift shells." Compared to the bounce motion, the drift motion is significantly slower and has a longer time period (Öztürk, 2012).

1.3.4 Magnetospheric Current System

A complex current system is known to exist in the near-Earth space that is related to the geomagnetic field through Ampere's law. The magnetosphere system includes: (a) a large-scale current system in the dayside flowing across the magnetic field lines, (b) currents flowing in the tail region, (c) Birkeland currents, flowing in and out of auroral regions close to the North and South Poles along geomagnetic field lines; and (d) the ring current, circulating at ~2-4 Re around the earth's equator. Figure 1.6 shows a schematic view of the magnetospheric current system.

In the magnetosheath region, the particle pressure is of key importance, whereas inside the magnetosphere, the magnetic pressure plays a major role since plasma here is more tenuous. An extensive current, called the *Chapman-Ferraro current* flows in the magnetopause region that separates the magnetosheath and magnetosphere. In equilibrium, the magnetic pressure inside the magnetopause, which is actually the magnetic pressures in the magnetosheath, equals the dynamic pressure of the solar wind, as represented in equation 1.9.

$$\frac{B^2}{2\mu_o} = \rho_{sw} u_{sw}^2 \tag{1.9}$$

Where, B is the Earth's magnetic field at the magnetosphere stand-off distance; μ_o is the permeability of free space; ρ_{sw} is the mass density of solar wind; and u_{sw} is the solar wind speed upstream of the bow shock.

This pressure balance leads to the compression in the dayside magnetosphere and the magnetopause current produces this distortion of the dipole magnetic field. Every time the solar

activity increases the dynamic pressure of the solar wind, the magnetopause current increases and the magnetopause drifts closer to the Earth.

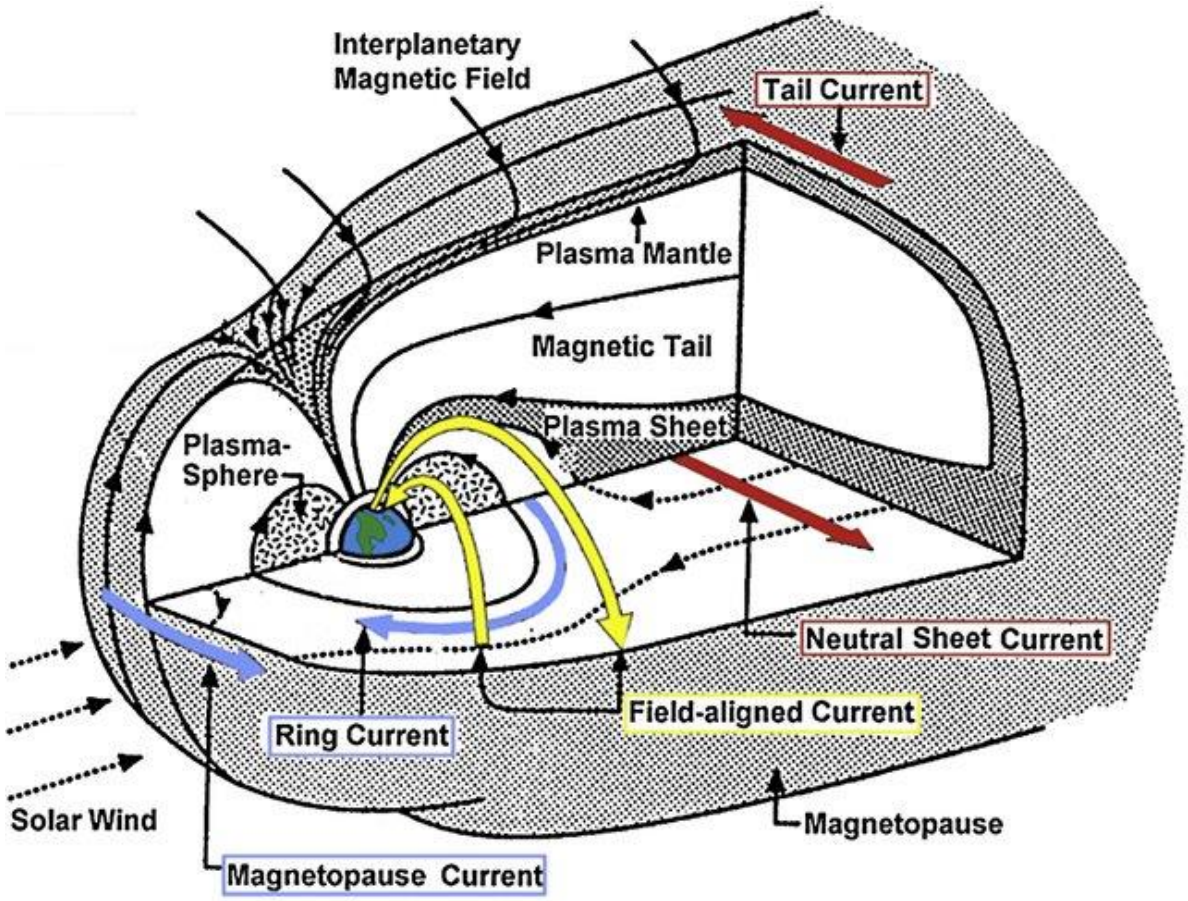

Figure 1. 6 Schematic view of the current system inside the Earth's magnetosphere. [Credit:(Hermann et al., 2017)]

Even beyond the Moon's orbit at 60 Re, the Earth's magnetic field lines on the nightside stretches far anti-sunward. Thin sheet of current was discovered in the magnetotail region where the magnetic field change direction in the near-equatorial plane. With nearly uniform magnetic fields pointing in the opposite directions, these '*neutral sheet*' *current* separates the magnetotail into two zones. The cross-tail current sheet has particular significance since it is a location where instabilities develop that can result in a magnetospheric substorm (E. W. Hones, 1979). The magnetotail neutral sheet current must continue to flow after reaching the magnetopause, and (Axford et al., 1965) discovered that it does so by passing through the magnetopause above and

below the relatively strong magnetic field regions of the tail, generating a structure that resembles the Greek letter θ. These are called *tail currents*. How near can the tail current get to Earth on the nightside and still be classified as a tail current by conventional definition is another debatable issue. The tail current is primarily described as an equatorial nightside westward current outside 6.6 RE that flows in the vicinity of stretched magnetic field lines, closes on the magnetopause, and is carried by particles with energy less than 20 keV.

Another important current in the inner magnetosphere is the *ring current* flowing around the Earth in the clockwise direction with the shape of a toroid. It is an electric current at a distance of 3-8 Re, carried by energetic (10-200 keV) trapped charged particles that drifts longitudinally. Since the ring current flows in the clockwise (or westward) direction and is confined to the equatorial plane, it produces a depression in the northward directed Earth's magnetic field in this region. The disturbances measured during *geomagnetic storms* using ground magnetometers in the equatorial region are attributed to the increase and decrease in the intensity of ring current.

All the current systems discussed above flows across the geomagnetic field lines at different regions inside the Earth's magnetosphere. Apart from these, there also exits current systems that flows parallel to the geomagnetic field lines and are called *field-aligned currents*. These current systems are of utmost importance in view of the present thesis, as it directly connects the magnetosphere to the Earth's upper atmosphere. In order to explain changes in the magnetic field recorded on the ground in the polar regions, these field-aligned currents were first proposed by Birkeland in 1908, and numerous hypotheses were later developed. A series of ground magnetic measurements at high latitude, near 60-80 degrees magnetic latitude, showed three components of the magnetic field in the northern polar regions: (1) parallel to the main geomagnetic field; (2) perpendicular to the main geomagnetic field in the magnetic east-west direction; and (3) perpendicular to the main geomagnetic field in the magnetic north-south direction. Variations with the largest amplitude was observed in the transverse magnetic east-west direction. According to these variations in the geomagnetic field, the field aligned current has the following direction at northern polar region: (i) in the pre-midnight sector, away from the Earth's surface in the poleward boundary and into the Earth's surface in the equatorward region; and (ii) in the post-midnight sector, into the surface in the poleward boundary and away from the surface in the equatorward boundary; as shown in figure 1.7. Further, these field-aligned currents are separated into '*Region 1'* and '*Region 2' currents*, where Region 1 currents are the poleward currents and Region 2 the equatorward currents.

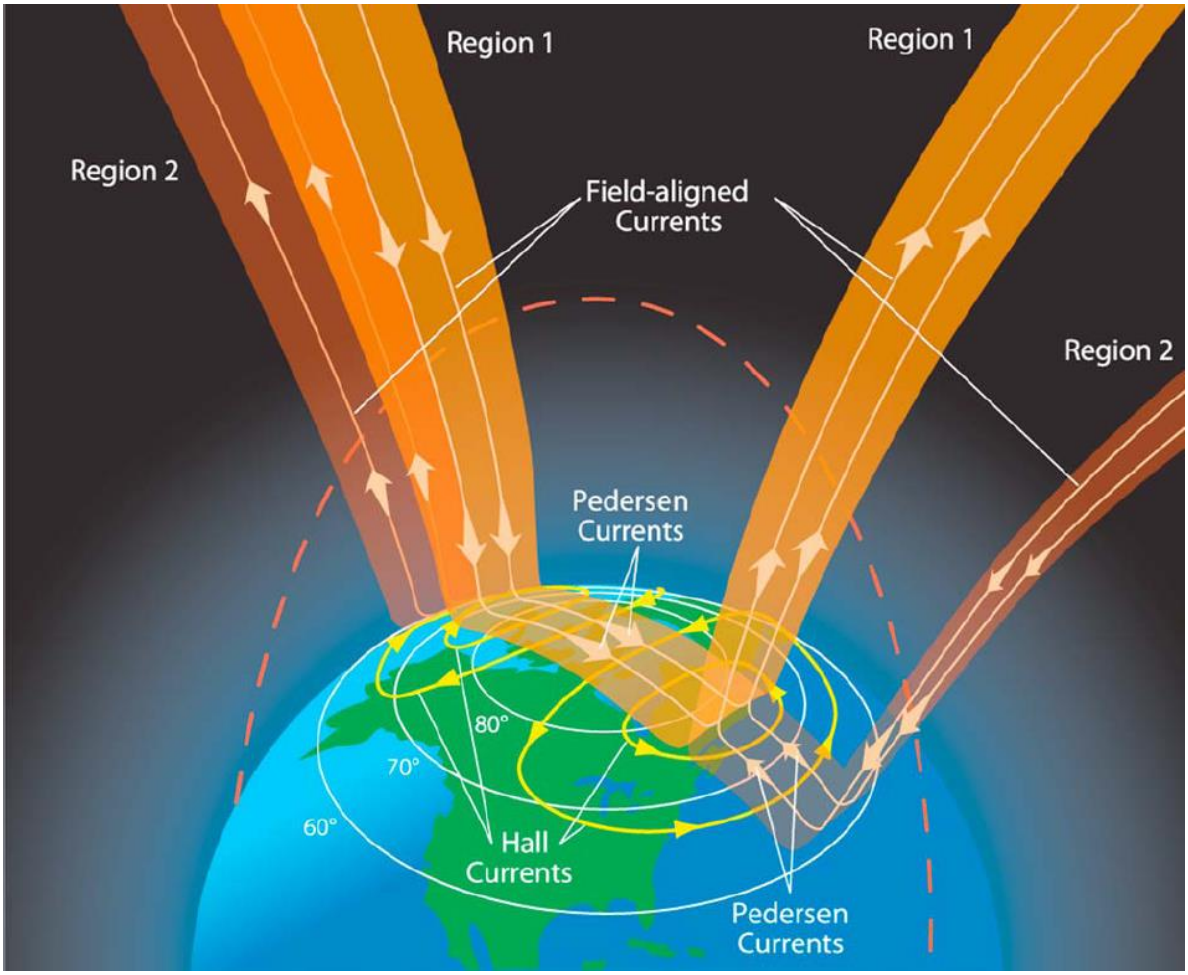

Figure 1. 7 Schematic diagram of the Region 1 and Region 2 field aligned currents as observed from the day side. [credits: Birkeland current. (2022, July 3). In Wikipedia. https://en.wikipedia.org/wiki/Birkeland_current]

The interaction between the magnetosphere and the ionosphere is significantly influenced by field-aligned currents (Ganushkina et al., 2018). The tangential drag of the solar wind causes magnetic field lines to circulate within the magnetosphere in a pattern of closed loops which in turn produces this field-aligned current system. The interface between field lines being driven tailward by the solar wind and field lines returning to Earth's dayside, is where the Region 1 current originates. Since there are no collisions to introduce resistance, magnetic field lines in the Earth's field are almost ideal current conductors. This enables the ionosphere at the base of the charged field lines to be coupled to the effects of the charge separation in the magnetosphere. Current can move from the positive to negative terminals because of how well the ionosphere conducts electricity. As a result, current flows from the positive terminal of the magnetospheric

"battery"; it moves down the field lines on the dawn side, and through the polar ionosphere, out on the dusk side. The Region 2 system must be taken into consideration in order to comprehend the closure of the Region 1 current system. Region 2 current flows in the direction opposite to Region 1 current; wherein enters the ionosphere from the dusk and leaves from the dawn. The field-aligned current system has the remarkable property that, despite significantly altering the field in space, its effects are virtually undetectable on the ground. The magnetic field of the field-aligned current system is almost fully contained between the two roughly parallel, oppositely directed current sheets that make up the system. But in one sense, the system's existence is obvious. It powers a secondary system of convective electrojets in the ionosphere known as the *Eastward* and *Westward electrojets*, which will be discussed in the next section.

1.4 Ionosphere at High Latitude

The Ionosphere is a region of the Earth's upper atmosphere located between 80 and 600 kilometers, where solar X-rays and extreme ultraviolet (EUV) radiation ionize atoms and molecules to produce a layer charged particles. Even though these charged particles make up a small portion of the neutral particle population in the ionosphere, they have a significant impact on the medium's electrical properties. The possibility of radio communication over long distances using one or more ionospheric reflections is made possible by their presence. The ionosphere is divided into three layers according to their free electron density profile that indicates the degree of ionization, namely: F-region, E-region and D-region (shown in figure 1.8). Since the ionosphere's existence depends upon the radiation from the sun reaching the atmosphere, it fluctuates in density from daytime to nighttime. During the day, all three layers are denser. At night, all layers drop in density with the D-Layer suffering the biggest reduction. The D-Layer almost essentially vanishes at night. The typical daytime characteristics of the D, E, F1 and F2 layers at midlatitude region are as follow:

- D-region, 60-90 km; electron density: 10^2 to 10^4 cm^{-3}
- E-region, 100-160 km; electron density: several times of 10^5 cm^{-3}
- F1-region, 160-200 km; electron density: several times of 10^5-10^6 cm^{-3}
- F2-region, around 300 km; electron density: up to several times of 10^6 cm^{-3}

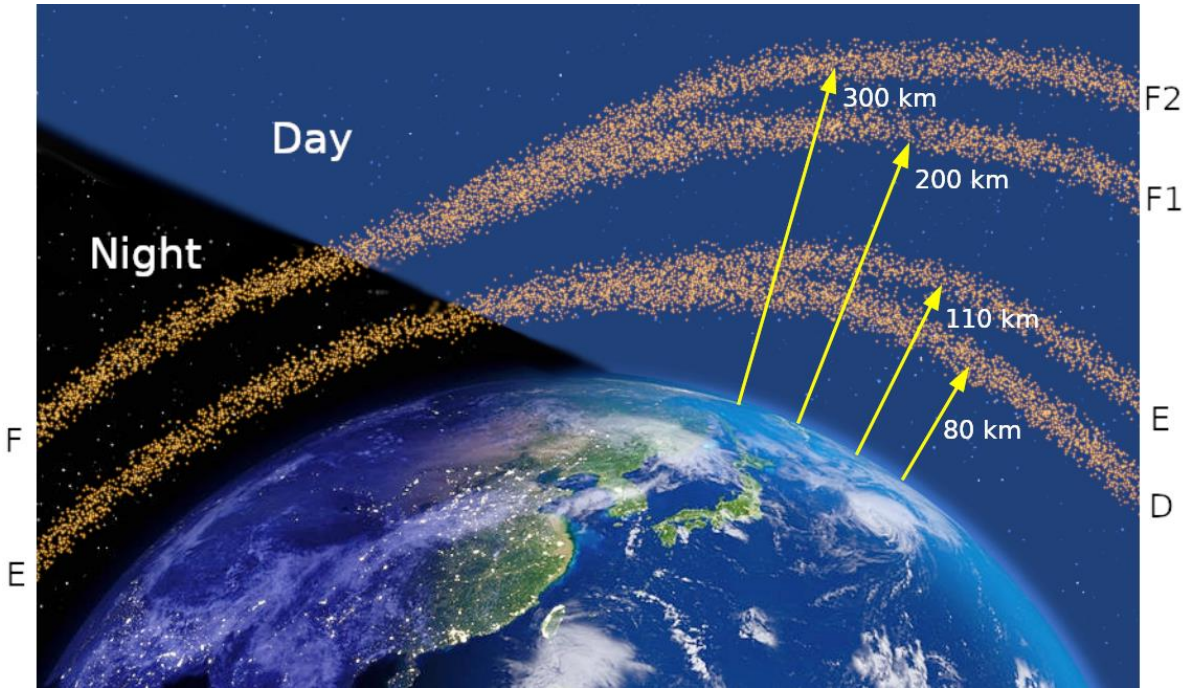

Figure 1. 8 A schematic representation of the different ionospheric sub-layers from day to night. [credit: https://en.wikipedia.org/wiki/Ionosphere]

According to the geomagnetic latitude, the terrestrial ionosphere can be roughly split into three areas that have distinctly different characteristics: low, mid and high latitude ionosphere. Most research has been done on the understanding of the mid-latitude region. There, the ionization is nearly exclusively caused by the Sun's powerful ultraviolet and X-ray rays, and it is then reversed by chemical recombination processes. At high latitudes, the ionization mechanism that govern the ionosphere at mid-latitudes do exist, but other processes also play a major role. Ionosphere at high latitude (auroral and polar) region is particularly different because solar-terrestrial energy transfer mainly happens here. The high-latitude ionosphere serves as a sink for a variety of solar and magnetospheric events, and its distinctive characteristics can be linked to such seemingly unrelated phenomena such as solar flares, wave-particle interactions, and magnetospheric substorms. The main sources of plasma in the high-latitude ionosphere apart from solar UV light are precipitating electrons. Since the flux of precipitating ions is much lower than that of the electrons, their effects on the ionospheric plasma can be neglected. While the plasma created by the sun's strong UV radiation changes in density smoothly, the plasma created by electrons precipitating may be highly structured. Other probable sources of structure include instabilities caused by free energy sources like field-aligned currents and magnetospheric electric fields.

1.4.1 High latitude Ionospheric Currents and Conductivities

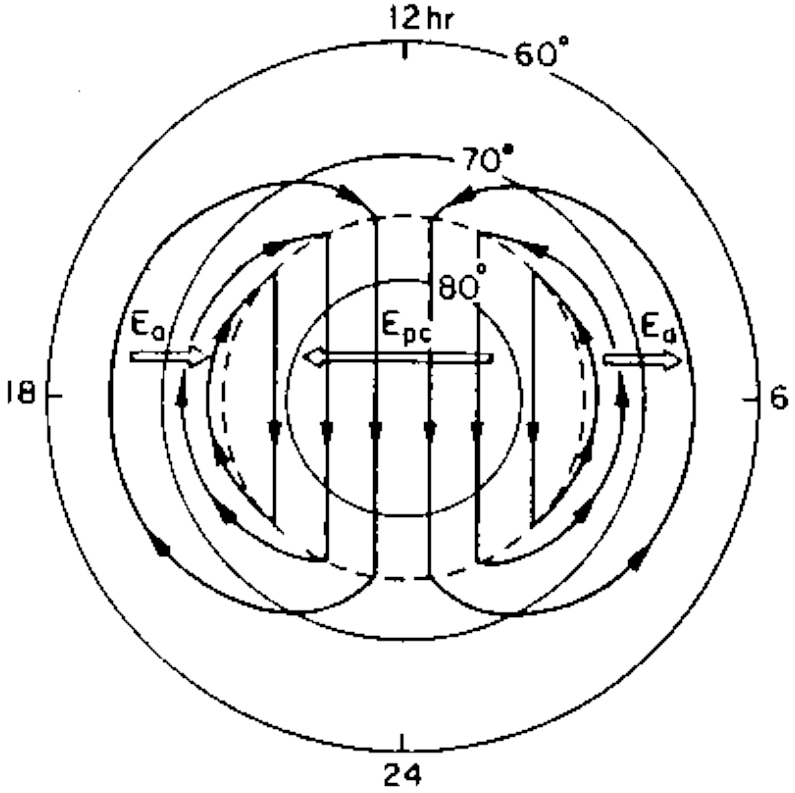

Figure 1. 9 Mapped from the magnetosphere to the ionospheric magnetic local time and corrected geomagnetic latitude coordinate system, an idealized two-cell plasma convection pattern with anti-sunward E×B flow in the polar cap and a sunward return flow at lower latitude. [credit: (Kelley & Hellis, 1989)]

As discussed in the previous section 1.3.4, the circuit connecting interplanetary space and the lower ionosphere comprises of large-scale currents that runs almost parallel to the geomagnetic field into and away from the ionosphere at auroral and polar regions. The exchange of particles between the magnetosphere-ionosphere system happens via these current systems. Due to the plasma convection along with the motion of magnetic field lines in the magnetosphere, the convection of plasma in the ionosphere is also affected. This is because the lower ends of these magnetic field lines connected at high latitude ionosphere are also set in motion, together with the plasma associated to it. Since the plasma in the ionosphere is highly conducting, the electric field associated with these conductive motion drives ionospheric currents. The convection pattern at high latitude is like a two-cell electric potential pattern as shown in figure

1.9. The convection of plasma in the magnetosphere-ionosphere system will be discussed in detail in the upcoming section 1.5.

Abundant collisions between the ionized and neutral particles in the presence of strong magnetic field of Earth leads to a finite anisotropic conductivity tensor in the lower part of the partially ionized ionosphere. This ionospheric conductivity has three different components; and thus, the convection electric field will generate three current systems in the high latitude ionosphere. For a magnetic field aligned in the positive z direction, the conductivity tensor is given by (Baumjohann & Truemann, 1996): -

$$\sigma = \begin{pmatrix} \sigma_P & -\sigma_H & 0 \\ \sigma_H & \sigma_P & 0 \\ 0 & 0 & \sigma_{||} \end{pmatrix} \tag{1.10}$$

And each conductivity component is given by:

(i) $$\sigma_P = \sigma_O \frac{{V_c}^2}{{V_c}^2 + {\omega_{ge}}^2} \tag{1.11}$$

called the *Pederson Conductivity* which governs the *Pederson current* that is in the direction of transverse electric field, $E_\perp$, and perpendicular to the magnetic field.

(ii) $$\sigma_H = \sigma_O \frac{\omega_{ge} V_c}{{V_c}^2 + {\omega_{ge}}^2} \tag{1.12}$$

called the *Hall Conductivity*, determines the *Hall current* perpendicular to both electric and magnetic fields, in the $-E \times B$ direction.

(iii) $$\sigma_{||} = \sigma_O = \frac{n_e e^2}{m_e V_c} \tag{1.13}$$

called the *Parallel Conductivity*, and governs the *field-aligned currents* parallel to the magnetic field driven by parallel electric field component, $E_{||}$. The parallel conductivity is the same as the plasma conductivity in an unmagnetized case.

Here, m_e is the mass of electron; e is the charge on electron; ω_{ge} is the electron gyro-frequency; n_e is the plasma density; and ν_c is the collision frequency.

The *Eastward and Westward Electrojets* flowing in the auroral zone are primarily the Hall currents that originate around noon (Baumjohann & Truemann, 1996). These currents are confined to the auroral oval because the precipitating particles reaches this area and causes significant enhancement in the ionization. As a result, the conductivity of auroral zone is much higher than the nearby latitudes. The eastward electrojet flows from afternoon to midnight

through dusk and terminates at *Harang* discontinuity. The westward electrojet on the other hand flows through morning and midnight extending till evening sector. The most notable currents at auroral latitudes are auroral electrojets. They transport around 10^6 A current which is of the same order of magnitude as the total current carried by the ring current. Since the auroral electrojet flow only 100 km above the Earth's surface, they produce the highest ground magnetic disturbance of all the current systems in the Earth's environment.

The field-aligned currents are the strongest while the Pederson currents are the weakest currents that flows at high-latitude ionospheric region. The directions of the Pederson currents are shown in figure 1.7. In the equatorward and poleward halves of the afternoon-evening auroral oval in the northern hemisphere, they are connected to the downward and upward field-aligned currents, respectively, pointing towards the north and is parallel to $\overrightarrow{E_a}$ as shown in figure 1.9. In the midnight-noon sector, it flows towards the equator, again parallel to $\overrightarrow{E_a}$, and connected by the downward field-aligned current in the poleward half and upward field-aligned current in the equatorward half of the auroral oval. Region 1 currents are actually the field-aligned current sheets in the poleward half of the auroral oval; and Region 2 currents are the those in the equatorward half.

1.4.2 Radio-Wave Propagation at High-latitudes

The early history of the ionosphere is closely related to the growth of radio-signal communication. Scientists realized that the radio waves could not have gone directly across the far-off regions due to the curvature of the Earth; instead, they must have been reflected from an ionized layer, and later named this layer as 'ionosphere'. The E and F regions set the primary characteristics of HF radio wave propagation, with the D region primarily serving as an absorbent layer that weakens the signal but infrequently interferes with communications for extended periods of time. Hence, the D region plays a secondary role in radio propagation near middle latitude. However, at high latitudes, D region is significantly enhanced mainly because of the energetic particle precipitation, and thus absorption becomes a major issue. Two main radio absorption phenomena occur, each specific to high latitude regions. The first is auroral radio absorption (AA) and second is Polar-cap absorption (PCA). Auroral absorption, which only happens in auroral regions, is caused by fluxes of incredibly energetic electrons that intermittently

precipitate from the magnetosphere during periods of auroral activity. PCA is driven by the solar energetic protons, that are frequently released during significant solar flare events.

The features of these two types of phenomena are quite dissimilar. In a year of intense solar activity, the PCA occurs only around once each month on average; this number drops significantly during quiet solar times. Yet, if an event does take place, there may be a significant amount of absorption lasting up to several days. Since the absorbing region is rather homogeneous throughout the entire polar cap, there will be an extensive HF blackout during PCA events. Auroral absorption, which is restricted to the auroral zones, is on the other hand typically more frequent. It does not reach the intensity that is observed during PCA. However, the spatial structure, which is generally not well understood, makes it more challenging to foresee the consequences on HF propagation.

The fundamental interactions between radio waves and matter are reflection, refraction, dispersion, diffraction, scattering, change of polarization, and attenuation. These processes explain the diverse phenomena of terrestrial radio propagation. Additionally, they have given us a variety of tried-and-true methods for examining the propagation media and their behavior, knowledge of which is crucial for comprehending radio communication and its issues. In the present thesis we will be focusing on the attenuation process of radio waves at high latitudes that takes place in the lower ionospheric region to study its characteristics during various space weather events. Attenuation leads to partial radio wave absorption in the ionized medium. In order to quantify the absorption, Appleton-Hartee equation (Booker, 1935) is used which defines the refractive index of an ionized medium in terms of its plasma properties, as follow:

$$\eta^2 = 1 - \frac{X}{1 - iZ - \frac{Y^2 sin^2\theta}{2 - (1 - X - iZ)} \pm [\frac{Y^4 sin^4\theta}{4(1 - X - iZ)^2} + Y^2 cos^2\theta]^{1/2}} \tag{1.14}$$

where,

$$X = \frac{{\omega_p}^2}{\omega^2} = \frac{n_e e^2}{\epsilon_O m_e \omega^2}$$

$$Y = \frac{\omega_H}{\omega} = \frac{eB}{m_e \omega}$$

$$Z = \frac{\nu_m}{\omega}$$

ω_p is the plasma frequency; ω is the angular frequency of radio wave; n_e is the electron number density, e is the charge on electron; m_e is the mass of electron; ϵ_O is the permittivity of free space; ω_H is the electron cyclotron frequency; B is the ambient magnetic field; ν_m is the electron momentum-transfer collision frequency; and θ is the angle between magnetic field and the wave propagation vector k.

When the radio wave travels in a medium with high collision frequency, it suffers a non-deviative absorption. Collisions between electrons and heavy particles change the refractive index (n), and the wave is absorbed, which is a result of the particles' transition from ordered momentum to random motion following the collision. A portion of the wave's energy is transmitted to the neutral molecules during each collision and manifests as thermal energy. The absorption of cosmic radio noise in the D-region ionosphere is of the non-deviative type. To calculate this non-deviative absorption, an assumption is made that the radio-wave propagates almost parallel to the magnetic field, which is nearly true in the case of high latitude propagation. Hence for θ→0, sin θ→0; and equation 1.14 becomes:

$$\eta^2 = \frac{\frac{{\omega_p}^2}{\omega^2}}{1 - \frac{i\nu_m}{\omega} \pm \frac{\omega_H cos\theta}{\omega}} \tag{1.15}$$

The imaginary part of the equation 1.15 represents the absorbed component of the wave usually expressed as κ in units of nepers. It is usual to express signal loss in decibels (dB), defined by the ratio between initial (P1) and final (P2) powers:

$$Absorption\ A\ (dB) = 10log_{10}(P1/P2) \tag{1.16}$$

Where, 1 neper= 8.686 dB

The final form of total absorption over a path after appropriate substitutions and trivial algebra becomes (Booker, 1935):

$$A\ (dB) = 4.61X10^{-5} \int \frac{n_e v}{v^2+(\omega \pm \omega_H)^2} dl \qquad (1.17)$$

1.5 Magnetosphere-Ionosphere Coupling

The magnetosphere-ionosphere system is coupled strongly at high latitudes via electric fields, particle precipitation and field-aligned currents. The general pattern of field-aligned current is composed of two continuous rings of current, "Region 1" at polar latitudes and "Region 2" at auroral latitudes. At dawn and dusk, these two currents have the opposite polarity, and they overlap somewhat in the Harang region before midnight. Although it is modified in size, strength, and form by the orientation and amplitude of the interplanetary magnetic field (IMF) as well as by geomagnetic disturbance, this current pattern has been determined to be a nearly constant characteristic of the magnetosphere-ionosphere system.

Precipitating electrons are widely acknowledged as the primary cause of ionization structure at high latitudes. They take on a dual role in this. They are first and foremost sources of free energy for specific plasma instabilities. Second, the ionization that is produced by magnetospheric electrons is structured because these electrons are of different energies. Hence, at high latitudes, the energy properties and geographic distribution of electron precipitation are varied. There is a large-scale convection electric field that carries the plasma through the auroral oval toward local noon and toward midnight within the polar cap when the interplanetary magnetic field contains a southward component. The entire high-latitude ionosphere's plasma structure may be produced and redistributed by this electric field.

1.5.1 Plasma Convection and Dungey-Cycle

Large-scale "convection motion" of plasma occurs in the magnetosphere as a result of the viscous interaction between solar wind and Earth's magnetosphere. This flow pattern maps down to the polar ionosphere of the earth, with plasma moving in the anti-sunward direction in the polar cap and sunward direction in the auroral zone. The magnetic field should be directed southward for the relatively stable two-cell structure to exist. When the magnetic field is moving in the northward direction, this convective flow pattern is severely disrupted, sometimes even fragmenting into several cells. The two-cell convection pattern can be understood with the help of the ‘open model magnetosphere’ proposed by J. W. Dungey (Dungey, 1961). The ‘Dungey cycle’ of magnetic field and plasma circulation in the magnetosphere is driven by ‘magnetic

reconnection' that takes place at the dayside magnetopause and in the magnetotail, with the rate of convection being controlled by solar wind conditions. The magnetospheric and ionospheric view of the Dungey cycle is shown in figure 1.10. Later, the Dungey cycle and its role in generating ionospheric convection began to take on a new, more dynamic perspective that recognized the independent driving mechanisms of the magnetopause and magnetotail (e.g., Cowley & Lockwood, 1992; Siscoe & Huang, 1985).

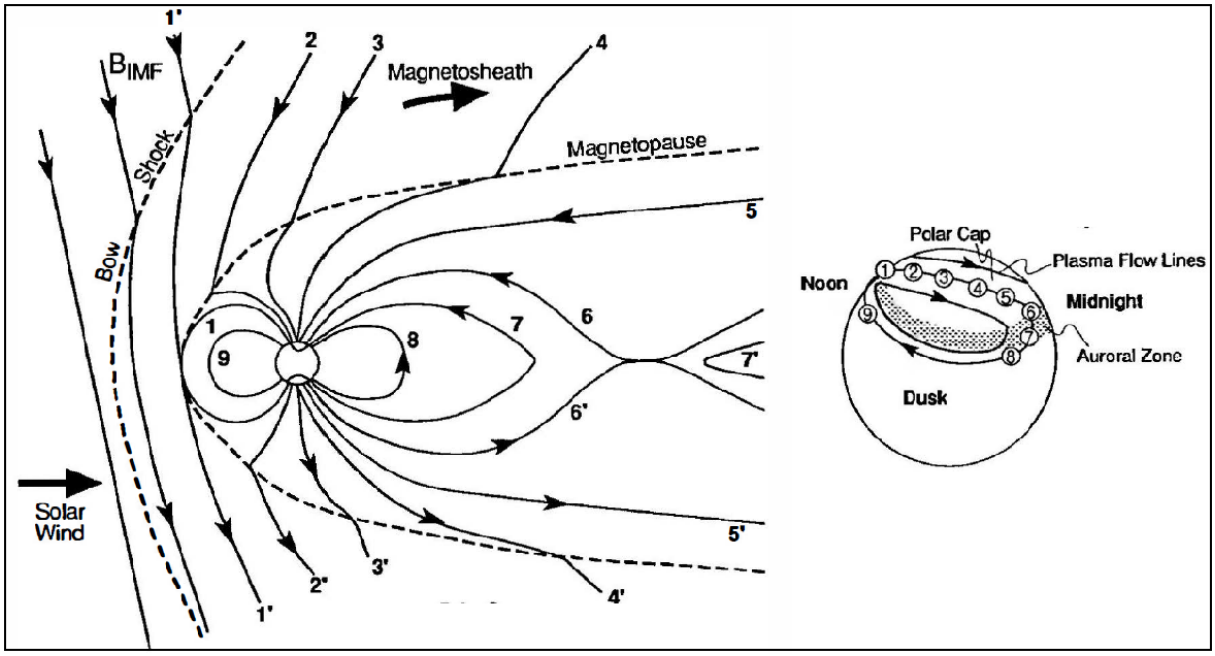

Figure 1. 10 The open magnetosphere of the Earth's Dungey cycle is shown in the figure. On the left, is seen a magnetospheric image of a southward IMF field merging with the northward directed Earth's magnetic field. The field line is then carried into the magnetotail by the solar wind, where it re-connects and travels Earthward before returning to the dayside through the flanks. The cycle's stages are all given numbers. The cycle and associated flows are projected into the ionospheric space on the right. [credit: (Cassak et al., 2006)]

In the solar-terrestrial interactions, 'magnetic reconnection' is a crucial process for converting and transporting energy from solar wind to inside the magnetosphere and then from the magnetotail to the high latitude ionosphere. When oppositely directed magnetic field lines in a plasma comes sufficiently close so that they can split and then re-connect, the process is referred to as *Magnetic Reconnection*. Plasma kinetic and thermal energy are produced as a result of the

conversion of magnetic field energy during the process; and two new field lines of completely different topologies are formed. Reconnection of magnetic field lines happens at every stage of the Sun-Earth interaction. For example, magnetic reconnection is thought to be the source of energy for solar flares that occur near sunspots, and solar activity then ejects high energetic charged particles into space. When the interplanetary magnetic field is directed southward, magnetic reconnection between the northward directed geomagnetic field and IMF happens at the subsolar point, as shown in figure 1.10. In case of IMF having no southward component, reconnection takes place somewhere near the flanks. Magnetic reconnection also happens in the magnetotail region between the oppositely directed field lines of the Earth.

Magnetic field lines are well known in plasma physics to be "frozen-in" to an infinitely conducting plasma. Infinitely conductive plasmas will not diffuse across field lines and mix because charged plasma particles are constrained to circular orbits around magnetic field lines. On the other hand, two independent field lines won't merge together since they can't pass through the gaping plasma. However, when plasmas with opposing magnetic field directions are brought together, a strong current sheet is created. In this environment, even a tiny amount of resistivity in a small volume can play a significant role in promoting plasma diffusion and magnetic reconnection. Soon after the reconnection, the plasma is then accelerated in the newly formed magnetic field lines. This process plays a vital role in the formation of ‘Auroras’, or the so-called ‘Northern Lights’, observed at high latitudes, and will be explained in detail in the next section.

1.5.2 Magnetospheric Substorm

The interaction between the solar wind and the magnetosphere is responsible for the most significant dynamical phenomenon, *magnetospheric substorms*. During the period of substorm activity, the shape of the magnetosphere changes, large-scale internal convection of plasma is driven by electric fields, currents flow along field lines and through the ionosphere, particles are injected inside the magnetosphere which precipitate into the Earth’s atmosphere following the geomagnetic field lines. Numerous effects in the ionosphere and upper atmosphere that happens during this process, acts as the ground signatures this activity. Substorms are believed to be typically a midnight phenomenon (S. I. Akasofu, 1964), which gets triggered mainly by the southward turning of the interplanetary magnetic field (Meng et al., 1973; Tsurutani & Meng, 1972). As discussed in the previous section, magnetic reconnection between the interplanetary

magnetic field (IMF) and the Earth's magnetic field near the dayside magnetopause transfers energy into the magnetotail (Dungey, 1961). This is often referred to as the 'loading' mechanism. Subsequent reconnection in the magnetotail results into the release of this stored magnetotail energy from the nightside into the auroral zones. The unloading, or energy release process, is associated with an episode of localized auroral brightening which happens due to the de-excitation of atoms in the ionosphere soon after the precipitating energetic particles excite them to higher levels. As a result, delightful and often intricate display of light is visible in the auroral and polar regions, known as the aurora or northern lights.

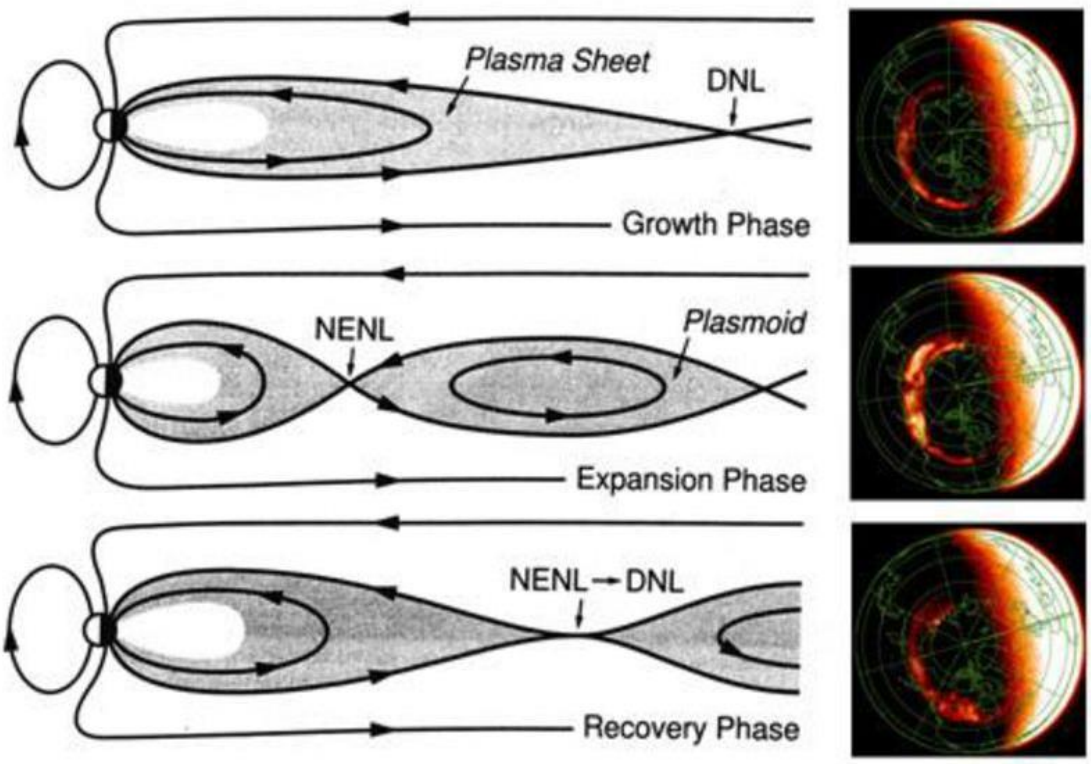

Figure 1. 11 Reconfiguration of plasma sheet in the night side magnetotail region and visual aurora in the high latitude ionosphere during different stages of Magnetospheric Substorm. [credit: (Baumjohann & Truemann, 1996)]

Substorms can be broadly divided into three stages, the growth phase, the expansion phase and the recovery phase, as shown in figure 1.11. The substorm starts with the *growth phase* that lasts for about one hour, and is a period of enhanced convection that results into the loading of magnetic flux into the magnetotail. During this phase the neutral sheet currents grows due to the

deposition of plasma in the tail lobes. This in turns leads to the stretching of the field lines into an intensified tail-like structure up to 100-200 Re and forming a distant-neutral-line (or DNL). At DNL, again reconnection takes place, which marks the beginning of *substorm expansion phase* and the time of *substorm onset*. This phase lasts for about 30-60 minutes and dramatic changes can be observed in the magnetosphere and high latitude ionosphere. During this phase, depolarization of magnetic field lines takes place at around 30 Re down-tail, forming a new neutral line called NENL (near-Earth neutral line). This is the point where the magnetic flux deposited in the tail during the growth phase is reconnected again to further precipitate down the field line into the auroral zone ionosphere. The region between the two neutral line, DNL and NENL, consists of closed loops of magnetic field and associated plasma, called *plasmoid*. Once the near-Earth reconnection takes place at NENL point, the precipitating particles enhances the conductivity, auroral electrojet currents and intensifies the visual aurora. The strengthening of convection electrojets is caused mainly by an increase in the convection electric field soon after the growth phase. In addition, the loading-unloading process during the expansion phase leads to the formation of a substorm current wedge in the midnight sector, as shown in figure 1.12. This current wedge is in the westward direction in the ionosphere; hence it further enhances the westward electrojet current in the midnight sector.

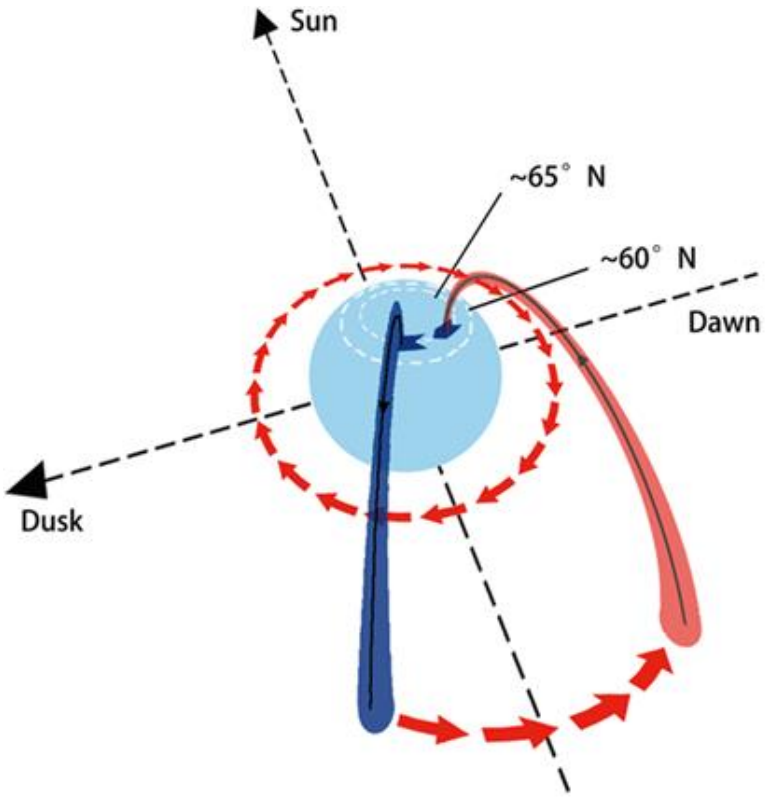

Figure 1. 12 Model of a Substorm Current Wedge. [Credit: (Zong et al., 2021)]

During the final stage, or the recovery phase, the dipolar field structure in the magnetotail region starts to decrease. The near-Earth reconnection and particle precipitation ceases; and the NENL point stretches to merge with DNL point. At this point the plasmoid is pushed into the interplanetary space. This phase ends when the magnetosphere returns to a quiet state, which may take about 1-2 hours.

All the three stages of the substorm can be very well observed with the help of visual auroras in the auroral zone (near 65° magnetic latitude). The aurora that appears as an arc of light in the midnight sector during the growth phase, suddenly expands and intensifies at the time of substorm onset and fills the whole sky. This intensified aurora expands in almost all the directions, particularly westward, soon after the auroral break-up. This lasts for the entire duration of the substorm expansion phase. At the time of the beginning of the recovery phase, the aurora also starts to fade away and retreats to high latitude regions.

1.5.3 Integrated Measurements of the Coupled System

The ability to continually monitor a very broad area of the magnetosphere-ionosphere system at high time resolution owing to ground-based observations from radars, ionosondes, riometers, all-sky cameras, magnetometer chains, and in-situ measurements using satellites, opens up new opportunities of understanding the coupled system in a better way. Integrated measurements conducted at various altitudes and locations can be used to estimate the rapidly varying currents and particle fluxes during several active periods. This helps in analyzing the events in a far advanced way in an extended range of space and time.

To study the coupled magnetosphere-ionosphere system during substorm activities, we start our observations with the ground magnetic measurements of the varying geomagnetic field using ground-based *magnetometers*. Since during substorms, the auroral electrojets enhances and a substorm current wedge is formed in the auroral zone, the locations falling under the influence of these current systems will observe a variation in the horizontal component of the geomagnetic field. The strength and sign (positive/negative) of this variation will depend upon the influence of the which electrojet that location comes under and at what magnetic local time. This is also the best way to confirm whether a location falls under the influence of substorm activity or not. Usually, during substorms, the stations falling in the midnight sector observes the maximum negative variation due to the superimposed effect of westward electrojet and substorm current wedge.

Next step is to trace the path of the precipitating energetic particles. To study the signatures of substorms in the ionosphere, electrons having energies ~1-100 keV becomes of utmost importance. This is because, the ~1-10-keV electrons deposit their energy an altitude range of ~100-160 km, i.e., the E-region of the ionosphere; while the ~10-100-keV electrons deposit their energy deeper into the D-region at ~75-100 km altitudes. These electrons result into the formation of visual auroras in the E-region and causes radio-wave absorption in the D-region, respectively. For analyzing the visual auroras, either ground-based or satellite-based *imagers* are used, that shows images of the development of auroras as the substorm progresses. For measuring the radio-wave absorption, the riometer technique can be very useful. This technique is extensively used in the present thesis to understand the D-region dynamics during various substorm events. This will be discussed in detail in Chapter 2 of the present thesis.

The in-situ measurements made by instruments on-board various satellites can be very useful in understanding the trajectory of the precipitating particles. Satellite observations studied in conjunction with the ground observation gives a better understanding of the ongoing mechanism in terms of space and time. We have used this multi-instrument technique in the present thesis to analyses several geomagnetic phenomena including all the interconnected mechanisms, right from the magnetopause boundaries down to the ionospheric heights. We have also made use of some of the pre-defined geomagnetic indices to estimate the disturbances during geomagnetic activities.

1.6 Geomagnetic Indices

Over the years, geomagnetic indices have been widely utilized to comprehend and predict the solar-terrestrial interactions. These indices include: K_p, A_p, A_m that represents the overall status of the magnetosphere; and $D_{st}, SYM, ASY, AE, AL, AU$ that aims at characterizing region specific activities in the magnetosphere. The following discussion includes a few of the indices that are pertinent to the current investigation:

1.6.1 Auroral indices (AU, AL, AE, SML, SMU and SME)

The auroral electrojet currents are known to intensify during substorm activity. These currents produce dramatic changes in the geomagnetic field in the high latitude auroral regions. The geomagnetic H-component disturbance, as observed at 10-12 longitudinally distributed

observatories located in the auroral zone of the northern hemisphere, are used to derive the auroral electrojet indices (Davis & Sugiura, 1966). A base value is first calculated for each station by averaging the datasets of five international quietest days of a month. For each station, the respective base value is then subtracted from the one-minute data obtained for any disturbed day of the same month. The largest positive and the most negative values then determine the AU and AL index, respectively, for any given UT. AU index corresponds to the eastward electrojet current, whereas, AL index represents the intensity of westward electrojet current. The difference between AU and AL defines the AE index; and their mean, i.e. (AU+AL)/2, defines the AO index. The AL index, in particular, is most suitable for defining the intensity of a substorm as it takes into account both the westward electrojet and substorm current wedge effect. The sharp sudden decrease in the AL index indicates the start of the substorm expansion phase and defines the substorm onset time, as shown in figure 1.13.

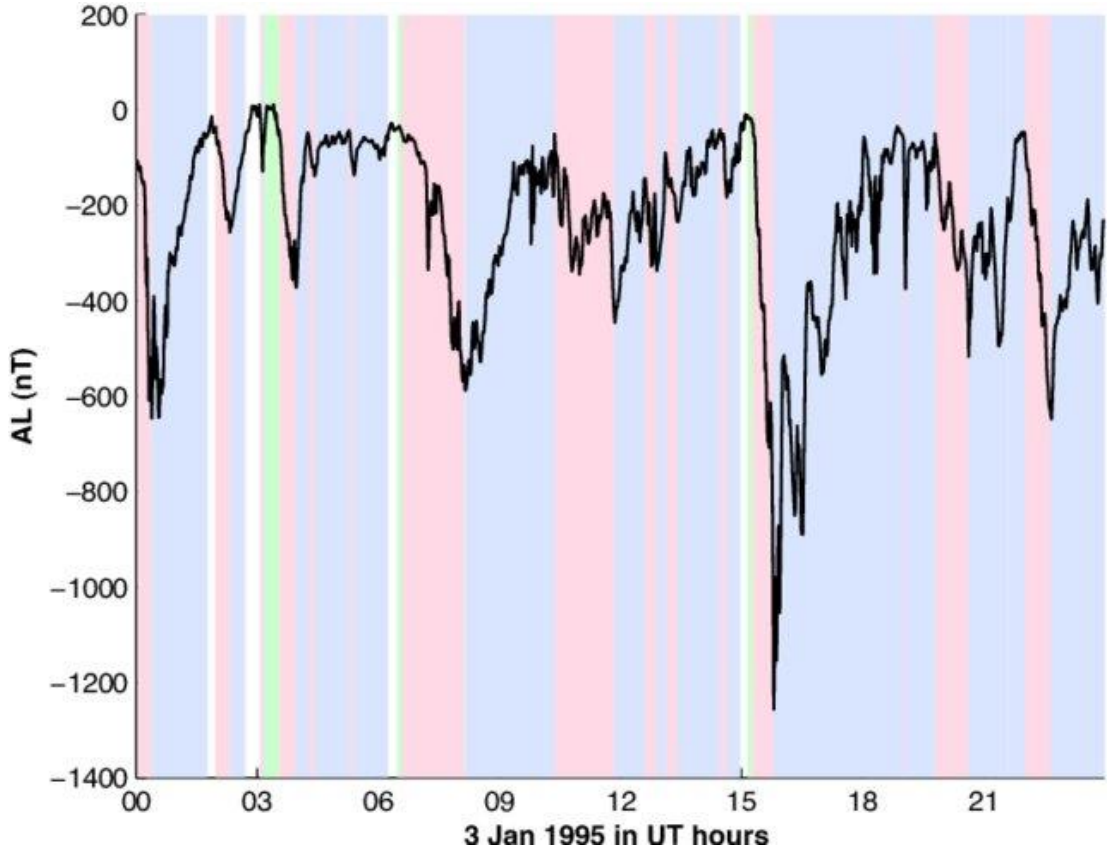

Figure 1. 13 AL index showing stages of Substorm: Green shaded region showing growth phase; pink shaded region showing expansion phase and blue shaded region showing recovery phase. [credit: (Partamies et al., 2013)]

The SML, SMU and SME indices are calculated in the same ways AL, AU and AE indices, the only difference being the number of stations considered. More than 100 northern hemispheric

stations are used to calculate the SuperMAG derived SML, SMU, and SME indices thereby being much more accurate than the AL, AU and AE indices (Newell & Gjerloev, 2011).

1.6.2 Dst and SYM-H indices

Ring current flows in the westward direction in the Earth's equatorial plane and brings about a negative variation or dip in the H-component of terrestrial magnetic field at low and mid latitudes. Using the low latitude H-component variation observed at 5 stations distributed in local times, the Dst index is calculated that represents the strength of the ring current. Dst is an hourly index, hence to have higher resolution ring current variation SYM-H was introduced which has a resolution of 1-min. The Dst or SYM-H index is used to categories the various stages of a geomagnetic storm, as shown in figure 1.14. The impact of the CME causes the Earth's magnetosphere to suddenly compress, enhancing the magnetopause current. This enhancement is seen in Dst as a storm's sudden commencement (SSC). The initial phase of the geomagnetic storm may last for some time while the magnetosphere remains compressed. The main phase of the storm starts when the ring current intensifies as a result of the particle injection. Later, as a result of particle dissipation and recombination, ring current begins to decline. This stage of the storm is referred to as the recovery phase. Dst returns to its pre-storm level during the recovery phase.

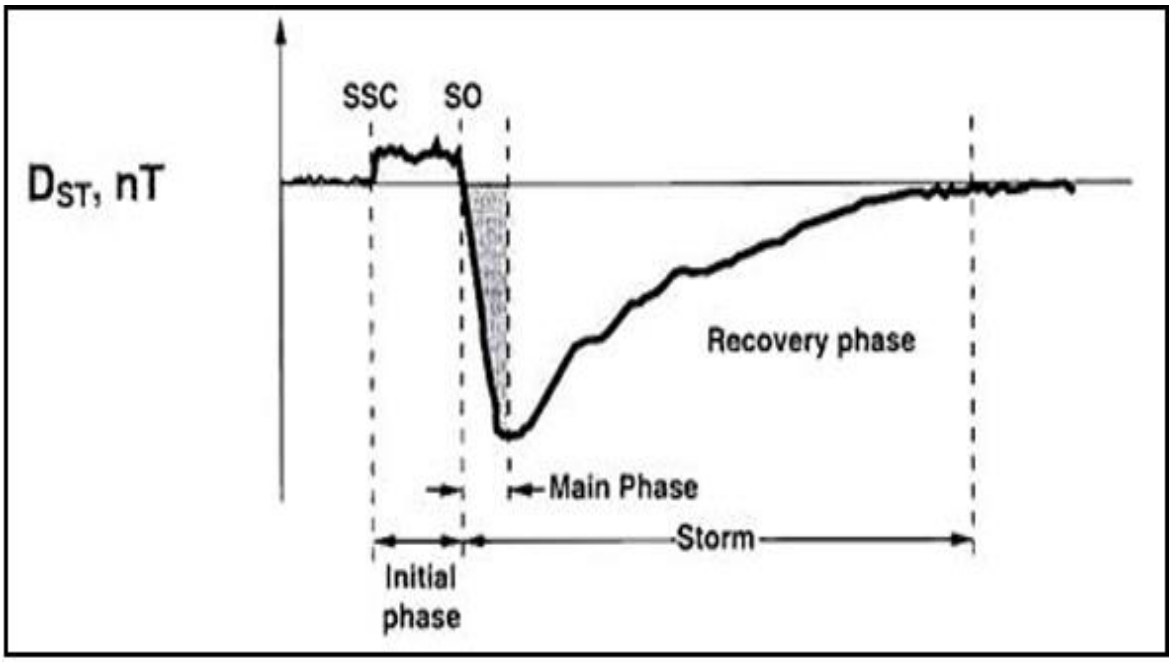

Figure 1. 14 Dst index showing phases of a Geomagnetic Storm. [credit: (Tsurutani et al., 2008)]

1.6.3 Kp and Ap indices

The *Kp and Ap* are 3-hourly indices used to estimate the overall status of the magnetosphere (Matzka et al., 2021). The Kp index is computed using magnetic data from 13 sub-auroral observatories located between 44° to 60° geomagnetic latitudes in northern and southern hemispheres, and distributed in local times. It is a quasi-logarithmic index which varies from 0 to 9_0 depending upon the geomagnetic activity level (Bartels, 1938), where Kp=0 represents the quiet time and Kp=9_0 represents the extremely disturbed magnetospheric conditions. The scale 0 to 9 is expressed in one third of a unit, e.g., 5- is 4*2/3,5 is 5, 5+ is 5*1/3. The Kp index is linearized to derive the 3-hourly ap index which varies from 0 to 400. The average of the eight ap values for a day is called Ap index. He values of Ap index also ranges from 0 to 400.

1.7 Scope of the Thesis

From decades scientists have been trying to understand the true nature of the magnetosphere-ionosphere coupled system. With the recent development in the multi-instrument analysis technology, much could be explained about the various current systems, instabilities, wave-particle interactions, precipitating particles, etc., that are a result of this coupling process. It also opens new door to the future understanding of this system in a far more advanced way and improvise the pre-existing theories.

The present thesis is an attempt to answer some of the unanswered questions and less understood theories of the magnetosphere-ionosphere system. Since we know from the discussion made so far that high latitude regions are the one directly getting affected due to the solar wind-magnetosphere-ionosphere coupling process, we have specifically concentrated our study on the dynamics at high latitudes. The processes happening in the magnetosphere are well projected at high latitude ionosphere, which facilitates to understand the dynamics happening at a much larger distance. We have used the multi-instrument analysis technique to understand how the magnetosphere and ionosphere responds to certain perturbations at a given point of time, and also after that. Much of our understanding comes from the study of intense substorm events conducted using ground-based instruments such as: riometers and magnetometers installed at high latitude stations; and satellite-based instruments such as: particle flux detectors, magnetometers and all-sky imagers. We also used some simulation results that supports our observational results. In Chapter 2 of the present thesis, we have discussed in detail the

instrumentation and datasets of *Riometer,* which is one of the main instruments that we have used to conduct our analysis.

Our main focus is to observe, analyze and understand the trajectory of precipitating particles during disturbed substorm activities. The study of energetic particle precipitation can act as tracers to understand the morphology of geomagnetic substorms, such as, identifying the location of magnetospheric substorm onset, classifying the latitudinal region of open and closed magnetic field lines, and examining the interplanetary conditions at magnetopause boundary. Since these precipitating particles can have a number of adverse consequences once they enter into the Earth's atmosphere, it is crucial to understand their behavior. Depletion of the ozone layer may eventually result from the ionization and dissociation of atmospheric elements brought on by the precipitation of highly energetic particles (Andersson et al., 2018). Additionally, these particles have the potential to disrupt communication and navigation systems as well as harm satellites and spacecraft.

In the present thesis, we have selected various intense substorm events having distinctly different interplanetary conditions to investigate the entry points of the precipitating particles and consequently its mechanism. As a result of high energetic particle precipitation, the ionospheric conductivities increase, the auroral electrojet current is strengthened, and enhanced visual auroras are also produced. Numerous ground- and space-based instruments have been installed worldwide to study these effects of the solar-terrestrial interactions. These instruments focus on various parts of the Earth's magnetosphere and ionosphere system, hence, help to examine the disturbances at various altitudes and locations. In the E-region of the ionosphere, for example, auroral electrojets currents flowing near 100 km altitude creates perturbation in the terrestrial magnetic field. These ground magnetic disturbance is then measured with the help of magnetometers installed at various high latitude stations. In order to track the changes in the galactic cosmic radio noise signals at D-region altitudes, riometers are set up. The formation of auroras, which also occur in the E-region of the ionosphere, is studied from a global perspective using all-sky imagers. Low-Earth orbiting (LEO), geostationary, and geosynchronous satellites equipped with magnetometers and particle detectors provide 'in-situ' measurements of the disturbances at the places where the satellites are positioned at that moment. The spatial and temporal dimension of the analysis can be enhanced by combining the results of all these devices whenever studying any geomagnetic event. This facilitates in comprehending the various interrelated mechanisms at play during any geomagnetic phenomena, from the magnetopause boundaries all the way down to the ionospheric heights.

It is known, and also discussed in the previous sections, that magnetic reconnection is a primary condition for magnetospheric substorms to happen. However, there are evidences that a solar wind sudden impulse, if intense enough, can also sometimes trigger a substorm. We have in the present thesis tried to understand the mechanism that leads to such impulse-induced substorms. Chapter 3 of the present thesis discusses a very intense substorm event that was triggered by a pressure pulse and not by IMF. A strong sudden impulse coincided with the substorm onset and a southward IMF Bz was absent hours prior to the time of the onset. This event is very unique because the ground observations associated with the substorm activity on this day could not be explained with the reconnection theory. According to the observed visual auroras, electrojet current enhancements and radio wave absorption pattern, it appears that the injection and precipitation of solar wind particles happened from the dawn and dusk and not from the typical midnight sector. Simulation results also support the observation of this day, showing absence of dipolarization and plasmoid formation after this substorm onset. Since viscous interaction via KH instability favors the injection of particles from dawn and dusk, we believe this mechanism might have triggered the substorm on this day.

Another pertinent question that may arise now is when do substorms behave like a normal Akasofu-type (particle injection via magnetic reconnection process) and when do they behave like an impulse-induced one (particle injection by viscous interaction). If both the triggering agents, i.e., IMF Bz component and a pressure pulse, are present at or prior to the time of onset, what type of substorm will occur? So, we have tried to answer this question in Chapter 4 of the present thesis using substorm events associated with different interplanetary conditions. Firstly, it is discussed how one can initially classify a substorm as either impulse-induced or IMF-induced on the basis of the SuperMAG SML-LT index. The midnight sector experiences an increase in ionospheric conductivity, the strongest aurora, and the auroral electrojet current during typical Akasofu-type substorms. However, during impulse-induced substorms, these substorm traces in the ionosphere are seen mostly near dawn and dusk. We then show how to further confirm the triggering mechanism associated with a substorm event when both IMF Bz and sudden impulse are present prior to or at the time of the onset. The main conclusion drawn is that when the pressure pulse is strong enough to overcome the influence of magnetic reconnection, the particles are injected from the flanks and precipitated down the field line from dawn and dusk sectors. However, when pressure pulse is not strong enough to inject the solar wind particle from the flanks, the particles follow the usual trajectory to precipitate from the night side via magnetic reconnection. Ultimately, the magnitude of pressure pulse and IMF will eventually determine

whether a substorm will have its onset from the mid-night sector or from the dawn/dusk when both the triggering agents are present.

Since, we are attempting to study in detail the high latitude ionospheric response during disturbed times, it is important to cover all the factors that leads to such disturbances. This includes the solar energetic proton (SEP) events and X-ray radiation during solar flares. The solar proton events (SPE), that are linked to these SEPs during intense solar flares activities, happen when high-energy protons enter the Earth's atmosphere directly from the cusp region. Polar Cap Absorption, or PCA, is the name given to the absorption process of radio waves in the D-region that happens as a result of the enhanced ionization during SPEs. Solar flares also emit powerful electromagnetic radiation in addition to energetic plasma particles. The X-ray radiation produced by solar flares penetrates deep into the atmosphere and ionizes the D-region. As a result, the entire solar lighted region experiences solar flare associated sudden cosmic noise absorption (SCNA). Chapter 5 of the present thesis discusses in detail the PCA and SCNA events, happening at high latitude region, and also their associated characteristics in those regions.

We summarize our important results and findings in the last chapter of this thesis. We discuss how the multi-instrument analysis technique has been used to examine various aspects of the Sun-Earth system. Majorly, the particle precipitation processes during substorms, cusp region precipitation during SPE, and solar X-ray radiation during intense flare activities, has been covered in the present thesis. The novel addition to the pre-existing theory via this thesis includes the finding of new entry points of particle injection during intense substorm activities, which are ‘the flanks of the magnetosphere’. A suitable theory has been proposed and relevant evidences has also been discussed, that supports our idea of considering substorm a more complex process that originates in the magnetosphere. Secondly, we also tried to understand the behavior of solar-flare effects at high latitudes. It is found that the background condition plays a very crucial role during isolated SCNA, which occurs when there is no concurrent substorm. We find a significant difference in SCNA characteristics in the high latitude D-region at nearly equal solar-illuminated parts of the two hemispheres, which one may not expect. The present thesis demonstrates the usefulness of conducting multi-instrument analysis in order find answers to peculiar questions related to the anomalous events happening as a consequence of the solar wind-magnetosphere-ionosphere coupling processes

Chapter 2

Instrumentation and Data Analysis

The multi-instrument analysis of disturbed geomagnetic events occurring as a result of the magnetosphere-ionophore coupling, forms the central theme of the present thesis. In this chapter, we describe in detail one of the main instruments used to conduct the analysis, '*Riometer*'. Riometers consists of a single passive dipole antenna or an array of antennas, that are tuned in to record the intensity of incoming cosmic radio noise signal at a certain frequency. These riometer technique is an excellent approach to analyze the disturbances in the ionospheric D-region. The datasets of riometers installed at high latitude stations like: Maitri (Antarctica), Halley (Antarctica), Australian riometer chain, Canadian riometer chain and Finland riometer chain, have been used to conduct the high-latitude ionospheric studies.

In conjunction, the datasets of ground and satellite-based magnetometers, satellite-based particle-flux detectors and all-sky imager, have also been used in the present thesis. The geomagnetic indices and ground magnetic data have been derived from WDC Kyoto, CDAWeb, SuperMAG, INTERMAGNET and IGRF Model. The simulation results supporting the observations as obtained from the Community Coordinated Modeling Center 'Block Adaptive Tree Solar Wind - Roe Type - Upwind Scheme' (CCMC BATS-R-US) model are incorporated as well.

In the following sections, we will be discussing the methodology used to analyze the datasets of riometer. The method of deriving the quiet day curve (or QDC), and calculating the CNA for a given location and time, has been discussed. The data processing of imaging riometer installed at Indian Antarctic base, Maitri, is explained in detail in this chapter.

2.1 Cosmic Noise Absorption using Riometer

Cosmic radio noise refers to the background radio frequency that are of solar or galactic origin. Its characteristics is comparable to thermal noise and the frequency falls in the radio frequency range, hence, the name given 'radio noise'. It can be detected via a radio receiver, which is an electronic device that detects a radio wave signal and converts the received intensity into units of power (volts or decibel). *Riometer* is one such instrument that measures the amplitude of cosmic radio noise, typically in a narrow frequency band between 30 and 60 MHz. Riometer stands for relative ionospheric opacity meter, and as the name suggests, it offers a routine ground-based method for monitoring the changes in the ionization of the ionosphere. As discussed in Chapter 1, section 1.4.3, when radio waves travel through an ionized medium, it attenuates by getting absorbed in the medium. Such phenomena happen in the Earth's ionosphere, where an enhancement in the ionization can cause absorption of these cosmic radio noise leading to decrease in the received intensity level.

Cosmic noise method was introduced for the very first time by Mitra & Shain, (1953), where the extraterrestrial radio wave intensity was used to measure the ionospheric absorption. Based on such works conducted in the early 1950s, Little & Leinbach, (1959) designed the riometer for the very first time and found it to be ideally suitable for studying the D-region dynamics. Since then, many works have been done to study the effects of various geomagnetic phenomena, at specially the D-region altitude, for an extended latitudinal range (Bhonsle, 1960; Jelly & Brice, 1967; A. Ranta & Ranta, 1990; H. Ranta et al., 1993; Stauning, 1996).

The selection of operating frequency of a riometer has great significance in studying the absorption patterns and several points has to be taken into consideration. First, the operating frequency should be well above the penetration frequency of the ionospheric region so that the cosmic noise reaches the altitude without significant deviation while passing the ionosphere. Second, the frequency should not be very high so that even at times of ionospheric disturbances it passes almost unaffected. The frequency dependence of the absorption has to be taken in account so that every major and minor variation in the level of absorption can be detected. Cosmic radio noise in the frequency range 30-60 MHz has found to meet the above criteria and is a commonly accepted range of riometer operating frequency.

The cosmic radio noise has a fairly constant intensity outside the Earth's environment. These waves get absorbed once they reach the ionosphere, and the intensity of absorption at any given time and location depends upon the enhancement in the electron density. Cosmic noise absorption (or CNA) at any time is specified by the difference between the received cosmic noise

power at that time and the power that would have been received if there was no absorption. The enhancement in ionization at high latitudes happens majorly due to precipitation during magnetospheric substorms and solar proton events.

2.1.1 Technique for deriving Quiet Day Curve (QDC) and CNA

In order to construct a CNA pattern for any disturbed day, it is important to first determine the baseline of the signal intensity. This baseline pattern of radio wave is called quiet day curve, or QDC. Imaging riometers can be utilized for both narrow and wide beam applications, however, most calculations primarily use wide beam datasets that are solar zenith and azimuth corrected. The wide beam dataset for a single day is obtained after averaging all the channel datasets, once the corrections are applied to them.

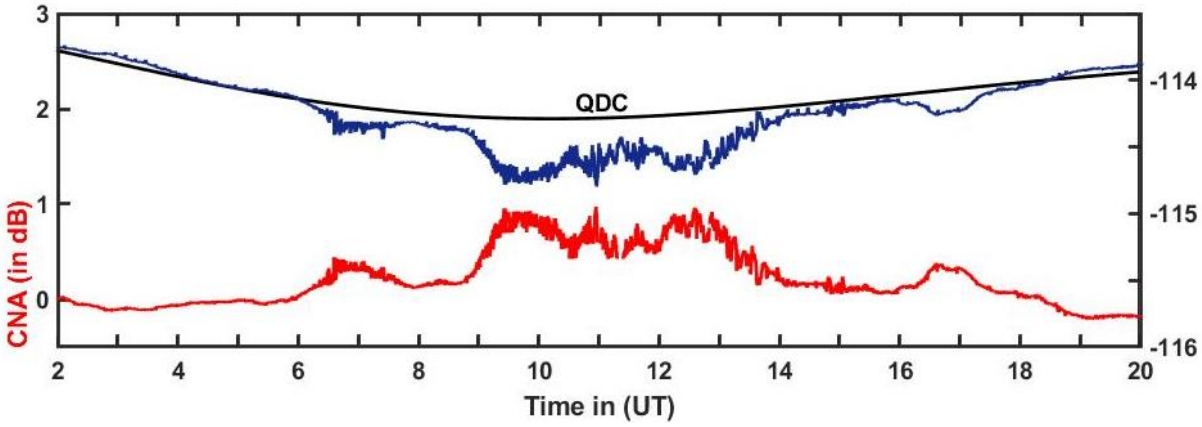

Figure 2. 1 QDC (black curve), disturbed day signal intensity (blue curve) and CNA curve (red curve) for the day 10th June, 2015, obtained using the datasets of riometer installed at Maitri.

The quiet days for a given month are known by looking into the Kp index values from the WDC Kyoto website. Normally, Kp index less than 3 is considered to be a quiet time. The method used to determine the QDC and CNA curves is extensively discussed by several authors (e.g., Behera et al., 2014; Mitra & Shain, 1953; Moro et al., 2012). In this method, firstly, any 5 international quiet days (Kp<3) for a given month is selected. Then the wide beam datasets of the selected 5 international quiet days are averaged to obtain the QDC.

After calculating the QDC, the CNA for any period of interest can be estimated. The CNA is actually the ratio of noise power during quiet period (say P1) to the noise power during any disturbed period of interest (say P2). It is given by the formula (Moro et al., 2012):

$$CNA\ (dB) = 10 \log \frac{P1}{P2} \tag{2.1}$$

An example of QDC and CNA as obtained from the riometer installed at Indian Antarctic Base Maitri is shown in figure 2.1

2.1.2 Types of Cosmic Noise Absorption (CNA)

At high latitude region, the Earth's magnetic field is almost vertical. It can be assumed that the transmission of cosmic noise signals through the ionosphere to the receiving antennas is "quasi longitudinal" with regard to the geomagnetic field for typical riometer frequencies (30-60 MHz) and for systems where the antenna beams are aimed close to zenith. The expression for the integrated radio wave absorption along a specified path has a particularly straightforward form in this instance, which is given by the Appleton-Hartey Equation (Booker, 1935):

$$A\ (dB) = \frac{q^2}{2\epsilon_o mc} \int \frac{Nv}{v^2 + (\omega \pm \omega_L)^2}\, dl \tag{2.2}$$

where q and m are the electron charge and mass; ϵ_o is the permittivity of free space and c is the speed of light; $\omega_L = \omega_c cos\theta$ is the longitudinal component of the electron cyclotron frequency ω_c. *N* and *v* are the local electron density and collision frequency values, respectively. The angular frequency of the wave travelling at an angle θ with the geomagnetic field is denoted by ω. The two distinctive quasi-circular polarizations are denoted by the + and – signs, respectively.

Appleton-Hartey equations provide a good approximation of absorption at ionospheric heights for typical riometer frequencies, which is much greater than the ionospheric plasma and gyro frequencies, provided the electron collision frequencies are velocity-integrated (Stauning, 1996). Equation 2.3 gives the formula of the “effective" electron collision frequency to be used in equation 2.1:

$$v_{eff} = \frac{\int_{v=0}^{\infty} \sum_N \sigma_m^n(v) v F(v) dv}{\int_{v=0}^{\infty} F(v) dv} \quad (2.3)$$

Where, σ_m^n is the velocity-dependent cross section for momentum transfer collisions (electrons with ions or neutrals); and *F(v)* is any velocity-distribution function. The collision frequency in a velocity-dependent cross-section will be different in different layers of the ionosphere, depending upon the dominant species (ions or neutrals). For example: in D region- electron-neutral collision; Lower E region- electron-neutral collision; Upper E region- electron-ion collision; and F-region- electron-ion collision.

On the basis of the latitude, local time, and season of the observation of CNA, different geomagnetic events leading to the observed absorption can be distinguish. It can be quite beneficial to have additional data from other ground-based instruments, such as magnetometers. Obviously, it is crucial to quantify the precipitating particle fluxes using in-situ satellites in order to correctly link absorption events to various geophysical conditions. CNAs are often categorized based on the source causing enhancement in the ionospheric ionization. Below are few of the majorly observed CNA types that are relevant to the present thesis:

1. Sudden Cosmic Noise Absorption (SCNA): Solar flares emits high amount of ultraviolet and soft X-rays, that are capable of enhancing the ionization in the D and lower E regions of the ionosphere over the entire solar illuminated part. Hence, during the daytime, the attenuation in radio waves is mostly due to photoionization caused by solar flares (Bhonsle, 1960; Bland et al., 2018; Brodrick et al., 2005). This may lead to a corresponding increase in the absorption of cosmic radio noise and are called solar flare associated CNA or SCNA (Ogunmodimu et al., 2018; Stauning, 1996). SCNA usually lasts for the duration of solar flare events and the observed magnitude is less compared to the CNA observed during solar energetic particle precipitation (Longden et al., 2007; Stauning, 1996).

2. Polar Cap Absorption (PCA): Large solar flare events can cause the sun to radiate intense high-energy electrons, protons, and α-particles. In contrast to lower latitudes where the atmosphere is typically protected by the Earth's magnetic field, this radiation has direct access to the atmosphere in the polar and auroral regions. In the D-region, the solar flare radiation that typically consists of electrons of energies greater than 100 keV and protons greater than 10 MeV, may result in significant ionization. The radio wave absorption caused as a result of such ionization enhancements are called Polar Cap Absorption or PCA. Such PCA episodes usually

begins about an hour after a significant solar flare. The HF radio blackout in the polar regions may endure for a few days, occasionally even one or two weeks, depending on how powerful the PCA absorption events are. The recombination during nighttime causes the PCA events to vary relatively smoothly with a recognizable day-night variation. Typically, the daytime absorption values are 2-10 times greater than the nighttime absorption intensity (H. Ranta et al., 1993).

3. Sudden Commencement Absorption (SCA): SCA absorption are linked to the concurrent geomagnetic SSC (storm sudden commencement) events. Sudden magnetospheric compression occur due to the arrival of shock fronts travelling in the solar wind flow, as well as other abrupt changes in the solar wind plasma pressure. Impulsive precipitation may result from such severe disruptions. Trapped population of electrons originally from central plasma sheet can scatter into the loss cone during magnetospheric compression (Liou et al., 2002b). Typically, 30-300 keV electrons may precipitate, that can lead to significant but transient ionization enhancements in the D-region (60-90 km). Increased radio wave absorption caused on by the enhanced ionization may result in events that can be picked up by riometers. These events could last a few minutes on average. The majority of the time, the incidents span a large geographic area (A. Ranta & Ranta, 1990).

4. Auroral Substorm Absorption (AA): These absorptions happen as a result of particle precipitation during substorm activities. The precipitating electrons are typically in the energy range 10-100 keV that reaches the lower E and D-region. These absorptions happen almost immediately in the midnight sector of the auroral zone and are often very intense and variable. Surges of strong and localized auroral disturbances may spread westward along the auroral oval shortly after the commencement of substorm activity. Since, the auroral electrojet current intensifies in a region influenced by the substorm activity, the presence substorm associated CNA is confirmed by checking for any variation in the geomagnetic H-component at that location (Stauning, 1996).

5. Dayside Cosmic Noise Absorption (DCNA): During disturbed geomagnetic conditions, intense clouds of energetic electrons are injected inside the magnetosphere from the night side across closed field lines. They may later drift eastward under the combined impact of the gradients in the geomagnetic field and the magnetospheric electric fields. These electrons can precipitate into the ionosphere by falling into the loss cone due to several wave-particle interactions. Such precipitations lead to radio wave absorptions in the extended regions of local times, away from midnight, and are called DCNA (Behera et al., 2016a).

2.2 Riometer at Indian Antarctic Base, Maitri (70.75°S, 11.75°E)

Figure 2. 2 Imaging Riometer at the Indian Antarctic Station, Maitri.

An imaging riometer was installed at the Indian Antarctic Base, Maitri during the austral summer of 2009-2010. The image of the installed riometer is shown in figure 2.2, that operates at 38.2 MHz frequency. It consists of 16 crossed dipole antennas arranged in a "4 x 4" matrix format. This system can be upgraded to 64 dipole antennas in "8 x 8" matrix format at later stages. This riometer has a field of view of "200 km X 200 km" at 90 km altitude, and a sampling frequency of 1 second. Each dipole antenna points to particular part of the sky and has its own field of view. The field of view at ionospheric D-region height (90 km from ground) as seen from above is shown in figure 2.3.

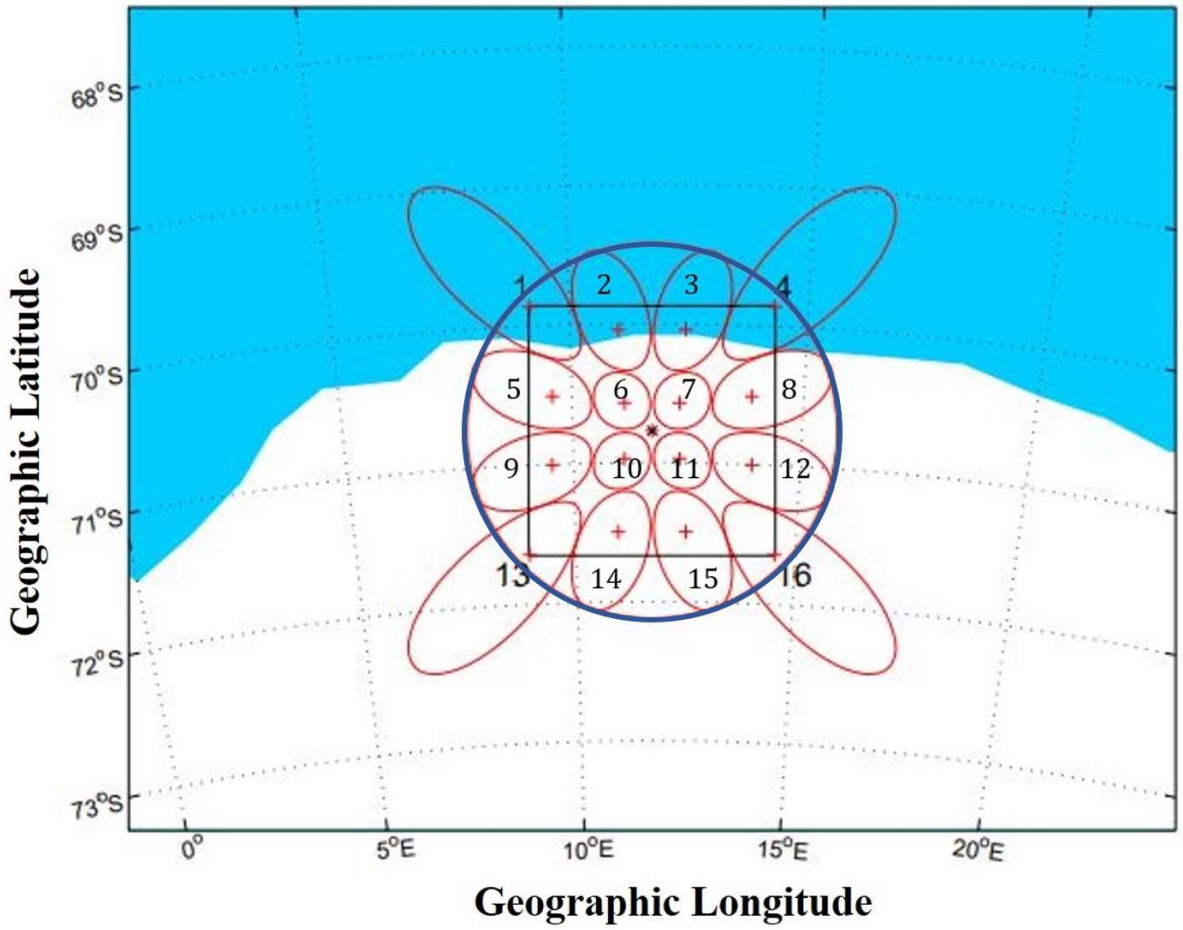

Figure 2. 3 Field of view of each dipole antenna individually (red ovals), and combined field of view of all the 16 antennas after zenith and azimuth corrections (blue circle), as seen from the top of the curved ionosphere.

The hardware, operations and data processing for the 4 × 4 imaging riometer at Maitri was designed and built by Lancaster University. The software that runs the imaging riometer and is in charge of recording all data is called ARCOM (Advanced Riometer Components). Software for loggers and controllers is built using components. To start, stop, or inquire about the status of any particular component, ARCOM uses the Common Object Request Broker Architecture (CORBA). MIA, which is a multi-instrument analysis toolbox for MATLAB programming, is used for all the riometer data processing stages. MIA can display image plots, keograms, and videos for every type of imaging device due to a cohesive structure. Data files are automatically merged so that processing of the data is not halted by file boundaries. Despite the availability of a graphical user interface, all actions can be carried out by scripts, allowing for the automated processing of big datasets and statistical analysis.

The output file of any day consists of 86400 rows and 32 columns. The first 16 columns consist of the dataset of each dipole antenna pointing towards a certain direction in the sky, for an entire day with a sampling frequency of 1 second (24 hours x 60 minutes x 60 seconds = 86400 seconds). The next 16 channels consist of the datasets of every antenna after applying the zenith and azimuth corrections. This correction estimates the value of each antenna that would have been received if they had zero zenith and azimuth angles, all pointing in the same direction and having the same field of view. When the datasets of the corrected channels are averages and used, it is called 'wide beam' CNA curve. When individual channels are used without corrections it gives the 'imaging beam' CNA curve of each channel. The table below, table 2.1, shows the width, azimuth and zenith of all the 32 channels.

Table 2. 1 Beam details

Beam No.	Raw Data			Corrected Data		
	Width (°)	Azimuth (°)	Zenith (°)	Width (°)	Azimuth (°)	Zenith (°)
1	25.54	-45.00	57.80	119.90	0.00	0.00
2	27.69	-18.70	43.70	119.90	0.00	0.00
3	27.69	18.70	43.70	119.90	0.00	0.00
4	25.54	45.00	57.80	119.90	0.00	0.00
5	27.69	-71.30	43.70	119.90	0.00	0.00
6	26.33	-45.00	19.30	119.90	0.00	0.00
7	26.33	45.00	19.30	119.90	0.00	0.00
8	27.69	71.30	43.70	119.90	0.00	0.00
9	27.69	-108.70	43.70	119.90	0.00	0.00
10	26.33	-135.00	19.30	119.90	0.00	0.00
11	26.33	135.00	19.30	119.90	0.00	0.00
12	27.69	108.70	43.70	119.90	0.00	0.00
13	25.54	-135.00	57.80	119.90	0.00	0.00
14	27.69	-161.30	43.70	119.90	0.00	0.00
15	27.69	161.30	43.70	119.90	0.00	0.00
16	25.54	135.00	57.80	119.90	0.00	0.00

2.2.1 QDC and CNA Calculations

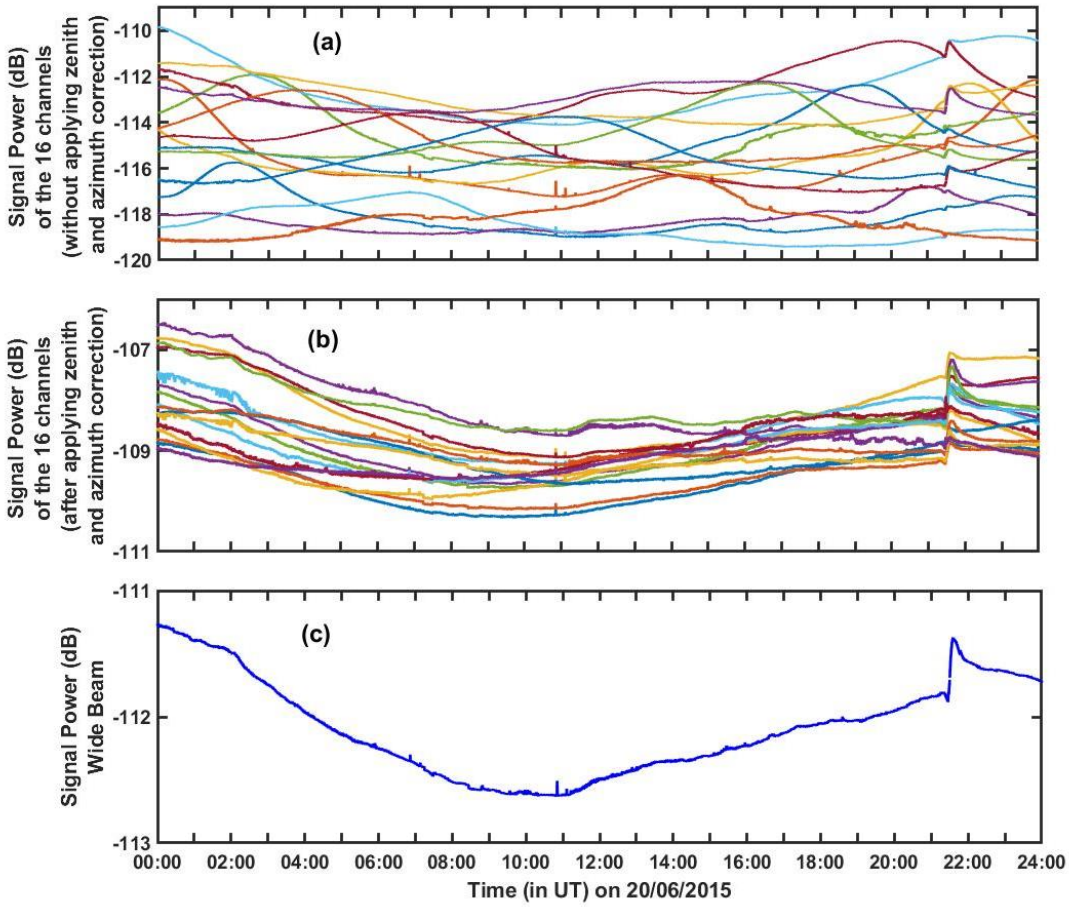

Figure 2. 4 (a) Absorption curves obtained using the datasets of the 16 antennas without applying zenith and azimuth corrections; (b) absorptions curves after applying the corrections to the 16 channels; (c) averaged wide beam dataset.

The QDC and CNA curves of Maitri is derived using the same process as discussed in section 2.1.1. Since, the output file of Maitri gives directly the absorption values in decibels (dB) and not in power units, we can simply subtract the outputs of the two days, i.e., QDC and any disturbed day of the same month, to obtain the final CNA curve.

To obtain the wide beam signal output for any specified day, the corrected datasets of the 16 channels are averaged. Figure 2.4 shows the initial 16 imaging beam datasets before correction, the next 16 (17-32) beam datasets after applying the corrections, and the final wide beam dataset for one day that is obtained by averaging the corrected channels. Such wide beam

curves are obtained for five international quiet days and averaged to obtain the QDC for any given month. Figure 2.5 shows the calculated QDC of every month for the year 2015.

2.2.2 Sidereal Time and Monthly variation of Quiet Day Curve (QDC)

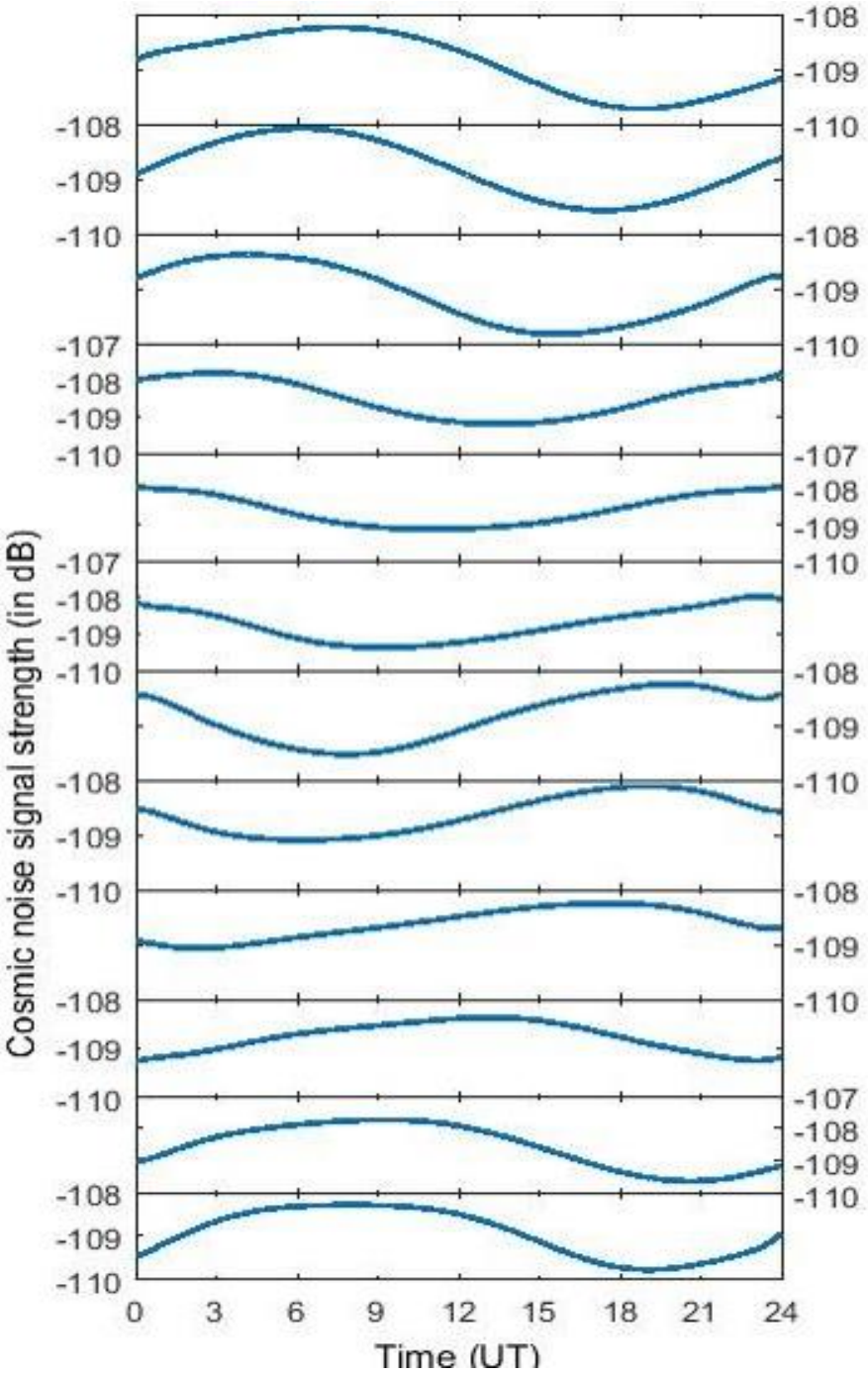

Figure 2. 5 Quiet Day Curve computed for each month of the year 2015 (from January to December, top to bottom), using datasets of riometer installed at Maitri.

Sidereal time refers to the time scale taken by the Earth to complete one rotate relative to any fixed star. In general, an average sidereal day is of about 23 hours and 56 minutes, whereas a solar day is of 24 hours. Hence, the sidereal day and the solar day has an approximate difference of 4 minutes. The signal strength of radio noises will vary based on this sidereal time for every month. This is because the imaging riometer output data is calibrated in the solar time format, or what we call Universal Time (UT) format. Therefore, while deriving the QDC with respect to UT format, the diurnal pattern of the signal strength is expected to shift for about 2 hours (4 minutes x 30 days) for every consecutive month, as shown in figure 2.5. This method is also used to validate the accuracy of the dataset of riometer instruments, and was initially done for the riometer at Maitri as well (Behera et al., 2014).

As seen from the figure 2.5, the maximum value of the signal strength for the month January, 2015 (topmost panel) was at around 08:00 UT. For February it shifted to 06:00 UT, and for March around 04:00 UT, so on and so forth. The strength of the observed radio signal has a day/night and seasonal dependency. Even during quiet days, when there is no external input of particle flux, the solar radiation will determine the level of absorption of the cosmic radio signal. Usually, during the month of equinox, there is a maximum drop observed in the signal strength. However, the signal strength of QDC do not completely follow the solar illumination pattern, and several other factors significantly contribute towards the seasonal variation at Maitri (Behera et al., 2014).

2.3 Usage of IRIS (Imaging Riometer for Ionospheric Studies)

Wide beam riometers usually consist of a single dipole antenna, whereas imaging riometers consists of an array of antennas, hence, it is quite obvious that imaging riometer can have a significant importance over wide-beam riometer. The wide beam riometer can be useful to get a general overview of the state of ionosphere at a particular time. However, within their field of view, it cannot provide any additional information about the dynamics and the spatial structure of the ionosphere at any particular altitude. This issue can be resolved if we replace one antenna with an array of antennas, as in the case of imaging riometer technique. This technique can be very useful in studying the spatial and temporal dynamics of energetic particle precipitation and solar radiation. In the following case-studies, this technique has been used to analyze the substorm precipitation and solar ionization patterns.

The imaging riometer technique is an excellent approach for identifying the extent of locations that experience energetic particle precipitation and tracking their dynamical evolution. However, it might not always show the exact behavior of an event since the source of ionization cannot be separately identified, if there are more than one which is normally the case. The oblique beams have a larger field of view than the zenith beam, especially in the radial direction (figure 2.3). Thus, the response of IRIS (Imaging Riometer for Ionospheric Studies) may differ slightly from the actual distribution of absorption if there are spatial gradients in absorption, specially towards the edges (Collis et al., 1996). By converging a theoretical distribution of absorption with the individual beam antenna designs, a model has been created to study this impact. The calculations show that if the absorption region is wider than 25 km, the majority of the beams will capture at least 90% of the actual absorption. This width would need to be 50-70 km for the beams near the edges. The results also quantitatively indicate the extreme corner beams' weak performance, which are mostly excluded when constructing an imaging pattern from the data (Collis et al., 1996).

The wide beam CNA curve efficiently serve the purpose of comparing the level of ionization between locations. Hence, in the present thesis we will be using the wide beam absorption pattern to compare the ionization enhancements for a given range of latitudes and longitudes.

2.3.1 Imaging Riometer Observation during Substorm

The injection of particles during a substorm takes place from the midnight sector. The near-Earth reconnection in the night side magnetotail region leads to the precipitation of particles in the auroral region following the field lines. It is expected that if a riometer station falls in the midnight sector at the time of substorm onset, all the channels would immediately observe enhancement in radio noise absorption due to this precipitation. However, when a station would fall in a local time sector away from midnight, all the channels might not observe similar absorption. The spatial and temporal variation may then depict the precipitation pattern in the ionosphere after a substorm onset. This should ideally be the case if the absorption is directly related to substorm particle precipitation only. However, in reality there can be several processes going on simultaneously that can lead to radio wave absorption, like: ionospheric plasma drifts, polar cap absorption, solar flare associated absorption etc.

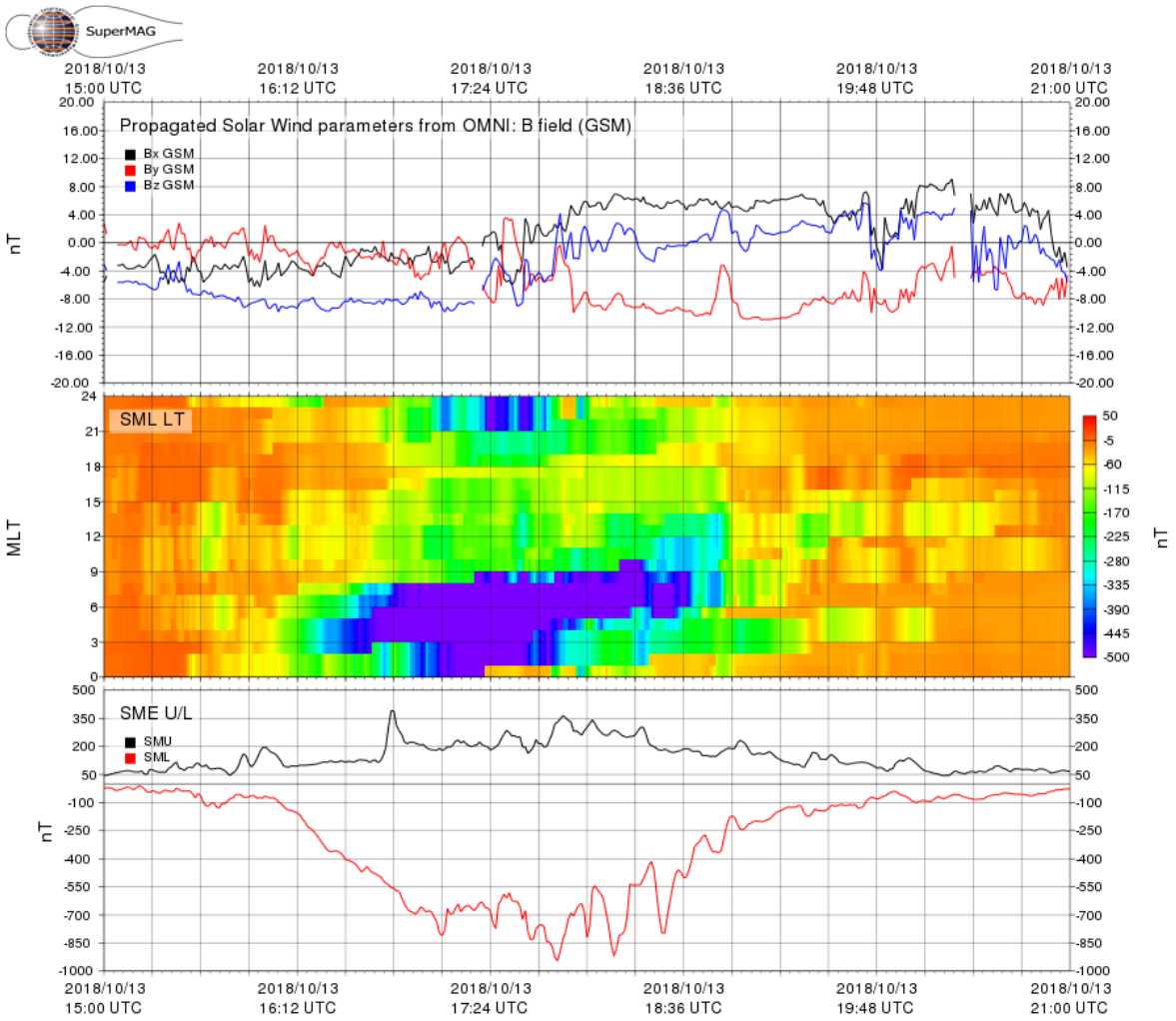

Figure 2. 6 The plot represents the solar wind and geomagnetic parameters of the substorm event on October 13, 2018 from 15:00 UTC to 21:00 UTC. The plot is obtained from the SuperMAG website [http://supermag.jhuapl.edu/]. From top to bottom, the panels show (a) interplanetary magnetic field (the three components in GSM coordinates), (b) SML LT, and (d) the SMU and SML indices showing onset and intensity of substorm.

In the following case studies, we show how imaging riometers can be used to analyze the spatial and temporal variation pattern and the difference between wide beam and imaging beam absorption curves. We compare the imaging results with and without the corrections employed.

Figure 2.6 shows the interplanetary condition and auroral indices on 13th October, 2018. The plot has been obtained from the SuperMAG website (http://supermag.jhuapl.edu/). The first panel of the figure shows the interplanetary magnetic field components. The second panel shows

the SML-LT variation, which is the SuperMAG derived westward auroral electrojet index at different local time sectors (Newell & Gjerloev, 2011). The third panel shows the SuperMAG AL (SML) and AU (SMU) indices, that determines the onset and intensity of substorm. On October 13, 2018, the substorm onset happened around 16:00 UT with a peak SML index of ~900 nT. It was a long duration substorm event that lasted for about four hours. The magnetic local time of Maitri is: MLT=UT-01:10; hence, at the time of substorm onset on this day Maitri was in the post noon-to-evening sector.

To obtain the imaging riometer pattern, CNA curves corresponding to each riometer antenna has been calculated separately. For obtaining these curves, a QDC needs to constructed for each channel, by using the method discussed in the previous section. Then eventually a CNA curve for each channel will be obtained by subtracting the signal strength on any given day from the respective QDCs. The spatial and temporal variations can be analyzed when the azimuth and zenith corrections has not been employed to the channels. This is because each antenna points to a particular part of the sky and gives the ionization information about that location. Once the zenith and azimuth corrections are applied it changes the field of view of all antennas to be the same. An example of the CNA curves obtained for different channels without applying the corrections is shown in figure 2.7 for the substorm on October 13, 2018. The field of view of each imaging beam is as shown in figure 2.2, and the corresponding absorption value gives the idea of the level of ionization in that area.

To obtain the wide beam CNA curves, the datasets of all the channel is averaged. However, this average can be done only if each antenna points in the same direction and has the same field of view. Hence, zenith and azimuth corrections are employed to the imaging beams after which all the antennas have 0° zenith and azimuth angles, as shown in table 2.1. Figure 2.8 shows that CNA curve of individual channels after applying the corrections as observed on October 13, 2018. It is observed that after employing the corrections all the channels show almost similar magnitude of absorption.

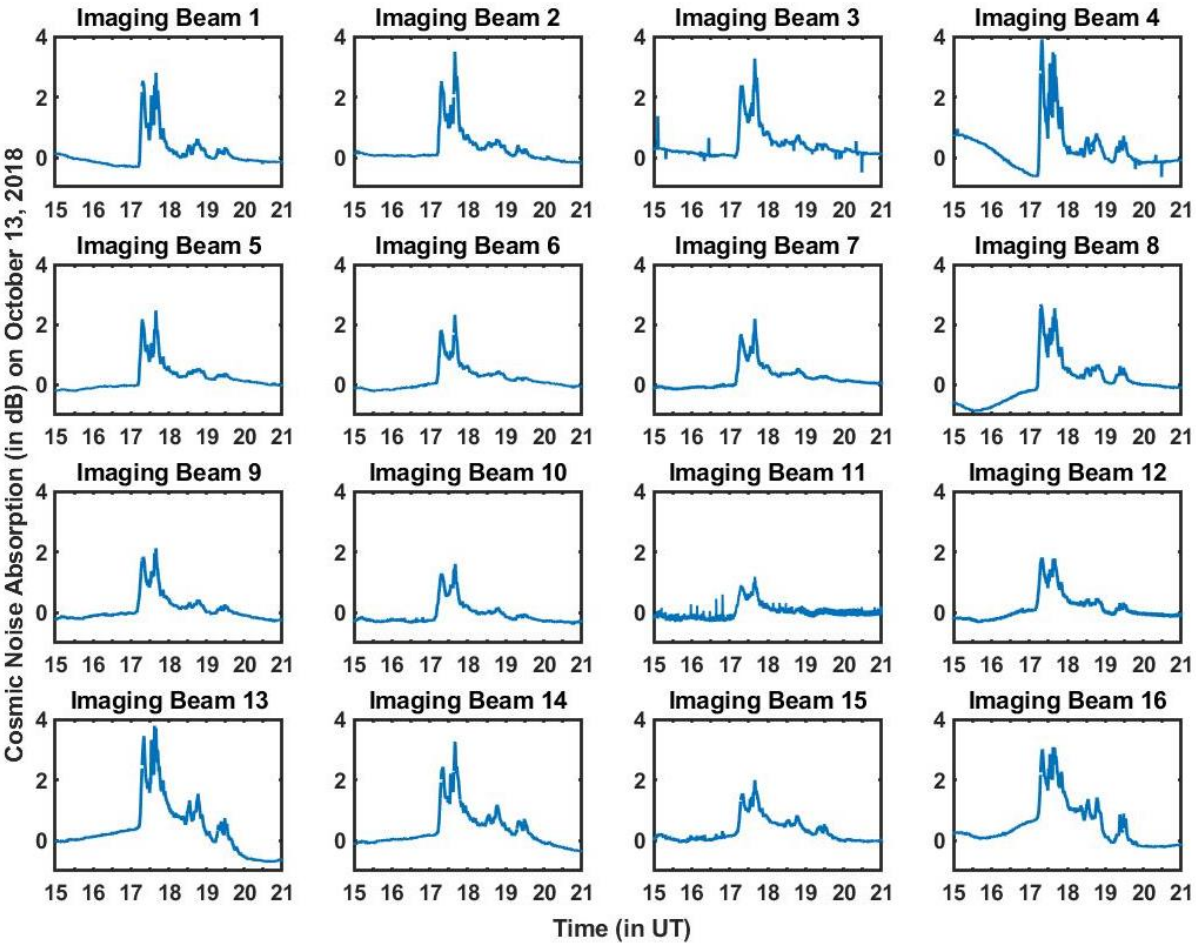

Figure 2. 7 CNA curves obtained for each channel without applying the zenith and azimuth correction. Each plot represents the substorm-associated absorption at different locations in the '200 km x 200 km' area of D-region on October 13, 2018.

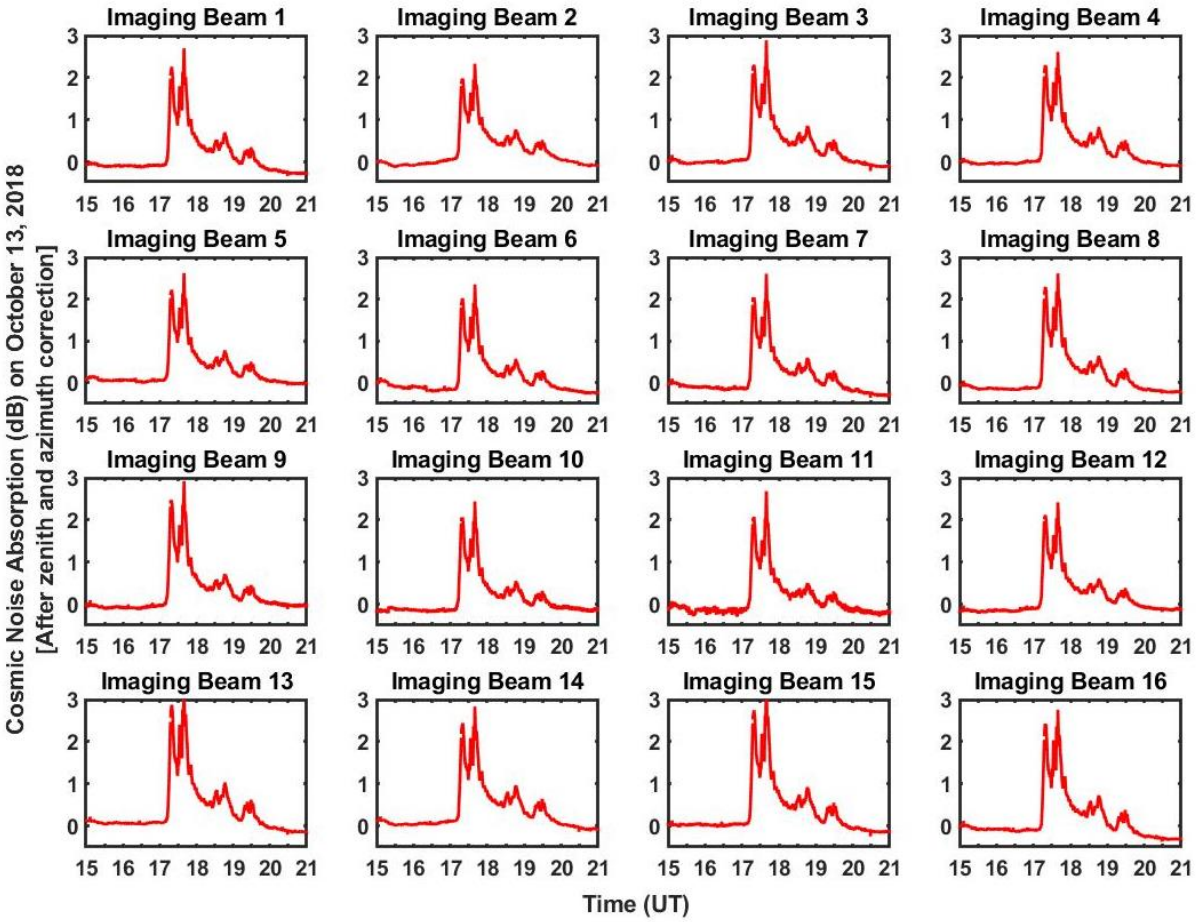

Figure 2. 8 CNA curves obtained for each channel after applying the zenith and azimuth correction. Each plot represents the substorm-associated absorption in the entire '200 km x 200 km' area of D-region as observed from different riometer antennas on October 13, 2018.

When the datasets of the corrected channels are averaged, we get the wide beam CNA curve for any specified day. Figure 2.9 shows the wide beam CNA curve for the October 13th 2018 substorm. Mostly, if the absorption of multiple stations needs to be compared to study the absorption pattern in an extended latitudinal and longitudinal range, the wide beam CNA curves are used.

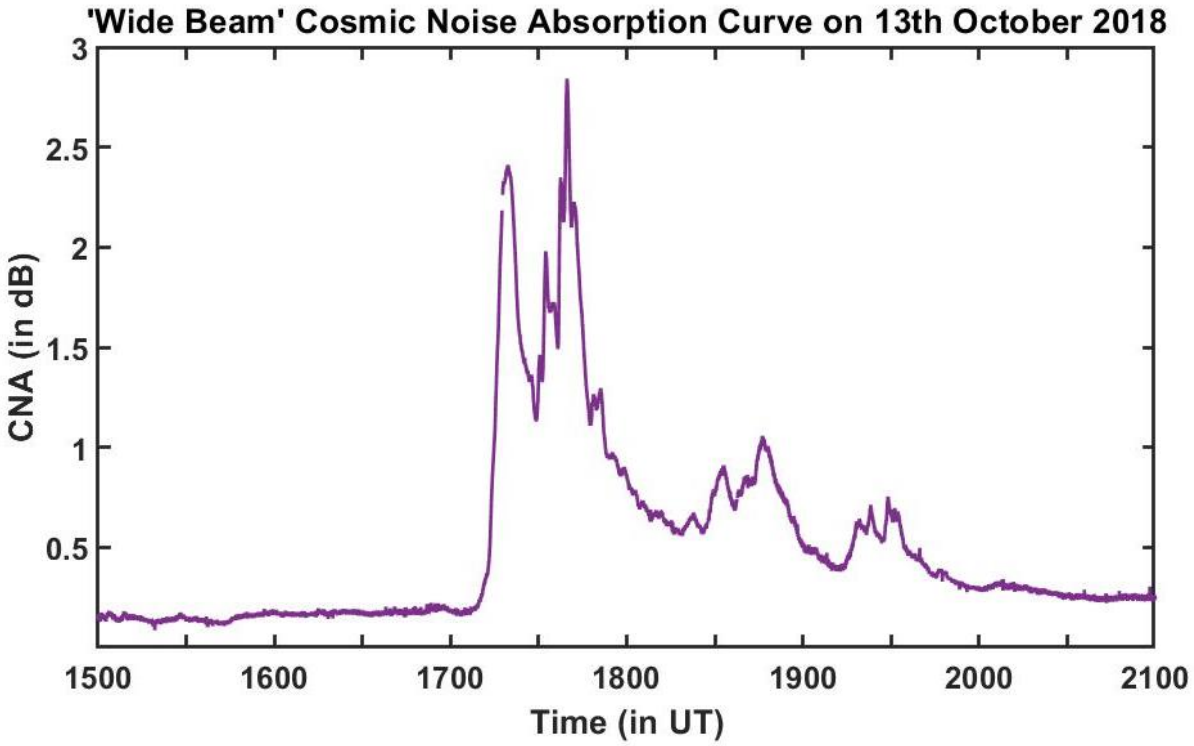

Figure 2. 9 Substorm associated CNA on October 13, 2018 as observed from Maitri.

The imaging beams shows a huge difference in the intensity of signal strength before and after the zenith/azimuth corrections are applied. Figure 2.10 shows the magnitude of absorption soon after the onset, as observed from different channels before and after corrections, on October 13, 2018. These values have been obtained from figure 2.6 and 2.7. The intensity of absorption before applying the corrections varies from 1 to 4.5; while after correction varies from 2 to 2.7 only. It is very clear from the figure that after applying the corrections the imaging property of the riometer is lost, and the array of antennas acts like one single antenna.

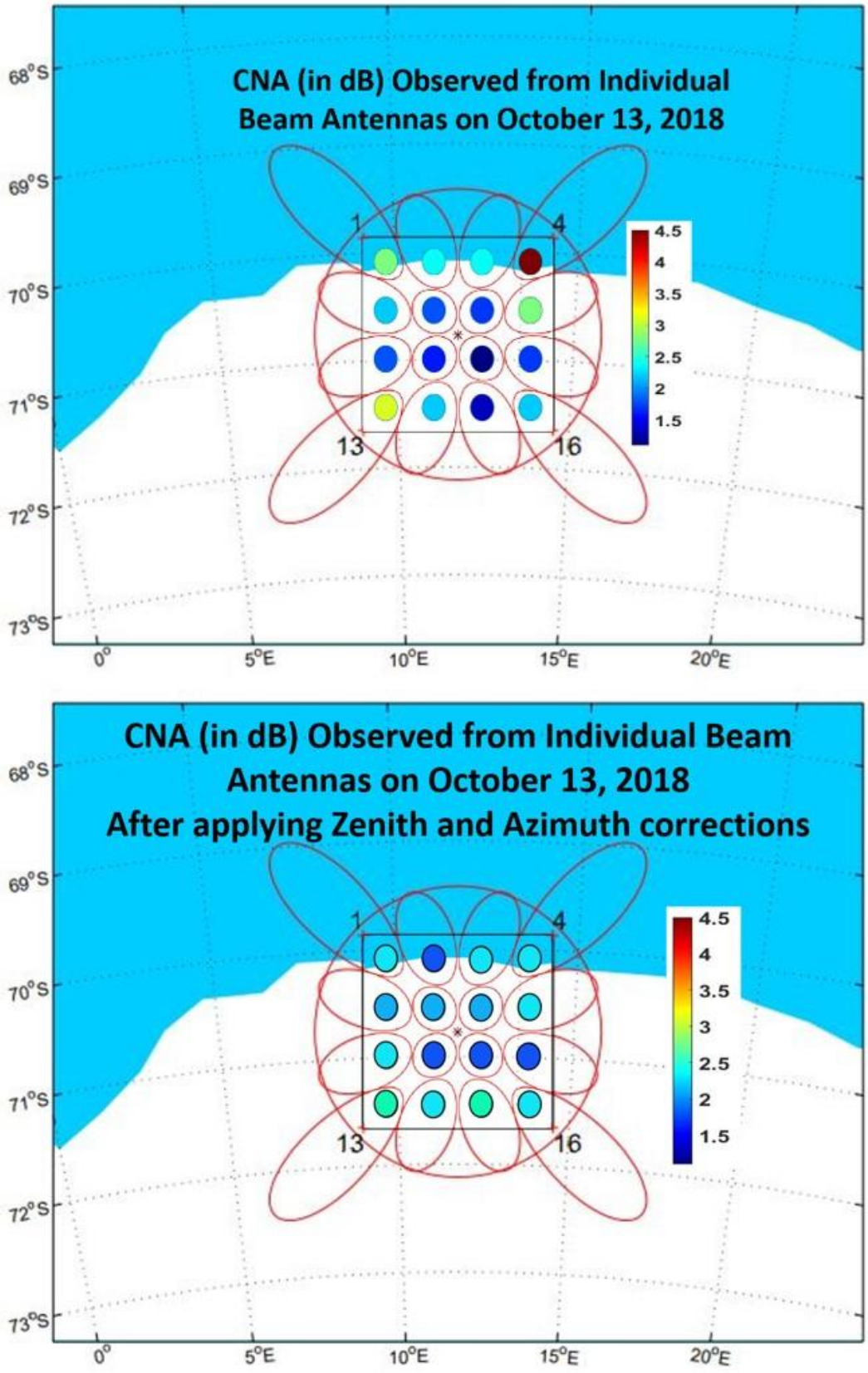

Figure 2. 10 Intensity of absorption as observed from each antenna (a) before and (b) after applying zenith and azimuth corrections on October 13, 2018. The color bar indicates CNA (in dB).

2.3.2 Imaging Riometer Observation during Solar Flare (SCNA)

Solar radiation is responsible for ionizing the atmosphere over the entire solar illuminated part of the Earth. X-ray radiation coming from the solar flares can penetrate up to the D-region of the ionosphere to further enhance the ionization. At high latitudes, both X-ray radiation and particle precipitation can be responsible for this enhancement. Hence, to analyze the effects of X-ray radiation during solar flare events, selecting a non-substorm time can be helpful. A strong X-class solar flare occurred on 26th October, 2014, that started on 10:04 UT and ended at 11:18 UT. During this time there was no ongoing substorm as seen in figure 2.11, which shows no variation in the SME U/L index.

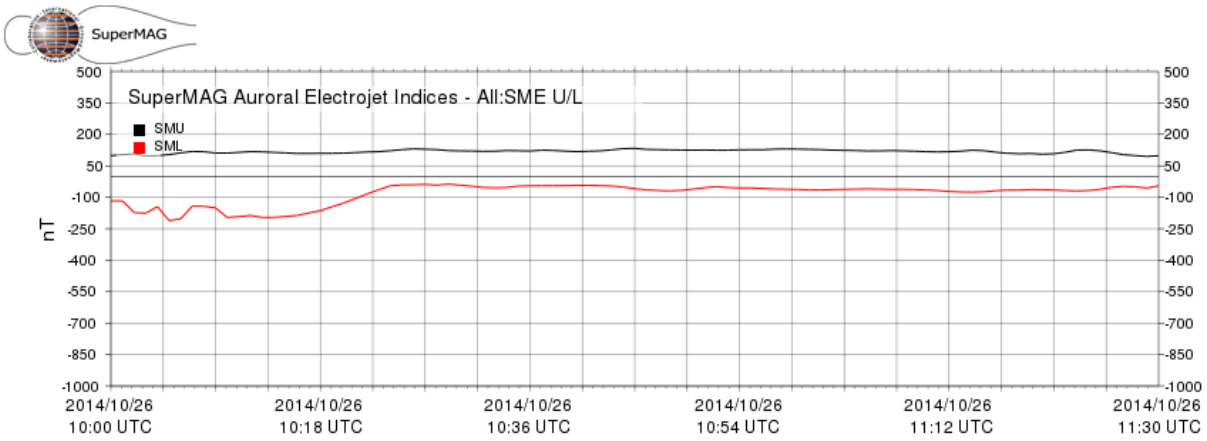

Figure 2. 11 SME U/L index on October 26, 2014 obtained from SuperMAG [http://supermag.jhuapl.edu/].

The solar flare associated cosmic noise absorption events might persist for as long as the flare event. This can be anywhere around few seconds to minutes, and the intensity of absorption will depend upon the class of flare and the season. Hence, for the given day the CNA, that started at around 10:35 UT and lasted till around 11:20 UT, was observed within the time window of the occurrence of flare. The channel wise SCNA plots of the imaging riometer on October 26, 2014 is shown in figure 2.12. The field of view of each antenna is as shown in the figure 2.2. There is a considerable difference in the absorption curves of different channels as observed in figure 2.12.

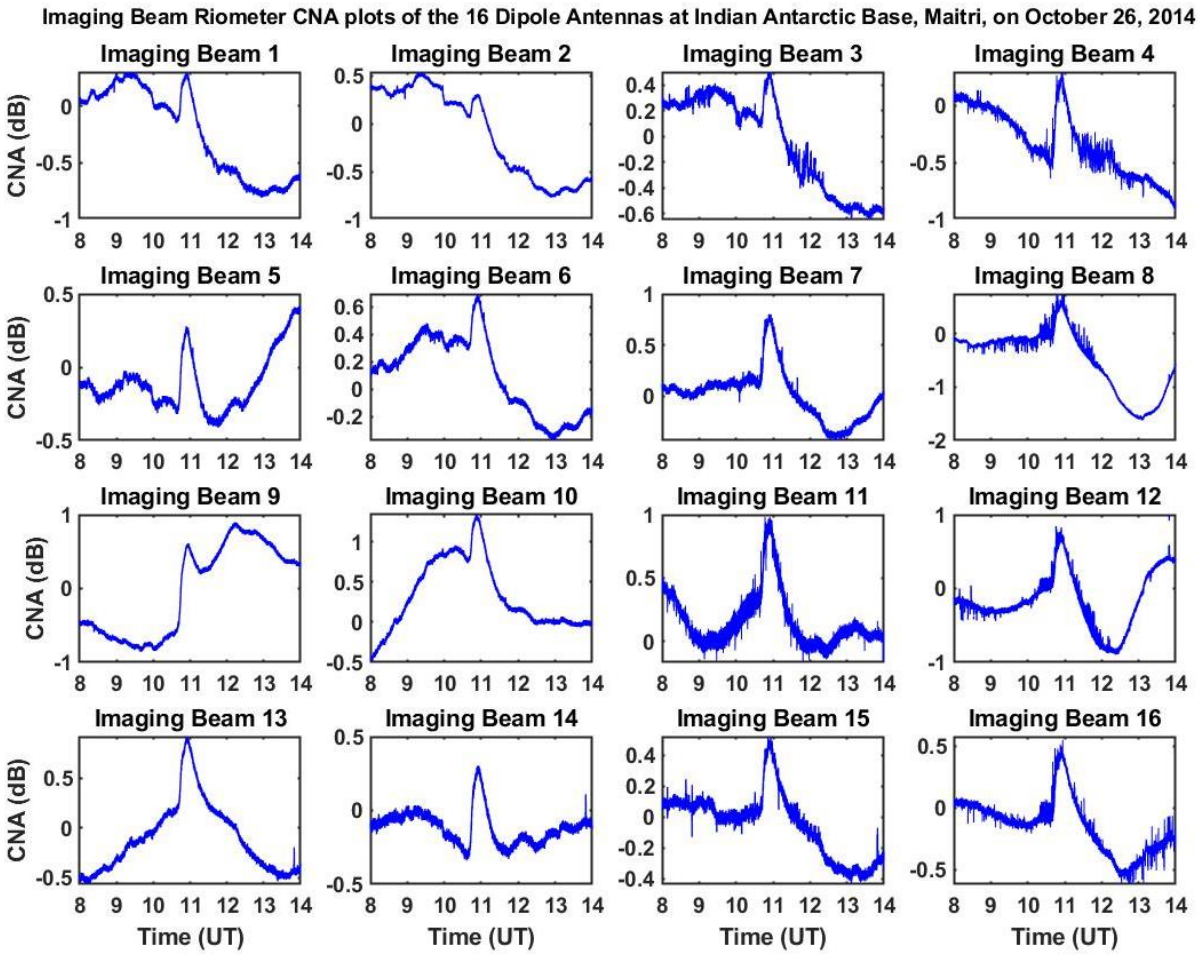

Figure 2. 12 SCNA curves obtained for each channel without applying the zenith and azimuth correction. Each plot represents the solar-flare associated absorption at different locations in the '200 km x 200 km' area of D-region ionosphere on October 26, 2014

The intensity of absorption as observed from each riometer antenna is shown in figure 2.13. The bar plot shows the variation in intensities to be from 0.3 dB to 1.2 dB. These intensity values are obtained before applying the zenith and azimuth corrections to the channels; hence, they represent the level of absorption in the field of view of each riometer antenna. Figure 2.14 shows the wide beam SCNA curve, which is obtained after averaging the corrected channels' datasets.

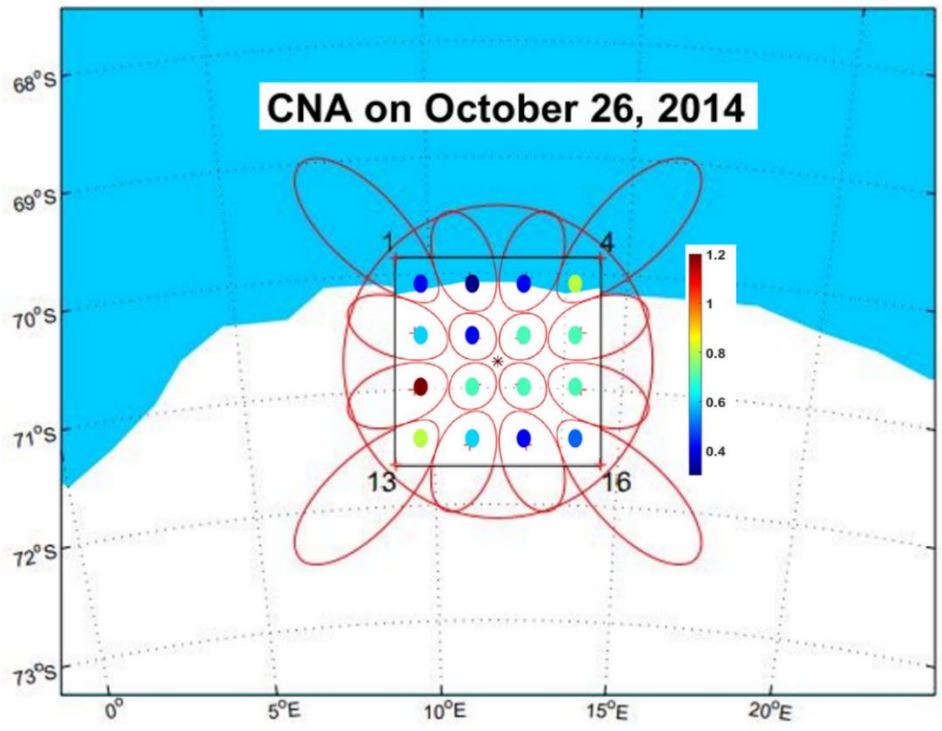

Figure 2. 13 Intensity of absorption as observed from each antenna before applying zenith and azimuth corrections on October 26, 2014

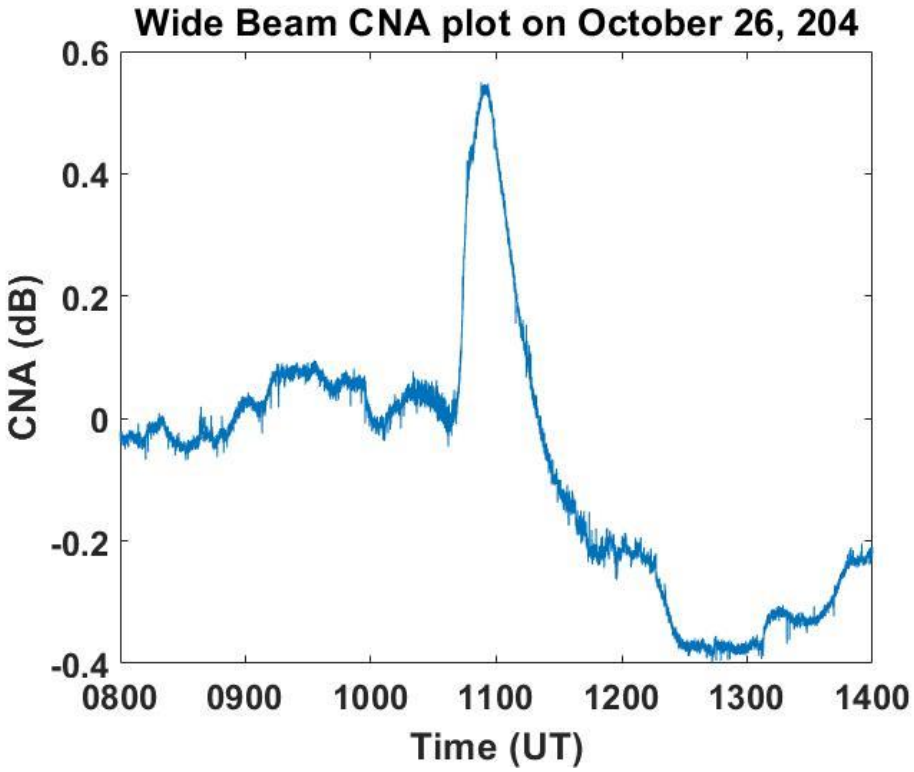

Figure 2. 14 Solar flare associated CNA on October 26, 2014 as observed from Maitri.

Chapter 3

Unusual Substorm Onset and Expansion on January 21, 2005

3.1 Introduction

Magnetospheric substorm is believed to be a typical midnight sector phenomenon (S. I. Akasofu, 1964), which gets triggered after the interplanetary magnetic field turns southward (Meng et al., 1973; Tsurutani & Meng, 1972). This preconditioning allows the magnetic energy to get transferred from the solar wind into the magnetosphere, and is stored in the magnetotail. When this stored magnetic energy becomes unstable, it gets released during substorm activity. Magnetic field dipolarization at ~10-15 Re along with Earthward and tail-ward ion bulk flows at 20-25 Re (indicating a near-Earth neutral line) can be concurrently seen at the time of substorm onset. This is considered to be a typical signature of the substorm expansion phase (Baumjohann et al., 1999; Baumjohann & Truemann, 1996). Since early 1970s, it is believed that for a substorm to arise, a southward IMF is necessary about ~1.5 hours prior to the onset, so that sufficient energy can be loaded into the magnetotail (Burch, 1972; Tsurutani and Meng, 1972; Zhou & Tsurutani, 2001 and references therein). However, there are also a number of studies that reported weak-to-moderate intensity substorms occurring during northward IMF conditions (S. I. Akasofu et al., 1973; Grocott et al., 2002; Kamide et al., 1977; Lee et al., 2010; Lui et al., 1976; Nishida, 1971). Miyashita et al. (2011) and Wu et al. (2002) have reported a series of substorm expansions occurring under prolonged northward IMF persistent for more

than 15 hr. The suggested mechanism was enhanced convection and energy accumulation in the magnetotail due to large IMF |By| effect. It was concluded that during persistent northward IMF periods, a large IMF |By| can possibly lead to dayside magnetic reconnection between the closed dayside geomagnetic field line and northward IMF fields, transferring solar wind energy into the magnetosphere (Freeman et al., 1993; Nishida et al., 1998; Ogino et al., 1986; Park et al., 2006; Reiff & Burch, 1985). These substorms follow the same loading-unloading mechanism as during typical southward IMF associated substorm (Miyashita et al., 2011; Petrukovich et al., 2000).

Further, it was also shown that the energy stored in the magnetotail during the loading done by a preceding southward IMF Bz can also lead to the occurrence of a substorm under northward IMF condition (A. I. Akasofu, 1975; Lee et al., 2010). Such substorms are expected mainly during the recovery phase of an intense storm (Lee et al., 2010). It is believed that the tail can be left with substantial amount of energy for the occurrence of a substorm even after releasing certain amount. The tail reconnection can operate for about one hour of northward turning of IMF suggesting that the magnetotail can contain enough energy for several tens of minutes for a substorm to take place even when IMF is not southward (A. I. Akasofu, 1975; Lee et al., 2010). Hence, for the onset of the expansion phase of a substorm either (i) a southward IMF Bz is required prior to the onset for directly or indirectly leading to the loading-unloading process; or (ii) large IMF |By| is necessary in case of persistent northward IMF condition. The mechanism of substorm expansion onset is same in all the cases, whether it is due to typical southward turning of IMF or during prolonged northward IMF Bz condition(Lee et al., 2010; Miyashita et al., 2011; Petrukovich et al., 2000).

However, other than these possible mechanisms, there are also reports suggesting that sudden compression of magnetosphere alone can trigger substorms, and is independent of the orientation of IMF (Kawasaki et al., 1971; Rostoker & Falthammar, 1967; Schieldge & Siscoe, 1970). There is no consensus on what mechanism do these impulse-induced substorms follow to get triggered. In this chapter we will be discussing about a strong substorm event of 21st January 2005, which has an onset/triggering mechanism different from the usual nightside loading-unloading process and is neither associated with southward IMF Bz nor with large IMF |By| component.

The supersubstorm (SML< -2500 nT) (Tsurutani et al., 2015) event of 21st January 2005 reported by Hajra & Tsurutani (2018), was different from other known substorm events in many ways, as listed:

(i) The energy input via magnetic reconnection prior to the onset was insufficient to power this event (Hajra & Tsurutani, 2018).

(ii) Unlike the usual auroral signatures, the onset and expansion of substorm aurora did not take place from the nightside and the intense aurora was located either in the pre-midnight or post-midnight sector (Hajra & Tsurutani, 2018).

(iii) Since, a sudden impulse coincided with the substorm onset, this event was called impulse-induced (Hajra & Tsurutani, 2018).

Some earlier studies demonstrating that interplanetary shocks can also at times trigger substorms even without the southward turning of IMF (Kawasaki et al., 1971; Rostoker & Falthammar, 1967; Schieldge & Siscoe, 1970), concludes that the percentage of occurrence of such events are less than 50 percent. However, this event is different from the ones studied before because of its very high intensity.

The features associated with the substorm of 21st January 2005 definitely marked this event unique, but the important aspects which remained unclear about this event were:

(i) where did the energy come from to power this event?

(ii) Whether the signatures of substorm expansion onset, viz., (a) the plasmoid formation and dipolarization in the magnetotail region, (b) particle precipitation mechanism and (c) intensification of the auroral electrojet currents; are same as those during a typical substorm?

(iii) Whether there is any special characteristic signature associated with the present substorm?

To find the answers to these questions we carried out a detailed multi-instrument analysis of this day. In the present chapter, this substorm event is revisited along with additional database to cover almost all the high latitude region and local time sectors. This includes the database of global cosmic noise absorption (CNA) which is calculated using riometer datasets, electron and proton auroral images by IMAGE satellite taking in account all the MLT (magnetic local time) sectors, energetic electron flux data from geostationary satellites, ground magnetic field measurements of various magnetometer stations and from SuperMAG (http://supermag.jhuapl.edu/). Observations were corroborated with BATS-R-US MHD simulation model results (https://ccmc.gsfc.nasa.gov/requests/requests.php).

For the case of 21st January 2005 substorm, the BATS-R-US MHD simulation results show that there was no signature of magnetic reconnection and dipolarization in the magnetotail

at/after the substorm onset at 17:11 UT. These processes which are considered to be the typical characteristics of substorm expansion phase (Baumjohann et al., 1999) were absent during the substorm onset of this day. The ground observations of CNA, aurora and electrojet currents were also found to be in accordance with the model results. The merging of magnetic field lines, dipolarization and plasmoid formation in the nightside started only after 17:21 UT. This was also the time when IMF Bz turned southward and, therefore, can allow the solar wind-magnetosphere coupling via magnetic reconnection. Hence, the substorm had a two-step onset; one at 17:11 UT which was completely impulse induced and the other at 17:21 UT which was associated with the typical southward turning of IMF. During the first ~10 minutes after the onset, i.e., from 17:11 UT to 17:21 UT, the decrement in AL index, which is used to describe substorm phases and activity (Davis & Sugiura, 1966), was almost -2000 nT indicating a very intense substorm. Our focus is to understand how this initial substorm onset of such huge intensity took place. There after the picture appears to be similar to that of any other typical substorm evolution associated with the southward turning of IMF.

Section 3.2 describes the observations from various instruments. Section 3.3 provides a summary and discussion including future implications of our study in brief. Section 3.4 highlights the conclusions.

3.2. Observations

3.2.1 Interplanetary Condition and Geomagnetic Indices

The interplanetary condition and the geomagnetic field parameters on 21st January 2005 from 15:30 UT to 18:30 UT is shown in figure 3.1. The plot is created using OMNI datasets obtained from CDAWeb (https://cdaweb.gsfc.nasa.gov/cgi-bin/eval1.cgi). A sharp decrease in the AL index at ~17:11 UT in panel (f) indicates the onset of the substorm and is marked by a black solid vertical arrow in the plot. This onset will be referred to as the first onset of the substorm in the chapter hereafter. The second step of AL index intensification at ~17:21 UT, indicated by a black dotted arrow, will be referred as the second onset of the substorm. The peak AL index recorded was ~3668 nT and the duration of the substorm was ~1.7 hours. Hence, this substorm was categorized as a supersubstorm (SSS) because of its high intensity and long duration. At the time of SSS onset, Sym-H which is used to indicate magnetic storm, was +37 nT, as shown in panel (g), and remained almost positive for the entire duration of the event. The fourth and fifth panel of the figure shows that the IMF Bz and By components were close to ~0

nT for at least ~1.5 hours prior to the substorm onset. This is a very remarkable feature of this substorm. The preconditioning of IMF *Bz* and *By* that leads to the substorm onset is missing in this case. It is only after the shock arrival and substorm onset at 17:11 UT, IMF Bz turned positive and remained northward for about ~10 to ~11 minutes; whereas IMF By turned negative. Panels (a), (b) and (c) shows a sudden increment in the solar wind dynamic pressure, velocity, and proton density, indicating the presence of a strong pressure pulse at the time of the first onset at 17:11 UT.

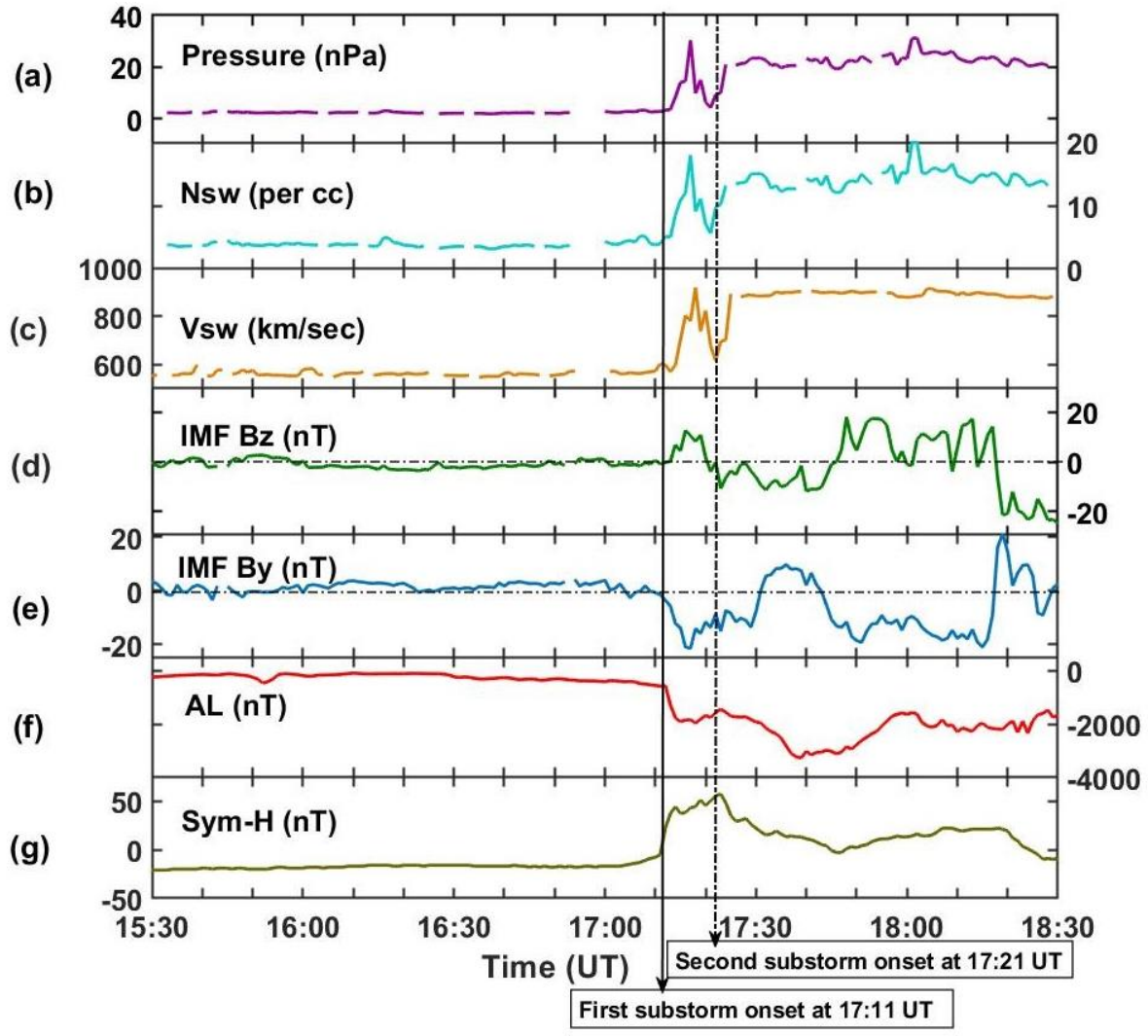

Figure 3. 1 The interplanetary condition and the geomagnetic indices during the supersubstorm event of 21 January 2005. The panels show (a) solar wind pressure (in nPa), (b) solar wind speed (Vsw in km/s), (c) solar wind proton density (Nsw in cm^{-3}), (d) IMF Bz and, (e) IMF By in GSM coordinates, (f) AL and, (g) Sym-H indices. Onset of the substorm is indicated by the vertical solid black line at 17:11 UT.

3.2.2 Auroral Observations

We looked into the satellite images of aurora taken by NASA's Imager on-board IMAGE (Magnetopause-to-Aurora Global Exploration; Mende et al., 2000) satellite from the southern hemisphere, keeping in account all the local time sectors. Figure 3.2 (a) and (b) shows the global view of aurora after the first and second substorm onsets respectively in three wavelength ranges, viz., 121.8 nm, 135.6 nm and 140-180 nm. The images in figure 3.2 (a) are at ~17:11 UT in the first row, ~17:13 UT in the second row and ~17:15 UT in the last row; marking the onset and expansion of aurora after the first onset at 17:11 UT. Figure 3.2 (b) corresponds to auroral images after the second onset at ~17:21 UT at an interval of 2 minutes each, i.e., at ~17:21 UT in the first row, ~17:23 UT in the second row and ~17:25 UT in the last row. The first columns of the figure 3.2 (a) and (b) show auroras of oxygen OI emission having 135.6 nm wavelength, generated mostly by electrons along with some contribution of energetic protons (Frey et al., 2003, 2004). The second columns of each figure show 121.8 nm aurora which is generated only by protons. And the third columns show wideband auroral images having wavelength 140-180 nm, generated due to molecular nitrogen excitation. In all the images, sun is at the top at 12:00 MLT, night-side (00:00 MLT) is in the bottom, dawn (06:00 MLT) is on the right side and dusk (18:00 MLT) is on the left side.

From the images shown in figure 3.2 (a), it is clear that the onset of auroras after ~17:11 UT took place predominantly from the dayside (middle row of Fig 3.2a). Dayside auroral intensification is caused by electron energy precipitation which increases significantly after shock/pressure pulse arrival (Tsurutani et al., 1981; Moen et al., 2001; Zhou et al., 2003; Frey et al., 2019 and Liu et al., 2019). Electron aurora remained dominant in the dayside even after the second substorm onset as shown in figure 3.2 (b) (first column). The longitudinal expansion of electron aurora from dawn and dusk was mainly at ~70 deg. MLAT, and the midnight sector was mostly devoid of intense aurora. The proton aurora and aurora @ 140-180 nm initially intensified from the dayside (figure 3.2(a) second and third column) and then expanded towards night side covering almost all the longitudes. If we look into the images of the second and third column of figure 3.2 (b), there is an enhancement in aurora near to post-midnight sector, in addition to the shock aurora in the afternoon hours. This suggests that the auroral onset at ~17:21 UT was in the midnight sector.

(a) Auroral Images after the first onset at 17:11 UT

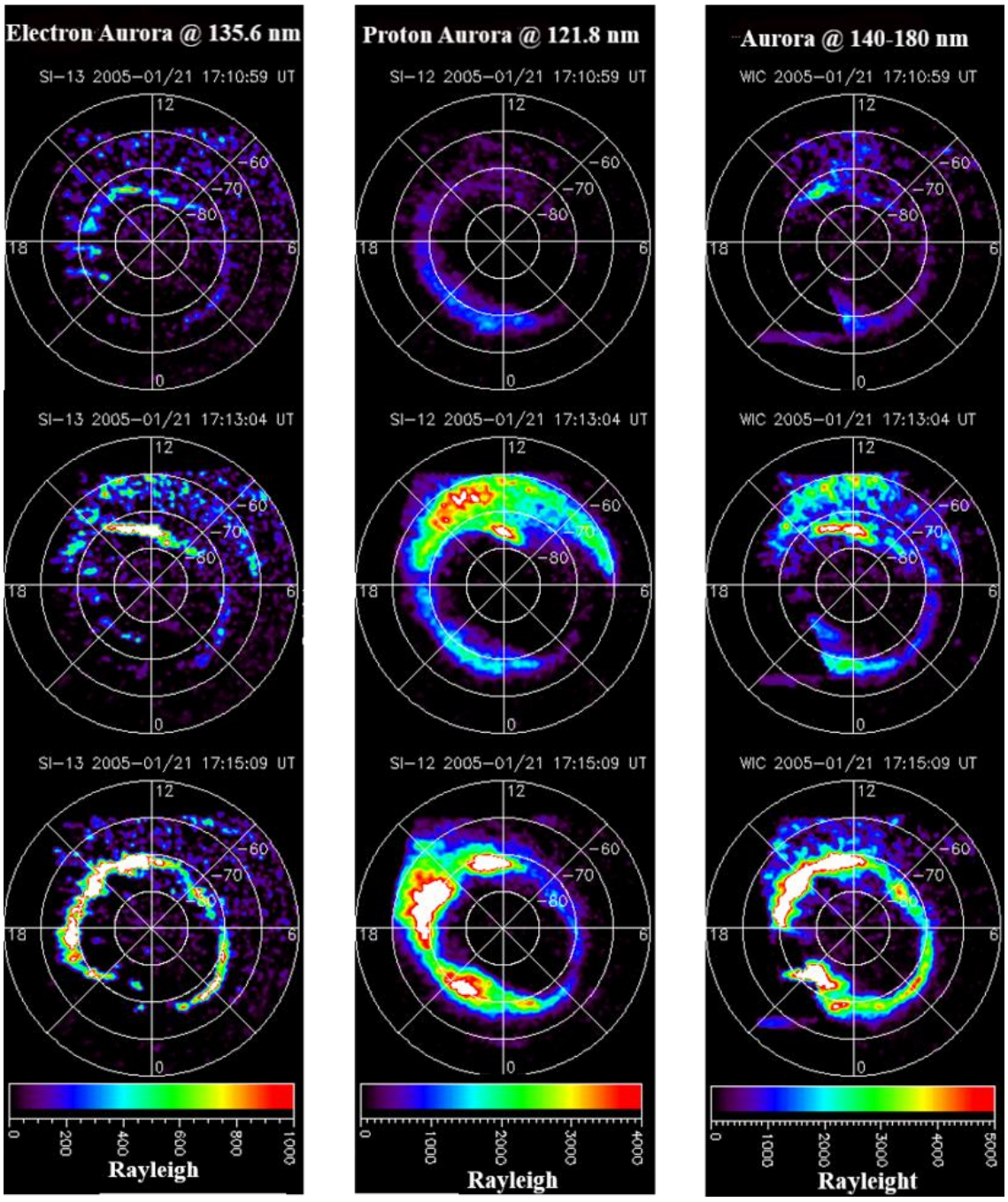

(b) Auroral Images after the second onset at 17:21 UT

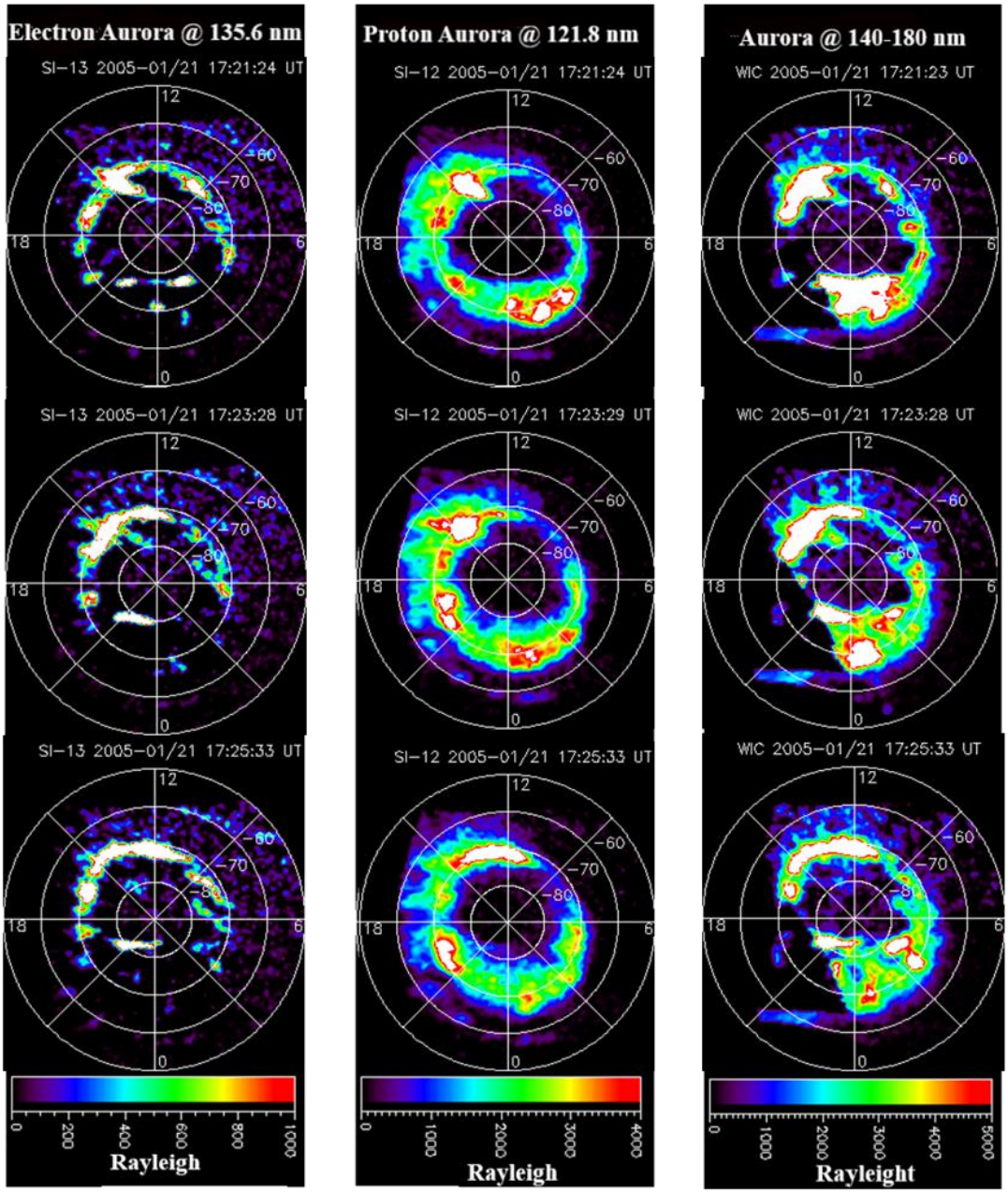

Figure 3. 2 Global view of aurora on 21st January 2005, obtained by IMAGE satellite. First columns of (a) and (b) shows Electron Auroral Images in FUV range having wavelength 135.6 nm, taken by SIC (Spectrographic Imaging Camera). Second columns of both the images show Proton Auroral Images of wavelength 121.8 nm in FUV range, taken by SIC. Third columns show Auroral Images having wavelength 140-180 nm in FUV range, taken by Wideband Imaging Camera (WIC). All the three types of auroral images in figure 2 (a) are shown from ~17:11 UT to ~17:15 UT, each after an interval of two minutes each; and similarly in 2 (b) are at ~17:21, ~17:23 and ~17:25 from top to bottom. Top of each image is at 12:00 MLT, bottom is 00:00 MLT, right is 06:00 MLT and left is 18:00 MLT.

3.2.3 BATS-R-US Model MHD Simulation Results

The model used in this chapter is the Block–Adaptive–Tree Solar–Wind Roe–Type Upwind Scheme (BATS–R–US) magnetosphere model from the Space Weather Modeling Framework (SWMF, Toth et al., 2005, 2012). BATS–R–US is configured to typically solve the ideal MHD equations, but is also in fact a multi-physics code that allows consistent modelling of the global magnetosphere (Glocer et al., 2013). The simulation of BATS-R-US is a powerful tool for studying magnetospheric physics, which covers the tail reconnection site along with an adaptive kinetic PIC (Paticle-In-Cell) region so that one can effectively study geomagnetic substorms in far more realistic way (Gombosi et al., 2021). This model takes the upstream SW/IMF inputs from OMNI database and gives output in the GSM coordinate system at an output frequency of 60 seconds. The RCM ring current model has been used for the present analysis.

An outlook of the evolution of the night side and dayside magnetopause is shown in Figure 3.3. The simulation of solar wind flow around the Earth along with IMF and geomagnetic field lines are depicted at different time intervals. The 2D cuts in the XZ plane of GSM coordinate displays a part of the larger 3D domain. Figure 3.3 (a) (i), (ii) and (iii) are at times 17:09 UT, 17:11 UT and 17:15 UT respectively, giving an idea of the magnetospheric condition before and after the first onset. The blue lines with arrows in the figure 3.3 (a) (i) and (ii), indicating the IMF lines, are pointing towards positive X-direction showing the absence or near zero values of IMF Bz. At 17:15 UT the IMF has turned towards positive Z-direction, indicating northward turning of IMF, which is consistent with the IMF Bz plot in Figure 3.1. The closed field lines of the Earth's magnetic field, which is indicated by red lines, remained unchanged in the night-side throughout until 17:20 UT (shown till 17:15 UT in the plot). At 17:21 UT, shown in figure 3.3 (b) (i), the closed field lines of Earth's magnetic field can be seen upto X= ~ -25 Re, which is a typical distance at which the NENL (near earth neutral line) reconnection during the substorm onset is expected. At this time, IMF was southward as shown by the blue arrows in the figure and is the second onset of substorm. Immediately after this reconnection there appeared a plasmoid formation and dipolarization in the nightside. These are believed to be the typical signatures of substorm expansion phase (Baumjohann et al., 1999). The closed geomagnetic field lines have then extended beyond in the figure 3.3 (b) (ii) and (iii), indicating the continuation of substorm expansion phase.

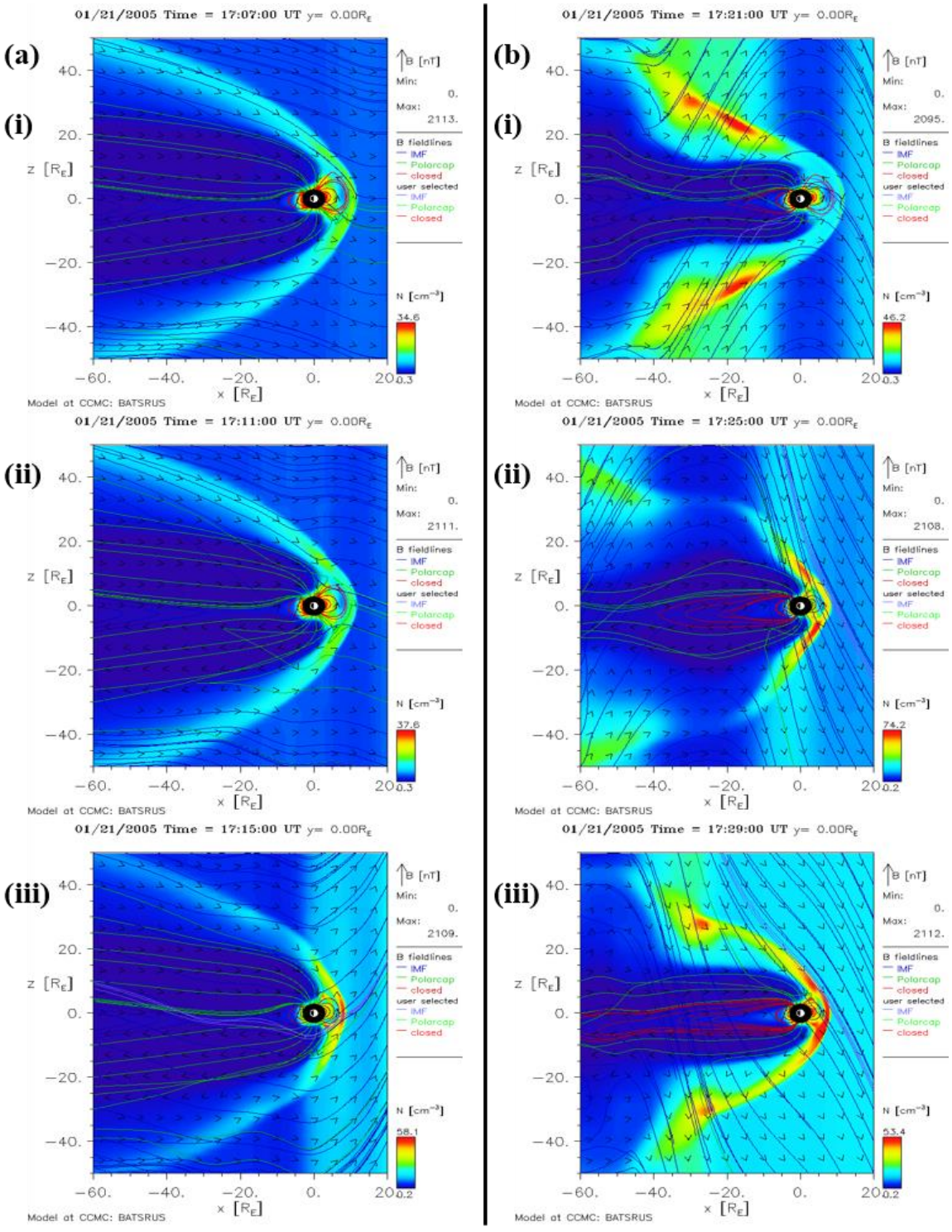

Figure 3. 3 BATSRUS simulation of solar wind flow around the earth in GSM coordinates in the XZ plane. The colourbar shows particle number density N (cm^{-3}), blue arrows indicate IMF, green lined indicate the open field lines of Earth's magnetic field and red lines indicate the closed ones. Figure (a) (i), (ii) and (iii) Shows the modeled global magnetosphere at 17:07 UT, 17:11 UT and 17:15 UT; before and after the first onset. Figure (b) (i), (ii) and (iii) are at times 17:21 UT, 17:25 UT and 17:29 UT; after the second onset. Sun is towards the positive x-axis.

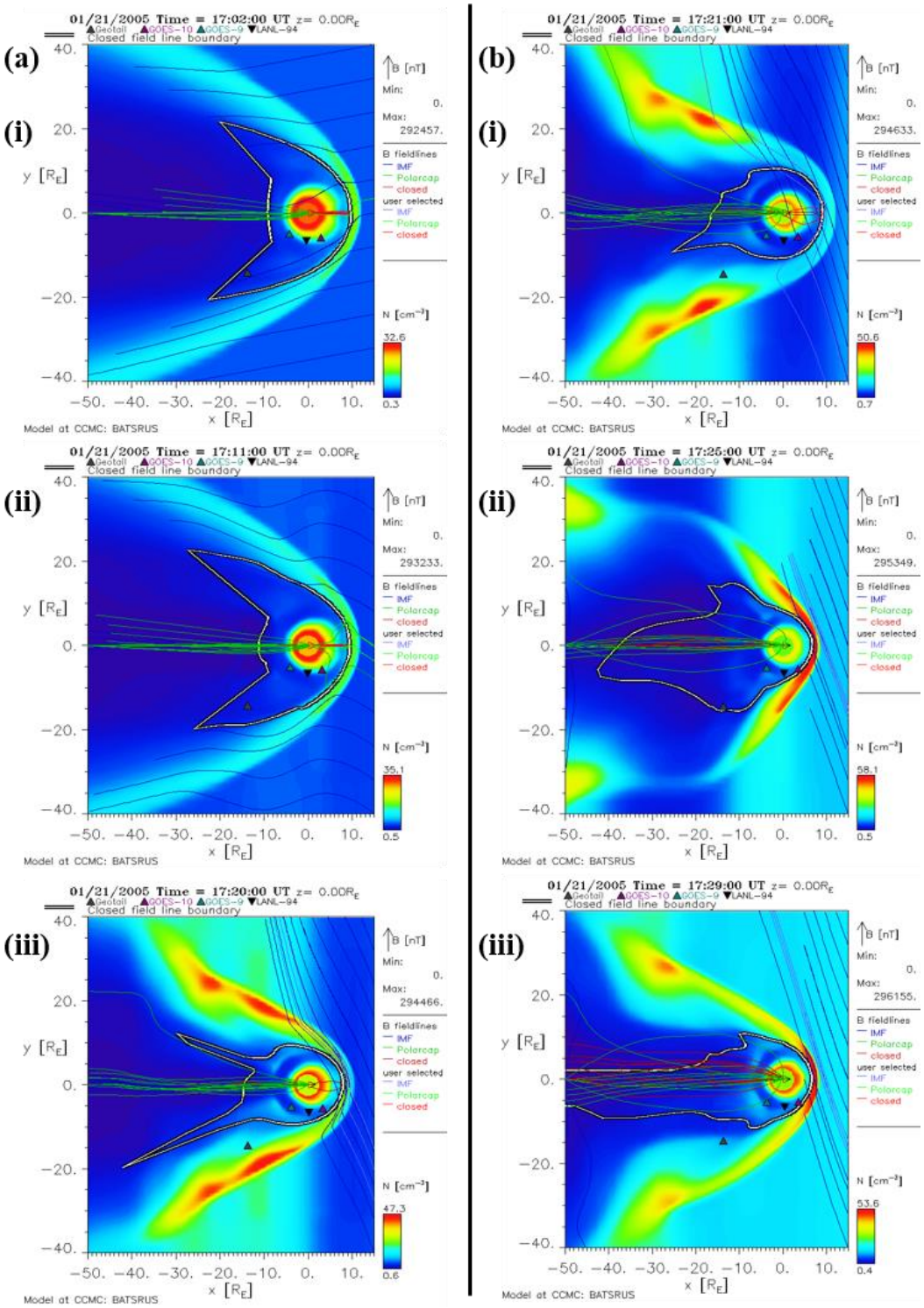

Figure 3. 4 BATSRUS simulation of solar wind flow around the earth in GSM coordinates in the XY plane. The colourbar shows particle number density N (cm^{-3}), blue lines indicate IMF, green lined indicate the open field lines of Earth's magnetic field, red lines indicate the closed field lines of Earth and the white solid curve shows the closed field line boundary. Figure 3.4 (a) (i), (ii) and (iii) shows the modeled global magnetosphere at 17:02 UT, 17:11 UT and 17:20 UT; before and after the first onset. Figure 3.4 (b) (i), (ii) and (iii) are at times 17:21 UT, 17:25 UT and 17:29 UT; after the second onset. Sun is towards the positive x-axis.

Figure 3.4 shows the 2D cuts of the magnetosphere in the XY plane of GSM coordinate. Two black lines separated by white colour indicate the boundary of the closed field lines. Figure 3.4(a) (i) depicts the scenario before the substorm onset at 17:02 UT. In Figure 3.4(a) (i) and (ii), the boundary of closed field lines was stretched in the dawn and dusk sector and the equatorial closed field line was at ~13 Re. At 17:20 UT, the boundaries of closed field lines were comparatively narrowed. After the start of nightside magnetic reconnection and dipolarization at ~17:21 UT (figure 3.4 (b) (i)) the closed field lines in the nightside can be seen stretching towards the dawn sector only, indicating that the NENL reconnection, which was previously seen in figure 3.3 (b) (i), got shifted towards the post-midnight sector and did not happen in the typical midnight sector. This is consistent with the appearance of aurora in the post-midnight sector after the second onset at ~17:21 UT as discussed in the previous section and shown in figure 3.2 (b).

3.2.4 Riometer and Magnetometer Observations

As discussed in the previous chapters, Riometer (Relative Ionospheric Opacity meter) is basically a radio receiver which continuously measures the cosmic noise level being incident on the surface of the Earth. A riometer interprets the decreased strength of cosmic radio noise of solar and galactic origin incident on the Earth's ionosphere and is used to investigate the enhancement in the ionization in the D-region ionosphere (Little & Leinbach, 1959). Particle precipitation results into enhanced ionization in D-region causing absorption of these cosmic radio noises leading to decreased intensity in the level of the received radio signal (Behera et al., 2014; Browne et al., 1995; Jelly & Brice, 1967; Stauning, 1996). Ionospheric absorption at any time is specified by the difference between the received cosmic noise power and the power that would have been received if there were no absorption at that time (Mitra & Shain, 1953). Hence, knowing the undisturbed 'Quiet Day' (QD) level, the ionospheric absorption can be calculated from the attenuated cosmic noise intensities which are recorded during the disturbed days (Jelly & Brice, 1967; Moro et al., 2012; Stauning, 1996).

We have examined the ground based riometers and magnetometers of various high latitude stations during the supersubstorm of 21st January 2005. Table 3.1 shows the list of Riometer stations used in the present analysis along with their geomagnetic locations. The CNA datasets calculated in dB has been directly obtained from the source data providers/official websites, and is used for the present analysis.

Table 3. 1 The list of riometer stations used in this study.

Sr. No.	Name of the station	Geomagnetic Latitude	Geomagnetic Longitude (°E)
1	Pinawa, Canada	60.19° N	331.27°
2	Sanae, Antarctica	61.55° S	44.08°
3	Macquarine Island, Antarctica	64.32° S	248.26°
4	Ivalo, Finland	65.18° N	108.49°
5	Abisko, Sweden	65.42° N,	101.70°
6	Dawson, Canada	65.92° N	331.27°
7	Gillam, Canada	66.28° N	332.53°
8	Rabbit Lake, Canada	67.05° N	318.48°
9	Fort Churchill, Canada	68.57° N	332.99°
10	Mawson, Antarctica	70.44° S	90.72°
11	Contwoyto Lake, Canada	72.97° N	303.93°
12	Hornsund, Svalbard	74.23° N	109.26°
13	Davis, Antarctica	74.71° S	100.83°
14	Taloyoak, Canada	78.54° N	330.93°
15	Casey, Antarctica	80.74° S	157.75°

I. Cosmic Noise Absorption (CNA) Characteristics of 21st January 2005

In Figure 3.5 the CNA curve of stations under study have been divided into two panels. Left panel shows the absorption plots of stations located in the dayside at the time of the first substorm onset and right panel shows the stations located in the night side at that time (17:11 UT). The absorption plots in each panel are arranged according to the latitude of the respective station, and starts from the sub-auroral station then moving towards the polar. The time of the first substorm onset is indicated by black solid vertical arrow. Not much variation is seen in the CNA curves before the first substorm onset, but after that absorption onsets at all the locations is observed, which is indicated by a sudden increase in each curve. The substorm onset and the CNA onsets in the auroral region (near ~65°) coincide in the night side as well as in the day-side.

Whereas, a delay is observed in the absorption onset as we start moving away either towards the equator or towards the pole. Green curves indicate CNA of stations showing sudden absorption onset and pink curves indicate CNA of stations having a delay in absorption onset from the first substorm onset. Figure 3.5 shows that the instantaneous enhancement of D-region ionization took place only in the auroral region soon after the substorm onset, and this simultaneity was observed almost at all the longitudes in the auroral region. The delay in CNA is latitude wise and not longitudinal, which is a very unique feature associated with the first substorm onset. The inference we get from figure 3.5 is further clearly explained in next section.

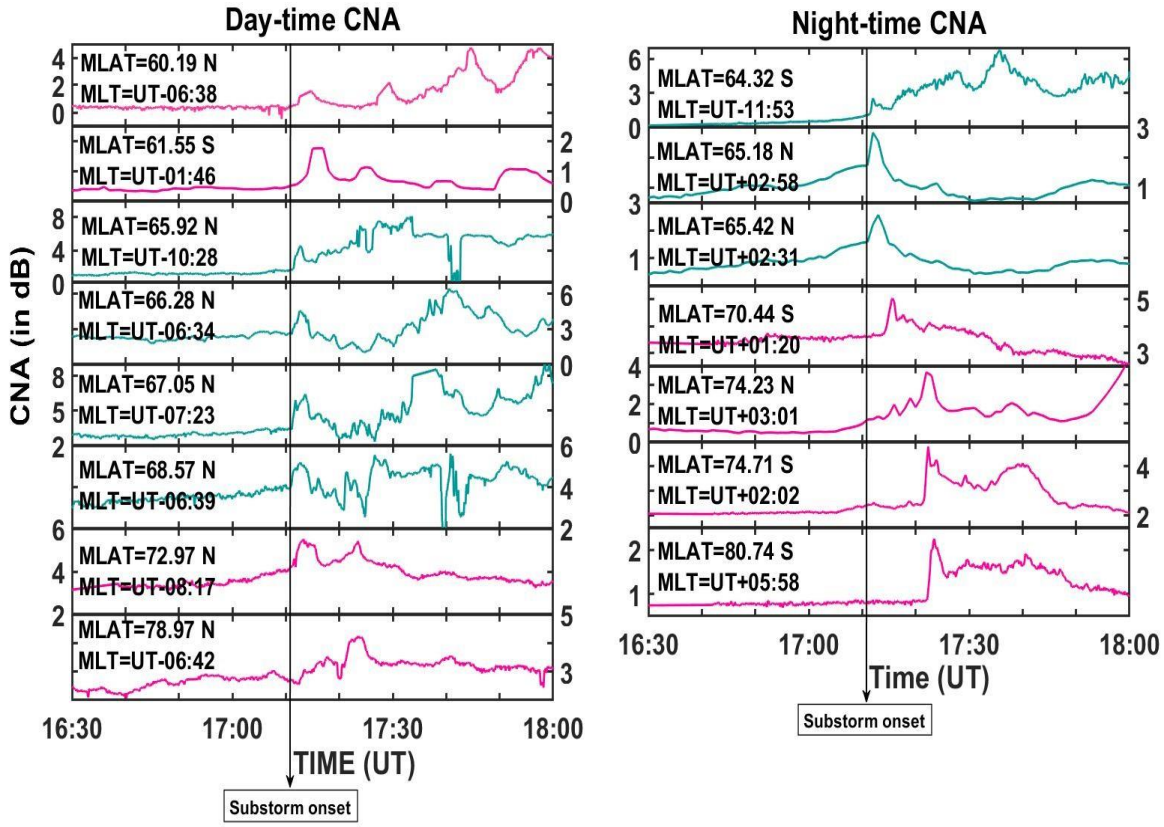

Figure 3. 5 Right column of this figure shows CNA observations of the stations located in the nightside (from 18:00 UT to midnight to 06:00 UT) during the time of first substorm onset, and left column of the figure shows CNA curves of stations located in the dayside (from 06:00 UT to Noon to 18:00 UT). In each column, CNA curves are arranged in the ascending order of the magnetic latitude the respective station, starting from the sub-auroral and moving towards the polar (from top to bottom). The black solid vertical arrow indicates the time of the first substorm onset.

II. Time Delay between the substorm and CNA onset

The time delay between the substorm and CNA onset obtained from Figure 3.5 has been plotted against varying geomagnetic latitude and is shown in Figure 3.6. Variation in the delay is shown on the (a) dayside and (b) nightside. It is clear from the plots in Figure 3.6 (a) and (b) that the stations showing no delay in the CNA onset have wider latitudinal coverage in the dayside than the nightside. The simultaneous substorm onset and CNA onset is concentrated near ~65° latitude in the night sector, whereas in the dayside, latitudes ranging from ~65°- ~69° exhibit this feature. The delay time is evidently less in dayside as compared to nightside. This suggests that the absorption and hence the precipitation is taking place more rapidly in the dayside, covering a wider latitudinal range.

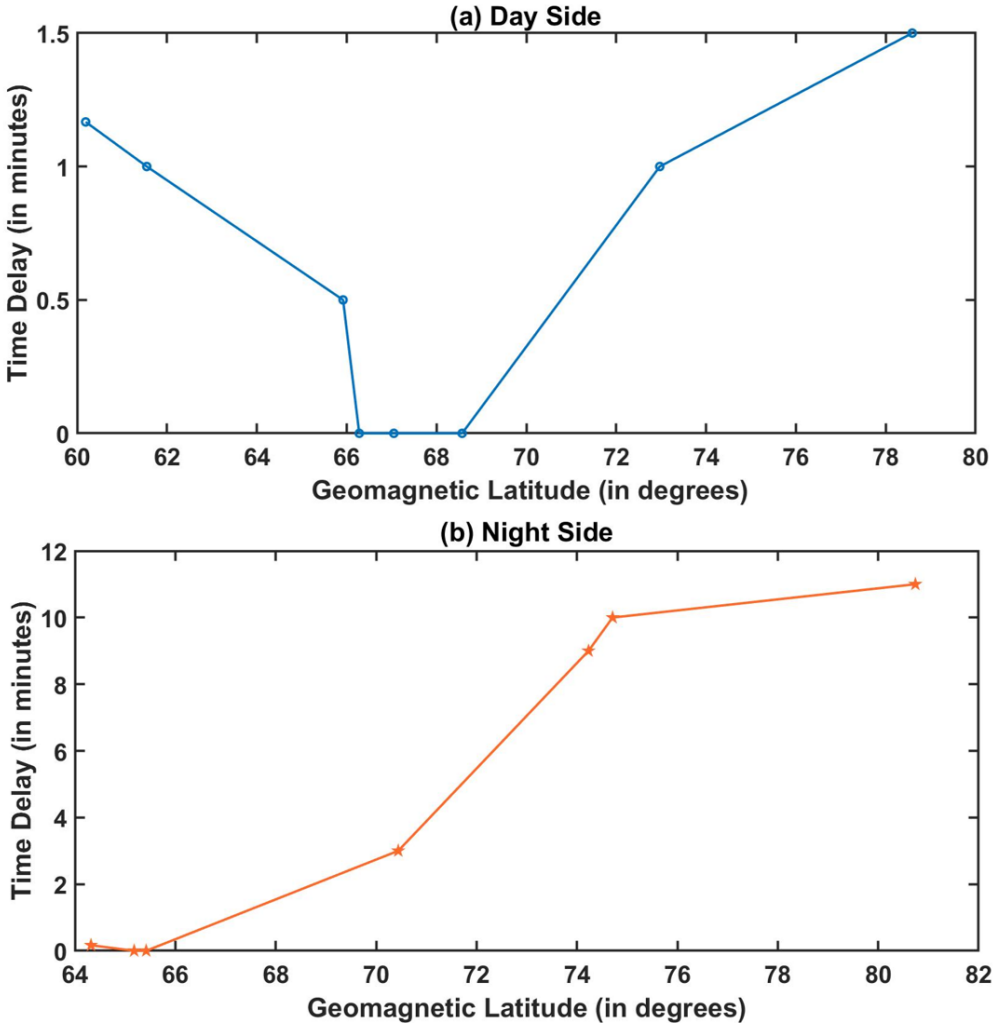

Figure 3. 6. Time delay between substorm and CNA onset Vs geomagnetic Latitude on (a) dayside and (b) night side.

III. MLT variation of increase in CNA

In order to understand how the intensity of the CNA varies with local time, we compared the increase in CNA values at stations exhibiting simultaneity in substorm onset and absorption onset.

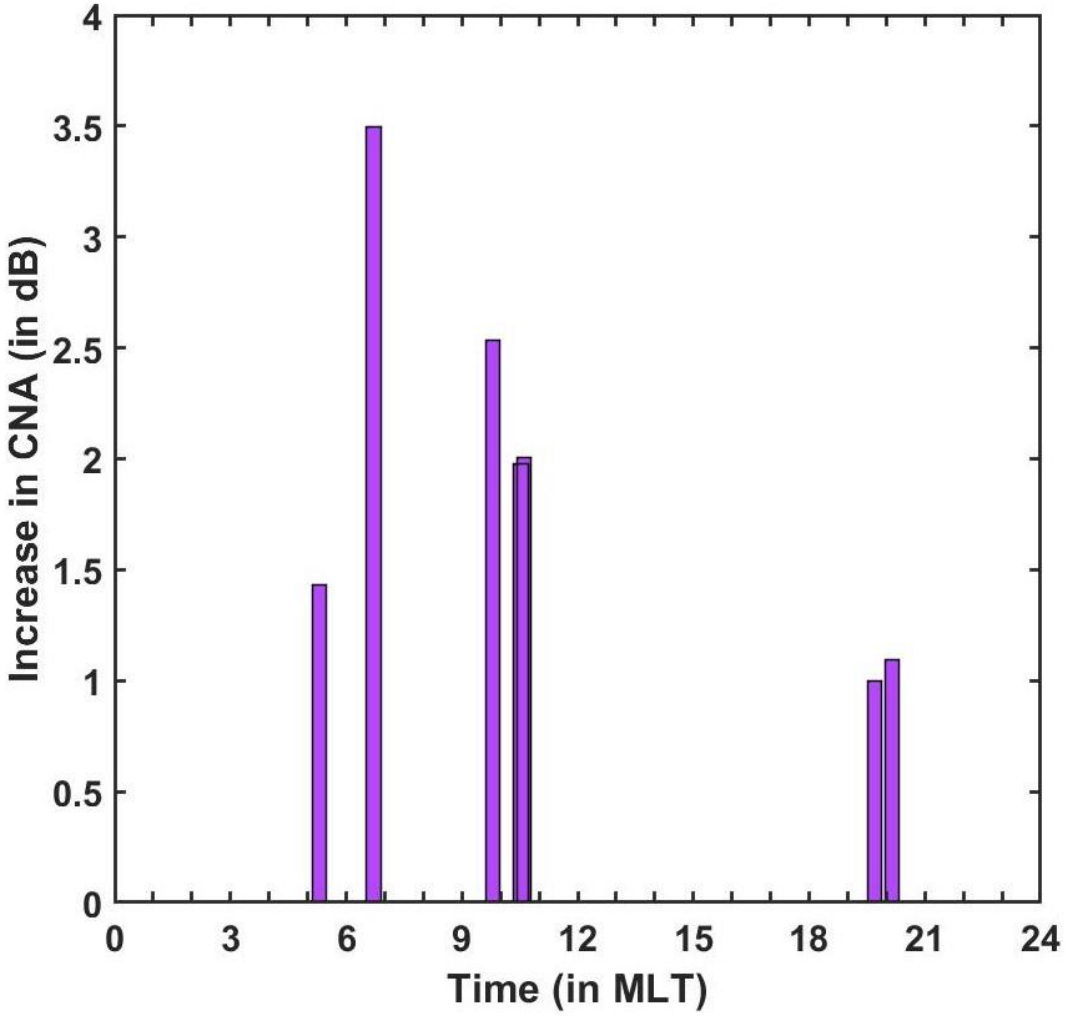

Figure 3. 7 The local time variation of the enhancement CNA level in the latitudinal belt of 64°-69° MLAT.

Figure 3.7 shows increase in the CNA at different magnetic local times in the latitudinal belt ~64° to ~69°. This latitudinal belt is particularly considered because the stations located in this region shows no delay between the first substorm onset and the absorption onset. Hence, in order to understand the characteristic distribution of precipitating particles at different local time sectors soon after the substorm onset, this region was taken into account. Unfortunately, there

was no station located in the exact midnight sector in the desired latitudinal belt among the stations showing instantaneous absorption. However, the station located in the morning sector (at 06:43 MLT) showed maximum absorption as compared to other locations.

3.2.5 Horizontal Magnetic Field variations and SuperMAG SML-LT index

In figure 3.8 we have plotted the magnetic field H-component variation of each station along with the corresponding absorption curve. The blue and the red curves in the figure shows CNAs of each station in day and night respectively, along with the black curve showing geomagnetic H-component variation. The H-components show negative excursion in the substorm interval, showing the presence of westward electrojet at those locations. Hence, there could be a significant contribution of substorm to the observed CNAs.

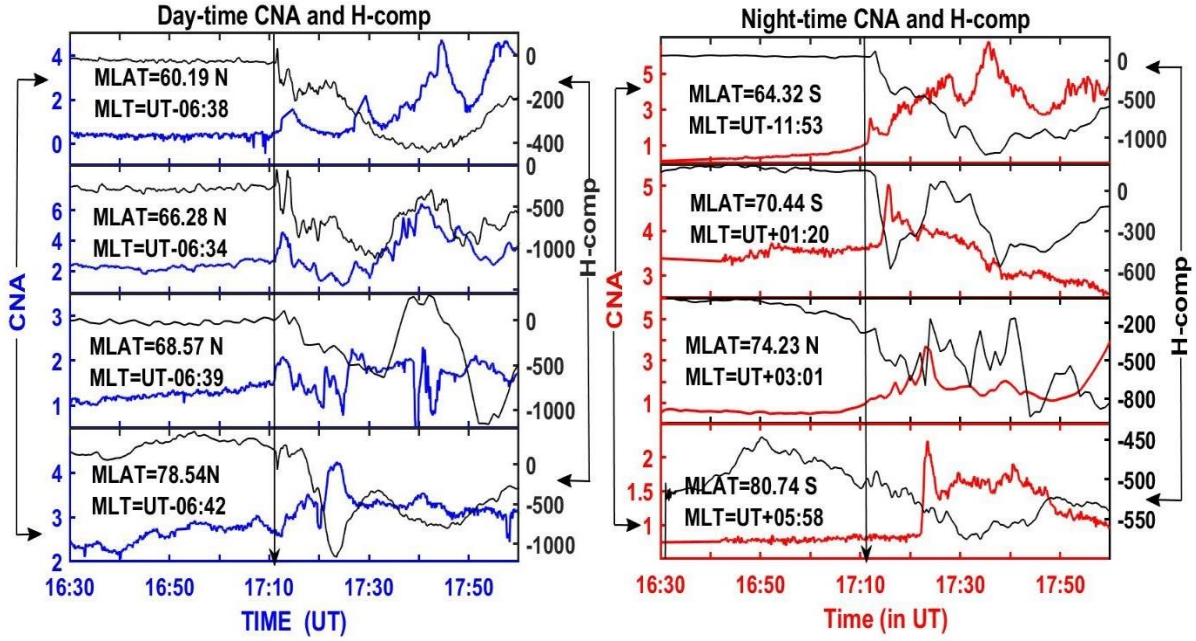

Figure 3. 8 The left panel shows CNA of stations located in the dayside at the time of substorm onset along with magnetic field H-component variation of respective stations. Blue curves show absorption in dB and black curves show geomagnetic H-component variation in nT. Similarly, the right panel shows CNA of stations located in the night time during the time of substorm onset along with magnetic field H-component variation of respective station. Red curves show absorption in dB and black curves show geomagnetic H-component variation in nT. Vertical arrows indicate the time of substorm onset.

Few stations (e.g., last two stations of the right panel in figure 3.8) show negative bays even prior to the substorm onset. This could be because these stations lie in the polar region and the geomagnetic perturbations in this region are caused not only by the auroral electrojets but are also due to some additional factors such as the polar region S_q^p current system and precipitation through cusp region, which can also contribute to the high latitude geomagnetic perturbations (Tomita et al., 2011).

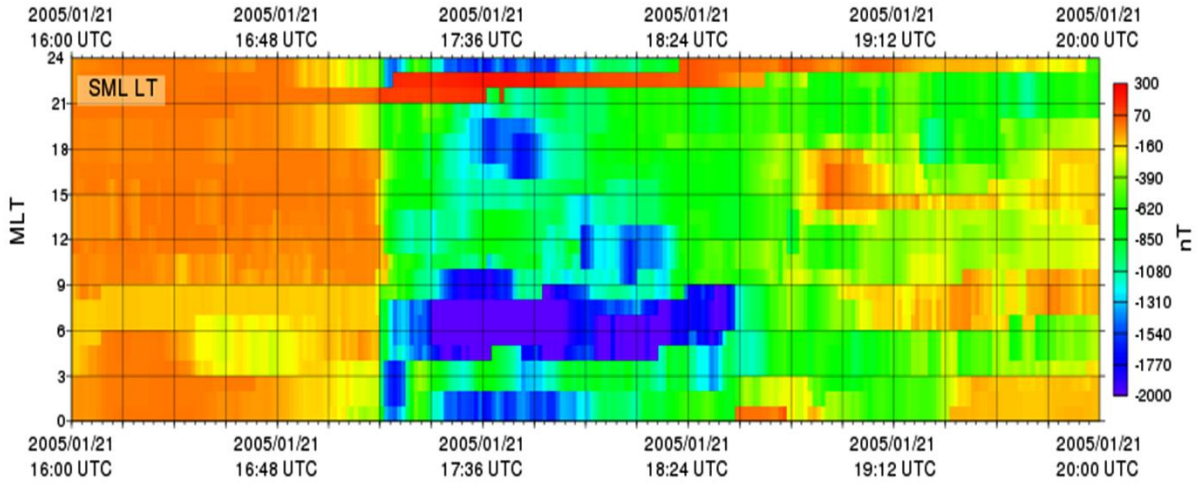

Figure 3. 9 Shows SML LT parameter, which is SuperMAG AL index, plotted at different magnetic local times at particular UTs obtained from the SuperMAG website (http://supermag.jhuapl.edu/). Time in UT is shown in the X-axis and MLT is shown in the Y-axis. The color bar shows the magnetic field variation, where negative values indicate dip in the H-component of the magnetic field and positive values shows enhancement in the geomagnetic H-component.

Figure 3.9 shows high latitude geomagnetic H-component variation on 21st January 2005 at different MLT for particular UT, called the SuperMAG SML-LT plot, obtained from the website http://supermag.jhuapl.edu/. Time in UT is shown in the x-axis and MLT in the y-axis. The color code shows strength of magnetic field ranging from -2500 nT to 300 nT. The negative values show decrease in the H-component of Earth's magnetic field and the positive values show enhancement in its value. From the figure, it can be seen that there is no significant variation in the magnetic field before the substorm onset at 17:11 UT and the magnitude remains close to ~0 nT in all MLT sectors. Immediately after the onset there is a very prominent variation everywhere

and it is quite evident from the figure that intense H-component variation was in the post-midnight to dawn sector. The intense magnetic field variations then centered near the dawn during the time of substorm expansion phase. This is a very important observation of this day which supports our idea of calling this substorm dawn centered.

The most intense H-component depression on this day is not observed in the midnight sector, which is usually expected. Normally, the current peaks at the point of brightest aurora and this is a common feature of the midnight sector (S. I. Akasofu, 1964; Newell & Gjerloev, 2011). However, in the present case westward electrojet current peaks in the post dawn/morning sector.

3.3. Discussion and Summary

During a typical substorm, large-scale geomagnetic perturbations are generally being accompanied by an enhancement in night-side particle precipitation and disruption of the auroral arc structure (Rostoker, 1968). Concomitant behavior of substorm associated auroral evolution; current and ionospheric absorption are expected since all are directly proportional to the amount of particle precipitated. Hajra & Tsurutani (2018) reported most intense aurora in the pre- and post-midnight sector, whereas the night side was devoid of intense aurora throughout the substorm event of 21st January 2005. This led to the initial belief that the loading-unloading process during this event did not follow the general mechanism of night side injection and precipitation. To further confirm this, in the present study we have looked into the other ground observation which is also directly related to the particle precipitation, i.e., cosmic noise absorption (CNA). Our analysis shows that the substorm associated CNA, as well as the westward electrojet current, were intense in the local time sectors away from midnight. Among the available longitudinal coverage of the riometer datasets, CNA too was found to be maximum in the dawn sector. Also, the maximum variation in the westward electrojet was concentrated in the dawn to morning sector. This observation is different as one might expect the westward electrojet to peak around midnight sector or where the substorm aurora is most intense (J. H. Allen & Kroehl, 1975; A. K. Singh et al., 2014a). Thus, this event does not fit well in the current understanding of the substorms. Therefore, present study reanalyzes the impulse-induced supersubstorm of 21st January 2005 with multi-instrument data of CNA obtained from global network of riometers, auroral images by IMAGE satellite and magnetic field measurements along with the BATS-R-US MHD simulation results.

The present work identifies the two successive substorm onsets, using the AL index, occurring at ~17:11 UT and ~17:21 UT. The magnitudes of peak AL depressions after these two onsets were ~ -2000 nT and - 3600 nT. The interplanetary conditions prior to these two onsets were significantly different. The study focuses on the differences in the characteristics and the triggering mechanisms of these two substorm onsets. The first substorm onset was accompanied with a strong impulse in the solar wind dynamic pressure, and hence the substorm event of 21st January 2005 was termed as impulse-induced super substorm. The IMF Bz was close to zero for more than 1.5 hr prior to the first substorm onset. Also, this substorm neither occurred during the recovery phase of any intense storm, nor was there any preceding southward component of IMF Bz before the onset. Hence one can infer that the idea of release of stored magnetotail energy after a certain interval is also not valid in this case. The IMF By was also near zero for hours prior to the onset, excluding the possibility of large IMF |By| contribution for dayside magnetic reconnection. Thus, viscous interaction due to the solar wind impulse appears to be the only triggering condition during the first onset. Whereas at the time of second onset, the IMF turned southward, which can be the source of energy input at that time.

To further understand how different the mechanisms of substorm onsets on this day were, it was important to check the dipolarization signature in the magnetotail. Various satellite observations and models, like the near-Earth neutral line (NENL) model (Baker et al., 1996; E. W., Jr., Hones, 1976) and the current disruption (CD) model (Lui, 1996), have proposed a theory that the magnetic reconnection first occurs around X ~ −20 Re in the pre-midnight tail for about 0–2 min prior to the substorm onset. Then, immediately after onset, the dipolarization occurs around X ~ −10 to −15 Re, which is simultaneous with substantial evolution of the plasmoid formation around X ~ −30 Re (Miyashita et al., 2003). The occurrence of dipolarization and plasmoid formation is believed to be a typical signature of a substorm expansion onset (Baumjohann et al., 1999).

The BATS-R-US MHD simulation results shows that from 17:11 UT to 17:21 UT there is no signature of NENL magnetic reconnection, dipolarization and plasmoid formation in the night side magnetotail region. Absence of these features suggests that the initial dip of ~-2000 nT in the AL index was not because of the traditional loading-unloading process and there was lack of particle precipitation from the nightside magnetotail region. For the second substorm onset at 17:21 UT, the nightside NENL reconnection took place but did not occur in the exact midnight sector, rather it occurred somewhere near the post-midnight to dawn sector.

The auroral image, when taken into consideration all the magnetic local time sectors, suggests that initially the auroral onset and evolution was from the dayside because of the shock. After the second onset at 17:21 UT, a second auroral onset (especially in the proton aurora), occurred from the post-midnight sector. This phenomenon was confirmed using the BATS-R-US simulation result, where the NENL reconnection and dipolarization, which was seen only after 17:21 UT, had the closed field lines tilted towards the post-midnight sector when viewed from the XY plane. The global signatures of a shock aurora are that the aurora first brightens near local noon in the auroral zone, and then propagates anti-sunward along the auroral oval at very high ionospheric speeds much faster than the typical aurora (X. Zhou & Tsurutani, 1999). Hence, it is also possible that the aurora we see at and after 17:21 UT is a combination of both substorm aurora and shock aurora.

Any time-delay between the time of CNA onset and substorm onset in different longitudes is often explained in terms of the longitudinal drifting of trapped particles (Behera et al., 2016). However, for the event studied here, no longitudinal time delay is found. In fact, in a narrow belt of latitudes near 65°, the CNA onset coincides with the substorm onset from dawn to dusk through daytimes. The pertinent question that is how these particles were present at almost all the longitudes for precipitation soon after the impulse. This could be due to the fast propagation of shock auroral along the auroral oval (X. Zhou & Tsurutani, 1999). We observe the time delays between substorm and CNA onsets varies with latitudes, and are longer on night sides and shorter (< 2 minutes) on dayside. This is also evident from the auroral images particularly from proton aurora that at the onset at 17:11 UT, the latitudinal spread of aurora is quite large on the dayside, while on night side the aurora is confined to narrower latitudinal belt near 65° (figure 3.2(a) middle row). It can also be noted that the most intense aurora on night side is observed at 17:21 i.e., after second onset. Hence, the observed delay between substorm and CNA onset of ~09-10 minutes on the night side can be linked to the time of peak proton aurora. However, the increased time delay could also be due to the evolving dynamics in the magnetotail. As the time evolves, the field lines in the magnetotail with larger L-values precipitate the particles, resulting in the increasing delay with latitudes towards poles. Thus, the reconfiguration of magnetotail electrodynamics with time can also result in the delay due to variable LLBL location.

Though the magnetic field variations/SML index show the presence of westward electrojet in the dayside where we are observing aurora and CNA, the occurrence of daytime aurora and CNA reported here are mainly due to the interplanetary shock. Three solar wind energy transfer mechanisms causing dayside shock auroras are outlined by Tsurutani et al., 2001:

(1) Adiabatic compression, (2) Field-aligned current intensifications and (3) Viscous interaction. These mechanisms are probably not just restricted to the formation the shock auroras only, but can also lead to CNA intensification.

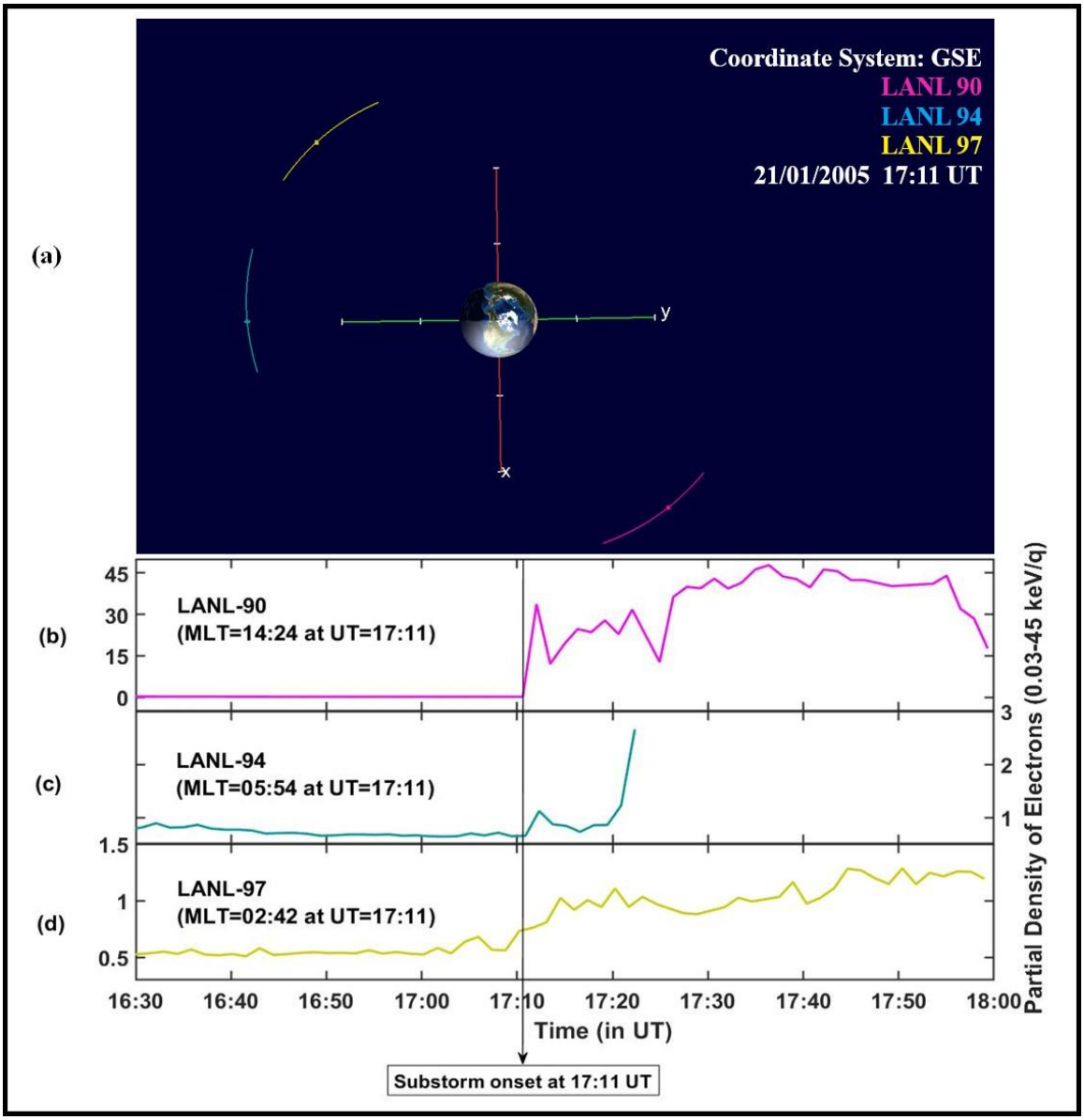

Figure 3. 10 (a) The orbital view of the satellites: LANL 90, LANL 94, and LANL 97 (Source: 4-D orbit viewer). In this figure, sun is towards the positive x-axis. The coloured dots indicate the positions of the satellites at 17:11 UT. (b) Density of electron (in cm^{-3}) of LANL-90 in the energy range 0.03-45 keV/q, (c) Density of electron (in cm^{-3}) of LANL-94 in the energy range 0.03-45 keV/q (d) Density of electron (in cm^{-3}) of LANL-97 in the energy range 0.03-45 keV/q. Black vertical line indicates the time of substorm onset.

In response to the compression of the magnetosphere by interplanetary shocks, midday sub-auroral patches (MSPs) are found to occur (Liou et al., 2002a), particularly around magnetic local noon at the onset time of sudden commencement. Trapped population of electrons of ~1-10 keV originally from central plasma sheet can scatter into the loss cone causing MSP during magnetospheric compression (Liou et al., 2002a). Hence, it is possible that electrons of this energy range might have precipitated and formed additional bright auroral patches in the dayside for the present case. To confirm, we checked the LANL-90, LANL-94 and LANL-97 electron densities in the energy range 0.03-45 keV/q. These are equatorial orbiting satellites at ~6.6 Re. The orbital view of these satellites was obtained from NASA's '4-D Orbit Viewer' software. LANL-90 was in the post-noon sector, LANL-94 in the dawn sector, and LANL-97 in the post-midnight sector as shown in figure 3.10 (a). The partial density of electron (0.03-45 keV/q) in the post noon sector shows a sudden enhancement at 17:11 UT and decreases after a short while (~1 minutes), as shown in figure 3.10 (b). This may indicate that with the shock arrival the electrons enhanced and lost in a very short time span by entering into the loss cone, which might be responsible for the MSP. The partial densities of other time sector showed no such behavior, and enhancement in flux was very less as compared to noon time, as shown in figure 3.10 (c) and (d).

It is well known that during the periods of prolonged northward IMF, the low latitude boundary layer (LLBL) which is a sub-layer of the magnetopause is thicker and steady (Mitchell et al., 1987; Terasawa et al., 1997). There have been four mechanisms proposed for the entry of solar wind plasma during northward IMF viz. Kelvin-Helmholtz (KH) waves on the magnetopause boundary (Ma et al., 2017; Tsurutani et al., 1995), cusp reconnection, kinetic Alfven waves (KAWs), and magnetosheath irregularities (Masson & Nykyri, 2018; Wing et al., 2014). During the episodes of sudden increase in the solar wind plasma pressure, the velocity shear across LLBL can drive field aligned currents. The turbulence generated in the magnetosheath can act as a seed for the KH instability and reconnection, which allows the solar wind plasma to move across the boundary (Miura, 1984, 1987). In the present case, we observe intense CNA in the dawn sector for which KH instability seems to be a plausible mechanism for the entry of solar wind particles. IMF Bz was ~0 nT hours prior to the first substorm onset at 17:11 UT, which turned northward immediately after the impulse arrival. It was a long duration event during which solar wind density was high. Hence the interplanetary condition seems to be favorable for viscous interaction via K-H instability (X. Y. Zhou & Tsurutani, 2004). At the magnetopause boundary, viscous interaction permits transfer of solar wind energy and momentum through the entry of diffusive into the magnetosphere (Axford W. I. & Hines, 2011). However, KH instability normally leads to dawn-dusk symmetry, whereas our observations of

particle precipitation are stronger on the dawn side. The reason for this asymmetry can be attributed to the role of IMF By component. Soon after the shock, the IMF By turned negative. This condition is favorable for lobe reconnection in the pre-noon sector (Sandholt et al., 2001; X. Y. Zhou & Tsurutani, 2004), allowing the particle injection from the dawn/morning sector. Hence, injection via KH instability and the negative IMF By component together may be the reason for the observed dawn-dusk asymmetry in particle precipitation and the auroral electrojet.

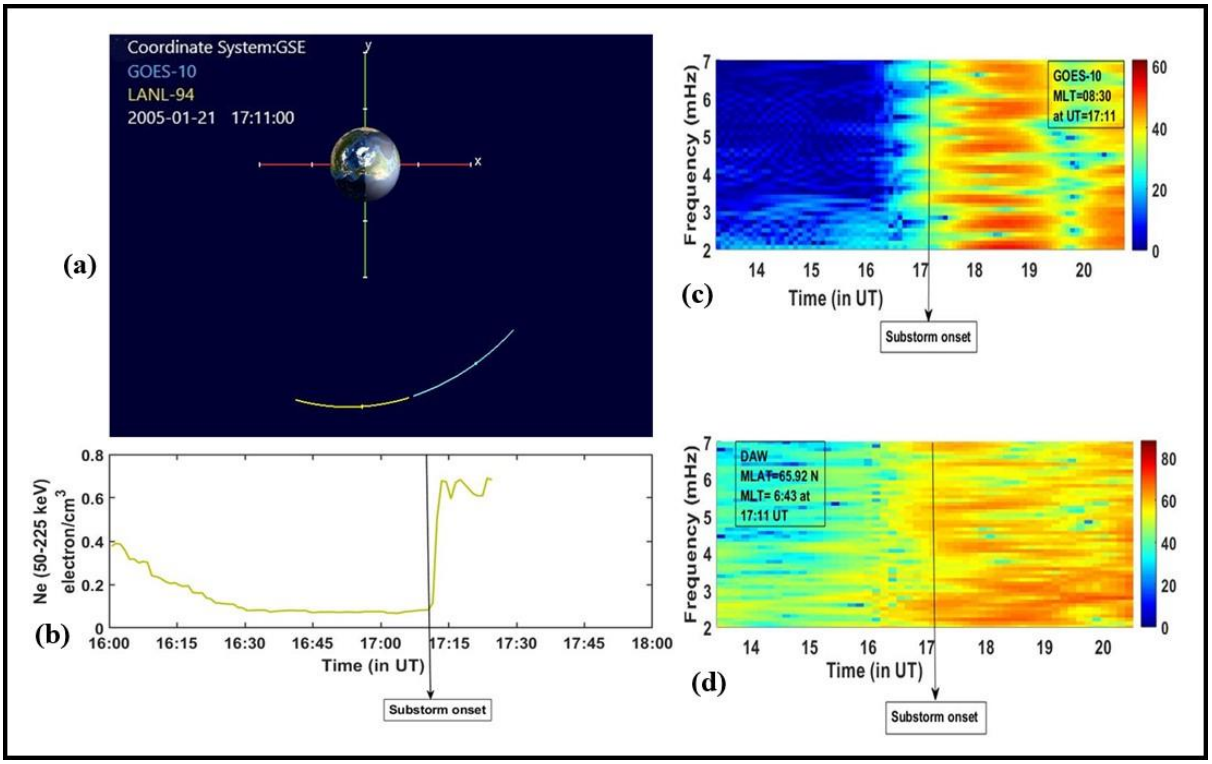

Figure 3. 11 (a) The orbital view of LANL-94 and GOES 10 (source: 4-D orbit viewer software). In the plot, sun is towards positive x-axis. The coloured dots indicate the position of the satellites at 17:11 UT. (b) Electron flux of the energy range 50-225 keV (in electron/cc) of LANL-94 satellite, (c) Pulsations in Pc5 range for GOES-10 satellite data (d) Pulsations in Pc5 range from ground magnetometer data of Dawson station. The solid vertical lines in (b), (c) and (d) marks substorm onset.

The precipitation during northward IMF can take place through wave-particle interaction in addition to lobe reconnection. We checked for ULF waves in the Pc5 range for both ground magnetometer data and satellite magnetometer data. GOES-10 and LANL-94 are the equatorial orbiting satellites located at ~6.6 Re. The orbital view of these satellites was obtained from

NASA's '4-D Orbit Viewer' software and is shown in Figure 3.11. The sun is in the direction of positive x-axis and the satellites are located in the morning sector at the time of substorm onset. Figure 3.11 shows (a) location of GOES-10 and LANL-94 at 17:11 UT, (b) electron density of LANL-94 satellite in the energy band ~50-225 keV, (c) pulsations in Pc5 range of GOES-10 magnetometer data, and (d) pulsations in Pc5 range for corresponding ground station 'Dawson'. CNAs and diffuse auroras are caused by electrons of energy range 10-100 keV (Rees, 1963). Hence, increment in the electron density of energy band 50-225 keV, as observed in Figure 3.11 (b), will contribute in particle precipitation causing enhanced CNA and aurora in the dawn sector. Interestingly, the enhancement in the pulsations in the Pc5 range has been observed only in the dawn/morning sector in both satellite and the corresponding ground station at the satellite's foot point, as shown in Figure 3.11 (c) and (d). It is worth mentioning, though not shown here, that we examined other time sectors as well, but did not observe any such simultaneous enhancement in Pc5 activity in ground and satellite. Long lived Pc5 can facilitate particles to be pushed in the loss cone (Behera et al., 2015, 2016b), resulting into precipitation of particles and hence the enhanced dawn time CNA in the present case. Waves other than Pc5 pulsations could not be checked because of unavailability of high-resolution ground and satellite magnetometer data.

3.4. Conclusion

The growth phase of a substorm traditionally starts with the loading/injection of solar wind particles into the magnetosphere from the nightside magnetotail region. According to the theory, this happens soon after the formation of DNL (Distant Earth Neutral Line) reconnection point (Baumjohann et al., 1999; Baumjohann & Truemann, 1996). The onset of expansion phase starts with the formation of NENL reconnection, dipolarization and plasmoid formation. The present study suggests that the solar wind particle injection in this case initially was not due to DNL reconnection in the night side, but due to injection via KH instability. The traditional DNL-NENL reconnection and substorm expansion took place after ~17:21 UT on this day, with the dipolarization and plasmoid formation shifted slightly to the post-midnight sector. Hence, the conclusion of this study is that the initial ~10 minutes of the AL index decrement of ~-2000 nT, may not be due to loading-unloading process from the nightside. Rather, it can be a result of dawn-dusk injection via KH instability and particle precipitation then after via wave-particle interaction and several other directly-driven shock related processes.

We emphasize on the point that substorms are more general phenomena than long been used description of nighttime increase in precipitation and auroral activity. This idea was proposed almost five decades before by Jelly & Brice (1967), where they said that auroral morphology during nighttime substorm represents only a part of a more general and more widely distributed disturbances that occupy a substantial portion of the magnetosphere. They also proposed the term 'elementary magnetosphere substorm' (EMS) for such widely distributed disturbance events, and we are in agreement with the same. The reason why this idea did not get ground could be due to lack of enough observational evidences. We suggest that, particle injection via only magnetic reconnection and precipitation from night side following the field line, should not limit the description of substorms.

Chapter 4

The Role of Interplanetary Magnetic Field (IMF) and Sudden Impulse (SI) in Triggering a Geomagnetic Substorm: A Comparative Analysis

4.1 Introduction

The solar wind energy accumulation in the magnetotail is caused by the magnetic reconnection of the interplanetary magnetic field (IMF) with the Earth's magnetic field at the dayside magnetopause. The energy held in the magnetotail is released, resulting in a substorm, when this loading of solar wind energy becomes unstable as a result of changes in the internal and external conditions. These substorms are also known as "Akasofu-type substorms," since Akasofu provided the definition for the first time in 1964 (S. I. Akasofu, 1964). An auroral substorm, according to Akasofu, is the series of auroral events that occur over the entire polar region as they transition from auroral quiet times through the various active phases to ensuing calm. The interplanetary magnetic field (IMF) turning southward was added to this concept by scientists in the early 1970s, who made it the essential prerequisite for substorms to develop (Mcpherron, 1979; Rostoker et al., 1980; Tsurutani & Meng, 1972).

It is generally known that southern IMF conditions efficiently allow for the storage of energy in the magnetotail, and that substorm expansions are typically initiated during or shortly after southward IMF periods. On the contrary, under northward IMF conditions, energy is not accumulated in significant amounts. Substorms can nevertheless develop even during northward IMF periods, according to a number of studies (e.g., Akasofu et al., 1973; Kamide, 1974; Lee et al., 2010; Liou & Newell, 2010; Miyashita et al., 2011; Ostgaard et al., 2011).

Two factors can be responsible for this:

1. A strong pressure impulse coinciding with the time of substorm onset.
2. A significant IMF |By| component as a pre-conditioning.

According to scientists, sudden impulses can sometimes trigger substorms if they are strong enough (Kawasaki et al., 1971; Schieldge & Siscoe, 1970). The likelihood increases when the IMF Bz component is negative before to the SSC (Storm Sudden Commencement) (Burch, 1972). According to Kawasaki et al. (1971) the direction of IMF is not an important parameter during SSC (storm sudden commencement) triggered substorms. It is so explained that magnetospheric substorm arises due to a sudden conversion of energy stored in the magnetotail prior to substorm onset. An interplanetary shock wave can trigger this conversion leading to what we call impulse-induced substorms.

Strong IMF By component is another element that could cause substorm onsets even during extended northward IMF Bz conditions (e.g., Fuselier & Lewis, 2011; Lee et al., 2010; Miyashita et al., 2011; Petrukovich et al., 2000; Wu et al., 2002). It has been observed that solar wind energy is transmitted into the magnetosphere during a long-lasting northward IMF period because of a significant IMF |By| component, which may result in magnetic reconnection between the closed dayside geomagnetic field line and northward IMF fields (Freeman et al., 1993; Nishida et al., 1998; Ogino et al., 1986; Park et al., 2006; Reiff & Burch, 1985). These substorms follow the same loading-unloading mechanism as conventional southward IMF related substorms (Miyashita et al., 2011; Petrukovich et al., 2000). Depending on the sign, magnitude, and hemisphere of IMF By, the substorm's onset owing to IMF |By| occurs in the local time sector somewhat away from midnight, in between 22 MLT to 00 MLT (Liou & Newell, 2010; Ostgaard et al., 2011).

Studies have demonstrated instances of substorms developing under northward IMF conditions because of a pressure pulse. We have seen in the previous chapter that these substorms differ from typical Akasofu-type substorms in terms of the local time dependence of particle injection and precipitation process. In contrast to the typical Akasofu-type substorm, impulse-induced substorms exhibit distinctive ground signatures that are not necessarily centered around or near midnight. However, it is not necessary that only one of the two triggering agents will be present before the substorm onset for all the cases. It is quite possible that during some substorm onsets we have both sudden impulse and an IMF Bz/By component present to trigger the onset. A pertinent question then arises is how a substorm's signatures would evolve when both the

triggering agents are present prior to the onset. Will the signatures of Akasofu-type substorm dominate over impulse-induced ones or vice-versa, is something that needs to investigated. Hence, we analyzed six substorm events having distinctly different interplanetary conditions, four of which are:

(i) Pure IMF Bz induced
(ii) Pure IMF By induced
(iii) Pure sudden impulse triggered and
(iv) Sudden impulse and IMF By present prior to the onset.

This has been done so as to understand how we can initially categorize a substorm as an impulse induced one or IMF triggered one based on the SuperMAG SML-LT index [http://supermag.jhuapl.edu/]. After this initial step further ground and satellite observations may confirm the dependence of a substorm to either of the two triggering agents. The next two substorms of 05th April 2010 and 22nd June 2015 has been analyzed using this method. On these days, the substorm onsets weren't merely accompanied by a sudden impulse; an IMF Bz/By component was also present before the onset. Our main objective is to determine which factor will predominate in triggering a substorm when both an IMF Bz/By component and a pressure pulse are present at or before the onset.

The observations of four isolated substorm events are presented in sector 4.2. Section 4.3 discusses the two substorm events having more than one triggering agents present. Section 4.4 provides a summary and discussion of our results. Section 4.5 highlights the conclusion.

4.2. SML-LT Variation of Substorms Having Different Preconditioning

As discussed in the previous section, substorm onsets can occur due to three different triggering agents, viz., (i) southward component of IMF Bz prior to the onset, (ii) intense IMF By prior to the onset and (iii) a strong pressure pulse at the time of onset. We investigate the SML-LT parameter of four distinct substorms that fall into various preconditioning parameter categories. The SML-LT parameter refers to SuperMAG [http://supermag.jhuapl.edu/] westward auroral electrojet index at different local time sectors (Newell & Gjerloev, 2011). In essence, it demonstrates the negative H-component variation for a specific UT at different MLT sectors. Other solar wind and geomagnetic parameters used for studying these events were also obtained from the SuperMAG website [http://supermag.jhuapl.edu/] like: solar wind dynamic pressure,

solar wind magnetic field vector and SME U/L parameter. SME U/L are SuperMAG derived indices that indicates the strength of eastward and westward electrojets in time series (UT). SuperMAG uses the OMNI 1-min-averaged field/plasma data sets shifted to the Earth's bow shock nose to derive solar wind parameters. Magnetic indices are derived from approximately 110 ground magnetometer stations extended from sub-auroral to Polar Regions (Gjerloev, 2012). Hence, we use these indices over AL and AU indices because of their better latitudinal and longitudinal coverage (e.g., Hajra et al., 2016, 2020; Hajra & Tsurutani, 2018; Oliveira et al., 2018, 2021; Oliveira & Raeder, 2015).

4.2.1 Isolated IMF Bz induced Substorm (Akasofu-type)

The IMF Bz-induced substorm, also known as the Akasofu-type of substorms, is the most prevalent type of substorm that has been well studied and accounted for decades (S. I. Akasofu, 1964). Prior to the commencement of these substorms, the IMF should have a southern component to facilitate with the loading and unloading of particles in the magnetosphere (Meng et al., 1973; Tsurutani & Meng, 1972). The midnight sector is largely dominated by the intense visual auroras, particle precipitation, and auroral electrojet current enhancements (S. I. Akasofu, 1964; S.-I. Akasofu et al., 1965; S.-I. Akasofu & Meng, 1969; J. H. Allen & Kroehl, 1975; Jelly & Brice, 1967; H. Ranta, 1978; Stauning, 1996). It is observed that the aurora initially appears in the midnight sector and is called the auroral breakdown. Depending on how strong the substorm is, it then expands in latitude and longitude (S. I. Akasofu, 1964). The auroral electrojet currents also has similar behavior. The strongest variation or dip in the H-component is seen in the midnight sector as a result of the formation of the substorm current wedge and the intensification of the westward electrojet current (Birn et al., 1999).

There are many examples of IMF Bz-induced substorms; figure 4.1 depicts one such case. The magnetic field parameters and the solar wind dynamic pressure indicate that there was no pressure pulse at the time of the substorm onset and that IMF Bz was negative prior to it. The SME U/L index, indicated by a black solid vertical line, is used to determine the onset time. We also observe that the SML-LT variation (figure 4.1.c) is most intense in the midnight and near midnight sector.

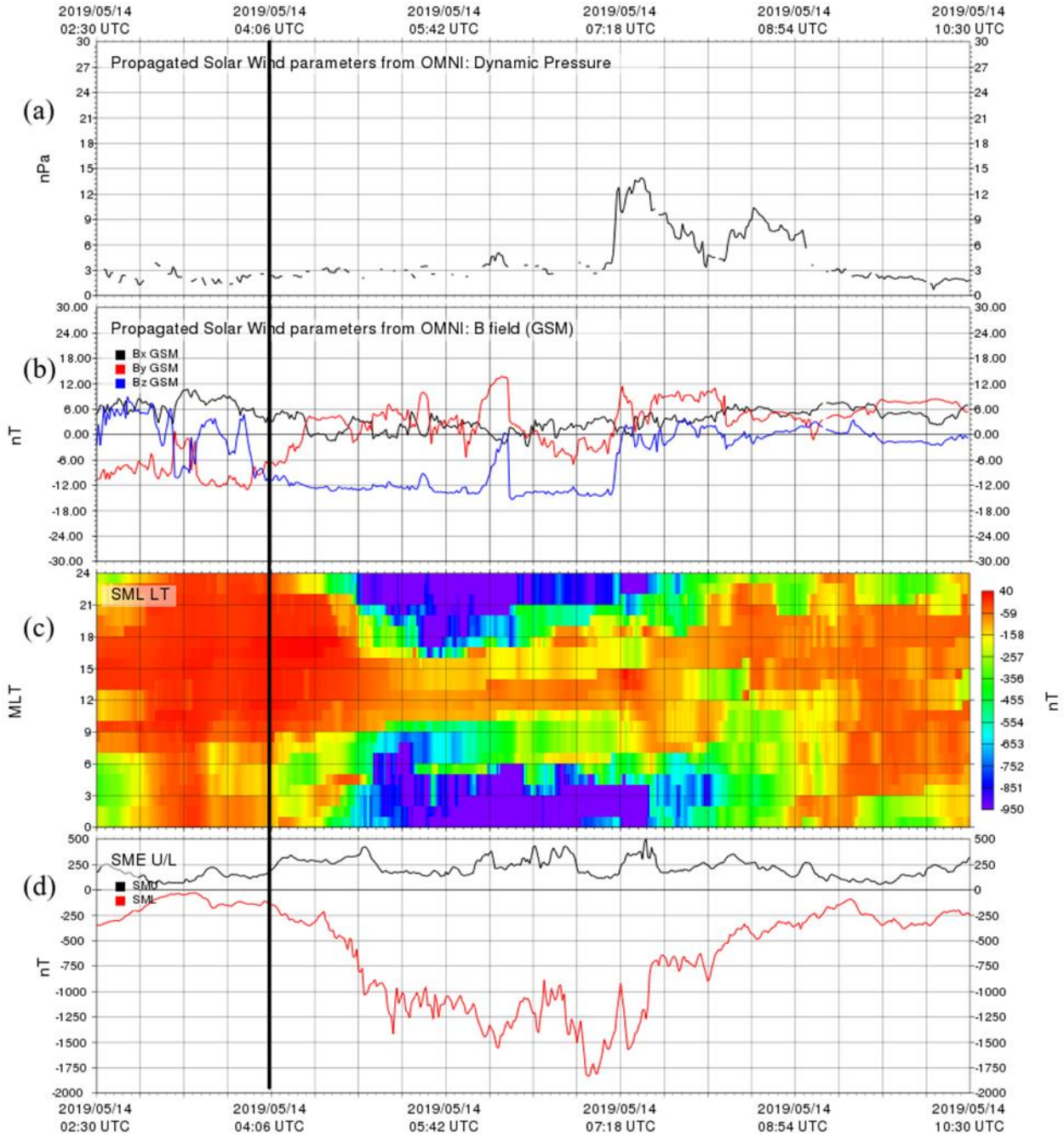

Figure 4. 1. The plot represents the solar wind and geomagnetic parameters of the substorm event on 14th April 2019. The plot is obtained from the SuperMAG website [http://supermag.jhuapl.edu/]. From top to bottom, the panels show (a) solar wind dynamic pressure, (b) interplanetary magnetic field (the three components in GSM coordinates), (c) SML LT, which is SuperMAG AL index plotted at different magnetic local times at particular UTs. UT time is shown in the X-axis, and MLT is shown in the Y-axis. The color bar shows the magnetic field variation, where negative values indicate a dip in the magnetic field's H-component and positive values show enhancement in the H-component of the magnetic field, and (d) the SMU and SML plot showing onset and intensity of substorm.

4.2.2 Isolated IMF By induced Substorm

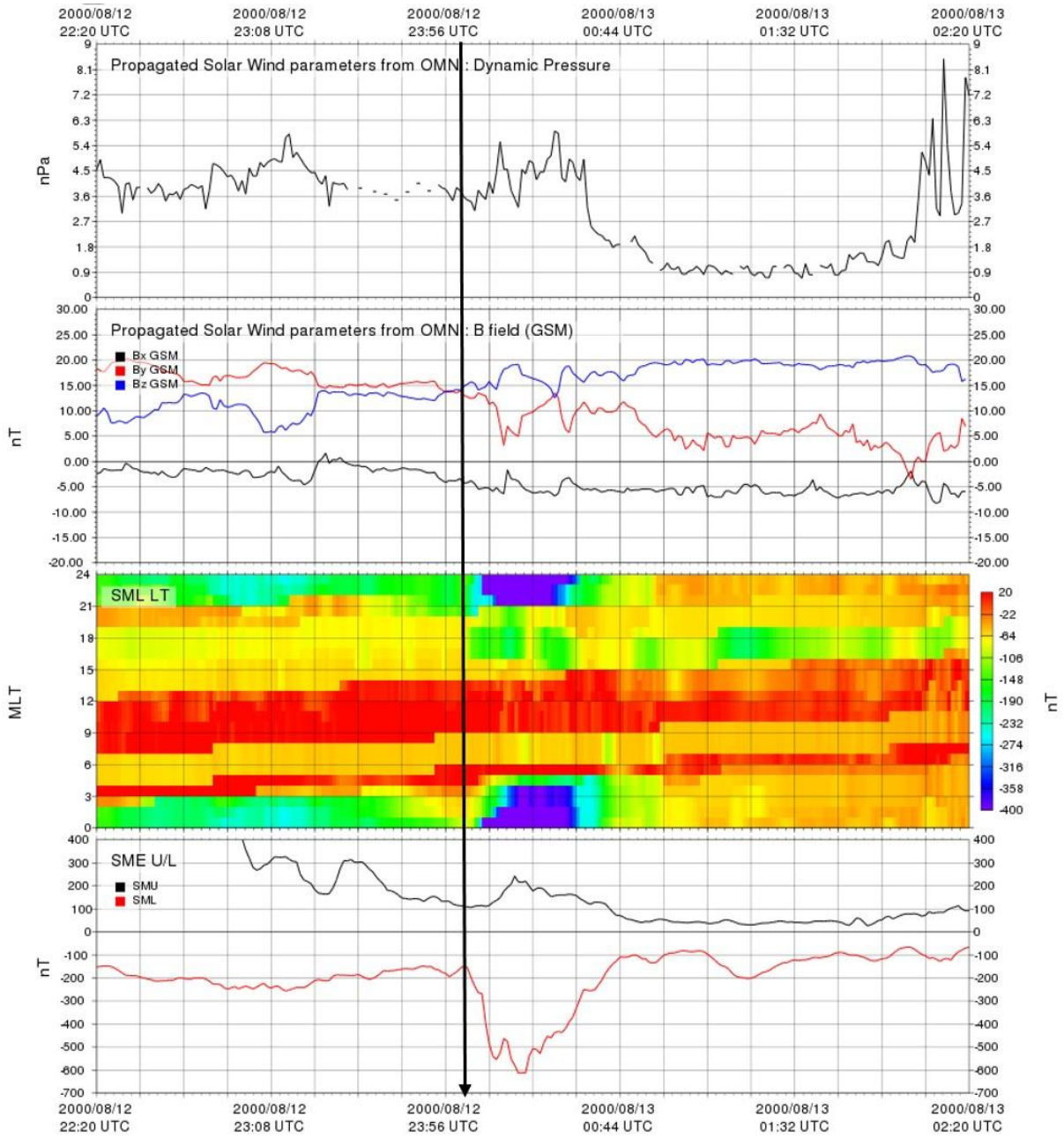

Figure 4. 2 The plot represents the solar wind and geomagnetic parameters of the substorm event on 12-13 August 2000. From top to bottom, the panels show (a) solar wind dynamic pressure, (b) interplanetary magnetic field (the three components in GSM coordinates), (c) SML LT, and (d) the SMU and SML plot showing onset and intensity of substorm. The plot is obtained from the SuperMAG website [http://supermag.jhuapl.edu/].

The substorm of August 12–13, 2000, described by Lee et al., 2010, was one induced by IMF By. The SuperMAG plot of August 12–13, 2000 is depicted in Figure 2.2, together with the geomagnetic field variation and solar wind condition for that day. Prior to the commencement of the substorm, IMF Bz, as depicted in figure 2.2, was prolonged northward for hours prior to the onset, whereas, IMF By component was strong and significant at that time. There was no sudden pressure impulse at that moment. As previously discussed, the IMF By generated substorm follows the same loading and unloading mechanism as normal Akasofu type. Hence, it is expected that the midnight sector should have the maximum variation in the SML-LT parameter, and this is also what we observe in figure 4.2.

4.2.3 Isolated Impulse Induced Event of 21st January 2005

The impulse-induced supersubstorm event of 21st January 2005 did not have sufficient energy input via magnetic reconnection and a sudden impulse coincided with the substorm onset (Hajra & Tsurutani, 2018). Figure 4.3 displays the interplanetary conditions and terrestrial magnetic observations on this day. According to the figure, IMF Bz and By were close to 0 nT for hours before the substorm started. At 17:11 UT, the beginning of the substorm, which is indicated by a black solid vertical line, coincides with a pressure pulse. This substorm was therefore initially thought to be entirely impulse-induced by Hajra and Tsurutani (2018), also stating that, contrary to what is generally seen, the aurora began to appear in the pre- and post-midnight sector rather than the midnight sector. Also, the midnight sector was generally devoid of most intense aurora throughout the substorm event (Hajra and Tsurutani, 2018). This observation may suggest that the initial ionospheric particle precipitation was not from the typical midnight sector but somewhere near dawn and dusk. We have analyzed this substorm event in detail in the previous chapter where we have shown that the dipolarization did not begin at 17:11 UT and the substorm associated ground observations maximized in the dawn sector and not in the typically expected midnight sector. A very important observation associated with this day is the SML-LT parameter shown in figure 4.3 (c). Typically, we expect the negative H-component variation to be most intense in the near midnight sector during Akasofu type of substorm and IMF By induced substorms, as seen before. However, for the present supersubstorm event it is most intense in the dawn-to-morning sector.

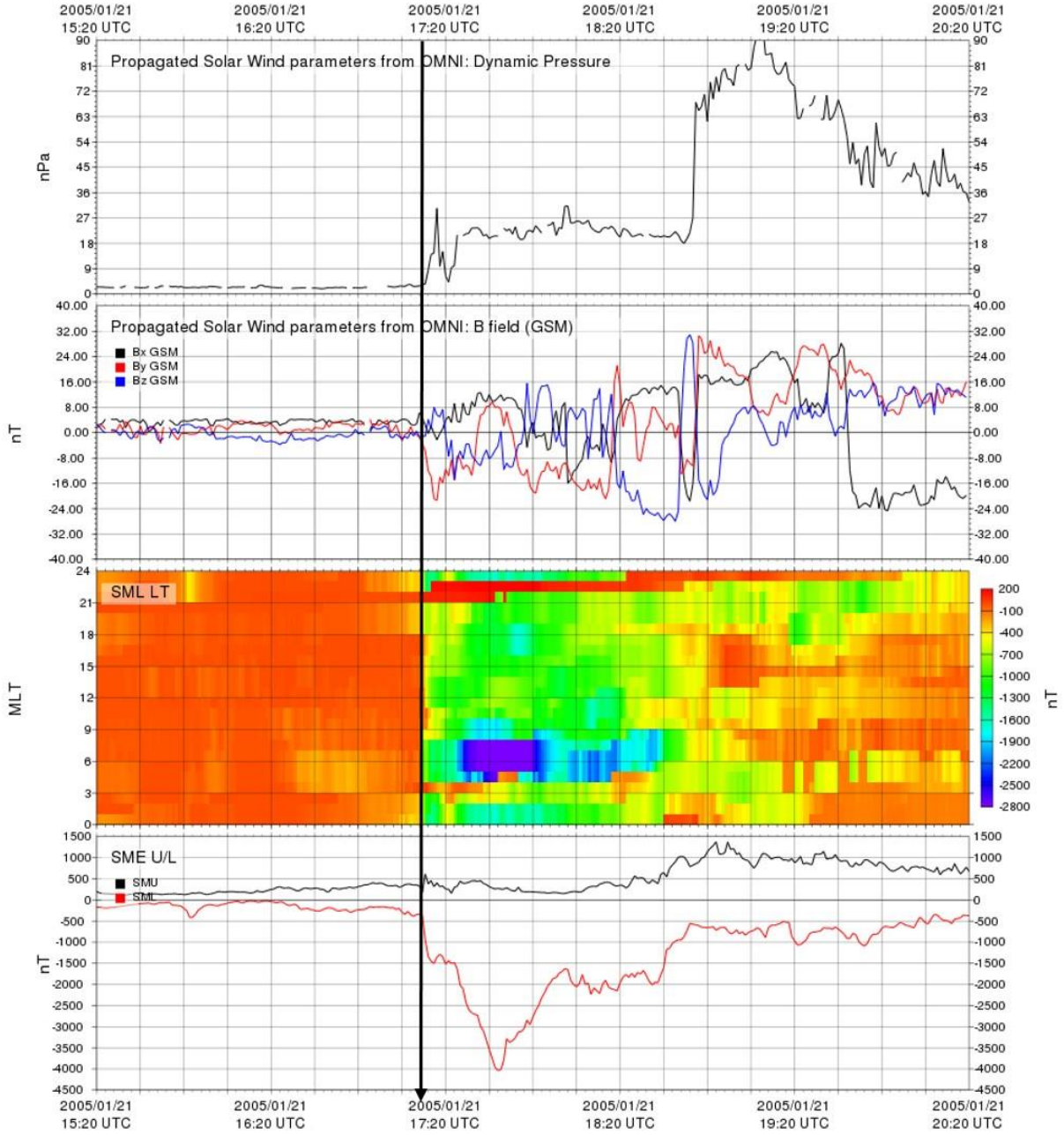

Figure 4. 3 The plot represents the solar wind and geomagnetic parameters of the substorm event on 21st January 2005. The plot is obtained from the SuperMAG website [http://supermag.jhuapl.edu/]. From top to bottom, the panels show (a) solar wind dynamic pressure, (b) interplanetary magnetic field (the three components in GSM coordinates), (c) SML LT, and (d) the SMU and SML plot showing onset and intensity of substorm. The black solid vertical arrows show substorm onset at 17:11 UT.

4.2.4 Impulse-induced substorm of 19th December 2015

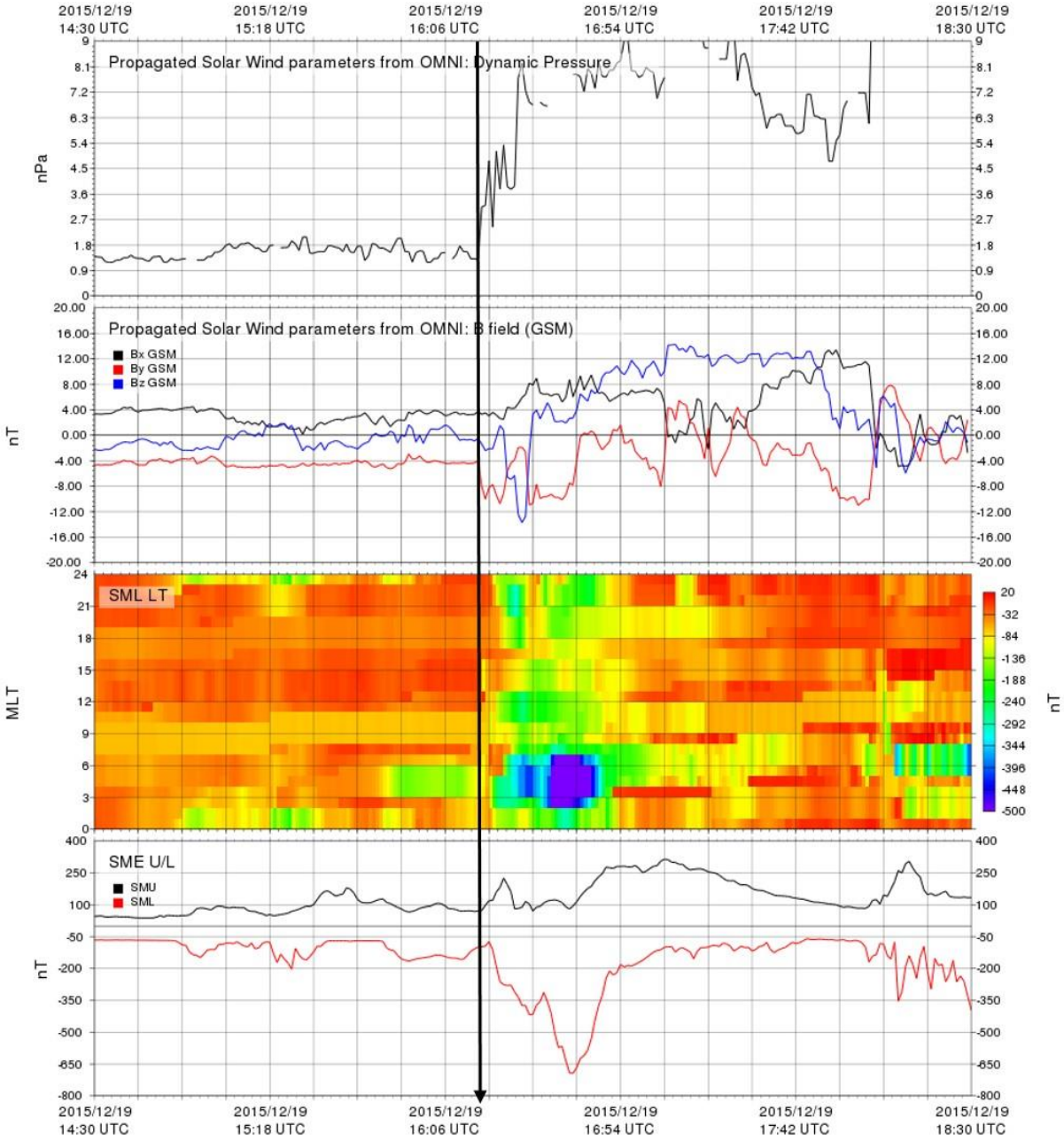

Figure 4. 4 The plot represents the solar wind and geomagnetic parameters of the substorm event on 19th December 2015 August 2000. The plot is obtained from the SuperMAG website [http://supermag.jhuapl.edu/]. From top to bottom, the panels show (a) solar wind dynamic pressure, (b) interplanetary magnetic field (the three components in GSM coordinates), (c) SML LT, and (d) the SMU and SML plot showing onset and intensity of substorm.

The substorm that occurred on December 19, 2015, is depicted in Figure 4.4 along with the associated geomagnetic field variation and solar wind condition. IMF Bz was 0 nT for the specified event hours before the substorm started at 16:15 UT, but the two triggering agents, namely, IMF By (approximately -6 nT) and pressure pulse (3.5 nPa), were present to aid in the substorm's initiation. Similar to what we saw during an impulse-induced substorm, the SML-LT parameter on this day indicates that the maximum H-component variation was in the dawn sector. As a result, on this day, the SML-LT index behaved like an impulse-induced one even when the IMF By component was significantly present.

The SML-LT index can therefore be used as a first step in classifying a substorm as impulse-induced or IMF Bz/By induced. An impulse-induced substorm can be detected by the presence of a pressure pulse coinciding with the time of substorm onset and an intense SML-LT variation centered far from midnight. To confirm, further ground based and satellite-based observations will be required. This procedure will be used in categorizing the substorms discussed in the next section to identify the dominance of one of the triggering agents.

4.3. Substorms with a presence of more than one triggering agents

4.3.1 Case Study of 05th April 2010 substorm

I. Solar Wind parameter and Geomagnetic Field

The solar wind and geomagnetic parameters for April 5, 2010, from 7:00 UTC to 12:00 UTC are shown in Figure 4.5 and were taken from the SuperMAG website (http://supermag.jhuapl.edu/). As indicated by the SME U/L parameter in figure 4.5 (d), the substorm on this day had multiple onsets. A sudden enhancement/depression in the SME U/L index is used to define the onset of the substorm (eg. Hajra and Tsurutani, 2018). The initial three sequential substorm onsets, which occurred at 0826 UTC, 0845 UTC, and 0901 UTC, are shown by three solid vertical arrows. A southward IMF Bz component of around 6 nT was present before the first onset at 0826 UTC, and this preconditioning enables the solar wind energy be transferred into the magnetotail via dayside magnetic reconnection (Meng et al., 1973; Phan et al., 2013; Tsurutani & Meng, 1972). IMF By reaches a minimum of -4 nT and otherwise is near 0 for most of the times before the onset. Also, a pressure pulse of ~10 nPa coincides with the onset. Hence, the injection of solar wind particles is possible via both magnetic reconnection and viscous interaction.

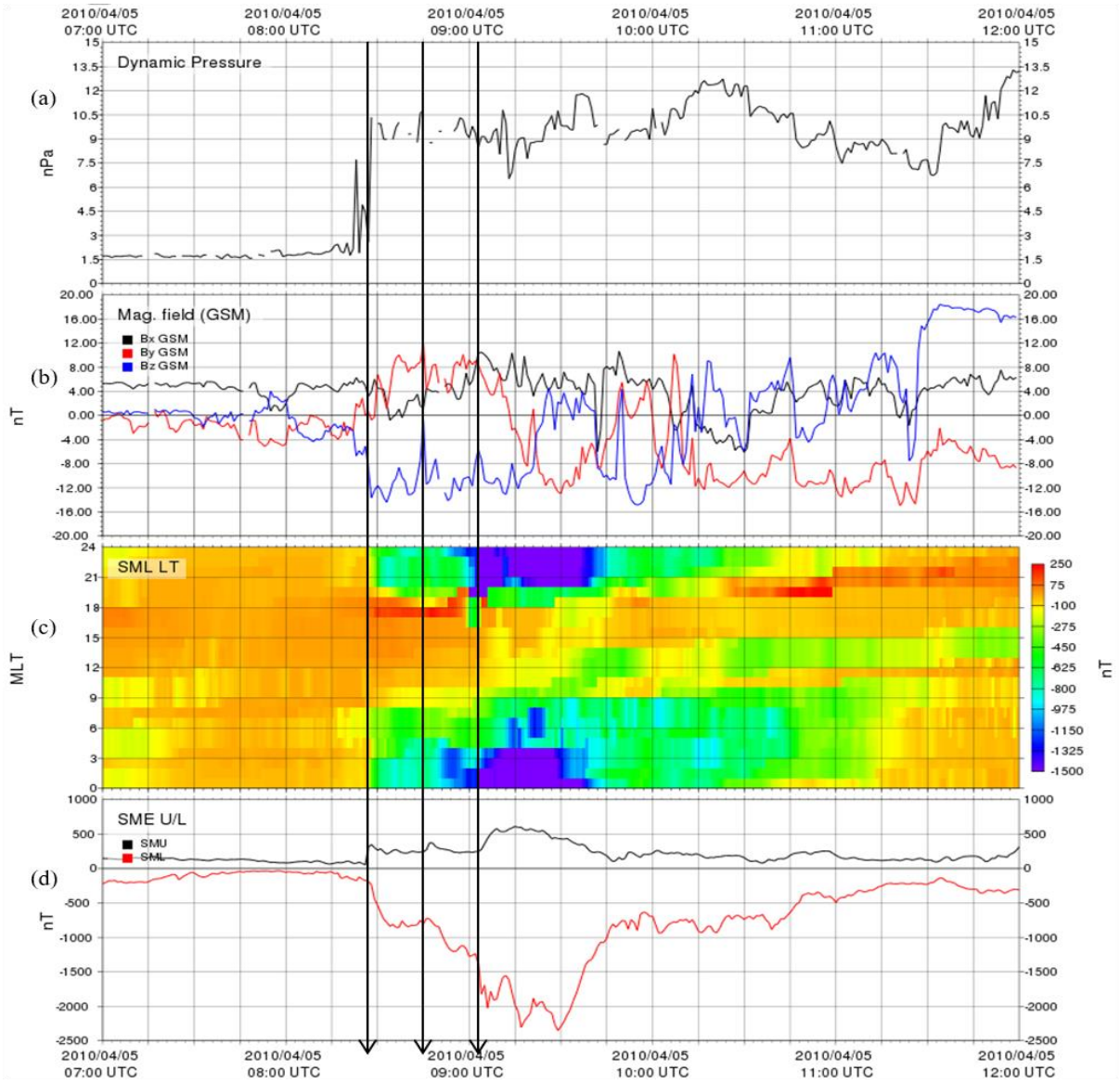

Figure 4. 5 The plot represents the solar wind and geomagnetic parameters of the substorm event on 05th April 2010 from 07:00 UTC to 12:00 UTC. The plot is obtained from the SuperMAG website [http://supermag.jhuapl.edu/]. From top to bottom, the panels show (a) solar wind dynamic pressure, (b) interplanetary magnetic field (the three components in GSM coordinates), (c) SML LT, and (d) the SMU and SML plot showing onset and intensity of substorm. The three black solid vertical arrows show three consecutive substorm onsets at 08:26 UT, 08:45 UT and 09:01 UT, respectively.

The second onset at 0845 UTC coincides with the sudden northward turning of IMF Bz from ~ -13 nT to ~ -1 nT, indicating the unloading of particles from the night side magnetotail region. The solar wind pressure is almost constant at this time, hence injection via viscous interaction will not happen. The third onset at 0901 UTC also corresponds to the magnetic reconnection process as the southward component of IMF Bz turns moderately northward at that time, and the pressure pulse is again almost constant. The first two onsets showed gradual enhancement of the substorm, as indicated by the SML index (figure 5 (d)), which decreased from ~ -100 nT to ~ -800 nT in the initial ~08 minutes and from ~ -800 nT to ~ -1200 nT in the next ~10 minutes. The third onset at ~0901 UTC was abrupt, showing a decrement in the SML index from ~ -1200 nT to ~ -1800 nT in just ~02 minutes.

This supersubstorm event was considered an impulse induced by Hajra and Tsurutani, 2018. However, Figure 5 (c) shows the behavior of auroral electrojet like one during a normal Akasofu-type of substorm. The maximum variation in the geomagnetic field at high latitude is concentrated in the midnight sector, as during IMF Bz induced substorms. To further understand the behavior of precipitating particles and to confirm that the substorm on this day behaved like normal Akasofu-type, we looked into the ground CNA (Cosmic Noise Absorption) characteristic and low earth orbiting (POES) satellite datasets.

II. Cosmic Noise Absorption (CNA) Characteristics

For our investigation, we used the datasets from multiple high latitude stations' riometer and ground-based magnetometers. The list of Riometer stations and their geomagnetic locations are shown in table 4.1. For the purpose of the present investigation, the CNA datasets estimated in dB have been directly retrieved from the primary data providers/official websites.

Table 4. 1 The list of Riometer stations whose datasets are used to study this event, along with their geomagnetic location.

Sr. No.	**Name of the station**	**Geomagnetic Latitude**	**Geomagnetic Longitude (°E)**
1.	Jyvaskyla, Finland	59.08° N	103.29°

2.	Maitri, Antarctica	63.12° S	54.05°
3.	Macquarine Island, Antarctica	64.05° S	248.26°
4.	Ivalo, Finland	65.28° N	108.49°
5.	Abisko, Sweden	65.45° N	101.70°
6.	Dawson, Canada	65.95° N	331.27°
7.	Gillam, Canada	66.28° N	332.53°
8.	Rabbit Lake, Canada	66.81° N	318.48°
9.	Fort Smith, Canada	67.26° N	305.71°
10.	Davis, Antarctica	74.80° S	100.83°

The CNA (purple) and H-component (black) fluctuations of all the stations under study are shown in figure 4.6 and are divided in two panels. The relative absorption plots of the daytime stations are shown in the left panel, while the nighttime stations are shown in the right panel, both at the time of substorm onset. Starting with sub-auroral and heading towards polar, all of the stations are arranged according to their latitudes. The three first substorm onsets, which were also depicted previously in Figure 4.5, are denoted by the black vertical arrows. The absorption curves do not exhibit considerable variation prior to the first substorm onset. The dayside auroral stations (IVA, ABI, and DAV) exhibit a sudden spike in the CNA curves with an absorption value of 1 dB after the first onset at 08:26 UT. The first onset is mainly because of shock, since the effect is observed more on the dayside.

The second onset, which was at ~08:45 UT, is not much reflected in the CNA observation. Only the MCQ (MLT=UT-11:59) station, located near the pre-midnight sector, shows a peak absorption of ~1.5 dB at this time. As this onset was associated with the particle unloading from the night side after magnetic reconnection, the CNA enhancement was observed only in the midnight sector as expected. The third subsequent onset at 09:01 UT was abrupt, and its effect observed in CNA was much most intense. It is worth mentioning, though not shown here, that the Wp index (Nosé et al., 2012) at this time was increased by a factor of 2, while that during the first onset at 0826 UT was increased by 1. Wp index is a substorm index introduced by Nose et al. (2012) which is derived from high-resolution geomagnetic field data of low latitude stations. Prompt increases in the Wp index are used to identify substorm onsets, and the magnitude of the Wp index depends upon the intensity of the substorm (Nosé et al., 2012). Hence, the onset at 09:01 UTC leads to a stronger substorm onset compared to the previous one.

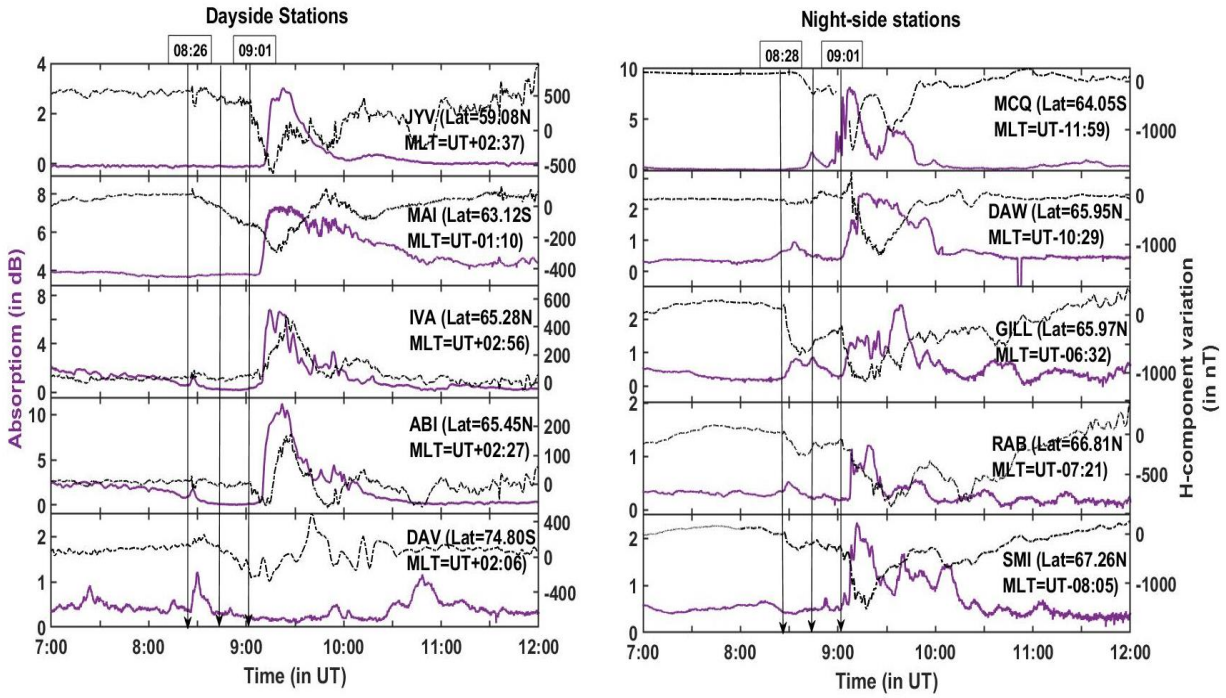

Figure 4. 6 The left column of the figure has CNA observations and H-component variations of stations lying in the dayside during the time of substorm onset, and the right column has stations that lie in the night side. The purple curves indicate the absorption and the black dotted curve indicate the H-component variation of that location. In each column the stations are arranged in ascending order of their magnetic latitude, starting from sub-auroral to polar latitude from top to bottom. The three vertical arrows indicate the time of the three initial substorm onsets.

At stations positioned on the night side (MCQ, DAW, and GILL), a rapid improvement in the absorption curves was seen with the third onset, as depicted in Figure 4.6. The absorption is delayed by around five minutes at the other two stations (RAB and SMI) on the night side. The dayside stations similarly exhibit significant absorption, but with a slight delay of roughly 8 minutes. Figure 4.5 (c) shows that all stations, whether they are on the dayside or the nightside, exhibit enhanced auroral electrojet (flowing either westward or eastward). Examining the geomagnetic H-component of the ground magnetometers at these places also supported this. Thus, all of the CNA curves shown in the figure are associated with substorms.

The MCQ station, which is in the pre-midnight sector, records the highest instantaneous absorption (6 dB) at 09:01 UT, after the third onset. As with a typical Akasofu-type substorm, this substorm's onset was caused by particle unloading from the night side after magnetic

reconnection. So, it could be predicted that the maximum instantaneous absorption would occur around midnight and is also the case. The overall largest absorption is, however, shown by ABI, which was in the dayside (about 11:28 MLT), but with a delay of 08 minutes. Additionally, after 09:01 UT, this station also showed an enhancement in the geomagnetic H-component, indicating the presence of a strong eastward electrojet. The delayed CNA could either be due to ionospheric plasma drift during substorms or due to particle drift and precipitation from the magnetosphere, as explained by Behera et al., 2016, or both. The other stations above ABI also show an appreciable amount of precipitation but again with a delay. Maitri (MAI), which was in the southern hemisphere morning sector, showed the presence of westward electrojet after the substorm onset and a delayed CNA of ~3 dB enhancement.

III. Satellite Observation

The Space Environment Monitor (SEM) instrument package on board the POES spacecraft in Sun-synchronous orbits at around 800–850 km altitudes collected the data used in this work. An emphasis on the timing of processes that drive particles into the atmosphere is made possible by the low altitudes of the POES platforms, which make them ideally suited for studying particles close to or in the loss cone (Evans & Greer, 2004; Rodger et al., 2010). SEM-2 monitors electron fluxes between 50 eV and 2700 keV. Since diffuse auroras and CNAs are both generated by electrons with energies between 10 and 100 keV, observations of precipitating electron fluxes for the energy range more than 30 keV have been employed for this investigation (Rees, 1963). Hence, the electron fluxes in this energy range can serve as a proxy for visual aurora and CNA observation. All the POES datasets are available on the website https://www.ngdc.noaa.gov/stp/satellite/poes/index.html.

The satellites used for the study are MetOp-02, NOAA-17, NOAA-18 and NOAA-19. The study used the MetOp-02, NOAA-17, NOAA-18, and NOAA-19 satellites. Figure 4.7 displays the satellites' electron counts (>30 keV) as well as their positions in terms of magnetic local time (MLT) and magnetic latitude (MLat). The third substorm began at 09:01 UT, as indicated by the solid black vertical line in the figure. In the satellite particle flux plot, the two preceding onsets are not well identified. The satellites may not have been in the ideal place to display the flux improvements, or there may not have been much precipitation before the third onset, which can be the two possible explanations. Both the dayside and nightside ground stations detected the first onset at around 18:26 UT predominantly in the area around 65 deg MLat (figure 4.6). To see an increase in electron flux, none of the satellites were near the auroral zone (around 65° MLat). The four satellites, METOP-02, NOAA-17, NOAA-18, and NOAA-19, were

positioned at 7°, 64°, 56°, and -21° magnetic latitudes, respectively, at 18:45 UTC. NOAA-17 was the only one, out of the four satellites, in the auroral zone and in the early morning sector. Because of its position, only this satellite noticed a modest increase in the electron flux around 18:45 UT (although it was much less than the enhancement at 19:01, which is consistent with the ground observations). The pre-midnight sector was where the ground CNA (figure 4.6) exhibited the largest increase in absorption at around 18:45 UT (MCQ station). Hence, we may say that the onsets were not observed by the satellite because they were not in the desired location (which is near 65° magnetic latitude).

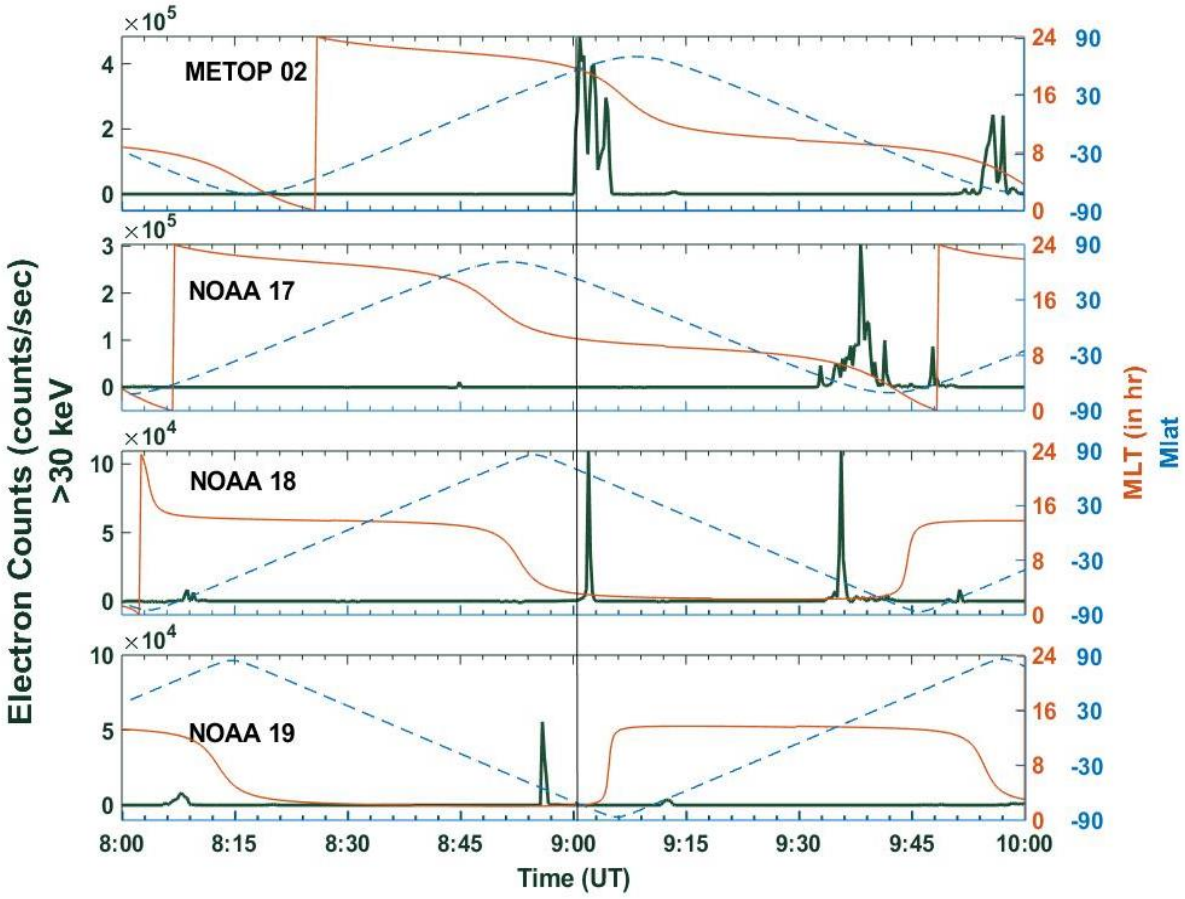

Figure 4. 7 The electron counts (>30 keV) as observed from each of the satellites: - MetOp-02, NOAA-17, NOAA-18 and NOAA-19 on 05th April 2010 are shown along with their latitude (MLat in degrees) and longitude (in terms of MLT). At 09:01 UT MetOp-02 was in northern hemisphere auroral zone pre-midnight sector, NOAA-17 in northern hemisphere sub-auroral near noon time, NOAA-18 in northern hemisphere auroral zone post-midnight sector and NOAA-19 in southern hemisphere polar region post-midnight sector. The dark green color plots correspond to the electron count data, orange for the MLT and blue dotted plots for the MLat of each satellite.

When the third substorm began (09:01 UT), MetOp-2, which was in the auroral zone before midnight, displayed a maximal and abrupt increase in electron counts (>30 keV). The immediate and maximum CNA values at 09:01 UT are also shown by the conjugate ground station, MCQ (Figure 4.6). NOAA-17, which was in the t he sub-auroral zone noon sector, did not exhibit any increase in electron flux at 09:01 UT. The ground CNA stations located in the auroral zone noon sector also do not show any enhancement at that time. Only after a delay of around 8 minutes was there any enhancement in ground absorption. NOAA-18, which was in the post-midnight sector, shows enhancement in electron flux with a delay of ~02 minutes. It is expected that the satellite in the post-midnight sector will observe these electrons with a slight delay since electrons flow counter-clockwise after entering from the night side. NOAA-19, which was in the auroral zone post-midnight sector at about 08:56 UT prior to the third onset), exhibits electron flux enhancement at that time. The satellite near the midnight sector will observe these electrons instantaneously, as we see in MetOp-2. At 09:01 UT, NOAA-19 was in the polar region and didn't have any dayside precipitation coming from the cusp region. Even figure 4.6 depiction of a DAV station in the dayside polar zone demonstrates that CNA did not increase at that time either. The ground observation is in perfect agreement with the satellite data, demonstrating that particle precipitation is the cause of the increase in CNA. Similar to what we see during typical Akasofu-type substorms, where particle injection and precipitation occur via magnetic reconnection from the night side, these satellite observations, ground magnetic field (SML-LT), and CNA observations show the same. The impact of the pressure pulse at 08:26 UT was very small, almost negligible, and was not significantly reflected in the ground and satellite measurements.

4.3.2. Case Study of 22nd June 2015 substorm

I. Solar Wind parameter and Geomagnetic Field

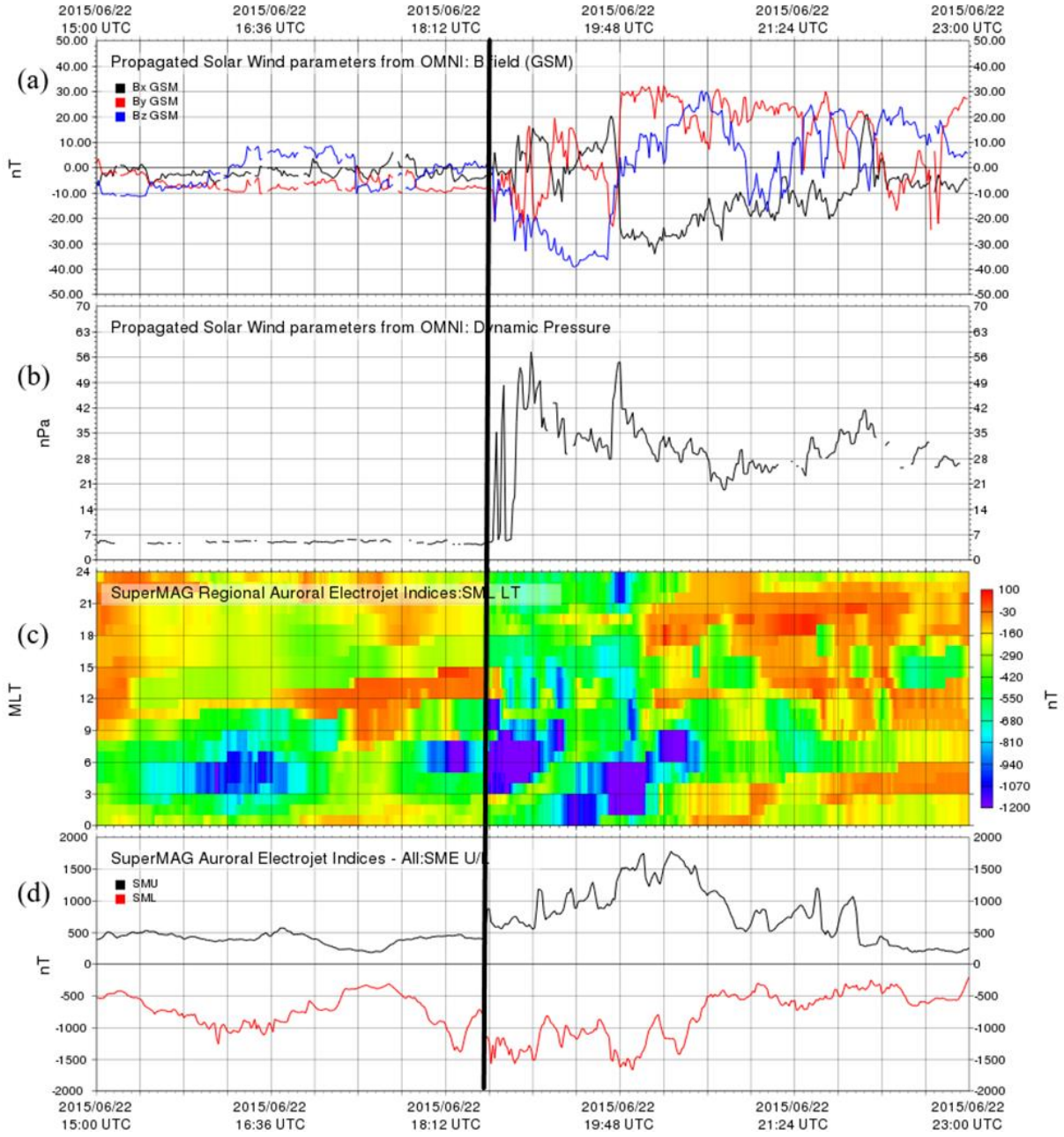

Figure 4. 8 represents **(a)** the interplanetary magnetic field in GSM coordinates, **(b)** Solar wind dynamic pressure, **(c)** SuperMAG auroral electrojet indices: SML-LT and **(d)** SuperMAG auroral electrojet indices: SME U/L on 22nd June 2015 from 15:00 UTC to 23:00 UTC. The plot was obtained from the SuperMAG website. The black solid vertical line indicated the pressure pulse at 18:34 UTC. Each box is 24 minutes.

Figure 4.8 represents the solar wind/interplanetary data in geocentric solar magnetospheric (GSM) coordinates and geomagnetic indices on 2015 June 22 from 15:00 UT to 23:00 UT. The onsets of the substorm, the timing of the pressure pulses, and the behavior of the geomagnetic field at high latitudes on this day were determined using the solar wind data and the auroral electrojet indices based on about 300 ground magnetometer stations of the SuperMAG network (Gjerloev, 2012). The red curve in Figure 4.8(d) depicts the SML parameter that has several onsets representing the variation in the westward electrojet current throughout this time period of the day. However, it wasn't until 18:34 UT that the SMU index significantly changed, indicating an eastward electrojet variation (black curve in figure 4.8(d)). The substorm onset at 17:38 UT, prominently seen from the SML parameter, is gradually increasing but intense. With few intermediate onsets, the SML index decreased from -300 nT to -1300 nT after 38 minutes. Besides, IMF Bz was southward before 16:12 UT having a magnitude ~ -09 nT, and after turning northward, it again turned southward at 17:24 UT. Therefore, there was a good chance of particle injection by magnetic reconnection before the substorm began at 17:38 UT. The SML-LT plot in figure 4.8(d) demonstrates that the auroral zone's most intense magnetic field variation was always confined to the dawn/morning sector. This characteristic of the impulse-induced substorm suggests that the pressure pulse significantly dominated the magnetic reconnection process. The SuperMAG and OMNI datasets show data gaps, which could be because WIND satellite had major data gaps at this time. Therefore, we cross-checked the ACE and THEMIS satellite data. We found that there was a pressure pulse (of comparatively much less intensity than the succeeding one) present prior to 18:34 UT which may have initiated the onset of the preceding substorm.

ACE solar wind proton number density (shown here in fig 4.9(a)) showed a signature of pulse before the pressure pulse shown in the SuperMAG plot at 18:34 UT. It should be noted here there will be a time lag of about 20-40 minutes for the OMNI database from the ACE satellite, depending upon the satellite's position. This is because ACE is at bow-shock and OMNI datasets are time corrected to ground level. The pressure pulse of 18:36 UT as observed by OMNI is seen at ACE at around 18:00 UT (big red circle in figure 4.9 (a)). The pressure pulse indicated by a smaller circle could be responsible for the previous substorm onset, but that is not primarily focused in the present chapter. A corresponding pressure enhancement was also observed by THEMIS-C at ~17:48 UT (which was in the solar wind at that time near ~62 Re) (fig 4.9(b)).

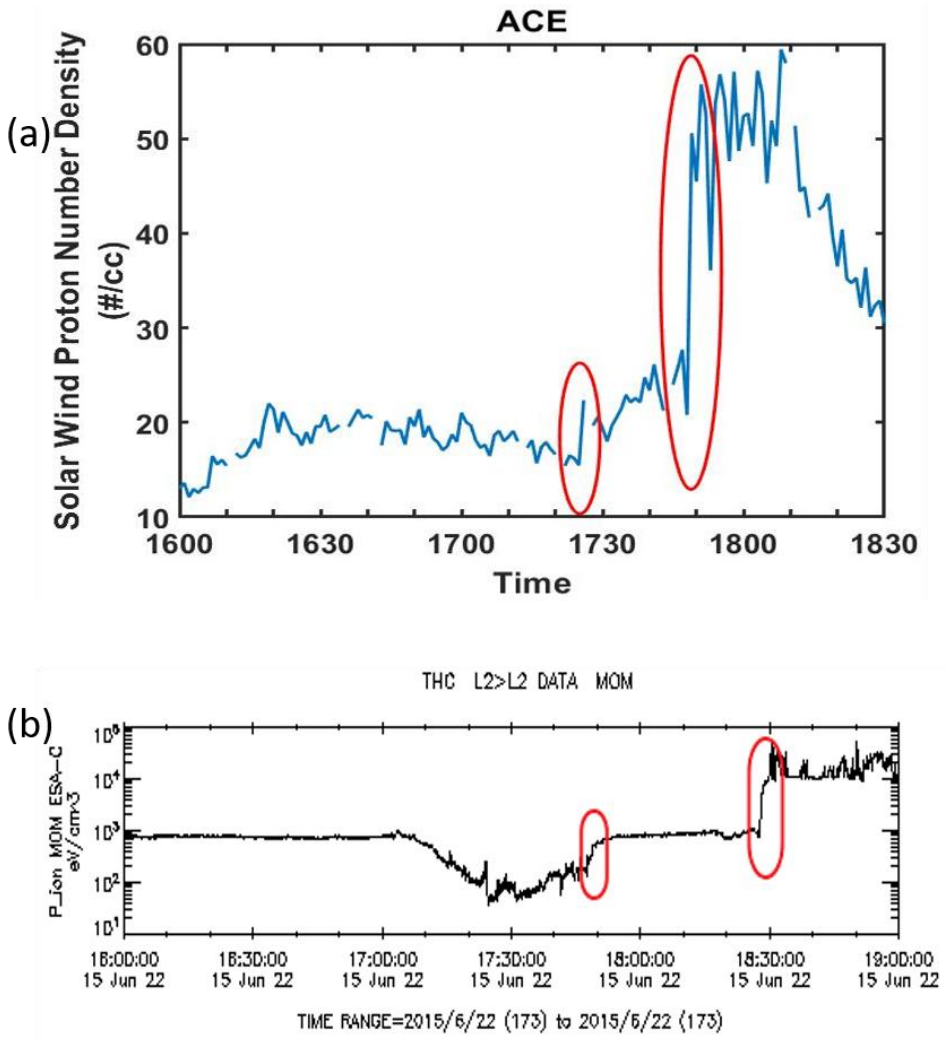

Figure 4. 9 (a) Solar wind Proton number density as observed from ACE satellite on 22nd June 2015. (b) Solar wind Ion total Pressure as observed from THEMIS C, obtained from CDAWeb. The red circles in the figure indicates the solar wind pressure pulses as observed from the two satellites.

In addition, we also checked the Wp index during this day as shown in figure 4.10. It is known that Wp index is a substorm index introduced by Nosé et al. (2012), which is derived from high-resolution geomagnetic field data of low latitude stations. A prompt increases in the Wp index is used to identify substorm onsets and the magnitude of the Wp index depends upon the intensity of the substorm (Nose et al., 2012). Wp index was highest (~ 2 nT) at 18:34 UT (fig. 4.10). Before that the index was high (0.5 nT) around 16 UT, more than two hours before. This suggests that at 18:34 UT there was a new substorm onset and can be considered as an isolated substorm event.

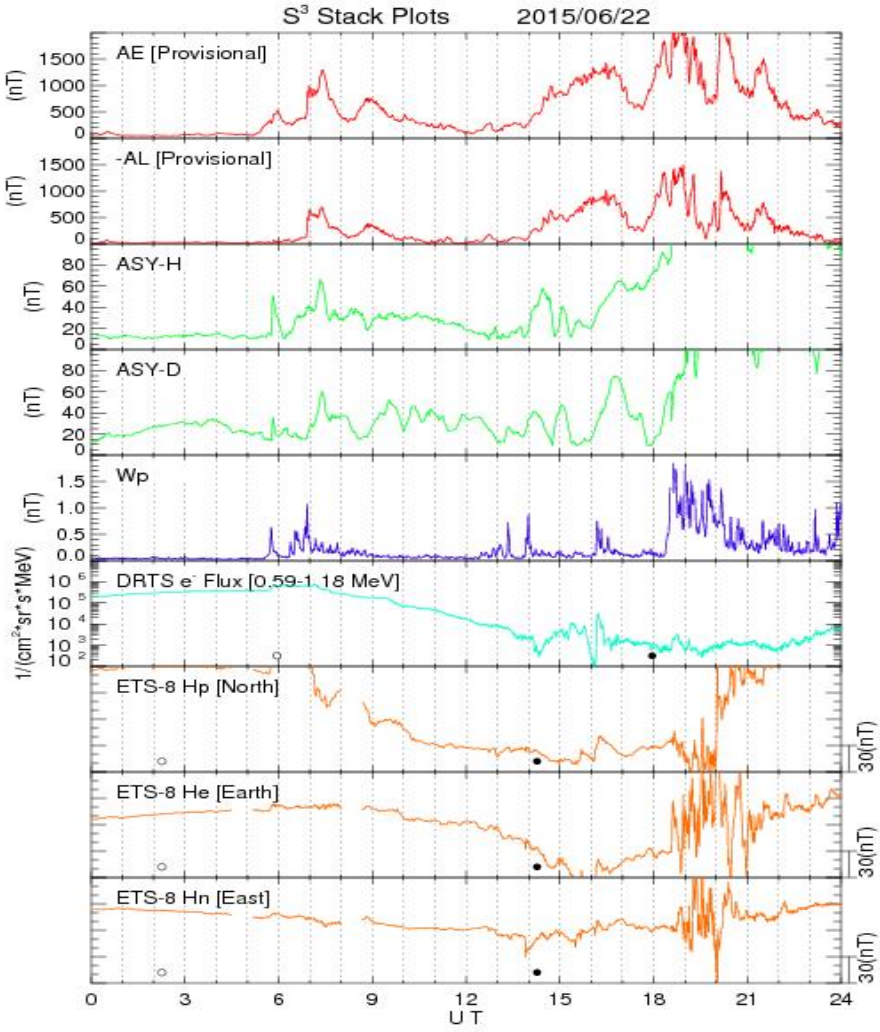

Figure 4. 10 Wp index (blue curve) on 22 June 2015 (http://www.isee.nagoya-u.ac.jp/~nose.masahito/s-cubed/index.html)

At 18:34 UT, the pressure pulse significantly increased three times, reaching peaks of 35 nPa, 48 nPa, and 54 nPa. These numbers suggest that there were very intense pressure pulses, which might have caused viscous interaction and particle injection from the flanks. At 17:56 UT, the IMF Bz's southward component shifted noticeably northward, from -10 nT to 0 nT. Therefore, magnetic reconnection also offered a chance for midnight sector particle injection. The SML-LT index, however, suggests that the pressure pulse impact predominated the latter. This is due to the fact that, unlike what we would expect during a normal Akasofu-type substorm, the peak auroral electrojet current and maximum fluctuation in the geomagnetic H-component did not occur around midnight. Rather it was concentrated near dawn/morning sector, far away from midnight. We used the ground and satellite observation of particle precipitation to further confirm our speculation after looking at the solar wind and geomagnetic parameters.

It is indeed important to note that at around 15:43 UT, a substorm with an SML-LT centering at 3-6 MLT was also present. In general, a large IMF By can also result in the onset of a substorm away from midnight (Ostgaard et al., 2011). IMF By was near -8 nT at 15:43 UT, which may have been relevant in this situation. Unfortunately, there were data gaps for OMNI solar wind dynamic pressure at this period. Therefore, without the availability of data for all parameters, it is difficult to conclusively determine the dominance of pressure or IMF By at 15:43 UT for this away midnight signatures. As a result, we focused on the latter substorm and did not include this substorm in our analysis.

II. Cosmic Noise Absorption (CNA) Characteristics

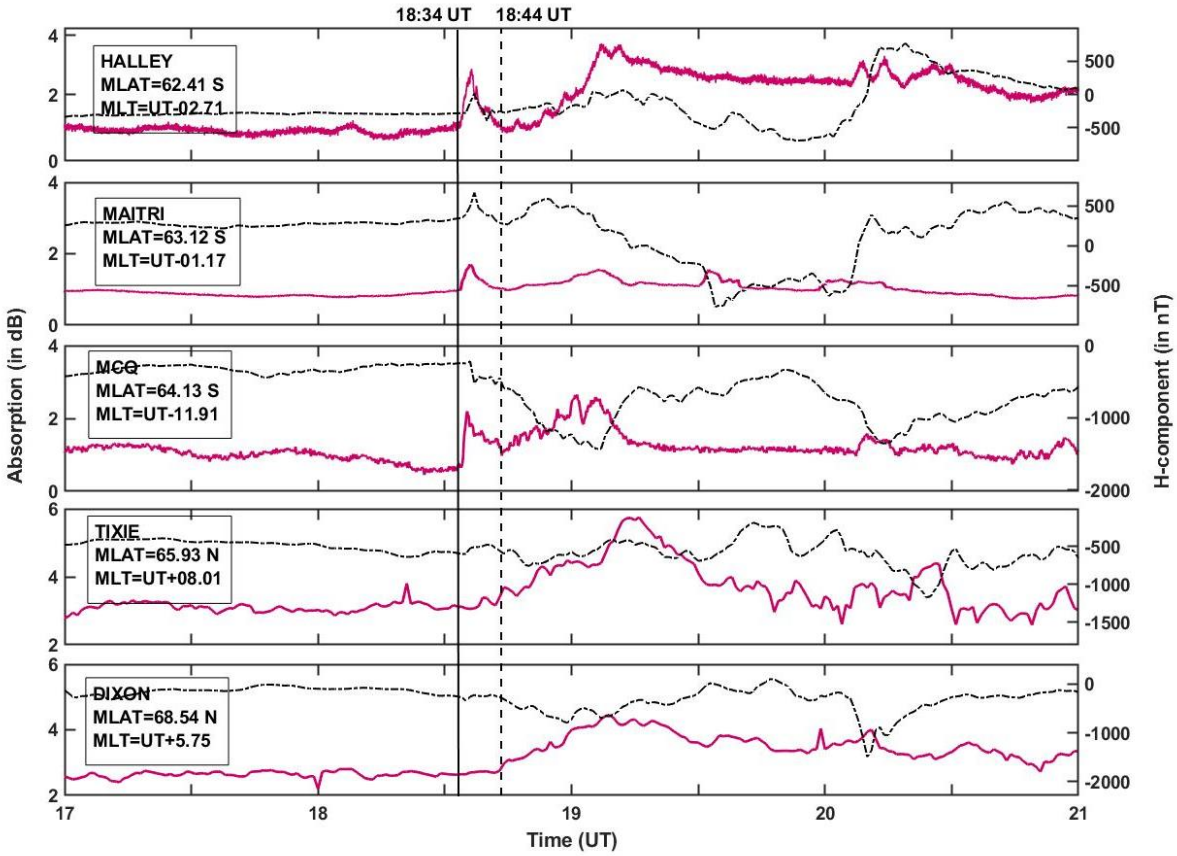

Figure 4. 11 shows CNA (in dB) and H-component variation of Halley, Maitri, MCQ, Tixie and Dixon stations on 22nd June 2015 from 17:00 UT to 21:00 UT. The magenta curves indicate the absorption and the black curve indicate the h-component variation of the locations. The two black solid vertical lines are at 18:34 UT and 18:44 UT. The stations are arranged from low to high latitudes.

Figure 4.11 shows the H-component variation and CNA curves for the Halley, Maitri, MCQ, Tixie, and Dixon stations. When the substorm began at 18:34 UT, these stations were

spread throughout various time sectors in the auroral zone. In comparison to other stations, Halley and MCQ, which were in the pre- and post-noon sectors, exhibit maximum absorption of around 2 dB at 18:34 UT as well as the presence of eastward and westward electrojets at the time of onset. Maitri exhibits a 1 dB absorption and an eastward electrojet in the evening sector. The magnetic field at the two stations, Tixie and Dixon, which were in the post-midnight and midnight at this time, shows no absorption. Only around 18:44 UT did all of the stations begin to gradually increase their CNA and change their H-components. The presence of CNA in the pre-and post-noon sector and not in the midnight sector is a typical impulse induced substorm signature.

III. Satellite Observation

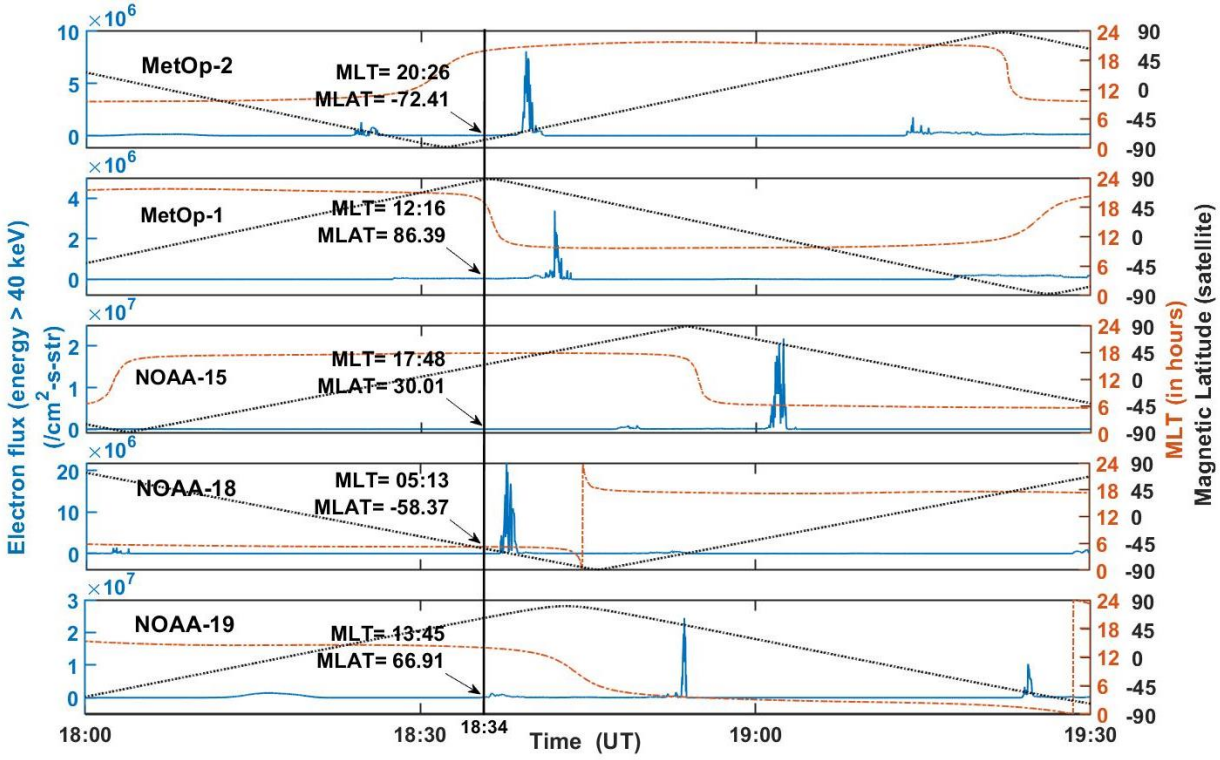

Figure 4. 12 Shows the electron flux data (> 40 keV) and position of MetOp-2, MetOp-1, NOAA-15, NOAA-18 and NOAA-19 on 22nd June 2015 from 18:00 UT to 19:30 UT. The blue color curves show the electron flux, orange curves show MLT and black dotted curves indicate the magnetic latitude of the foot point of each spacecraft. The black solid vertical line indicates the time of pressure pulse at 18:34 UT.

We examined the electron measurements made by the Space Environment Monitor (SEM) instrument set on board the POES and GOES spacecraft to further solidify our understanding of this event. GOES is an equatorial orbiting satellite at 6.6 Re, while POES is a low earth orbiting (LEO) spacecraft at an altitude of about 850 km. The NOAA website (link:

https://www.ngdc.noaa.gov/stp/satellite/poes/index.html) makes the data we used publicly available.

For energies larger than 40 keV, Figure 4.12 displays the electron fluxes for MetOp-1, MetOp-2, and NOAA-15, NOAA-18, and NOAA-19. In order to compare it with the ground-based CNA observation, which examines particle enhancement in the D-region ionosphere, we chose this energy range. At 18:34 UT, the black solid vertical line denotes the onset of the substorm and the pressure pulse. Each panel includes information about the spacecraft's location in terms of MLT (orange curve) and magnetic latitude (black curve) at different UT. For each spacecraft in the illustration, the blue curves represent the electron fluxes, the orange curves the MLT, and the black curves the magnetic latitude. At 18:34 UT, MetOp-2 and NOAA-19 were in the auroral zone, but neither instrument detected an increase in the electron flux at that time. They were in the pre-midnight and noon sector, respectively. MetOp-2, NOAA-18, and NOAA-19 entered the auroral zone after around 2 to 3 minutes. At this point, NOAA-18, which was in the morning sector, displayed an increase in electron flux. A few minutes later, MetOp-2, which was in the pre-midnight sector, also displayed an increase. Again, after about ~3-4 minutes, MetOp-1 entered the auroral zone in the noon sector and showed enhancement in the flux. This shows that electrons reached the evening sector before the noon sector. The dusk sector could not have been reached before the noon sector if the electrons had entered the Earth's atmosphere from the night side since electrons move counterclockwise. Because of this, the only explanation left is that the electrons had entered from the flanks, as during impulse-induced substorms. For this reason, both in satellite and ground CNA observations, the pre- and post-noon sector observes the electrons first and in the greatest amount relative to other local time sectors. NOAA-15 and NOAA-19 observe an enhancement in flux only when they enter the auroral region from the morning sector, as shown in the figure.

NOAA satellites also provide information on proton (50 eV to 20 keV) and electron (50 eV-20 keV) energy fluxes at 120 km altitude. These energy fluxes are excellent proxies for visual electron and proton auroras as the altitude of the formation of auroras are also the same. Plot 4.13 shows the enhancements of these protons and electrons and they exhibit same behavior as electron fluxes greater than 40 keV at 850 km altitude. The plot suggests that the electron and proton auroras maximize instantaneously in the dawn sector (NOAA-18). This dawn-centered enhancement is similar to the supersubstorm case of 21st January, 2005 and is a completely impulse-induced characteristic.

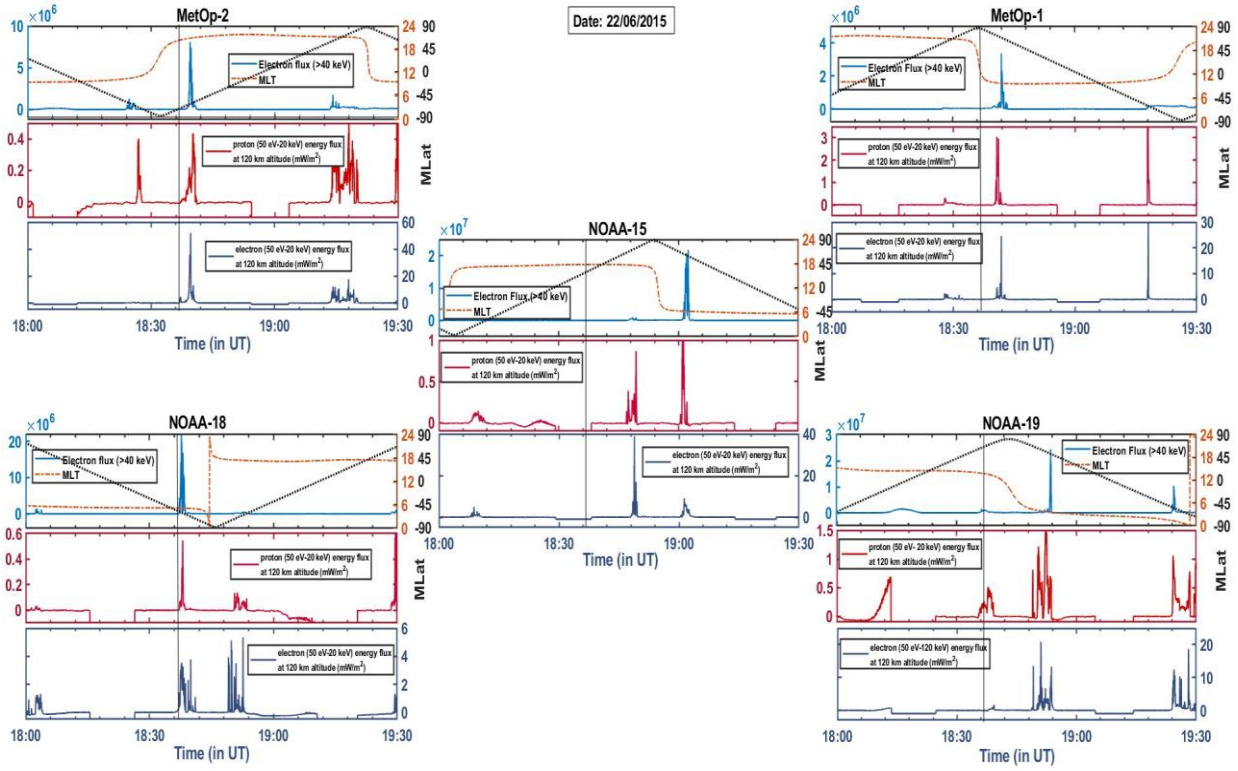

Figure 4. 13 Electron flux data (> 40 keV) and position of MetOp-2, MetOp-1, NOAA-15, NOAA-18 and NOAA-19 on 22nd June 2015 on the top panel of each plot. The red curve (middle panel) shows proton flux enhancements (50 eV-20 keV) at 120 km altitude of each satellite. The dark blue plots (third panel) show the electron flux enhancement (50 eV-20 keV) at 120 km altitude for each satellite.

4.4. Discussion and Summary

We analyzed in total six substorms, four of which were used to signify the importance of SML-LT index in the initial categorization of a substorm as impulse-induced one or IMF Bz/By induced one. It is observed that the impulse-induced substorm are associated with a pressure pulse coinciding with the substorm onset. Also, during pressure induced substorms, the most intense (negative) SML-LT variation is centered far away from usual midnight. Normally, during IMF Bz triggered substorms, SML-LT is observed to be midnight centered. Studies have earlier reported that IMF By can also lead to away midnight particle precipitation (eg. Ostgaard et al., 2011), however, the event studied in this paper (figure 2) shows that the substorm triggered by IMF By had SML-LT centered in the midnight like during a normal Akasofu-type one.

Below is a table, table 4.4, of the interplanetary conditions of all six events taken as case studies in this paper to brief the similarities and differences in the geomagnetic variations along with the probable triggering agent.

Table 4. 2 Interplanetary condition and ground geomagnetic field variation of the six substorms taken as case studies.

Sl. No.	Substorm Event (Date)	Pressure Pulse (approx. peak value at onset)	IMF Bz (max value ~1.5 hr prior)	IMF By (max value ~1.5 hr prior)	SML-LT (centered)	Substorm Intensity (approx. Peak SML index)	Substorm onset triggered by: -
1.	14 April 2019	0.1 nPa	-10 nT	-12 nT	Mid-night	-1850 nT	IMF Bz
2.	12-13 Aug 2000	0.2 nPa	+14 nT	+19 nT	Mid-night	-600 nT	IMF By
3.	21 Jan 2005	27 nPa	-3 nT	+3 nT	Morning	-4000 nT	Pressure Pulse
4.	19 Dec 2015	4 nPa	-2 nT	-4 nT	Dawn	-700 nT	Pressure Pulse
5.	05 April 2010	8 nPa	-6 nT	-4 nT	Mid-night	-2300 nT	IMF Bz
6.	22 June 2015	30 nPa	-10 nT	-10 nT	Morning	-1500 nT	Pressure Pulse and/or IMF By

We further analyzed two substorm events that occurred on 05th April 2010 and 22nd June 2015 using ground Riometer datasets and Satellite particle flux datasets. On both days, a southward component of IMF was present prior to the substorm onset, and a strong pressure pulse was also observed coinciding with the substorm onset. Hence, the possibility of solar wind particle entry from the magnetosphere into the Earth's atmosphere could be due to any of the two mechanisms, i.e., magnetic reconnection or viscous interaction.

We examined the ground and satellite observations of both substorm events in order to categorize which substorm was influenced by which factor and comprehend the dominance of one mechanism over the other. Despite the presence of the two triggering agents, the substorm on 05th April 2010 behaved like a normal Akasofu type substorm, and that on 22nd June 2015 appeared like an impulse-induced substorm. The difference between the Akasofu-type and impulse-induced substorm has been observed and accounted for using the two case studies. Our main observations during these events are: -

1. Substorm on 05th April 2010- Akasofu-type

(i) The SML-LT parameter on 05th April 2010 showed that the maximum variation of H-component at high latitudes was concentrated in the midnight sector during the substorm expansion phase. This means that the westward electrojet was strongest in this time sector as normally expected.

(ii) CNA characteristic on this day showed maximum and instantaneous enhancement in the absorption on the night side. The dayside stations showed enhancement with a delay of ~8 minutes. This could be the time taken by particles to either 'drift and precipitate' from the magnetosphere or due to ionospheric plasma drift, or both. All the stations covering day and night show the presence of enhanced electrojets (H-component variation). This indicates that the observed CNAs are substorm-associated.

(iii) It was found that the effect of pressure pulse on ground CNA observation was very small (at 08:26 UT in figure 6), almost negligible, and that due to magnetic reconnection was significant (at 09:01 UT in figure 6).

(iv) POES satellite observation was in accordance with the ground CNA observation, showing maximum instantaneous enhancement in electron flux in the midnight sector.

2. Substorm on 22nd June 2015- Impulse Induced

(i) This day, the SML-LT parameter showed intense negative H-component variation concentrated in the morning to noon sector. This is a typical impulse-induced substorm characteristic where westward electrojet can maximize at any local time away from midnight.

(ii) CNA characteristic on this day showed maximum absorption in the pre and post noon sector, coinciding with the time of pressure pulse (figure 9). The midnight sector did not show any enhancement in the CNA curve. All the stations were under the effect of enhanced auroral electrojets.

(iii) After the enhancement of the pressure pulse, the POES satellites which was in the auroral zone dusk sector (MetOP-2) showed enhancement in the electron flux before the POES satellite (NOAA-19) which was in the auroral zone noon sector (figure 10). This cannot happen if electrons enter from the night-side moving anticlockwise. The electron flux enhancement was also observed to be maximum in the dawn and dusk sectors through POES satellites (figure 10), which is in accordance with ground CNA observation (figure 9). GOES satellites showed loss of electrons at ~6.6 Re from the pre and post noon sector at the time of impulse (figure 11).

Thus, the substorms of 05 April 2010 and 22 June 2015, even after having the presence of similar triggering mechanisms, behaved differently. One behaved like a normal Akasofu- type and the other like an impulse-induced one. It appears that the intensity of pressure pulse and IMF Bz determines whether a substorm will behave like Akasofu-type or impulse-induced type. As indicated in table 4.2, the pressure pulse was much stronger on 22nd June 2015 (30 nPa) than 05th April 2010 (8 nPa), hence, the later behaved like a normal Akasofu-type. For the previous 22nd June 2015 case, the away midnight signature is definitely similar to that during an impulse-induced substorm (eg. 21st January 2005, figure 3), but there was also a presence of strong IMF By (-10 nT) component at the time of substorm onset. This makes the case study of 22nd June 2015 quite complex because the factors responsible for shifting the onset away from midnight are more than one. There have been several relevant works done to establish the connection between substorm onset location and strong IMF By component, like Ostgaard et al. (2011) and Liou and Newell (2010). According to these studies, in the southern hemisphere, the average local time for the auroral breakup or substorm onset increases (from 22.5 MLT to 23.5 MLT) with increase in IMF By (negative to positive). They also showed that the location of individual auroral breakup can spread widely in local times (earliest ~19 hr MLT and latest ~03-hr MLT). However, in our study we observe that on 22nd June 2015 (figure 8, 9, 10 and 11), the entry of particles is from dawn ranging from 5-7 MLT (much later than ~03 MLT) and dusk from 16-20 MLT (earlier than ~19 MLT). Since the IMF By on 22nd June 2015 is near -10 nT before the substorm onset, the maximum instantaneous enhancement in the flux should be near ~22 MLT in the southern hemisphere if the triggering is due to IMF By only (Ostgaard et al., 2011; and Liou and Newell 2010). However, the ground Riometer CNA and POES satellite particle flux datasets show that the maximum instantaneous enhancement in particles were at both dawn and dusk and in much extended MLT sectors in the southern hemisphere. In addition, the SML-LT parameter on 22nd June 2015 (figure 8) shows intense enhancement in the morning sector, similar to what we observe during a completely impulse-induced event of 21st January 2005

supersubstorm (figure 3). On the other hand, during the substorm event of 12-13 August 2000 (figure 2) which was completely triggered by IMF By component, the SML-LT variation was near midnight. Nevertheless, we cannot completely eliminate the role of IMF By during 22nd June 2015 event. The average MLT onset location for IMF By discussed in Ostgaard et al. 2011, is an average and the variance around that average could be substantial. In view of this, it is also possible that IMF By is also having contribution in addition to pressure pulse at 18:43 UT. Also, the location and strength of the substorm can be influenced by the preconditioning of the magnetosphere due to the effects of the previous substorm's recovery phase. The event of 22nd June 2015 was not isolated and another substorm precedes the substorm at 18:34 UT at around 15:43 UT. Hence, it is possible that the shift in substorm onset MLT location away from midnight at 18:43 UT is a combined effect of multiple factors, one of which is pressure pulse.

Shock impact angle can also influence the intensity and delay-time of particle precipitation during substorms (Oliveira et al., 2021). The impact angle obtained from Oliveira et al. (2018), was ~174° on 22nd June 2015 and ~172° on 05th April 2010. This means that the shock on both these days were nearly frontal. According to Oliveira et al., 2021, during frontal shocks, the substorm onsets are centered near the mid-night sector and the 05th April 2010 event is in accordance with that. For 22nd June 2015 event, SMU index was highly enhanced in the afternoon sector and the SMR-LT (SuperMAG ring current index) increased nearly simultaneously at all local time sectors within 2-3 minutes. Oliveira et al., 2021, concludes that these are the signatures of head-on or Nearly Frontal Shock (NFS), hence, these observations are consistent with the findings of this paper. However, for the same event (i.e., 22nd June 2015), SME-LT and SML-LT indices are extremely asymmetric, both being most intense in the morning sector, which is not consistent with Oliveira et al. (2021). Thus, the morning centered SML-LT index, which is one of the key indices of our paper may not be explained using impact angle contribution. Also, depending upon the impact angle the onset could be delayed, but it would still be in the near midnight sector. Impact angle do not relate to the shift in the location of substorm onset or particle injection to dawn-dusk MLTs. Hence, we may conclude that the observations on 22nd June 2015 substorm cannot be explained without considering the effect of pressure pulse.

4.5. Conclusion

Substorms are more general phenomena than long being used descriptions of night side injection and precipitation. The local time sector and the behavior of precipitating particles cannot

be limited to a single mechanism. If intense enough, pressure pulse can sometimes play a major role in triggering a substorm away from midnight. The scenario of substorm onset is simple when the southward component of IMF is present prior to the onset or when just a pressure pulse coincides with the onset. It may be a complex task to understand the behavior of substorm when both the triggering agents are present. For cases where a substorm has its onset and expansion from a local time sector away from midnight, either a large IMF By component or a pressure pulse could be responsible. The process via which a pressure pulse can inject solar wind particles inside the magnetosphere is viscous interaction. Since particle injection via viscous interaction due to KH instability is dawn/dusk favorable (Axford and Hines, 1961), these time sectors become the most probable region for particle injection from the magnetosphere. When the pressure pulse is not strong enough to inject the solar wind particle from the flanks, the particles will follow the field line and precipitate from the night side via magnetic reconnection. Since, the onset locations are also influenced by large IMF By components, it is important to select isolated substorm events having small IMF Bz and By components and a coinciding pressure pulse at the time of onset. For assigning cutoff values to the triggering agents, viz. IMF and pressure pulse, a statistical analysis of such events is required.

Chapter 5

Cosmic Noise Absorption due to Solar Flare

5.1. Introduction

The D-region electron density enhancement at high latitude is primarily due to energetic particle precipitation during substorms and polar cap absorption (PCA) events. Strong PCA events are observed when high-energy (>10 MeV) protons from the Sun impact the Earth's atmosphere in the polar regions causing increased ionization of the D-region (Bailey, 1964; Hargreaves et al., 1987; Bland et al., 2018). The solar proton events (SPE) that eventually lead to PCAs are associated with the solar flare activities originating from the surface of the Sun (Bland et al., 2018). During SPE, high energetic protons get direct access into the Earth's atmosphere at high latitudes and can reach D-region ionosphere, thereby, enhancing the ionization at those altitudes.

Solar flares are also responsible for the emission of ultraviolet and soft X-rays that can enhance the ionization in the D-region ionosphere over the entire solar illuminated part. During the daytime, the attenuation in radio waves is mostly due to photoionization caused by solar flares (Bhonsle 1960; Brodrick et al., 2005; Bland et al., 2018). This may lead to a corresponding increase in the absorption of cosmic radio noise and are called solar flare associated CNA or SCNA (P. Stauning, 1994; Ogunmodimu et al., 2018). SCNA usually lasts for the duration of solar flare events and the observed magnitude is usually less compared to the CNA observed during solar energetic particle precipitation (P. Stauning, 1996; Longden et al., 2007).

In this chapter, we discuss the phenomena of SCNA and PCA at high latitudes, associated with strong solar flare events in detail

5.2 Solar Flare Effects at High Latitudes

Studies have shown the latitudinal and local time dependence of SITEC (sudden increase of total electron content) at high latitude during a solar flare event (Tsugawa et al., 2006). The TEC observation is basically used to study the F-region ionospheric disturbances and does not give much information about the dynamics of the D-region ionosphere. The X-ray radiation coming from the solar flares, however, penetrates deeper into the atmosphere and ionizes the D-region. Hence, we focus to study the D-region response to solar-flare events at high latitudes. The earlier reports, which discuss the effects of solar flares in the D-region ionosphere have been mostly limited to the low and mid latitudes (Bhonsle, 1960; Contreira et al., 2005; Mitra & Shain, 1953; Quan et al., 2021; Shain & Mitrat, 1954; A. K. Singh et al., 2014b). These reports have shown the correlation between solar-flare intensity and D-region response in terms of SCNA, radio signal fading events, reflection height and electron density variation, by using various instruments such as Riometer, VLF receivers and MF radar. There are very limited reports on SCNA at high latitude and not much is known about the characteristics and factors they depend upon. Mainly, the reported events that have discussed the dayside CNA at high latitudes are a result of solar proton events (SPE) leading to PCAs, ionospheric plasma drift during substorms, or particles falling into the loss cone during gradient and curvature drift (DCNA) (Ansari, 1964; Behera et al., 2016b; Matthews et al., 1988; Newell & Meng, 1992; Østgaard et al., 1999; Rogers et al., 2016).

Understanding the effects of solar flare radiations at high latitude becomes more complicated due to the additional ionization processes related to particle precipitations with various sources. Ionosphere at the polar cap regions is ionized by the direct access of solar wind particles precipitating from the cusp region. At auroral regions, high energy particles precipitate along the magnetic field lines eventually producing optical auroras in the ionosphere and CNA in the D-region. It is difficult to separate the magnitude of disturbance caused by different processes if they occur simultaneously. Hence, in this chapter we have focused on the solar flare events that occurred without the simultaneous presence of substorms. We selected two near conjugate (geographic) stations for our study, Maitri (Geographic: 70.75°S, 11.75°E; Geomagnetic: 63.25°S, 53.96°E) and Abisko (Geographic: 68.4°N, 18.9°E; Geomagnetic: 65.55°N, 100.1°E). Although these two stations are near conjugate geographically, the Maitri station falls in the sub-auroral and Abisko station lay in the auroral regions geomagnetically.

The observations of the SCNA events as detected from Maitri and Abisko are presented in section 5.2.1. Section 5.2.2 provides a summary and discussion of our results.

5.2.1 Observations

We have analyzed the CNA response to solar flares at Maitri and Abisko for the year 2014, which was the year of solar maxima of the solar cycle 24, having the maximum number of solar flares observed. There were in total 1776 C-Class Flares, 207 M-Class Flares and 16 X-Class Flares in the year 2014 (https://www.spaceweatherlive.com/). Out of all these, the events for our study were shortlisted on the basis of their time of occurrence. The time window that was selected for the occurrence of a flare was from 07:00 UT to 15:00 UT. This was because the two stations under study were at LT=UT+00:44 (Maitri) and LT=UT+01:16 (Abisko) and the observations had to lie during the solar illuminated period of the day for the two stations (~ 08:00 LT to ~16:00 LT). Since these stations lie in two different hemispheres, either of them would always fall in sun-lit hours, even at different seasons of the year. We also concentrated our analysis only on the M class and X class flares because below these classes no SCNA is observed at high latitudes (Ogunmodimu et al., 2018). There were in total 37 M-class flares out of 207 M-class flares and 6 X-class flares out of 16 X-class flares that occurred in our desired time window (7-15 UT). Out of the six X-class flares, three were during northern summer and three during northern winter, ensuring equal distribution of intense flare events during the year for our study.

I. Maitri Station CNA analysis

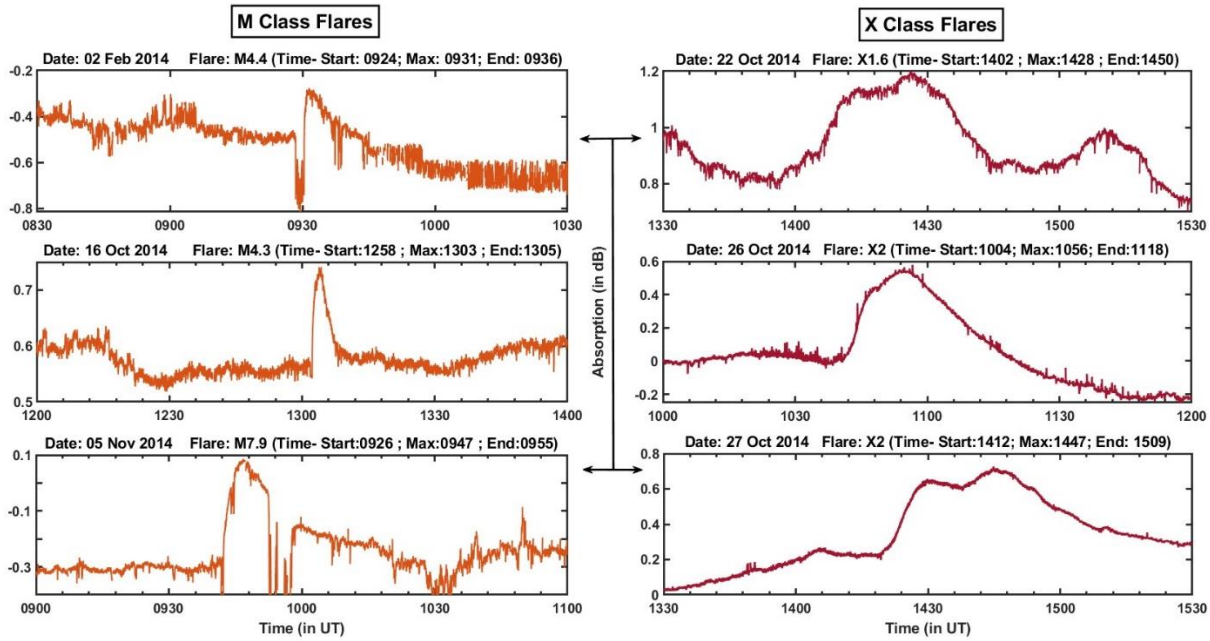

Figure 5. 1 CNA curves of M class (left) and X class flares (right) for Maitri station. X-axis has time in UT and Y-axis has absorption values in dB. The time, class and duration of each event is mentioned on the top of each panel.

Figure 5.1 shows the CNA observations of Maitri Station for M and X class flare events. The CNA curves have been plotted by using the method discussed in the previous section. In each plot, x-axis shows Time in UT and y-axis shows CNA in dB. The left column illustrates the CNA curves of three M-class flare event occurring on 02nd February 2014 (M4.4 class), 16th October 2014 (M4.3 class) and 05th November 2014 (M7.9 class). The start and end time of each flare event is mentioned on the top of each plot. The values of absorption for the three M-Class flares were 0.2 dB (for M4.4 class flare), 0.2 dB (for M 4.3 class flare) and 0.4 dB (for M7.9 class flare) for the three days respectively; and the observed CNAs lasted for the duration of flare event. Similarly, the right column illustrates the CNA curves observed at Maitri station for the three X-class flares occurring in our specified time window. The observed CNAs were of 0.4 dB (for X1.6 class flare on 22nd October 2014), 0.58 dB (for X2 class flare on 26th October 2014) and 0.5 dB (for X2 class flare on 27th October 2014).

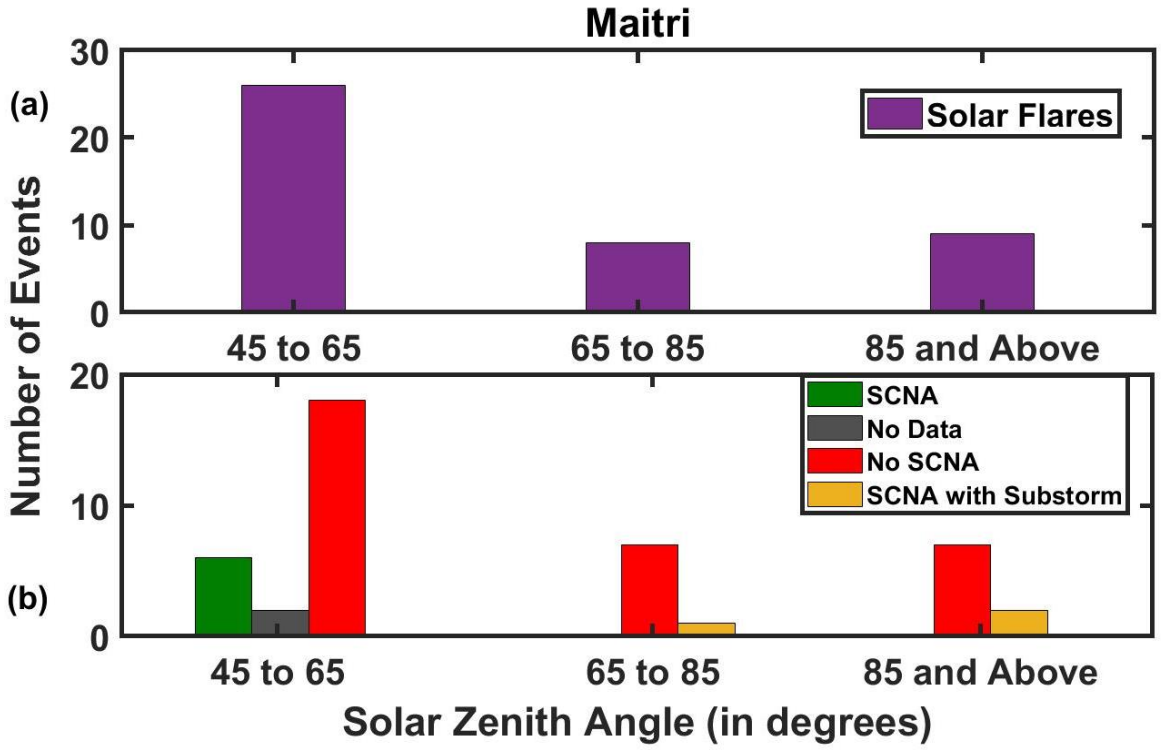

Figure 5. 2 The bar plot (a) shows the total number of M and X class solar flare events for a given solar zenith angle range for Maitri station; and (b) shows the number of (1) events showing SCNA (2) events showing no SCNA (3) flare events coinciding with substorm activity and (4) events whose datasets had gaps at the desired time, as observed at Maitri for a particular solar zenith angle range.

Figure 5.2 (a) and (b) are bar plots showing number of solar flare events and associated SCNA events observed at Maitri station for different solar zenith angle values. The top bar plot shows that the maximum number of the solar flare events among the events studied in this chapter had zenith angle in between 45 degrees and 65 degrees. Out of the forty-three events under study, twenty-six events had solar zenith angle in between 45-65 degrees, eight had solar zenith angle in between 65-85 degrees and nine events have solar zenith angle above 85. Due to the location of Maitri station, none of the events had solar zenith angle less than 45. The lower panel shows that the number of days we observe SCNA out of the total number of solar flare events observed in a particular zenith angle range. All the events that showed a presence of SCNA at Maitri station had zenith angle between 45 to 65 degrees. There were some flare events during which the datasets were not available for the given time range. There were few events where we did observe CNA, but there was a substorm event happening at the same time, which made it difficult to separate the SCNA and the substorm associated CNA. The onset of these CNAs started before the onset of the flare and lasted beyond that. It is possible that during the time window of the flare event, we had a combined absorption due to both the processes, but there is no way via which we could separate the effects. Hence, we excluded those days from our statistics.

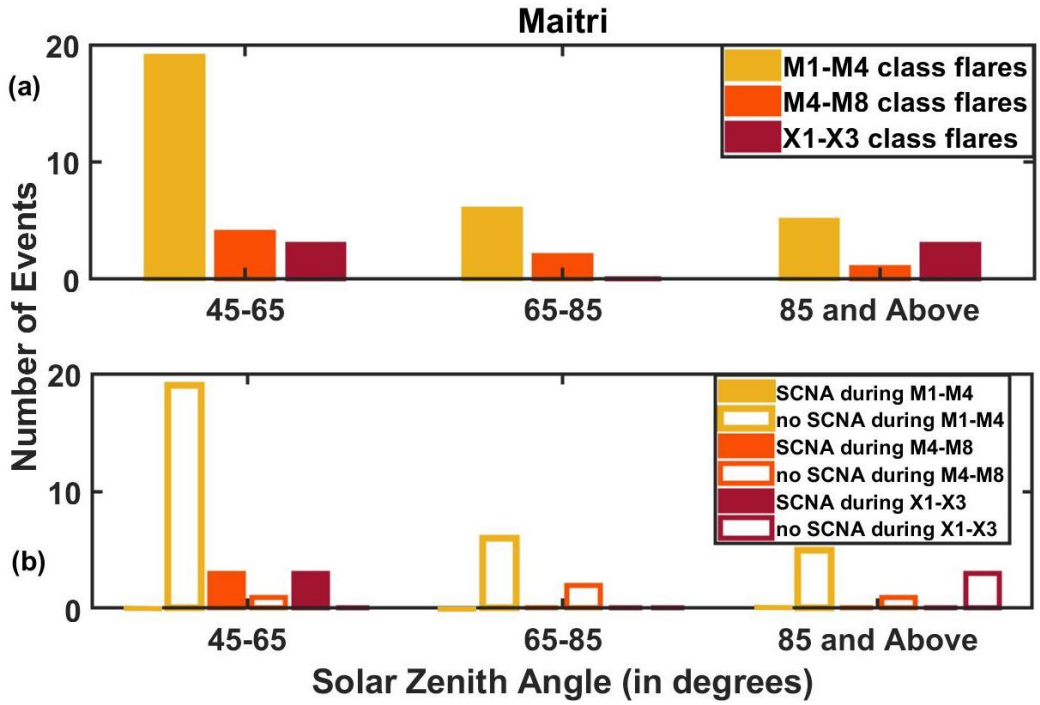

Figure 5. 3 (a) Shows the total number of M1-M4 class flare events, M4-M8 class flare events and X1-X3 class flare events in different solar zenith angle ranges. The corresponding number of events observing SCNA and not observing SCNA for each category is shown in bar plot (b) in the right column.

In figure 5.3, bar plot (a) shows the total number of M1-M4 class flare events, M4-M8 class flare events and X1-X3 class flare events in the three solar zenith angle range. The corresponding number of events observing SCNA and not observing SCNA for each category is shown in lower bar plot of figure 5.3.(b). It also shows that all the six solar flare events that observed SCNA at Maitri in the solar zenith angle range 45°-65° (figure 5.2 (b)) were from M4-M8 class and X1-X3 class. The events that did not observe SCNA in 45°-65° SZA range were associated with a lower intensity flare i.e., M1-M4 class. Hence, below M4 class no absorption can be seen at Maitri location even for low solar zenith angle events. One event that did not show SCNA in M4-M8 class for 45°-65° SZA range was because there was no Riometer dataset present for that day.

II. Abisko station CNA analysis

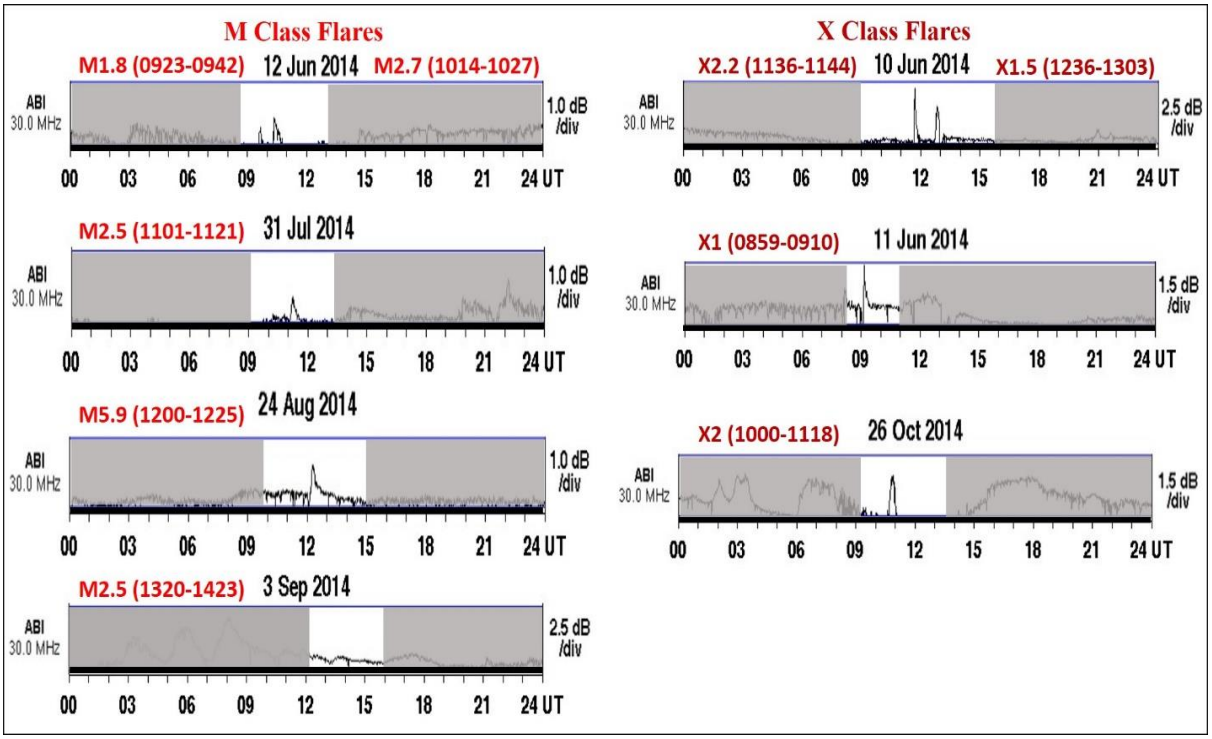

Figure 5. 4 CNA curves of M class (left) and X class flares (right) for Abisko station. X-axis has time in UT and y-axis has absorption values in dB. The time, class and duration of each event is mentioned on the top of each panel.

Figure 5.4 shows the Abisko station's CNA plots, each associated with five M-Class flares and four X-class flares respectively. These flare events happened during the desired time

window in the year 2014 and showed absorption at Abisko station. The plots were obtained from the official website of Sodankylä Geophysical Observatory (https://www.sgo.fi/Data/Riometer/rioData.php). The left column shows CNA plots of M-class flares and the right panel shows the CNA plots of X-class flares. The time and duration of each flare event is mentioned on top of each plot. The M1.8 class flare on 12th June 2014 occurring at 09:23 UT showed 0.25 dB absorption; M2.7 class flare on 12th June 2014 occurring at 10:14 UT showed 0.4 dB absorption; M2.5 class flare on 31st July 2014 showed 0.4 dB absorption; M5.9 class flare on 24th Aug 2014 occurring at 12 UT showed 0.7 dB absorption; and M2.5 class flare on 03rd Sep 2014 occurring at 1320 UT showed 0.4 dB absorption. The right panel on the other hand shows CNA plots of four X-class flare events. The X2.2 class flare on 10th June 2014 at 11:36 UT showed absorption of 2 dB; X1.5 on 10th June 2014 showed 1.8 dB absorption at 12:36 UT; X1 class flare on 11th June at 08:59 UT shows 1 dB absorption; X2 class flare on 26th Oct 2014 showed 1 dB absorption at 10 UT.

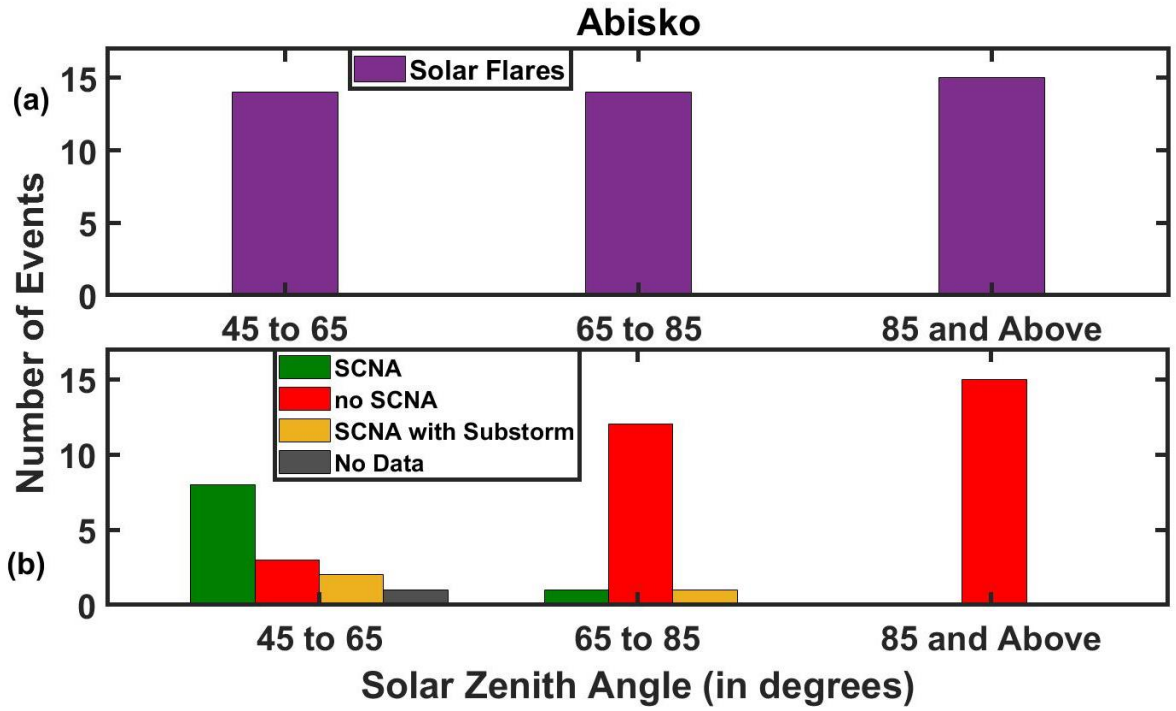

Figure 5. 5 In this figure, the top bar plot shows the total number of M and X class solar flare events for a given solar zenith angle range for Abisko station; and the bottom bar plot shows the number of (1) events showing CNA (2) events showing no CNA (3) flare events coinciding with substorm activity and (4) events whose datasets had gaps at the desired time, as observed at Abisko for a particular solar zenith angle range. (b) Shows the total number of M1-M4 class flare events, M4-M8 class flare events and X1-X3 class flare events in different solar zenith angle ranges.

Fig 5.5. (a) and (b) show the bar plots of number of solar flare events and CNA events observed at Abisko station for different solar zenith angle values. The top bar plot shows that there were fourteen out of total forty-three M and X class solar flare events present in the desired time window having solar zenith angle in between 45 to 65 degrees. Fourteen events also had zenith angle between 65-85 degrees and fifteen had solar zenith angles above 85 degrees. Out of the fourteen events having solar zenith angle between 45-65 degrees, Abisko station observed CNA for eight events. Three events did not show CNA, two events had coinciding substorm associated CNA and one event had data gap, out of these fourteen events. Out of the next fourteen events having solar zenith angle between 65-85 degrees, only one event showed absorption at Abisko and one event had coinciding substorm CNA. None of the fifteen events that had solar zenith angle above 85 degrees showed absorption at Abisko station. This plot shows a clear dependency of absorption with the solar zenith angle. Although, there are almost same number of events present at all the three solar zenith angle range, the maximum CNA events are present during 45°-65° range.

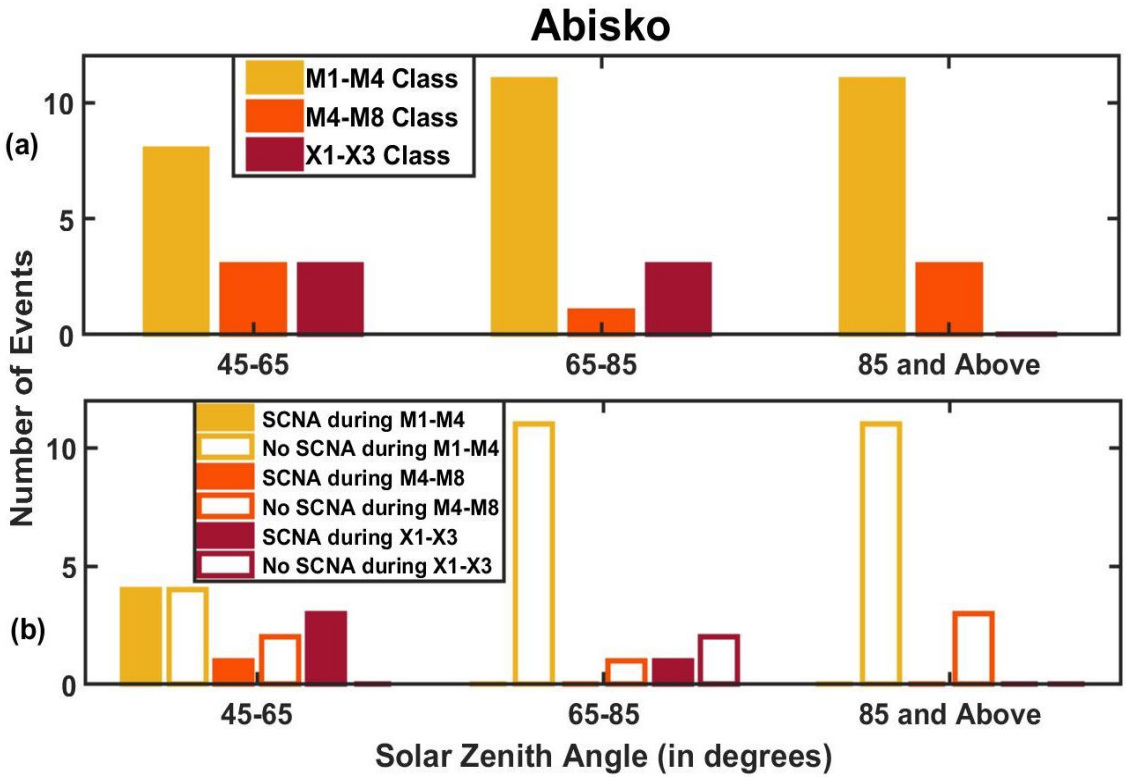

Figure 5. 6 shows the total number of M1-M4 class flare events, M4-M8 class flare events and X1-X3 class flare events at Abisko in the three solar zenith angle ranges. The corresponding number of events observing SCNA and not observing SCNA for each category is shown in lower bar plot, fig. 5.6 (b). Abisko shows SCNA in all solar flare intensity range having SZA 45°-65°. In the 65°-85° SZA range only one X-class flare shows associated SCNA.

5.2.2 Discussion

We observed the Cosmic Noise Absorption (CNA) response of forty-three M and X class solar flare events for the year 2014 occurring in between 07:00 UT and 15:00 UT for two near conjugate stations, Maitri and Abisko. Table 5.1 summarizes the class of flares, date of occurrence, time duration of flare event, solar zenith angle and CNA observed at Maitri and Abisko of all forty-three events under study.

Table 5. 1 The class of flare, date and time of occurrence, solar zenith angle and CNA observed at Maitri and Abisko stations of all the 43 solar flare events that occurred in the year 2014 from 7:00 to 15:00 UT.

Sl No	**Flare Class**	**Date**	**Time (in UT) (Start; Max; End)**	**Maitri (GLat= 70S; GLong= 11E) (Mlat= 63S; MLong= 54 E)**	**CNA (Maitri)**	**CNA (Abisko)**	**Abisko (Glat= 68 N; Glong= 18.9 E) (MLat= 65.42 N; MLong =101 E)**
1	M1.3	4/1/14	1016; 1025; 1041	51.4	0	0	92.6
2	M7.2	7/1/14	1007; 1013; 1037	51.9	No data	0	92.7
3	M1.4	28/1/14	1134; 1138; 1141	52.8	0	0	86.6
4	M1.3	28/1/14	1233; 1246; 1250	52.3	0	0	86.9
5	**M4.4**	**2/2/14**	**0924; 0931; 0936**	**60.0**	**0.2**	0	89.2
6	M1.4	4/2/14	0938; 0949; 0958	59.4	0	0	87.7
7	M1.6	14/2/14	1229; 1240; 1245	57.4	0	0	81.6
8	M1.1	14/2/14	1321; 1328; 1339	58.2	0	0	82.9
9	M1.2	16/2/14	0920; 0926; 0929	64.6	0	0	85.0
10	M1.1	24/2/14	1103; 1117; 1142	62.1	0	0	78.1
11	M1.3	24/2/14	1200; 1205; 1210	61.1	0	0	77.8
12	M1.7	11/3/14	1158; 1207;1214	66.8	0	0	72.1
13	M2.5	12/3/14	1055; 1105; 1111	68.4	0	0	72.2
14	M2.1	30/3/14	1148; 1155; 1202	74.4	0	0	64.6
15	M7.3	18/4/14	1231; 1303; 1320	81.7	0	No data	58.9
16	M5.3	8/5/14	0959; 1007; 1018	99.0	Substorm	Substorm	53.7
17	**X2.2**	**10/6/14**	**1136; 1142; 1144**	93.6	0	**2**	**45.4**
18	**X1.5**	**10/6/14**	**1236; 1252; 1303**	93.6	0	**1.8**	**46.1**
19	**X1**	**11/6/14**	**0859; 0906; 0910**	99.0	0	**1**	**51.0**
20	**M1.8**	**12/6/14**	**0923; 0937; 0942**	97.6	0	**0.25**	**49.8**
21	**M2.7**	**12/6/14**	**1014; 1021; 1027**	95.7	0	**0.4**	**47.9**
22	M1.1	15/6/14	1110; 1139; 1150	93.9	0	0	45.1
23	M1.4	01/7/14	1105; 1123; 1159	94.0	0	0	45.5
24	**M2.5**	**31/7/14**	**1101; 1114; 1121**	89.4	0	**0.4**	**50.5**
25	M3.4	21/8/14	1319; 1331; 1342	83.4	Substorm	Substorm	58.8

26	**M5.9**	**24/8/14**	**1200; 1217; 1225**	81.4	0	**0.7**	**57.6**
27	**M2.5**	**3/9/14**	**1320; 1354; 1423**	79.6	0	**0.4**	**62.9**
28	**M4.3**	**16/10/14**	**1258; 1303; 1305**	**62.0**	**0.2**	0	78.9
29	M3.9	20/10/14	0900; 0911; 0920	65.0	Substorm	Substorm	83.0
30	M1.2	21/10/14	1335; 1338; 1340	61.5	0	0	82.4
31	**X1.6**	**22/10/14**	**1402; 1428; 1450**	**62.6**	**0.4**	0	83.9
32	M1.1	23/10/14	0944; 0950; 0956	62.4	0	0	81.7
33	**X2**	**26/10/14**	**1004; 1056; 1118**	**60.4**	**0.58**	**1**	**82.3**
34	**X2**	**27/10/14**	**1412; 1447; 1509**	**60.9**	**0.5**	0	85.6
35	M1.6	28/10/14	1354; 1406; 1423	60.4	0	0	86.3
36	M1.2	29/10/14	0954; 1001; 1006	59.5	0	0	83.2
37	M2.2	3/11/14	1123; 1153; 1217	55.3	0	0	83.8
38	**M7.9**	**5/11/14**	**0926; 0947; 0955**	**59.4**	**0.4**	0	86.9
39	M1	7/11/14	1013; 1022; 1030	56.1	0	0	85.6
40	M3.3	15/11/14	1140; 1203; 1210	51.9	no data	0	87.1
41	M1.5	05/12/14	1133; 1225; 1247	48.0	0	0	91.2
42	M1.3	19/12/14	0931; 0944; 0954	51.7	0	0	94.3
43	M1	21/12/14	1124; 1217; 1257	46.9	0	0	92.1

Out of the forty-three events studied, Maitri station showed CNA for six events. These were 3 M-class and 3 X-class flare events. Abisko station on the other hand showed CNA for nine events, out of which five were M-class and four were X-class. There is a clear asymmetry in the flare associated CNA observations for these two locations, with Abisko showing more absorption than Maitri.

Table 5.1 shows the solar zenith angle (SZA) range within which one can expect SCNA at the two locations. For Maitri station we do not observe any SCNA for SZA higher than 65 degrees, as shown in figure 5.2. For Abisko, although there are almost same number of events distributed in all the SZA ranges, the maximum SCNA events were observed in the SZA range 45-65 degrees, as shown in fig 5.5. From table 5.1 we also see that the highest value of SZA for M-Class flare that shows CNA was 62° for Maitri and 62.9° for Abisko. Hence, in general, the cutoff value of SZA for SCNA associated with M-class flare at high latitude could be near 62°. For X-class the highest SZA showing CNA was 62.6° for Maitri and 82.3° for Abisko. This huge difference in the cutoff SZA of X-class for the two stations can be because there was no X-class flare with SZA between 62.6° to 93.6° at Maitri. Hence, it is difficult to say whether Maitri might have shown CNA for SZA near 82° or not.

Figure 5.7 shows the intensity of absorption observed at Maitri and Abisko for different classes of flare events along with the solar zenith angle (SZA). The purple curves in the figure shows the class of flare vs CNA plot for Maitri station and the orange curves for Abisko station. For both Maitri and Abisko the value of SCNA increases with an increase in the class of flare.

Which means, the SCNA directly depends upon the intensity of flare. In general, the intensity of SCNA observed at Abisko was more than Maitri for similar class of flare and SZA. There appears to be a hemispheric asymmetry in the observation of SCNA at high latitudes. For the M-class flares, no absorption was observed below M4.3 class at Maitri and below M1.8 class at Abisko station. Maitri and Abisko also did not show absorption for some M-class flares higher than M4.3 and M1.8 (respectively) because the SZA were higher than the cutoff SZA for these two locations. Hence, the intensity of flare and SZA cumulatively determines the occurrence of SCNA. For X-class flares, both the stations show higher absorption than comparatively the M-class flares. Maitri station shows absorption for the three X-class flares occurring during northern winter (October, 2014). On the other hand, Abisko shows absorption for four X-class flare, three occurring during northern summer (June, 2014) and one during northern winter (October, 2014). The three X-class flares that occurred during the northern winter (October, 2014) had SZA almost same at Abisko (as shown in Table 5.1) and were also of similar intensity. The Kp were also nearly same at the time of solar flares on these three days. However, only one of them showed absorption at Abisko, which occurred during local noon.

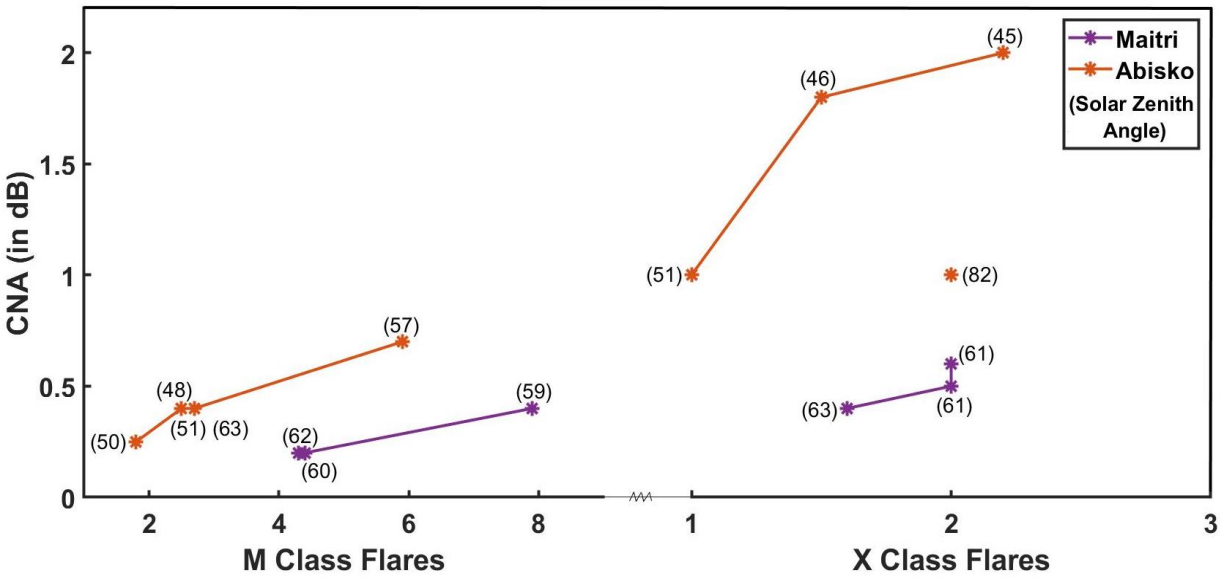

Figure 5. 7 The variation of CNA observed with an increase in flare class at Maitri and Abisko stations.

From figure 5.7, it can be seen that the two X-class flares (X2.2 on 10th June, 2014 and X2 on 26th October, 2014, shown in Table 5.1) showed a major difference in the absorption at Abisko. The X2.2 class flare showed an absorption of 2 dB, while the X2 class flare showed an

absorption of only 1 dB. This difference was because of the dependency of SCNA intensity to the SZA. It was 45 degrees for X2.2 class and 82 degrees for X2 class flare event. Hence, this difference can be expected. However, the noticeable difference is between the observations of Abisko and Maitri stations for X2 class flare event occurring on 26th October, 2014. Despite the intensity of the solar flare events being same, Maitri showed less absorption than Abisko. Even though the SZA was higher at Abisko (SZA 82 degrees on 26th October, 2014), it showed more absorption than Maitri (SZA 61 degrees). This hemispheric asymmetry can be attributed to the location of the two stations. Abisko lies in the auroral region, whereas, Maitri lies in the sub-auroral region. Polar cap absorption, if intense enough, can sometimes reach the auroral latitudes and enhances the background ionospheric condition for SCNA. There were several intense solar flare events present in the month of October, 2014. Following these flares, the polar cap of the Earth is bombarded by energetic particles of solar origin. These particles ionize the lower regions of the ionosphere and can lead to intense absorption lasting for a period of several days. These are called Polar Cap Absorption (PCA) events which occur only at geomagnetic latitudes greater than 62 degrees (Bailey, 1964; Hargreaves et al., 1987; Rose & Ziauddin, 1962). It is possible that the effect of PCA reached Abisko and not Maitri. Additionally, previous substorm events can also alter the ionospheric conditions at auroral region. Hence, different ionospheric background conditions at the two locations might have led to the different intensity of SCNA, resulting into the hemispheric asymmetry observed.

5.3. Polar Cap Absorption Event (PCA)

The term "polar cap absorption" (or PCA) refers to the intense radio wave absorption at high magnetic latitudes (60° to 90° magnetic latitude) that occurs when there is an increase in the flux of high-energy (>10 MeV) protons from the Sun. The polar regions of Earth's atmosphere are bombarded by these solar energetic protons, increasing the D region's ionization (Bailey, 1964). PCA occurrences can continue for several days, hence, they have significant consequences for high-latitude HF communications (Bland et al., 2018). The disruption of radio communications can lead to Polar blackout events lasting from hours to days.

If a location has come under the effect of prolonged PCA, a simultaneous substorm activity, and also SCNA, it is difficult to conclude the magnitude of absorption due to either one of them. In other words, when more than one process led to absorption at high latitudes, it becomes impossible to separate the effect of all the processes occurring simultaneously. The

expected observations and extent of ionization will have a superimposed effect. In this section, we will show how a prolonged background PCA that occurred during the month of September, 2017, affected the observations of SCNA.

Major solar proton events (SPEs) occurred in September, 2017, that led to long duration PCA events in the polar ionosphere. These events, reported by Bland et al. (2018), were identified using a standard definition based on proton flux measurements from NOAA-GOES spacecraft. In this section we will be discussing about two intense solar flare associated SCNA events that occurred during one of the major SPE event in the month of September,2017.

5.3.1 Background Enhancement of Ionospheric Ionization during PCA

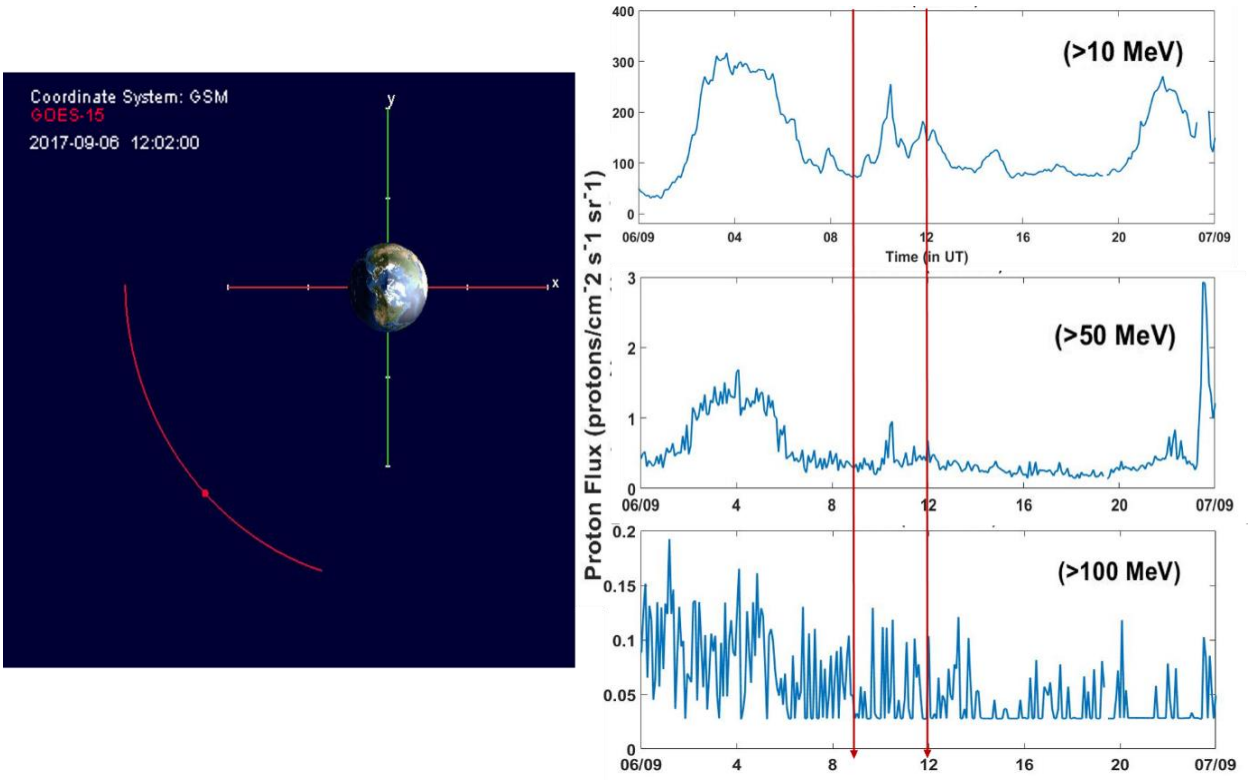

Figure 5. 8 The orbit of Goes-15 is shown in GSM coordinate system (red) from 09:00 UT to 14:00 UT on 06th September, 2017. The red dot on the orbit indicates the Goes-15 position at 12:02 PM, as it moves from the midnight to dawn sector. The left image shows the proton flux as observed from GOES-15 in three energy range, >10 MeV, >50 MeV and >100 MeV. The two red vertical lines indicates the time of two X-class solar flare activity on this day.

Since PCAs are long duration events, it leads to an overall background enhancement in the ionospheric absorption. If a location comes under the effect more than one phenomenon occurring simultaneously, any short-lived absorption enhancement will be a result of the superimposed effect on the already existing PCA. The SPE event that occurred on 06th September 2017, as detected by the GOES 15 instrument, is shown in figure 5.8. The SPE event and the associated PCA event on this day is important because two very intense X-class solar flares also occurred on this day.

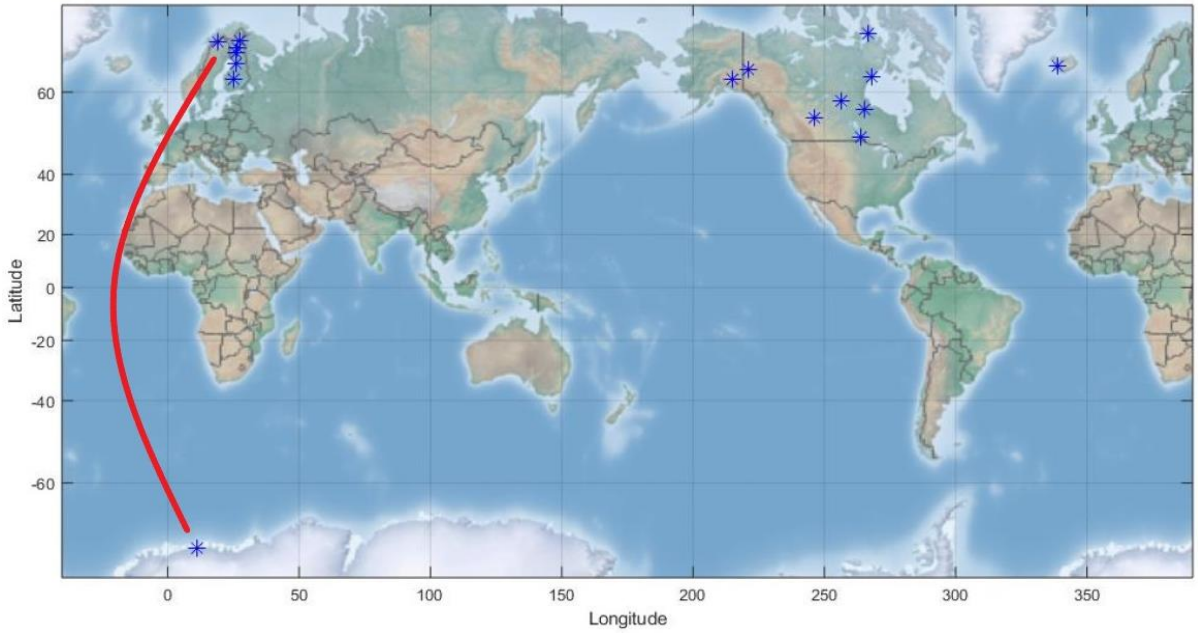

Figure 5. 9 Location of riometer stations under study (marked by blue stars) in the world map. The red curve connects two near conjugate stations: - Maitri (Geographic: 70.75°S, 11.75°E) and Abisko (Geographic: 68.4°N, 18.9°E)

PCAs occur during solar proton events (SPEs) that arise during strong solar flare eruptions. Solar flare also releases intense electromagnetic radiation towards the Earth, with emissions being virtually across the entire electromagnetic spectrum. During the flare activity, enhancement in the ionization of D-region and lower E-region ionosphere takes place over the entire solar illuminated part of the Earth due to the emitted solar EUV and soft X-ray radiation. Such enhancements can lead to the absorption of radio waves passing through the medium. These absorption phenomena generally last for the duration of the associated flare event. Two X-class solar flares was observed on 06th September 2017. These events occurred during near solar

equinox; hence, symmetric spread of radiation is expected across the hemisphere. Figure 5.9 shows the location of riometer stations whose datasets are used to check the SCNA and background PCA events on these days. In figure 5.10, the CNA curves on 06th September, 2017 of various high latitude stations are plotted. The time and duration of the two flare events that occurred on this day are marked by red box in the plot.

The table 5.2 below lists observed CNA and solar zenith angle of the stations whose absorption curves are shown in figure 5.10. Among all the Finland stations, only Abisko is taken into account as all the stations show same values of CNA and solar zenith angle.

Table 5. 2 High latitude riometer stations along with the solar zenith angle and CNA observed on 06th September, 2017

Name of the high latitude station	X2.2 Class Flare on 06th Sep 2017		X9.3 Class Flare on 06th Sep 2017	
	Solar Zenith Angle	CNA observed	Solar Zenith Angle	CNA observed
Maitri (GLat: -70.4; MLat: -63.2)	80	0.3 dB	77	1 dB
Abisko (GLat: 68.4; MLat: 65.4)	68	1.5 dB	63	2.5 dB
Pin (GLat: 50.2; MLat: 60.2)	56	0	43	0.2 dB
Ran (GLat: 62.8; MLat: 66.7)	64	0	56	0.1 dB
Hus (GLat: 64.7; MLat: 65.2)	65	0.8 dB	57	4 dB
Tal (GLat: 69.5; MLat: 78.6)	68	0	63	0.1 dB

It is observed from figure 5.10 that the effect of X2.2 class flare, that occurred around 09:00 UT, is very less at high latitudes, with some stations showing no absorption at all. Whereas, the X9.3 class flare occurring around 12:00 UT showed intense absorption at all the stations, much more compared to X2.2 class flare. This can be due to multiple reasons as listed below:

1. Solar flare intensity
2. Solar Zenith angle
3. Background condition

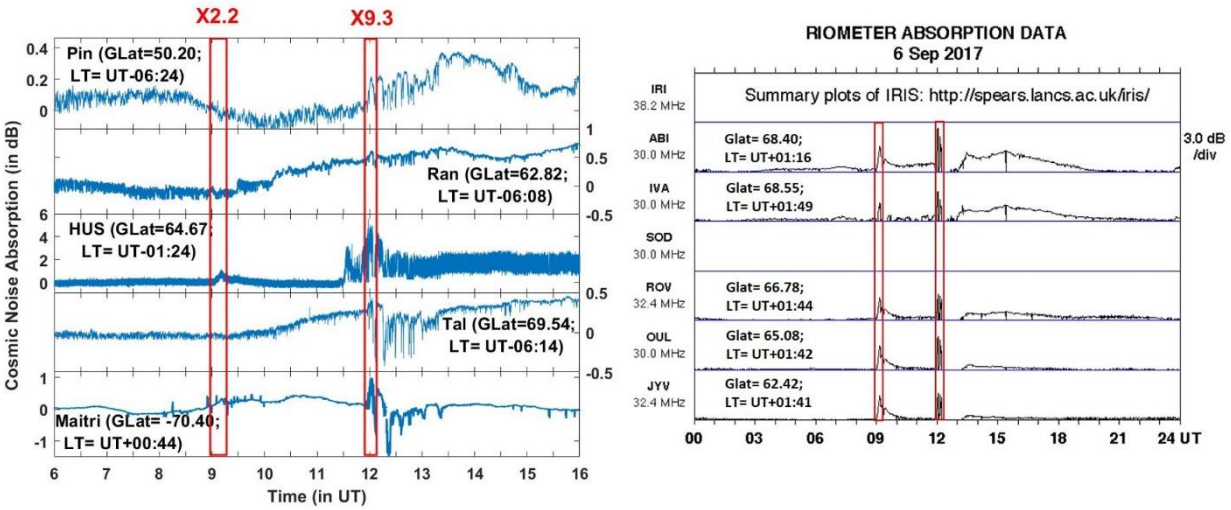

Figure 5. 10 The CNA curves on 06th September, 2017, of various high latitude stations are plotted along with the location and local times of the stations from 06:00 UT to 16:00 UT. In the left panel CNA curves of Pin, Ran, Hus, Tal and Maitri are shown. The absorption plot of Finland stations in the right panel were obtained the official website of Sodankyla Geophysical observatory. The red boxes in both the panels indicate the time and duration of two X-class flare events on 06th September, 2017.

The flare intensity in the two cases is definitely different, one being X2.2 and the other being X9.3, which can lead to a difference in the level of ionization with X9.3 being more. However, it is not expected that X2.2 would show such less or absolutely no absorption in the sunlit side of the Earth. Hence, the flare intensity is not the factor that can completely explain the observed difference in the CAN intensities for the two cases. The second factor, being solar zenith angle, is also of much relevance and it is expected that locations with less solar zenith angle will show more absorption. This is true for the two near conjugate stations Maitri and Abisko, where Abisko shows more absorption that Maitri since solar zenith angle is less in both the cases for Abisko (table 5.2). However, for station like Pin, Rab, Hus and Tal, the solar zenith angle does not explain the observed CNA, especially in the X2.2 class flare case. These stations have much less solar zenith angles than Maitri and Abisko, still the observed absorption is either less or zero. The third factor, being background PCA, can be important in this case. We observe from figure 5.8. that during the first flare event there was no enhancement in background proton flux as observed from GOES-15. On the other hand, during the second solar flare event the proton flux had an already enhanced value. This suggests that the ongoing PCA event has enhanced the background ionospheric condition that is reflected in the CNA curves during the second solar flare event. At the time of the first flare event, the background proton flux was suddenly decreased

after being enhanced for quiet sometime. The effect of the decrement in the background PCA was so high that it overpowered the enhancement due to solar radiation, and hence no or very less SCNA was observed. This was not the case during the second flare activity, since both the proton flux and solar radiation led to the enhancement in the absorption values.

5.4. Conclusion

The D-region response to the enhanced solar X-ray radiation associated with intense solar flare events in the year 2014 is studied in this chapter, using CNA observations at near conjugate locations: Maitri in the southern hemisphere and Abisko in the northern hemisphere. Total 43 solar flare events (37 M-class and 6 X-class), which occurred during sunlit hours at these two stations are investigated. It is observed that the SCNA amplitude depends upon the intensity of solar flare for both M and X class flares and on the solar zenith angle. The SZA plays crucial role and it is found that the upper cutoff of SZA to observe the SCNA signature for M-class flares is ~62°. The upper cutoff of SZA for the X-class flare appears to be different at Maitri (63°) and Abisko (82.3°), which could be merely due to the non-availability of any X-class flare with 63° < SZA < 90° at Maitri. For similar class of flare, there was a significant difference in the SCNA intensity observed at Abisko, which is because of the difference in SZA values. The higher SZA (82.3° for X2 class) showed less absorption (1dB) than the lower one (SZA 45.6° for X2.2 class, absorption 2 dB). Apart from the intensity of flare and the solar zenith angle, the latitudinal position also seems to play a role in the SCNA effects. For the same X2 class flare event, Abisko showed more absorption than Maitri, though the SZA was higher at Abisko than that at Maitri. In general, for all the flare events, Abisko showed more absorption than Maitri. We attribute this asymmetry to the location of these stations- Abisko is located in the auroral region and Maitri is sub-auroral station. Ionospheric background condition due to previous processes like PCA and substorms, may have contributions to the SCNA even though the events are isolated.

In addition, the background PCA can highly perturb the intensity of absorption during SCNA. The resulted may either increase enormously or decrease tremendously, depending upon the phase of the PCA. If the time of flare activity coincides with the declining phase of the PCA then the resultant SCNA is decreased and when coinciding with the enhanced background condition it will be increased.

Chapter 6

Conclusions and Scope for Future Research

6.1. Conclusions

We present an elaborated study of peculiar space weather events that gives an insight of how diverse the mechanisms involved in the solar wind-magnetosphere-ionosphere coupled system are. With the recent advancement in technology, there is certainly a better understanding than before of how the energy exchange in the Sun-Earth system takes place. However, there are still numerous complexities that require investigation and comprehension. Our aim of exploring the high-latitude dynamics during disturbed geomagnetic conditions is because of the fact that these regions show direct imprints of space weather events occurring at larger distances in the Earth's environment. High-latitude regions are significantly exposed to the energy deposition processes, like, geomagnetic substorms, solar flares and solar proton events, as compared to mid and low latitudes that are perfectly shielded by the Earth's magnetic field. The integrated measurements made at high latitude regions, right from the ground to ionospheric heights to the magnetopause boundary, are useful in identifying the source mechanisms and understanding its evolution that begins at distant solar-terrestrial environment.

The study of geomagnetic substorms forms a very essential part of the present thesis. This is because of the fact that substorms are the most frequent phenomena that occur at high-latitudes as a result of the magnetosphere-ionosphere coupling. The understanding of substorm related mechanisms in the magnetosphere started from the observations made on the ground level, and theories then progressed accordingly. It was only after Akasofu observed and explained the features of auroras in the midnight sector (S. I. Akasofu, 1964) and coined the term 'substorm' for it, that later led to the inclusion of magnetic reconnection theory as the triggering mechanism of these substorms by Tsurutani and Meng (Tsurutani & Meng, 1972).

Theories then progressed and the midnight-sector particle injection and precipitation processes were explained by the (i) loading-unloading mechanisms happening at distant neutral line (DNL) and near-Earth neutral line (NENL), (ii) substorm current wedge formation and (iii) dipolarization of the Earth's magnetic field. These theories explain the onset and expansion of substorms happening from the midnight sector and the observations made at ground level that intensifies and expands from the midnight. However, in the present thesis we see cases of substorm events where the associated ground observations have its emergence, intensification and expansion from dawn and dusk. Hence, these variation in the substorm associated ground observation will require a modified theory to explain it.

In Chapter 3 of the present thesis, we conducted a multi-instrument analysis of a very strong and unique substorm event that took place on 21st January, 2005. IMF Bz and By was near 0 nT for hours prior to the substorm onset on this day and a pressure pulse of about ~27 nPa coincided with the onset. The most intense aurora, auroral electrojet current and CNA associated with the substorm on this day peaked near the dawn. Simulation results show absence of NENL formation, dipolarization and plasmoid formation at the time of onset, which are necessary for the initiation of the expansion phase during Akasofu-type of substorms. This suggests that the substorm on this day had a different driving mechanism than typical magnetic reconnection. We believe viscous interaction via KH instability to be the possible alternate mechanism because it is dawn-dusk favorable. Now that we know substorms can have more than one onset mechanism, it is important to classify them on the basis of it. Substorm can be categorized based on its triggering agent and onset mechanism as:

- **IMF Bz Induced or Akasofu-type:** These substorms has a southward component of IMF Bz present about ~1.5 hours prior to the substorm onset. The onset of these substorms is always in the midnight sector. The SuperMAG SML-LT index, indicating maximum dip in the geomagnetic H-component, is most intense in the midnight sector.
- **IMF By Induced:** These substorms occur under prolonged northward IMF Bz condition with large IMF |By| component. There can be slight variation in the onset location from the typical midnight sector depending upon the sign of IMF By, but the mechanism is the same as during normal Akasofu-type. Hence, the SML-LT index during these types of substorm also maximizes near midnight.
- **Impulse-Induced:** These substorms has a strong pressure pulse coinciding with the substorm onset, with no contribution of IMF Bz or By in triggering the onset. The

onset of these substorms is not from the midnight, and the SML-LT index maximizes near dawn/morning sector.

In this thesis, we have focused primarily on identifying the various particle precipitation processes during different types of geomagnetic substorms. As previously discussed, the precipitating particles can have various implications like:

- An understanding of their trajectories can help in determining the morphology of various geomagnetic phenomena.
- The precipitating particles causes significant increase in the ionospheric conductivity leading to a total current flow of about 10^6 A at ~100 km altitude that creates the largest ground magnetic disturbances compared to any other current system. This may sometimes lead to the failure of the power grids.
- The ionization and dissociation of atmospheric constituents brought on by the precipitation of highly energetic particles may eventually lead to ozone layer depletion.
- These particles have the capability to damage satellites and spacecraft, as well as interfere with navigation and communication systems.

Hence, a complete understanding of their injection and precipitation mechanisms becomes important. Our study reveals that:

1. All magnetic substorms may not necessarily have the same driving mechanism for injecting energetic particles inside the magnetosphere. If a strong pressure impulse coincides with the time of the substorms onset, injection of particles in these cases are likely to happen via viscous interaction due to Kelvin-Helmholtz instability and not via typical magnetic reconnection process.
2. New entry points of the energetic particles during impulse-induced substorms have been revealed. Observations indicate these entry points to be near the flanks of the magnetosphere. Hence, it is very likely that Kelvin-Helmholtz instability leads to the injection of particles, which is most favorable near the flanks.
3. The particle injection from the flanks of the magnetosphere further leads to their precipitation in the dawn and dusk sectors. This shifts substorm onset location from being in the midnight sector to being centered near dawn and dusk.
4. We have categorized substorms based on its triggering agent and onset mechanism with the help of SuperMAG SML-LT index. The idea of identifying substorms as IMF-Bz

induced, or IMF-By induced or impulse-induced, using the SML-LT index is new and is the contribution of the present thesis. More often it is seen that more than one triggering agent is present to initiate the onset process. Identifying the driving mechanism, thus, becomes challenging. Using SML-LT index for the classification of substorms becomes important in cases when it is difficult to categorize them by simply looking at the interplanetary conditions, and an additional identification is required.

5. Substorms may not always be isolated and often more than one triggering agent is present at or prior to the onset. The next step is to understand which driving mechanism will overpower the other and how will a substorm evolve in cases where multiple triggering agents are present. Based on our analysis, it has been shown that it is the intensity of the triggering agents, i.e., IMF (Bz and By) and pressure pulse, that will determine the likelihood of dominance. If pressure pulse is sufficiently strong to overcome the impact of magnetic reconnection, the substorm will have its onset and expansion from a local time sector away from midnight.

6. Even IMF By can lead to onset locations away from midnight, but the two cases are different in terms of the mechanisms that leads to the onset. IMF By induced substorms follow the magnetic reconnection process and impulse-induced substorms follow the viscous interaction process for the injection of particles. However, the deviation in the onset locations is limited to pre- and post-midnight sectors during IMF By induced substorms and does not reach dawn and dusk.

7. In addition, we have also investigated alternate ionization enhancement processes at high latitudes that are brought about by intense solar flare activities and solar proton events. These include the Polar Cap Absorption (PCA) and solar flare associated Sudden Cosmic Noise Absorption (SCNA) events. Our analysis reveals that magnitude of SCNA directly depends upon the flare intensity and solar zenith angle. In addition, latitudinal position is also an important factor for determining the effects of SCNA. If a station falls in the auroral or polar region, the effects of previously occurred substorm and PCA can alter the background condition. This leads to variations in the actual effects of solar flares. These variations get further amplified if there is an ongoing PCA event coinciding with the time of SCNA. The perturbation in the solar flare effects will then depend upon phase (inclining or declining) of PCA.

6.2. Scope for Future Research

Geomagnetic substorms happen very frequently, with more than one event happening in a single day. Nevertheless, these events are very unique and distinct from each other. In order to categorize them on the basis of either their triggering agents or onset mechanism, it is important to conduct a case-to-case analysis. This will help in determining the number of categories or types of substorms occurring in nature. Thereafter, conducting a statistical analysis of substorm events falling in the same category will lead to a more generalized theory. We intend to do the same in future as an extension of the present research work.

In future, we will attempt to advance the proposed theory of "dominance of triggering agents" by assigning cut-off values to the them. These cut-off values will determine the minimum magnitude required by one to dominate the other. This can be done by conducting a statistical analysis of similar substorm events that have more than one triggering agents present prior to the onset.

We will also be interested to see if we can come up with a method to separate the effects solar proton events and solar flare for any given location based on the (i) intensity of flare, (ii) time of flare activity and (iii) latitudinal position during SCNA and (iv) energy range of the solar energetic protons during PCA.

Bibliography

Akasofu, A. I. (1975). The roles of the north-south component of the interplanetary magnetic field on large-scale auroral dynamics observed by the DMSP satellite. *Planetary and Space Science*, *23*(10), 1349–1354.

Akasofu, S. I. (1964). The Development of the Auroral Substorm. *Planet. Space Sci. , 12*, 273–282.

Akasofu, S. I., Perreault, P. D., Yasuhara, F., & Meng, C. I. (1973). Auroral Substorms and the Interplanetary Magnetic Field. *Journal of Geophysical Research*, *78*(31), 7490–7508. https://doi.org/10.1029/JA078i031p07490

Akasofu, S.-I., Chapman, S., & Meng, C.-I. (1965). The polar electrojet. In *Journal of Atmospheric and Terrestrial Physics* (Vol. 27). Pergamon Press Ltd.

Akasofu, S.-I., & Meng, C.-I. (1969). A study of polar magnetic substorms. *Journal of Geophysical Research*, *74*(1), 293–313. https://doi.org/10.1029/JA074i001p00293

Allen, J. H., & Kroehl, H. W. (1975). Spatial and temporal distributions of magnetic effects of auroral electrojets as derived from AE indices . *Journal of Geophysical Research*, *80*(25), 3667–3677. https://doi.org/10.1029/ja080i025p03667

Andersson, M. E., Verronen, P. T., Marsh, D. R., Seppälä, A., Päivärinta, S. M., Rodger, C. J., Clilverd, M. A., Kalakoski, N., & van de Kamp, M. (2018). Polar Ozone Response to Energetic Particle Precipitation Over Decadal Time Scales: The Role of Medium-Energy Electrons. *Journal of Geophysical Research: Atmospheres*, *123*(1), 607–622. https://doi.org/10.1002/2017JD027605

Ansari, Z. A. (1964). The aurorally associated absorption of cosmic noise at College, Alaska. *Journal of Geophysical Research*, *69*(21), 4493–4513. https://doi.org/10.1029/jz069i021p04493

Axford W. I., & Hines, C. O. (2011). A unifying theory of high-latitude geophysical phenomena and magnetic storms. *Canadian Journal of Physics* , *39*(10), 1433–1464.

Axford, W. I., Petschek H E, & Siscoe, G. L. (1965). Tail of the Magnetosphere. *Journal of Geophysical Research*, *70*(5), 1231–1236. 10.1029/JZ070i005p01231

Bailey, D. K. (1964). Polar Cap Absorption. *Planet. Space Sci*, *12*.

Baker, D. N., Pulkkinen, T. I., Angelopoulos, V., Baumjohann, W., & McPherron, R. L. (1996). Neutral line model of substorms: Past results and present view. *Journal of Geophysical Research: Space Physics*, *101*(A6), 12975–13010. https://doi.org/10.1029/95ja03753

Bartels, J. (1938). Potsdamer erdmagnetische Kennziffern, 1. *Mitteilung. Zeitschrift f Ür Geophysik*, *14*, 68–78.

Baumjohann, W., Hesse, M., Kokubun, S., Mukai, T., Nagai, T., & Petrukovich, A. A. (1999). Substorm dipolarization and recovery. *Journal of Geophysical Research: Space Physics*, *104*(A11), 24995–25000. https://doi.org/10.1029/1999ja900282

Baumjohann, W., & Truemann, R. A. (1996). *Basic Space Plasma Physics* . Imperial College Press. https://doi.org/10.1142/p015

Behera, J. K., Sinha, A. K., Singh, A. K., Rawat, R., Vichare, G., Dhar, A., Pathan, B. M., Nair, K. U., Selvaraj, C., & Elango, P. (2014). First results from imaging riometer installed at Indian Antarctic station Maitri. *J. Earth Syst. Sci.*, *123*(3), 593–602.

Behera, J. K., Sinha, A. K., Singh, A. K., Vichare, G., Dhar, A., Labde, S., & Jeeva, K. (2015). Substorm related CNA near equatorward boundary of the auroral oval in relation to interplanetary conditions. *Advances in Space Research*, *56*(1), 28–37. https://doi.org/10.1016/j.asr.2015.03.036

Behera, J. K., Sinha, A. K., Vichare, G., Kozyreva, O., Rawat, R., & Dhar, A. (2016a). Dayside cosmic noise absorption at the equatorward boundary of auroral oval as observed from Maitri, Antarctica (L = 5; CGM 62.45°S, 55.45°E). *Journal of Geophysical Research: Space Physics*, *121*(4), 3198–3211. https://doi.org/10.1002/2016JA022418

Behera, J. K., Sinha, A. K., Vichare, G., Kozyreva, O., Rawat, R., & Dhar, A. (2016b). Dayside cosmic noise absorption at the equatorward boundary of auroral oval as observed from Maitri, Antarctica (L = 5; CGM 62.45°S, 55.45°E). *Journal of Geophysical Research: Space Physics*, *121*(4), 3198–3211. https://doi.org/10.1002/2016JA022418

Bhonsle, R. v. (1960). Study of Solar Flares Using Cosmic Radio Noise on 25 Mc./s. at Ahmedabad (23 N, 72 E). *Proc. Lnd. Acacl. Sci*.

Birn, J., Hesse, M., Haerendel, G., Baumjohann, W., & Shiokawa, K. (1999). Flow braking and the substorm current wedge. *Journal of Geophysical Research: Space Physics*, *104*(A9), 19895–19903. https://doi.org/10.1029/1999ja900173

Bland, E. C., Heino, E., Kosch, M. J., & Partamies, N. (2018). SuperDARN Radar-Derived HF Radio Attenuation During the September 2017 Solar Proton Events. *Space Weather*, *16*(10), 1455–1469. https://doi.org/10.1029/2018SW001916

Booker, H. G. (1935). The Application of the Magneto-Ionic Theory to the Ionosphere. *Proceedings of the Royal Society of London. Series A, Mathematical and Physical Sciences*, *150*(870), 267–286.

Brodrick, D., Tingay, S., & Wieringa, M. (2005). X-ray magnitude of the 4 November 2003 solar flare inferred from the ionospheric attenuation of the galactic radio background. *Journal of Geophysical Research: Space Physics*, *110*(A9). https://doi.org/10.1029/2004JA010960

Browne, S., Hargreaves, J. K., & Honary, B. (1995). An imaging riometer for ionospheric studies. *Electronics and Communication Engineering Journal*, 209–217.

Burch, J. L. (1972). Preconditions for the Triggering of Polar Magnetic Substorms by Storm Sudden Commencements. *Journal of Geophysical Research*, *77*(28), 5629–5632. https://doi.org/10.1029/JA077i028p05629

Carpenter, D. L. (1966). Whistler Studies of the Plasmapause in the Magnetosphere 1. Temporal Variations in the Position of the Knee and Some Evidence on Plasma Motions near the Knee. *Journal of Geophysical Research*, *71*(3), 693–709.

Carpenter, D. L., & Anderson, R. R. (1992). An ISEE/Whistler Model of Equatorial Electron Density in the Magneto sphere. *Journal of Geophysical Research*, *97*(A2), 1097–1108.

Cassak, P. A., Shay, M. A., & Drake, J. F. (2006). Catastrophe Model for Fast Magnetic Reconnection Onset. *Physical Review Letters*, *95*(23).

Chappell, C. R., Harris, K. K., & Sharp, G. W. (1970). A Study of the Influence of Magnetic Activity on the Location of the Plasmapause as Measured by OGO 5. *Journal of Geophysical Research: Space Physics*, *75*(1), 50–56. https://doi.org/10.1029/JA075i001p00050

Collis, P. N., Hargreaves, J. K., & White, G. P. (1996). A localised co-rotating auroral absorption event observed near noon using imaging riometer and EISCAT. In *Ann. Geophysicae* (Vol. 14). EGS-Springer-Verlag.

Contreira, D. B., Rodrigues, F. S., Makita, K., Brum, C. G. M., Gonzalez, W., Trivedi, N. B., da Silva, M. R., & Schuch, N. J. (2005). An experiment to study solar flare effects on radio-communication signals. *Advances in Space Research*, *36*(12), 2455–2459. https://doi.org/10.1016/j.asr.2004.03.019

Cowley, S. W. H., & Lockwood, M. (1992). Excitation and decay of solar wind-driven flows in the magnetosphere-ionosphere system. *Annals of Geophysics*, *10*, 103–115.

Davis, T. N., & Sugiura, M. (1966). Auroral Electrojet Activity Index AE and Its Universal Time Variations. *Journal of Geophysical Research*, *71*(3), 785–801. https://doi.org/https://doi.org/10.1029/JZ071i003p00785

Dungey, J. W. (1961). NUMBER 2 INTERPLANETARY MAGNETIC FIELD AND THE AURORAL ZONES. *Physical Review Letters*, *6*(2), 47–48. https://doi.org/https://doi.org/10.1103/PhysRevLett.6.47

Evans, D. S., & Greer, M. S. (2004). *NOAA Technical Memorandum Polar Orbiting Environmental Satellite Space Environment Monitor-2: Instrument Descriptions and Archive Data Documentation*.

Freeman, M. P., Farrugia, C. J., Burlaga, L. F., Hairston, M. R., Greenspan, M. E., Ruohoniemi, J. M., & Lepping, R. P. (1993). The Interaction of a Magnetic Cloud With the Earth' Ionospheric Convection in the Northern and Southern Hemispheres for a Wide Range of Quasi-Steady Interplanetary Magnetic Field Conditions. *Journal of Geophysical Research*, *98*(A5), 7633–7655. https://doi.org/10.1029/92JA02350

Fuselier, S. A., & Lewis, W. S. (2011). Properties of near-earth magnetic reconnection from in-situ observations. *Space Science Reviews*, *160*(1–4), 95–121. https://doi.org/10.1007/s11214-011-9820-x

Ganushkina, N. Y., Liemohn, M. W., & Dubyagin, S. (2018). Reviews of Geophysics Current Systems in the Earth's Magnetosphere. *Reviews of Geophysics*, *56*, 309–322. https://doi.org/10.1002/2017RG000590

Gjerloev, J. W. (2012). The SuperMAG data processing technique. *Journal of Geophysical Research: Space Physics*, *117*(9), 1–19. https://doi.org/10.1029/2012JA017683

Glocer, A., Fok, M., Meng, X., Toth, G., Buzulukova, N., Chen, S., & Lin, K. (2013). CRCM + BATS-R-US two-way coupling. *Journal of Geophysical Research: Space Physics*, *118*(4), 1635–1650. https://doi.org/10.1002/jgra.50221

Gombosi, T. I., Chen, Y., Glocer, A., Huang, Z., Jia, X., Liemohn, M. W., Manchester, W. B., Pulkkinen, T., Sachdeva, N., al Shidi, Q., Sokolov, I. v., Szente, J., Tenishev, V., Toth, G., van der Holst, B., Welling, D. T., Zhao, L., Zou, S., & Gombosi, T. I. (2021). What sustained multi-disciplinary research can achieve: The space weather modeling framework. *Journal of Space Weather and Space Climate*, *11*. https://doi.org/10.1051/swsc/2021020

Gopalswamy, N. (2006). Coronal Mass Ejections of Solar Cycle 23. In *J. Astrophys. Astr* (Vol. 27).

Grocott, A., Cowley, S. W. H., Sigwarth, J. B., Watermann, J. F., & Yeoman, T. K. (2002). Excitation of twin-vortex flow in the nightside high-latitude ionosphere during an isolated substorm. *Ann. Geophys.*, *20*, 1577–1601.

Hajra, R., & Tsurutani, B. T. (2018). Interplanetary Shocks Inducing Magnetospheric Supersubstorms (SML < −2500 nT): Unusual Auroral Morphologies and Energy Flow. *The Astrophysical Journal*, *858*(2), 123. https://doi.org/10.3847/1538-4357/aabaed

Hajra, R., Tsurutani, B. T., Echer, E., Gonzalez, W. D., & Gjerloev, J. W. (2016). Supersubstorms (SML < −2500 nT): Magnetic storm and solar cycle dependences. *Journal of Geophysical Research: Space Physics*, *121*(8), 7805–7816. https://doi.org/10.1002/2015JA021835

Hajra, R., Tsurutani, B. T., & Lakhina, G. S. (2020). The Complex Space Weather Events of 2017 September. *The Astrophysical Journal*, *899*(1), 3. https://doi.org/10.3847/1538-4357/aba2c5

Hargreaves, J. K., Banta, H., Banta, A., Tubunen, E., & Turunen, T. (1987). OBSERVATIONS OF THE POLAR CAP ABSORPTION EVENT OF FEBRUARY 1984 BY THE EISCAT INCOHERENT SCATTER RADAR. In *Planer. Space Sci* (Vol. 35, Issue 7).

Harrison, R. A. (1995). The nature of solar flares associated with coronal mass ejection. *Astron. Astrophys.*, 304–585.

Hermann, L., Chao Xiong, Nils, O., & Le, G. (2017). Near-Earth Magnetic Field Effects of Large-Scale Magnetospheric Currents. *Space Science Reviews*, *206*(1–4), 521–545. https://doi.org/10.1007/s11214-016-0267-y

Hones, E. W. (1979). TRANSIENT PHENOMENA IN THE MAGNETOTAIL AND THEIR RELATION TO SUBSTORMS*. *Space Science Reviews*, *23*, 393–410. 10.1007/BF00172247

Hones, E. W. , Jr. ,. (1976). *The magnetotail: Its generation and dissipation, in Physics of Solar Planetary Environments* (D. J. Williams, Ed.; pp. 558–571). AGU.

Jelly, D., & Brice, N. (1967). Changes in Van Allen Radiation Associated with Polar Substorms. *Journal of Geophysical Research*, *72*(23), 5919–5931.

Kamide, Y. (1974). Association of DP and DR fields with the interplanetary magnetic field variation . *Journal of Geophysical Research*, *79*(1), 49–55. https://doi.org/10.1029/ja079i001p00049

Kamide, Y., Perreault, P. D., Akasofu, S. I., & Winningham, J. D. (1977). Dependence ooe Substorm Occurrence Probability on the Interplanetary Magnetic Field and on the Size ooe the Auroral Oval ’. *Journal of Geophysical Research*, *82*(35), 5521–5528. https://doi.org/10.1029/JA082i035p05521

Kawasaki, K., Akasofu, S.-I., Yasuhara, F., & Meng, C.-I. (1971). Storm sudden commencements and polar magnetic substorms. *Journal of Geophysical Research*, *76*(28), 6781–6789. https://doi.org/10.1029/ja076i028p06781

Kelley, M. C., & Hellis, R. A. (1989). *The Earth’s Ionosphere, Plasma Physics and Electrodynamics*. Academic Press.

Lee, D.-Y., Choi, K.-C., Ohtani, S., Lee, J. H., Kim, K. C., Park, K. S., & Kim, K.-H. (2010). Can intense substorms occur under northward IMF conditions? *Journal of Geophysical Research: Space Physics*, *115*(A1), n/a-n/a. https://doi.org/10.1029/2009ja014480

Liou, K., & Newell, P. T. (2010). On the azimuthal location of auroral breakup: Hemispheric asymmetry. *Geophysical Research Letters*, *37*(23). https://doi.org/10.1029/2010GL045537

Liou, K., Wu, C. C., Lepping, R. P., Newell, P. T., & Meng, C. I. (2002a). Midday sub-auroral patches (MSPs) associated with interplanetary shocks. *Geophysical Research Letters*, *29*(16), 18-1-18–4. https://doi.org/10.1029/2001gl014182

Liou, K., Wu, C.-C., Lepping, R. P., Newell, P. T., & Meng, C.-I. (2002b). Midday sub-auroral patches (MSPs) associated with interplanetary shocks. *Geophysical Research Letters*, *29*(16). https://doi.org/10.1029/2001GL014182

Little, C. G., & Leinbach, H. (1959). The Riometer —A Device for the Continuous Measurement of Ionospheric Absorption. *Proceedings of the IRE*, *47*(2), 315–320. https://doi.org/10.1109/JRPROC.1959.287299

Longden, N., Honary, F., Kavanagh, A. J., & Manninen, J. (2007). The driving mechanisms of particle precipitation during the moderate geomagnetic storm of 7 January 2005. *Annals of Geophysicae*, *25*, 2053–2068. https://doi.org/10.5194/angeo-25-2053-2007

Lui, A. T. Y. (1996). Current disruption in the Earth's magnetosphere: Observations and models. *Journal of Geophysical Research: Space Physics*, *101*(A6), 13067–13088. https://doi.org/10.1029/96ja00079

Lui, A. T. Y., Akasofu, S. I., Hones, E. W., Bame, S. J., & McIlwain, C. E. (1976). Observation of the Plasma Sheet During a Contracted Oval Substorm in a Prolonged Quiet Period. *Journal of Geophysical Research*, *81*(7), 1415–1419. https://doi.org/10.1029/JA081i007p01415

Ma, X., Delamere, P., Otto, A., & Burkholder, B. (2017). Plasma Transport Driven by the Three-Dimensional Kelvin-Helmholtz Instability. *Journal of Geophysical Research: Space Physics*, *122*(10), 10,382-10,395. https://doi.org/10.1002/2017JA024394

Masson, A., & Nykyri, K. (2018). Kelvin–Helmholtz Instability: Lessons Learned and Ways Forward. In *Space Science Reviews* (Vol. 214, Issue 4). Springer Netherlands. https://doi.org/10.1007/s11214-018-0505-6

Matthews, D. L., Rosenberg, T. J., Benbrook, J. R., & Bering, E. A. (1988). Dayside energetic electron precipitation over the South Pole ($\lambda = 75°$). *Journal of Geophysical Research*, *93*(A11), 12941. https://doi.org/10.1029/ja093ia11p12941

Matzka, J., Stolle, C., Yamazaki, Y., Bronkalla, O., & Morschhauser, A. (2021). The Geomagnetic Kp index and Derived Indices of Geomagnetic Activity. *Space Weather*, *19*. https://doi.org/10.1029/2020SW002641

McPherron, R. L. (1970). Growth phase of magnetospheric substorms. *Journal of Geophysical Research*, *75*(28), 5592–5599. https://doi.org/10.1029/ja075i028p05592

Mcpherron, R. L. (1979). Magnetospheric Substorms. *Reviews of Geophysics and Space Physics*, *17*(4), 657–681.

Meng, C.-I., Tsurutani, B., Kawasaki, K., & Akasorv, S.-I. (1973). *Cross-Correlation Analysis of the AE Index and the Interplanetary Magnetic Field Component The interplanetary magnetic field data of the Goddard magnetometer experiment aboard Ex-617* (Vol. 78, Issue 4). https://doi.org/10.1029/JA078i004p00617

Mitchell, D. G., Kutchko, F., Williams, D. J., Eastman, T. E., Frank, L. A., & Russell, C. T. (1987). An extended study of the low-latitude boundary layer on the dawn and dusk flanks of the magnetosphere. *Journal of Geophysical Research*, *92*(A7), 7394. https://doi.org/10.1029/ja092ia07p07394

Mitra, A. P., & Shain, C. A. (1953). The measurement of ionospheric absorption using observations of 18.3 Mc/S cosmic radio noise. *Journsl of Atmospheric and Terrestrial Physics*, *4*, 204–218.

Miura, A. (1984). Anomalous Transport by Magnetohydrodynamic Kelvin-Helmholtz Instabilities in the Solar Wind-Magnetosphere Interaction. *Journal of Geophysical Research*, *89*(A2), 801–818. https://doi.org/10.1029/JA089iA02p00801

Miura, A. (1987). Simulation of Kelvin-Helmholtz instability at the magnetospheric boundary. *Journal of Geophysical Research*, *92*(A4), 3195. https://doi.org/10.1029/ja092ia04p03195

Miyashita, Y., Kamide, Y., Liou, K., Wu, C. C., Ieda, A., Nishitani, N., MacHida, S., Saito, Y., & Mukai, T. (2011). Successive substorm expansions during a period of prolonged northward interplanetary magnetic field. *Journal of Geophysical Research: Space Physics*, *116*(9). https://doi.org/10.1029/2011JA016719

Miyashita, Y., Machida, S., Liou, K., Mukai, T., Saito, Y., Hayakawa, H., Meng, C. I., & Parks, G. K. (2003). Evolution of the magnetotail associated with substorm auroral breakups.

Journal of Geophysical Research: Space Physics, *108*(A9). https://doi.org/10.1029/2003JA009939

Moro, J., Denardini, C. M., Correia, E., Abdu, M. A., Schuch, N. J., & Makita, K. (2012). A comparison of two different techniques for deriving the quiet day curve from SARINET riometer data. *Annales Geophysicae*, *30*(8), 1159–1168. https://doi.org/10.5194/angeo-30-1159-2012

Newell, P. T., & Gjerloev, J. W. (2011). Evaluation of SuperMAG auroral electrojet indices as indicators of substorms and auroral power. *Journal of Geophysical Research*, *116*(A12211). https://doi.org/10.1029/2011JA016779

Newell, P. T., & Meng, C.-I. (1992). Mapping the Dayside Ionosphere to the Magnetosphere According to Particle Precipitation Characteristics. *Geophysical Research Letter*, *19*(6), 609–612. https://doi.org/https://doi.org/10.1029/92GL00404

Nishida, A. (1966). Formation of Plasmapause, or Magnetospheric Plasma Knee, by the Combined Action of Magnetospheric Convection and Plasma Escape from the Tail. *JOURNAL OF GEOPHYSICAL RESEARCH*, *71*(23), 5669–5679.

Nishida, A. (1971). Interplanetary origin of electric fields in the magnetosphere. *Cosmic Electrodyn*, *2*, 350–374.

Nishida, A., Mukai, T., Yamamoto, T., Kokubun, S., & Maezawa, K. (1998). A unified model of the magnetotail convection in geomagnetically quiet and active times. *Journal of Geophysical Research*, *103*(A3), 4409–4418. https://doi.org/10.1029/97JA01617

Nosé, M., Iyemori, T., Wang, L., Hitchman, A., Matzka, J., Feller, M., Egdorf, S., Gilder, S., Kumasaka, N., Koga, K., Matsumoto, H., Koshiishi, H., Cifuentes-Nava, G., Curto, J. J., Segarra, A., & Elik, C. (2012). Wp index: A new substorm index derived from high-resolution geomagnetic field data at low latitude. *Space Weather*, *10*(8). https://doi.org/10.1029/2012SW000785

Ogino, T., Walker, R. J., Ashour-Abdalla, M., & Dawson, J. M. (1986). An MHD Simulation of the Effects of the Interplanetary Magnetic Field Component on the Interaction of the Solar Wind With the Earth's Magnetosphere During Southward Interplanetary Magnetic Field. *Journal of Geophysical Research*, *91*(A9), 29–39. https://doi.org/10.1029/JA091iA09p10029

Ogunmodimu, O., Honary, F., Rogers, N., Falayi, E. O., & Bolaji, O. S. (2018). Solar flare induced cosmic noise absorption. *NRIAG Journal of Astronomy and Geophysics*, *7*(1), 31–39. https://doi.org/10.1016/j.nrjag.2018.03.002

Oliveira, D. M., Arel, D., Raeder, J., Zesta, E., Ngwira, C. M., Carter, B. A., Yizengaw, E., Halford, A. J., Tsurutani, B. T., & Gjerloev, J. W. (2018). Geomagnetically Induced Currents Caused by Interplanetary Shocks With Different Impact Angles and Speeds. *Space Weather*, *16*(6), 636–647. https://doi.org/10.1029/2018SW001880

Oliveira, D. M., & Raeder, J. (2015). Impact angle control of interplanetary shock geoeffectiveness: A statistical study. *Journal of Geophysical Research: Space Physics*, *120*(6), 4313–4323. https://doi.org/10.1002/2015JA021147

Oliveira, D. M., Weygand, J. M., Zesta, E., Ngwira, C. M., Hartinger, M. D., Xu, Z., Giles, B. L., Gershman, D. J., Silveira, M. v.d., & Souza, V. M. (2021). Impact Angle Control of Local Intense dB/dt Variations During Shock-Induced Substorms. *Space Weather*, *19*(12). https://doi.org/10.1029/2021SW002933

Ostgaard, N., Laundal, K. M., Juusola, L., Åsnes, A., Håland, S. E., & Weygand, J. M. (2011). Interhemispherical asymmetry of substorm onset locations and the interplanetary magnetic field. *Geophysical Research Letters*, *38*(8). https://doi.org/10.1029/2011GL046767

Østgaard, N., Stadsnes, J., Bjordal, J., Thorsen, E., Vondrak, R. R., Cummer, S. A., Chenette, D. L., Parks, G. K., Brittnacher, M. J., & Mckenzie, D. L. (1999). Global Scale Electron Precipitation During Substorm Expansions. *Journal of Geophysical Research*, *104*(10), 191–210. https://doi.org/10.1029/1999JA900004

Öztürk, M. K. (2012). Trajectories of charged particles trapped in Earth's magnetic field. *American Journal of Physics*, *80*(5), 420–428. https://doi.org/10.1119/1.3684537

Park, K. S., Ogino, T., & Walker, R. J. (2006). On the importance of antiparallel reconnection when the dipole tilt and IMF By are nonzero. *Journal of Geophysical Research*, *111*(A05202), 1–12. https://doi.org/10.1029/2004JA010972

Partamies, N., Juusola, L., Tanskanen, E., & Kauristie, K. (2013). Statistical properties of substorms during different storm and solar cycle phases. *Annales Geophysicae*, *31*(2), 349–358. https://doi.org/10.5194/angeo-31-349-2013

Petrukovich, A. A., Baumjohann, W., Nakamura, R., Mukai, T., & Troshichev, O. A. (2000). Small substorms: Solar wind input and magnetotail dynamics. *Journal of Geophysical Research: Space Physics*, *105*(A9), 21109–21117. https://doi.org/10.1029/2000ja900057

Phan, T. D., Paschmann, G., Gosling, J. T., Oieroset, M., Fujimoto, M., Drake, J. F., & Angelopoulos, V. (2013). The dependence of magnetic reconnection on plasma β and magnetic shear: Evidence from magnetopause observations. *Geophysical Research Letters*, *40*(1), 11–16. https://doi.org/10.1029/2012GL054528

Quan, L., Cai, B., Hu, X., Xu, Q., & Li, L. (2021). Study of ionospheric D region changes during solar flares using MF radar measurements. *Advances in Space Research*, *67*(2), 715–721. https://doi.org/10.1016/j.asr.2020.10.015

Ranta, A., & Ranta, H. (1990). STORM SUDDEN COMMENCEMENTS OBSERVED IN IONOSPHERIC ABSORPTION. In *Planer. Space Sci* (Vol. 38, Issue 3).

Ranta, H. (1978). The onset of an auroral absorption substorm. *Journal of Geophysical Research*, *83*(A8), 3893. https://doi.org/10.1029/ja083ia08p03893

Ranta, H., Ranta, A., Yousef, S. M., Burns, J., & Stauning, P. (1993). D-region observations of polar cap absorption events during the EISCAT operation in 1981-1989. *Journal of Atmospheric and Terrestrial Physics*, *55*(5), 751–766. https://doi.org/10.1016/0021-9169(93)90018-T

Rees, M. H. (1963). Auroral Ionization and Excitation by Incident Energetic Electrons. *Planet. Space Sci. , 11*, 1209–1218.

Reiff, P. H., & Burch, J. L. (1985). IMF By-dependent plasma flow and Birkeland currents in the dayside magnetosphere: 2. A global model for northward and southward IMF. *Journal of Geophysical Research*, *90*(A2), 1595–1609. https://doi.org/10.1029/JA090iA02p01595

Rodger, C. J., Clilverd, M. A., Green, J. C., & Lam, M. M. (2010). Use of POES SEM-2 observations to examine radiation belt dynamics and energetic electron precipitation into the atmosphere. *Journal of Geophysical Research: Space Physics*, *115*(4). https://doi.org/10.1029/2008JA014023

Rogers, N. C., Kero, A., Honary, F., Verronen, P. T., Warrington, E. M., & Danskin, D. W. (2016). Improving the twilight model for polar cap absorption nowcasts. *Space Weather*, *14*(11), 950–972. https://doi.org/10.1002/2016SW001527

Rose, D. C., & Ziauddin, S. (1962). The Polar Cap Absorption Effect. *Space Science Reviews*, *1*, 115–134.

Rostoker, G. (1968). Relationship between the Onset of a Geomagnetic Bay and the Configuration of the Interplanetary Magnetic Field. *Journal of Geophysical Research*, *73*(13).

Rostoker, G., Akasofu, S.-I., Foster, J., Greenwald, R. A., Kamide, Y., Kawasaki, K., Lui, A. T. Y., McPherron, R. L., & Russell, C. T. (1980). Magnetospheric substorms—definition and signatures. *Journal of Geophysical Research*, *85*(A4), 1663. https://doi.org/10.1029/ja085ia04p01663

Rostoker, G., & Falthammar, C. G. (1967). Relationship between Changes in the Interplanetary Magnetic Field and Variations in the Magnetic Field at the Earth's Surface. *Journal of Geophysical Research*, *72*(23), 5853–5863. https://doi.org/https://doi.org/10.1029/JZ072i023p05853

Sandholt, P. E., Farrugia, C. J., Cowley, S. W. H., & Lester, M. (2001). Dayside auroral bifurcation sequence during By-dominated interplanetary magnetic field: Relationship with merging and lobe convection cells. *Journal of Geophysical Research: Space Physics*, *106*(A8), 15429–15444. https://doi.org/10.1029/2000ja900161

Schieldge, J. P., & Siscoe, G. L. (1970). A correlation of the occurrence of simultaneous sudden magnetospheric compressions and geomagnetic bay onsets with selected geophysical indices. In *Journal of Atmospheric and Terrestrial Physics* (Vol. 31). Pergamon Press.

Schulz, M., & Koons, H. C. (1972). Thermalization of Colliding Ion Streams beyond the Plasmapause. *Journal of Geophysical Research*, *77*(1), 248–254. https://doi.org/10.1029/JA077i001p00248

Shain, C. A., & Mitrat, A. P. (1954). Effects of solar flares on the absorption of 18.3 MC/S cosmic noise. In *Journal of Atmospheric and Terrehrlal Physlca* (Vol. 5). Pergamon Press Ltd.

Singh, A. K., Singh, A. K., Singh, R., & Singh, R. P. (2014a). Solar flare induced D-region ionospheric perturbations evaluated from VLF measurements. *Astrophysics and Space Science*, *350*(1), 1–9. https://doi.org/10.1007/s10509-013-1699-4

Singh, A. K., Singh, A. K., Singh, R., & Singh, R. P. (2014b). Solar flare induced D-region ionospheric perturbations evaluated from VLF measurements. *Astrophysics and Space Science*, *350*(1), 1–9. https://doi.org/10.1007/s10509-013-1699-4

Singh, N., & Horwitz, J. L. (1992). Plasmasphere Refilling: Recent Observations and Modeling. *JOURNAL OF GEOPHYSICAL RESEARCH*, *97*(A2), 1049–1079. https://doi.org/10.1029/91JA02602

Siscoe, G. L., & Huang, T. S. (1985). Polar Cap Inflation and Deflation. *Journal of Geophysical Research*, *90*, 543–547.

Stauning, P. (1996). Investigations of ionospheric radio wave absorption processes using imaging riometer techniques. In *Journal of Atmospheric and Terrestrial Physics* (Vol. 58, Issue 6).

Terasawa, T., Fujimoto, M., Mukai, T., Shinohara, I., Saito, Y., Yamamoto, T., Machida, S., Kokubun, S., Lazarus, A. J., Steinberg, J. T., & Lepping, R. P. (1997). Solar wind control of density and temperature in the near-Earth plasma sheet: WIND/GEOTAIL collaboration. *Geophysical Research Letters*, *24*(8), 935–938. https://doi.org/10.1029/96GL04018

Tsugawa, T., Sadakane, T., Sato, J., Otsuka, Y., Ogawa, T., Shiokawa, K., & Saito, A. (2006). Summer-winter hemispheric asymmetry of sudden increase in ionospheric total electron content induced by solar flares: A role of O/N2 ratio. *Journal of Geophysical Research: Space Physics*, *111*(11). https://doi.org/10.1029/2006JA011951

Tsurutani, B. T., Echer, E., Guarnieri, F. L., & Kozyra, J. U. (2008). CAWSES November 7-8, 2004, superstorm: Complex solar and interplanetary features in the post-solar maximum phase. *Geophysical Research Letters*, *35*(L06S05). https://doi.org/10.1029/2007GL031473

Tsurutani, B. T., Gonzalez Instituto de PesquiSas Espaciais, D., Jose Dos Campos, S., & Paulo, S. (1995). *The efficiency of "viscous lnterachon" between the solar wind and the magnetosphere during intense northward IMF events* (Vol. 22, Issue 6).

Tsurutani, B. T., Hajra, R., Echer, E., & Gjerloev, J. W. (2015). Extremely intense (SML ≤2500 nT) substorms: Isolated events that are externally triggered? *Annales Geophysicae*, *33*(5), 519–524. https://doi.org/10.5194/angeo-33-519-2015

Tsurutani, B. T., & Meng, C. I. (1972). Interplanetary Magnetic-Field Variations and Substorm Activity •. *Journal of Geophysical Research*, *77*(16), 2964–2970. https://doi.org/10.1029/JA077i016p02964

Tsurutani, B. T., Zhou, X. Y., Vasyliunas, V. M., Haerendel, G., Arballo, J. K., & Lakhina, G. S. (2001). Interplanetary shocks, magnetopause boundary layers and dayside auroras: The importance of a very small magnetospheric region. *Surveys in Geophysics*, *22*(2), 101–130. https://doi.org/10.1023/A:1012952414384

van Allen, J. A., & Frank, L. A. (1959). RADIATION AROUND THE EARTH TO A RADIAL DISTANCE OF I 07,400 KM. *Nature*, *183*, 430–434.

Wing, S., Johnson, J. R., Chaston, C. C., Echim, M., Escoubet, C. P., & Lavraud, B. (2014). Review of solar wind entry into and transport within the plasma sheet. *Space Science Reviews*, *184*, 33–86.

Wu, C., Liou, C. K., Lepping, R. P., Le, G., & Meng, C. I. (2002). Observations of substorms during prolonged northward interplanetary magnetic field. In R. M. Winglee (Ed.), *Sixth International Conference on Substorms*.

Zhou, X., & Tsurutani, B. T. (1999). Rapid intensification and propagation of the dayside aurora: large scale interplanetary pressure pulses (fast shocks). *Geophysical Research Letters*, *26*(8), 1097–1100. https://doi.org/10.1029/1999GL900173

Zhou, X., & Tsurutani, B. T. (2001). Interplanetary shock triggering of nightside geomagnetic activity: Substorms, pseudobreakups, and quiescent events. *Journal of Geophysical Research: Space Physics*, *106*(A9), 18957–18967. https://doi.org/10.1029/2000ja003028

Zhou, X. Y., & Tsurutani, B. T. (2004). Dawn and dusk auroras caused by gradual, intense solar wind ram pressure events. *Journal of Atmospheric and Solar-Terrestrial Physics*, *66*(2), 153–160. https://doi.org/10.1016/j.jastp.2003.09.008

Zong, Q. G., Yue, C., & Fu, S. Y. (2021). Shock Induced Strong Substorms and Super Substorms: Preconditions and Associated Oxygen Ion Dynamics. *Space Sci Rev*, 217–240. https://doi.org/10.1007/s11214-021-00806-x

SYNOPSIS OF THE THESIS TO BE SUBMITTED

TO THE

UNIVERSITY OF MUMBAI

FOR THE DEGREE OF

DOCTOR OF PHILOSOPHY

IN THE SUBJECT OF

PHYSICS

NAME OF THE STUDENT:	SHIPRA SINHA
TITLE OF THE THESIS:	MAGNETOSPHERE-IONOSPHERE COUPLING USING INTEGRATED MEASUREMENTS
DEGREE & SUBJECT:	Ph.D. (PHYSICS)
REGISTRATION NO. /DATE:	43/15-02-2020
NAME OF THE RESEARCH GUIDE:	Prof. GEETA VICHARE
DATE OF SUPERANNUATION:	30 NOVEMBER 2032
NAME OF RESEARCH CENTER:	INDIAN INSTITUTE OF GEOMAGNETISM, NEW PANVEL, NAVI MUMBAI- 410218.

SIGNATURE OF STUDENT:

SIGNATURE OF GUIDE:

DATE OF SUBMISSION OF SYNOPSIS:

SEAL OF COLLAGE: HEAD/DIRECTOR/PRINCIPAL RESEARCH CENTRE (STAMP)

Synopsis

Our Earth is surrounded by a layer of weakly ionized gas called the Ionosphere, which in turn is surrounded by a large cavity-like structure consisting of magnetic field lines and trapped charged particles, called the Magnetosphere. These layers, although are classified separately, forms a continuous magnetosphere-ionosphere system and is quiet complex in nature. There is a continuous exchange of charged particles between the two via magnetic field lines of the Earth. This leads to the formation of several current systems, which in turn controls the motion of these charged particles. The study of magnetosphere-ionosphere coupling constitute an essential part of the solar-terrestrial research. The solar energetic particles do not have a direct entry into the surface of the Earth, except for Polar Regions, due to the Earth's own protective shield of closed magnetic field lines. Rather, they enter indirectly into the magnetosphere from the night side once magnetic reconnection changes the topology of the closed field lines (Tsurutani and Meng, 1972; Meng et al., 1973). The magnetic flux eroded on the dayside magnetopause, after the magnetic reconnection, is transported into the tail and this period of enhanced convection is often referred to as the 'loading' mechanism (Baumjohann and Treumann, 1996). When the loading becomes unstable, particles precipitate down the field line to reach the Earth's atmosphere. The process of loading and unloading of charged particles from the night-side magnetotail region into the Earth's atmosphere following the field lines is called magnetospheric substorm (Burch, 1972; Tsurutani and Meng, 1972; Zhou & Tsurutani, 2001). In addition, during the loading mechanism, some high energetic particles can move across the field lines as well. During their gradient and curvature drift they fall into the loss cone, eventually precipitating down the field line (Rogers et al., 2016; Ansari, 1964; Matthews et al., 1988; Newell and Meng, 1992; Østgaard et al., 1999; Behera et al., 2016). At times, there can also be a direct entry of these particle from the cusp region into the polar atmosphere where magnetic field lines are open (Bailey, 1964; Hargreaves et al., 1987). Either ways, they reach the atmosphere at high latitude regions, i.e. ~60° and above, due to the highly conducting magnetic field lines. The precipitating particles causes significant increase in the ionospheric conductivity that leads to a current flow of about 10^6A at ~100 km altitude. These current systems create the largest ground magnetic disturbances compared to any other current system present in the Earth's environment (Allen and Kroehl, 1975). Hence, altogether it forms a complicated feedback system. In order to

understand the coupling of the magnetosphere-ionosphere system, the study of high-latitude dynamics, thus, turns out to be of utmost importance.

The study of energetic particle precipitation can act as tracers for several geomagnetic morphological problems, such as identifying the location of magnetospheric substorm onset, classifying the latitudinal region of open and closed magnetic field lines and examining the interplanetary conditions at magnetopause boundary. Once these precipitating particles enter the Earth's atmosphere, they can lead to several adverse effects, hence, their study becomes important. The ionization and dissociating of atmospheric constituents due to high energetic particle precipitation, can eventually lead to ozone layer depletion (Andersson et al., 2018). Furthermore, these particles are also capable of damaging the satellites and spacecrafts, and can disturb the communication and navigation systems.

In the present thesis, we have selected various intense substorm events having distinctly different interplanetary conditions to investigate the entry points of precipitating particles and consequently its mechanism. The energetic particles that precipitate during substorms are majorly electrons having energies ~1-100 keV that ionize the lower E and D regions of the ionosphere (Rees, 1963; Carlson et al., 1998; Swift, 1978; Tsurutani et al., 2019). The magnetospheric electrons of energy range ~1-10 keV deposit their energy in ~160 to ~100 km altitude. On the other hand, electrons of energy range ~10-100 keV deposit their energies deeper into the atmosphere in the ~75-100 km altitude range (Rees, 1963; Artamonov et al., 2016; Jones et al., 2009). The precipitation of these electrons increase the ionospheric conductivities, enhances the auroral electrojet current, and also leads to the formation of visual auroras. There are various ground and satellite based instruments that are set up widely to study the solar-terrestrial interactions. These instruments target different regions of the Earth's magnetosphere-ionosphere system to study the perturbations at those altitudes and locations. For instance, the ground magnetometers set up at high latitudes measure the ground magnetic perturbation due to the currents mainly flowing at ~100 km and above in the E-region of the ionosphere (Newell and Gjerloev, 2011). The riometer set-ups are used to monitor the D-region ionization by measuring the fluctuations in the galactic cosmic radio noise signals at ~90 km altitude (Little, 1954; Little and Leinbach, 1958; Little and Leinbach, 1959; Jelly and Brice 1967). All-sky imagers are used to study the global view of auroras which are also formed in the E-region of the ionosphere near

~120 km altitude (Frey et al., 2004, Kellerman, 2009). When instruments like magnetometers and particle-detectors are on-board low-Earth orbiting (LEO), geostationary and geosynchronous satellites, they give the 'in-situ' measurements of the perturbations at locations where the satellites are positioned at that time. Combining the results of all these instruments to study any geomagnetic event allows us to widen the dimension of the analysis in terms of space and time. This helps in understanding all the interconnected mechanisms involved during several geomagnetic phenomena right from the magnetopause boundaries down to the ionospheric heights. This forms the central theme of the present thesis where the study of the magnetosphere-ionosphere coupling is performed by integrated measurements using instruments like magnetometers, riometers, auroral imagers, particle flux detectors etc. For this we have selected the times of disturbed geomagnetic conditions, such as magnetospheric substorms, solar flares and solar proton events (SPE).

Chapter 2 of the present thesis describes the instrumentation and methodology in detail. At D-region ionospheric heights, the incoming cosmic radio waves of galactic origin, get absorbed and their intensity is reduced. More the ionization, more will be the absorption of these radio waves. Riometer uses these cosmic radio waves as signal source and measure the intensity variation in terms of power units. The riometer can be a single dipole antenna or an array of antennas (called Imaging Riometer) that can be tuned to a certain operating frequency. The datasets of Imaging Riometer installed at Indian Antarctic base, Maitri, is used to show the spatial and temporal variation at D-region heights during geomagnetically disturbed periods. Analysis of a very intense substorm is shown in Chapter 3 which was done using riometer datasets installed at several high latitude stations, in conjunction with magnetometer, all-sky imager and energetic particle detector datasets. This case study shows the evidence of particle entry points from the flanks during substorms and a suitable mechanism is proposed based on the observations of this day. Chapter 4 comprises a study which is further carried forward towards the classification of substorms based on its triggering mechanism. This is a novel work and is an important addition to the existing theory of particle injection and precipitation during substorms. Chapter 5 discusses the effects of solar flares in the D-region ionosphere at high latitudes. Chapter 6 summarizes the conclusion and scope of the thesis.

The chapter wise work description of all the 6 chapters of the thesis is given below:

Chapter I

The first chapter of this thesis provides a general introduction of solar-terrestrial interactions and their impact on the Earth's environment. Basic concepts such as solar wind, solar flares, interplanetary magnetic field, magnetic reconnection, Earth's magnetosphere and ionosphere, and current systems have been explained. This chapter consists of a brief discussion of the injection and precipitation mechanisms of solar energetic particles into the Earth's environment which is a major consequence of the solar wind-magnetosphere-ionosphere coupling. The process of magnetospheric substorm is given major attention, since, important results and major part of the conclusion of the present thesis utilizes substorm events. Along with a review of the current understanding of the magnetosphere-ionosphere coupling system, the importance of conducting the analysis using integrated measurements and an insight to future directions has been outlined.

Chapter II

This chapter discusses the instruments used for the analysis in this thesis, their datasets and methodologies. One of the main instrument whose datasets has been used is Riometer. Hence, in this chapter, the riometer instrument description, method of deriving the quiet day pattern (QDC) and the principle of CNA measurements using riometer datasets, has been explained.

Riometer (Relative Ionospheric Opacity meter) is a very sensitive radio receiver, continuously measuring the cosmic noise level incident on the earth's surface. A riometer is used to investigate the enhancement in the ionization of D-region ionosphere by interpreting the decrease in the strength of incident cosmic radio noise signal (Little, 1954; Little and Leinbach, 1958; Little and Leinbach, 1959). Particle precipitation that results into enhancement of D-region ionization causes absorption of these cosmic radio noise, leading to a decrease in the level of intensity observed (Jelly and Brice, 1967; Browne et al., 1995; P. Stauning, 1994; Behera et al., 2014). Ionospheric absorption (or CNA) at any time is specified by the difference between the intensities

of received cosmic noise and the signal that would have been received if there were no absorption at that time (Mitra et al., 1953; Jelly and Brice, 1967; Stauning, 1994; Moro et al., 2012).

Riometer can be a single dipole antenna or an array of antennas arranged in '*nxn*' matrix format. These array of antennas are also called 'Imaging Riometer' and has quiet an advantage over the single antenna usage. Each antenna of the Imaging Riometer points at particular part of the sky and cumulatively they give a good estimate of the spatial and temporal variation over a wide area, unlike single antenna whose field of view is confined to one point. One such imaging riometer was installed at Indian Antarctic Base, Maitri (70.75°S, 11.75°E) which consists of 16 antennas arranged in 4x4 matrix in the magnetic north-south direction (Behera et al., 2014). It operates at 38.2 MHz frequency and the field of view at 90 km altitude is 200X200 km^2. In this chapter we have used the Imaging Riometer technique for conducting a spatial and temporal study of disturbed days at Maitri's location for the first time. We have shown the variation in the disturbance in 200X200 km^2 range at D-region altitude over the sub-auroral latitude of Maitri during substorm and solar flare activity.

In addition to the riometer measurements, this chapter also includes a brief description of all the other instruments used in our study. These include both ground based and satellite based instruments, such as magnetometer, all-sky imager and energetic particle detectors. The details of ACE/Wind, GOES, POES and LANL missions along with the instruments have also been discussed.

Chapter III

Southward component of Interplanetary Magnetic Field (IMF) is necessary for magnetic reconnection between the IMF and the Earth's magnetic field at the sub-solar point. This reconnection eventually leads to the entry of energetic particles of solar origin from midnight sector, followed by loading and unloading of particles in the magnetotail resulting in geomagnetic substorms. These substorms are often referred to as Akasofu-type substorms. Other than this classical understanding of substorm, there can also be an alternate particle entry mechanism which can trigger weak to moderate substorms. Some earlier studies have

demonstrated that there is a ~50% probability that an interplanetary shock, if strong enough, will trigger a substorm even when there is no southward turning of IMF prior to the onset (Rostoker 1968; Schieldge and Siscoe, 1970; Kawasaki et al., 1971). However, the mechanism involved during such shock-induced substorms are not well understood. An intense substorm event of 21st January 2005, reported by Hajra and Tsurutani (2018), was anticipated to have been triggered by a sudden impulse of solar wind. There was a strong pressure pulse coinciding with the substorm onset and southward component of interplanetary magnetic field was absent for more than ~1.5 hours prior to the onset. The authors of Hajra and Tsurutani (2018) concluded that the magnetospheric energy input through magnetic reconnection either prior to the shock arrival or during the event were insufficient to power this event. There is no clear understanding of how such intense substorm can get triggered without the southward turning of IMF. This formed the motivation of our work. In order to understand the impulse induced supersubstorm evolution and energetics with better latitudinal and longitudinal coverage, we analyzed this substorm by using multi-instrument analysis technique. In this chapter, this event is revisited with additional database of global cosmic noise absorption (CNA), electron and proton auroral images by IMAGE satellite, energetic electron flux data from geostationary satellites and magnetic field measurements covering almost all the available latitudinal and local time sectors. It is observed that during the initial ~ 10 minutes of the substorm onset, AL index reached ~-2000 nT with particle precipitation being centered near dawn and not midnight. The prominent mid-night sector ground observations during a substorm, like most intense aurora, maximum westward electrojet current and highest cosmic noise absorption, were all observed in the dawn sector for the present event. The usual substorm expansion phase during which dipolarization and plasmoid formation takes place in the night side, started when IMF turned southward after ~10 minutes of the first onset of this day. Using this case study we explain in this chapter the characteristics of shock-triggered substorms and the energy source to power such strong events. The mechanism we suggest for the entry of particles into the magnetosphere during this substorm is the injection from the flanks due to K-H instability which is caused by strong velocity shear. Further, the precipitation of these injected particles into the ionosphere during the initial ~10 minutes of this substorm is attributed to localized wave-particle interactions.

In this chapter we emphasize on the fact that the local time sector and the behavior of precipitating particles during substorms cannot be limited to a single mechanism. If intense enough, pressure pulse can play a major role in triggering a substorm away from midnight.

Chapter IV

After establishing the fact that shock-induced substorms can have particle entry mechanism different from that during the normal Akasofu-type substorms, we discuss in this chapter the differences in their ground-based observations such as visual aurora, cosmic noise absorption (CNA) characteristics, and auroral electrojet current signatures. This is done using substorm events having distinctly different IMF and sudden impulse conditions. It is explained how one can initially categorize a substorm as an impulse-induced one or an IMF-induced one based on the SuperMAG SML-LT index (Newell and Gjerloev, 2011; Gjerloev, 2012). During normal Akasofu-type substorms, enhancement in ionospheric conductivity, most intense aurora and strengthening of auroral electrojet current happen in the midnight sector. Whereas, these prominent substorm signatures are observed in the extended local time either during impulse-induced substorms or during IMF By induced substorms. The average local time for the auroral breakup or substorm onset also changes (from 22.5 MLT to 23.5 MLT) with change in IMF By (negative to positive) (Ostgaard et al., 2011; Liou and Newell, 2010). With the help of unique events, having the presence of both IMF Bz and sudden impulse prior to the onset, we then explain how to further confirm the triggering mechanism associated with a substorm event.

A strong pressure pulse can inject solar wind particles inside the magnetosphere via viscous interaction. Since particle injection via viscous interaction due to KH instability is dawn/dusk favorable (Axford and Hines, 1961), these time sectors become the most probable region for particle injection from the magnetosphere. We show in this chapter that when pressure pulse is not strong enough to inject the solar wind particle from the flanks, the particles follow the usual trajectory to precipitate from the night side via magnetic reconnection. For the case when the pressure pulse is strong enough to overcome the influence of magnetic reconnection, and hence the particles are injected from the flanks and precipitated down the field line from dawn and dusk sectors. It is concluded in this chapter that it is the magnitude of pressure pulse

and IMF that will eventually determine whether a substorm will have its onset from the mid-night sector or from the dawn/dusk when both the triggering agents are present.

Chapter V

In addition to the substorm phenomena, solar energetic particle precipitation can also take place from the cusp region during solar proton events (SPE). These SPEs are associated with a sudden release of magnetic energy from the surface of the Sun, or as we call 'solar flares' (Bland et al., 2018). During SPE, high energetic protons get direct access into the Earth's atmosphere at high latitudes and can reach D-region ionosphere, thereby, enhancing the ionization at those altitudes. The absorption of cosmic radio signals due to these events are referred to as Polar Cap Absorption or PCA. In this chapter, PCA event has been discussed with the help of suitable case studies.

Along with energetic plasma particles, solar flare also releases intense electromagnetic radiation towards the Earth. The X-ray radiation coming from the solar flares penetrates deep into the atmosphere and ionizes the D-region. This leads to solar flare associated cosmic noise absorption or SCNA over the entire solar illuminated part. In this chapter, we also discuss SCNA events at high latitudes associated with strong solar flare events. It is concluded that even for similar solar zenith angles, the effects of the M and X class flares are stronger in the auroral region than the sub-auroral region. This asymmetry in SCNA is attributed to the background ionization of D-region at auroral latitudes during Solar Proton Events (SPE).

Chapter VI

This chapter summarizes the important results and findings of the present thesis along with the scope of future work. Different aspects of magnetosphere-ionosphere coupling system, whether it be via particle precipitation during substorms, or cusp region precipitation or solar X-ray radiation causing enhancement in ionization, has been analyzed using the multi-instrument analysis technique. We emphasize that the idea of substorms being a more general phenomena is a very important addition to the understanding of magnetosphere-ionosphere

coupling system. The evidences of new entry points from the flanks during impulse-induced substorms, discussed in this thesis, is a novel addition to the current theory of substorms. The study of solar flare associated CNA at high latitudes reveals that the background condition plays a very crucial role during isolated SCNA, when there is no substorm happening simultaneously. We observe significant difference in the SCNA at nearly equal solar-illuminated parts of the two hemispheres at high latitude D-region, which one would not expect to observe.

Present thesis highlights the importance of conducting integrated multi-instrument analysis, to understand the mechanisms involved in the solar-terrestrial interactions during disturbed periods like substorms, SPEs and solar X-ray radiations, leading to the better understanding of magnetosphere-ionosphere coupling.

Bibliography

Allen J. H. and Kroehl H. W. (1975), Spatial and temporal distributions of magnetic effects of auroral electrojets as derived from AE indices; *J. Geophys. Res*. 80 3607–3677.

Andersson, M. E., Verronen, P. T., Marsh, D. R., Seppälä, A., Päivärinta, S.-M., Rodger, C. J., M. A. Clilverd, N. Kalakoski, and M. van de Kamp, M. (2018). Polar ozone response to energetic particle precipitation over decadal time scales: The role of medium-energy electrons. *Journal of Geophysical Research: Atmospheres*, 123, 607–622.https:// doi.org/10.1002/2017JD027605

Ansari Z. A. (1964). The aurorally associated absorption of cosmic noise at college, Alaska; *J. Geophys. Res*. 69 4493–4513.

Artamonov, A.A., Mishev, A.L., & Usoskin, I.G. (2016). Atmospheric ionization induced by precipitating electrons: Comparison of CRAC: EPII model with a parametrization model. *Journal of Atmospheric and Solar-Terrestrial Physics*, 149, 161–166, https: //doi.org/10.1016/j. jastp.2016.04.020

Axford W. I., C.O Hines. (1961). A unifying theory of high-latitude geophysical phenomena and magnetic storms. Can. J. Phys., 39 (1961), p. 1433

Bailey D. K., (1964). Polar Cap Absorption. Planet. Space Sci. 1964. Vol. 12. pp. 495 to 541.

Baumjohann, W. and Treumann, R. (1996). Basic space plasma physics. World Scientific.

Behera, J. K., A. K. Sinha, A. K. Singh, R. Rawat, G. Vichare, A. Dhar, B. M. Pathan, K. U. Nair, C. Selvaraj, and P. Elango (2014), First results from imaging riometer installed at Indian Antarctic station Maitri, *J. Earth Syst. Sci*., 123(3), 593–602.

Behera, J. K., A. K. Sinha, G. Vichare, O. Kozyreva, R. Rawat, and A. Dhar (2016), Dayside cosmic noise absorption at the equatorward boundary of auroral oval as observed from Maitri, Antarctica (L=5; CGM 62.45°S, 55.45°E), J. Geophys. Res. Space Physics, 121, 3198–3211, doi: 10.1002/2016JA022418.

Bland, E. C., Heino, E., Kosch, M. J., & Partamies, N. (2018). SuperDARN radar-derived HF radio attenuation during the September 2017 solar proton events. Space Weather, 16. https://doi.org/10.1029/2018SW001916

Browne, S., J.K. Hargreaves and B. Honary (1995). An imaging riometer for ionospheric studies, *Electronics and Communication Engineering Journal*. Doi: 10.1049/ecej: 19950505

Burch, J. L. (1972). Preconditions for the Triggering of Polar Magnetic Substorms by Storm Sudden Commencements, *J. Geophys. Res.*,vol 77, no. 28. Page: 5629-5632 https://doi.org/10.1029/JA077i028p05629

Carlson, C. W., Pfaff, R. F., & Watzin, J. G. (1998). The Fast Auroral SnapshoT (FAST) mission. Geophysical Research Letters, 25(12), 2013–2016. https://doi.org/10.1029/98GL01592

Frey H. U., Mende S. B., Angelopoulos V. and Donovan E. F. (2004). Substorm onset observations by IMAGE-FUV; *J. Geophys. Res.* 109 A10304.

Gjerloev, J. W. (2012). The SuperMAG data processing technique, *J. Geophys. Res.*, 117, A09213, doi: 10.1029/2012JA017683.

Hajra R., Tsurutani B. T. (2018). Interplanetary Shocks Inducing Magnetospheric Supersubstorms (SML<−2500nT): Unusual Auroral Morphologies and Energy Flow, *The Astrophysical Journal*, 858:123 (6pp), doi: 10.3847/1538-4357.

Hargreaves J. K., H. Banta, A. Banta and E. Turunen and T Turunen. Observations of the Polar Cap Absorption event of February 1984 by the Eiscat Incoherent Scatter Radar. Planer. Space Sci., Vol. 35, No. 7, pp. 947-958, 1987

Jelly, D., and N. Brice (1967), Changes in Van Allen radiation associated with polar substorms, J. Geophys. Res., 72(23), 5919–5931, doi: 10.1029/JZ072i023p05919

Jones, S. L., Lessard, M. R., Fernandes, P. A., Lummerzheim, D., Semeter, J. L., Heinselman, C. J., et al. (2009). PFISR and ROPA observations of pulsating aurora. Journal of Atmospheric and Solar-Terrestrial Physics, 71(6-7), 708–716. https://doi.org/10.1016/j. jastp.2008.10.004

Kawasaki, K., S.-I. Akasofu, F. Yasuhara, and C.-I. Meng (1971). Storm sudden commencements and polar magnetic substorms, *J. Geophys. Res.,* 76, 6781.

Kellerman, A. C. (2009). On the relationship between auroral absorption, electrojet currents and plasma convection; *Ann. Geophys.* 27473–486.

Liou, K., & Newell, P. T. (2010). On the azimuthal location of auroral breakup: Hemispheric asymmetry. *Geophysical Research Letters*, **37**(23), 1– 5. https://doi.org/10.1029/2010GL045537

Little C. G. (1954). High latitude ionospheric observations using extra-terrestrial radio waves. Proc. IRE 42, 1700.

Little C. G. and Leinbach H. (1958). Some measurements of high-latitude ionospheric absorption using extra-terrestrial radio waves. Proc. IRE 46, 33&348.

Little C G and Leinbach H. (1959). The riometer – a device for continues measurement of ionospheric absorption; Proc. IRE 47 315–320.

Matthews, D. L., T. J. Rosenberg, J. R. Benbrook, and E. A. Bering III (1988), Dayside energetic electron precipitation over the South Pole (g = 75), J. Geophys. Res., 93, 12,941–12,945, doi: 10.1029/JA093iA11p12941.

Meng, C. I., Tsurutani, B., Kawasaki, K., & Akasofu, S. I. (1973). Cross-correlation analysis of the *AE* index and the interplanetary magnetic field B_z component. *Journal of Geophysical Research*, **78**, 617– 629. https://doi.org/10.1029/JA078i004p00617

Mitra A. P. and Shain C. A. (1953). The measurement of ionospheric absorption using observations of 18.3 Mc/s cosmic radio noise; *J. Atmos. Terr. Phys.* 4 204–218.

Moro J, Denardini C M, Correia E, Abdu M A, Schuch N J and Makita K. (2012). A comparision of two different techniques for deriving the quiet day curve from SARINET riometer data; *Ann. Geophys.* 30 1159–1168.

Newell, P. T., and J. W. Gjerloev (2011). Evaluation of SuperMAG auroral electrojet indices as indicators of substorms and auroral power, *J. Geophys. Res.*, 116, A12211, doi: 10.1029/2011JA016779.

Newell, P. T., and C.-I. Meng (1992), Mapping the dayside ionosphere to the magnetosphere according to particle precipitation characteristics, Geophys. Res. Lett., 19(6), 609–612, doi: 10.1029/92GL00404.

Østgaard, N., J. Stadsnes, J. Bjordal, R. R. Vondrak, S. A. Cummer, D. Chenette, G. K. Parks,M. J. Brittnacher, and D. L.McKenzie (1999), Global scale electron precipitation features seen in UV and X rays during substorms, J. Geophys. Res., 104, 10,191–10,204, doi: 10.1029/1999JA900004.

Østgaard, N., Laundal, K. M., Juusola, L., Åsnes, A., Håland, S. E., & Weygand, J. M. (2011). Inter hemispherical asymmetry of substorm onset locations and the interplanetary magnetic field. *Geophysical Research Letters*, **38**(8), 1– 5.https://doi.org/10.1029/2011GL046767

Rees, M. H. (1963). Auroral ionization and excitation by incident energetic electrons. Planetary and Space Science, 11(10), 1209–1218. https://doi.org/10.1016/0032-0633 (63)90252-6

Rogers, N. C., A. Kero, F. Honary, P. T. Verronen, E. M. Warrington, and D. W. Danskin (2016). Improving the twilight model for polar cap absorption nowcasts, Space Weather, 14, 950–972, doi: 10.1002/2016SW001527.

Rostoker, G. (1968). Relationship between the Onset of a Geomagnetic Bay and the Configuration of the Interplanetary Magnetic Field, *J. Geophys. Res.* vol 73, no. 13.

Schieldge, J.P., and G. L. Siscoe (1970). A correlation of the occurrence of simultaneous sudden magnetospheric compressions and geomagnetic bay onsets with selected geophysical indices, *J. Atmos. Terr. Phys.*, 32, 1819.

Stauning, P., 1996. Investigations of ionospheric radio wave absorption processes using imaging riometer techniques. J. Atmos. Terr. Phys. 58 (6), 753–764.

Swift, D. W. (1978). Mechanisms for the discrete aurora—A review. Space Science Reviews, 22(1), 35–75. https://doi.org/10.1007/ BF00215813

Tsurutani, B. T., and C. I. Meng (1972). Interplanetary magnetic-field variations and substorm activity, *J. Geophys. Res.*, 77, 2964–2970, doi: 10.1029/JA077i016p02964.

Tsurutani, B. T., Hajra, R., Echer, E., & Lakhina, G. S. (2019). Comment on "First Observation of Mesosphere Response to the Solar Wind High-Speed Streams" by W. Yi et al. Journal of Geophysical Research: Space Physics, 124, 8165- 8168. https://doi.org/10.1029/ 2018JA026447.

Zhou, X., Tsurutani B. T. (2001). Interplanetary shock triggering of nightside geomagnetic activity: Substorms, pseudobreakups, and quiescent events. *J. Geophys. Res.* Paper number2000JA003028, doi: 0148-0227/01/2000JA003028

(Shipra Sinha) (Prof. Geeta Vichare)

Candidate Supervisor